UNIVERSITY OF CAMBRIDGE

Hydrogen Cryosorption of Micro-Structured Carbon Materials

Xiao Teng

Queens' College

Department of Materials Science and Metallurgy

University of Cambridge

Dissertation submitted for the degree of Doctor of Philosophy

May 2017

Declaration

This dissertation is the result of my own work and includes nothing which is the outcome of work done in collaboration except as declared in the Preface and specified in the text. It does not exceed the prescribed word limit by the Degree Committee for the Faculty of Physics & Chemistry.

It is not substantially the same as any that I have submitted, or is being concurrently submitted for a degree or diploma or other qualification at the University of Cambridge or any other University or similar institution except as declared in the Preface and specified in the text. I further state that no substantial part of my dissertation has already been submitted, or is being concurrently submitted for any such degree, diploma or other qualification at the University of Cambridge or any other University or similar institution, except as declared in the Preface and specified in the text.

Xiao Teng

Acknowledgement

I would like to thank all those who have offered their selfless support during my PhD study. I would like to express sincere gratitude to my supervisor, Prof. Bartek A. Glowacki, for his invaluable tutorials and guidance in my research, as well as his encouragement in the pursuit of excellence. I would like to thank Dr Simon Hopkins for his consistent technical support and appreciate his time to proofread this thesis. I appreciate the continuous support from Dr Vassilka Tsaneva in collecting, analysing and discussing the Raman results. I would like to thank Dr Rumen Tomov for his vital support in experimental design and his valuable ideas for understanding the results.

I would also like to express my appreciation of the support from Katarzyna Juda for the plasma carbon analysis, Dr Witold Kwapinski for the pyrolysed Miscanthus samples, and the University of Limerick for access to the characterisation facilities. I am grateful to DZP Technologies for providing the superb graphene nanoplatelets for my project.

I would like to thank all former and current members of our big family in ASCG, Simon Hopkins, Anup Patel, Rumen Tomov, Vassilka Tsaneva, Tom Mitchell-Williams, Algirdas Baskys, who create a relaxed and friendly atmosphere for living and studying. I am very grateful to all my friends for making my life fun and enjoyable in Cambridge.

I would like to acknowledge the China Scholarship Council (CSC) and Cambridge Overseas Trust (COT) for funding my study. I would also like to thank the Education Office of Embassy of the People's Republic of China for their continuous support during my life in UK.

Finally, I am deeply indebted to my parents for all their loving support, and thank them for giving me the chance to study in such a lovely place.

Abstract

In comparison with the high-pressure adsorption at room temperature, hydrogen adsorption at cryogenic temperatures can be significantly improved at low pressures, which has great potential for prospective mobile applications. In this study, a differential pressure based manometry system was designed and constructed for fast analysing hydrogen adsorption uptakes of sorbents up to a maximum of 10 wt% at 77 K and up to 11 bar. The safety design of the system in compliance with European ATEX directives (Zone 2) for explosive atmospheres was discussed in detail, together with additional pneumatic systems for remote control of the experiments. A thorough error analysis of related experimental tests was also performed.

Common carbon sorbents, including several Norit branded activated carbons and graphene nanoplatelets (GNPs) with various surface areas, were characterised for their pore structures. The structural differences among GPNs of different surface areas were also studied. The hydrogen adsorption isotherms of these sorbents, examined in the newly-built manometry system, were further analysed and discussed with reference to the assessed microstructural properties. The carbonisation processes of plasma carbons from the microwave splitting of methane, and biochars from the pyrolysis of *Miscanthus,* were intensively studied primarily based on Raman spectroscopy, in conjunction with other characterisation techniques such as XRD, FTIR and XPS, for exploring the formation of graphitic structures and crystallinity under various conditions.

Two selected types of carbons, the activated carbon AC Norit GSX with a specific surface areas of 875 m^2/g and the graphene nanoplates with a specific surface area of 700 m^2/g, were decorated with palladium nanoparticles in different compositions. The growth and distribution of doped palladium particles in the carbon substrates were studied, and their effects on porous properties and microstructures of the sorbents were also reviewed. Hydrogen adsorption tests of the decorated carbons were further conducted and discussed, to explore the potential effects of Pd contents on the adsorption kinetics and hydrogen absolute uptakes.

List of Abbreviations

AC	Activated Carbons
ATEX	ATmosphères EXplosibles – European ATEX directives for equipment designed for working in an explosive atmosphere
a.u.	Arbitrary Unit
BET	Brunauer – Emmett - Teller methods for determining surface areas
BJH	Barrett - Joyner - Halenda method for pore size distribution analysis
BSE	Back Scattered Electrons
CFRP	Carbon Fibre Reinforced Plastic
CT	Carbon Template
DOE	U.S. Department of Energy
EDX	Energy Dispersive X-ray analysis
FEGSEM	Field Emission Gun Scanning Electron Microscopy
FFT	Fast Fourier Transform
FR	Ferrari and Robertson theory / model for interpreting Raman results of graphitic structures
FTIR	Fourier Transform Infrared Spectroscopy
FWHM	Full Width at Half Maximum
GNPs	Graphene Nano-Platelets
HJ	Harkins and Jura equation for t-method
LdB	Lippens and de Boer theory for t-method
MOFs	Metal-Organic Frameworks
SE	Secondary Electrons
SEM	Scanning Electron Microscopy
SSA	Specific Surface Area, normally in the unit m^2/g
STP	Standard condition for Temperature and Pressure (0 °C, 101.325 kPa)
TEM	Transmission Electron Microscopy
TGA	Thermal Gravimetric Analysis
XPS	X-ray Photoelectron Spectroscopy
XRD	X-Ray Diffraction analysis

List of Symbols

a_{BET}	BET specific surface area
a_{ext}	External (or meso- and macropore) surface area
a_{micro}	Micropore surface area
C	BET parameter
K_{c}	Shape factor in Scherrer's equation
d_{hkl}	Lattice plane spacing of (hkl) planes
L_{a}	Crystallite size in a-direction (sizes of graphitic layers)
L_{c}	Crystallite size in c-direction (size of graphitic structures in layer stacking direction)
N_A	Avogadro constant, 6.02×10^{23} mol^{-1}
n_{m}	Monolayer capacity in adsorption
n_{micro}	Adsorbed quantity in micropores (specific micropore capacity)
n_{ref}	The quantity adsorbed in a α_{s} reference data
$n_{\mathrm{ref\,(0.4)}}$	The quantity adsorbed at the relative pressure of 0.4 in a α_{s} reference data
ΔP	The induced differential pressure in sorption experiment
p	The general expression for pressure conditions
p_0	Saturated vapour pressure
p/p_0	Relative pressure
P_{i}	The initial static pressure in the reservoir bottles of both systems at step 2 (Figure 6.6.1 in section 6.6) of the hydrogen cryosorption experiment
p^{g}	The pressure of gas phase in Young-Laplace equation
p^{l}	The pressure of liquid phase in Young-Laplace equation
R	Gas constant, 8.314 J/(K·mol)
r_{m}	Mean radius of curvature

T	The general expression for temperature condition
T_{c}	The cryogenic temperature – 77 K achieved with liquid nitrogen bath in hydrogen cryosorption tests
T_{r}	Room temperature measured by the average of two temperature sensors in hydrogen cryosorption tests
$\overline{v}$	Specific volume in Van der Waals equation of state
v^{g}	Molar volume of gas phase
v^{l}	Molar volume of liquid phase
v_{micro}	Specific micropore volume
V_{r}	The reservoir volume in the testing system where the adsorbate is located before it is released into the sorbent chamber under vacuum during the experiment
$V_{\mathrm{ref-r}}$	Analogous reservoir volume to V_{r} in the reference system
V_{s}	The revised sample chamber volume submerged in liquid nitrogen with the sorbent volume (mass/density) subtracted in the testing system
$V_{\mathrm{ref-s}}$	The sample chamber volume in reference system
V_{t}	The tubing volume below the sample-inlet valve (V2 valve in Figure 6.7.1) at room temperature
$V_{\mathrm{ref-t}}$	Analogous tubing volume to V_{t} in the reference system
wt%	Weight percentage of hydrogen uptake regarding the weight of sorbent
Z	The compressibility factor in real gas law
Z_1	The compressibility of hydrogen gas at room temperature during the cryosorption test
Z_2	The compressibility of hydrogen gas at 77 K during the cryosorption test
α_{s}	Alpha-s method for analysing micropore properties
γ	Surface tension of liquid
β	Full width at half maximum (FWHM)
λ	Wavelength

Table of Contents

1 Introduction

There are two primary tasks of the research presented in this thesis. The first task is to present a detailed design for implementing differential manometry to measure hydrogen cryosorption at 77 K and pressures up to 10 bar. The second task is to evaluate some carbon based porous sorbents for their porous properties and to measure their hydrogen adsorption capacities at 77 K using the constructed measuring system.

By contrast with the popular Sievert's type volumetric system based on single or multiple static pressure transducers, differential manometry – which directly measures the induced differential pressure by gas adsorption – offers better accuracy and a faster response to small gas uptakes during hydrogen adsorption thanks to the application of a differential pressure transducer with small pressure range. Although several designs of differential manometry have been reported for measuring hydrogen adsorption at room temperature and high pressures of hundreds of bars, the differential manometry for measuring hydrogen adsorption at cryogenic temperatures, such as 77 K, has not been reported. In this thesis, the design of a differential manometry system for hydrogen adsorption tests at 77 K is presented. In addition to the basic construction of a volumetric system, several precautions for handling potential safety risks of compressed hydrogen gas have also been presented, such as the construction of a pneumatic control system, automated measuring processes and a reinforced hydrogen cell with high flowrate extraction.

The sorbents studied include both amorphous carbons, such as activated carbons AC Norit GSX and AC Norit ROW, and porous carbons with high crystallinity, such as graphene nanoplatelets (GNPs), GNPs-500 and GNPs-700. These carbon sorbents were studied systematically for their pore sizes, pore areas and pore volumes on both the micropores and the mesopores, depending on the nitrogen adsorption isotherms at 77 K. A study of two carbons, plasma carbons from the microwave splitting of methane and biochars from the pyrolysis of *Miscanthu*s, was conducted to investigate the structural evolution of carbon contents during manufacturing. The evolution of structural properties in graphene nanoplatelets was also studied in relation to the increase in surface areas. Several theoretical methods, including the BET method, the Harkins-Jura t-method, and the α_s-method, which have been discussed in section 2.3, and characterisation techniques, including TEM, SEM, XRD

and Raman spectroscopy, were implemented to analyse the micro-structures of the sorbents. Hydrogen cryosorption at 77 K and pressures up to 11 bar were measured on these carbon sorbents in comparison with microporous zeolites 13X and NaY. The decoration of Pd on two carbons, AC Norit GSX and GNPs-700, and its influence on hydrogen cryosorption behaviour was also studied.

In this thesis, section 2 reviews the background of previous hydrogen storage research, including an overview of the hydrogen economy, the common sorbents for hydrogen adsorption, the relevant theories for studying adsorption behaviours and the general apparatus designs for measuring adsorption uptakes. Section 3 illustrates the hypotheses raised in this study, and section 4 describes the origins and manufacturing processes of the materials investigated. The characterisation techniques, including equipment details and measurement parameters, are reported in section 5. Section 6 covers every aspect of the design and construction in building the differential manometry system. The porous properties of sorbents, structural evolution of plasma carbon, biochars and graphene nanoplatelets, and the hydrogen cryosorption uptakes of these porous sorbents, are discussed in detail in section 7. Finally, section 8 presents the conclusions of this study in addressing the hypotheses in section 3.

2 Background

2.1 The rise of the hydrogen economy

After Thomas Newcomen developed a practical steam engine in 1712, the great improvements in engine efficiency introduced by James Watt provided the ability to convert fuels into mechanical energy [1], which led the world into a remarkable industrial era and introduced coal as the main fuel. As a result of the invention of the oil refinery in the late 19th century and its prosperity in the early 20th century, oil began to play a vital role due to its high-energy density and convenience to transport, gradually achieving its position as the most important energy medium for transport and portable generators in the world after the 1950s. Because of restrictions in oil supply, there were several energy crises in the past several decades, as well as the realisation that there are limited reserves of oil, which has driven researchers to seek energy alternatives. The competition for strategic reserves of oil among nations introduced political tensions, and the excessive burning of fossil fuels has caused serious environment pollution all over the world. For example, excessive emissions of greenhouse gases, including CO_2, NO_x, etc., have led to global warming.

As a result, the Paris Agreement was reached around the world to reduce carbon emissions with the objective of limiting further deterioration of the environment. The atomic ratio of carbon to hydrogen in a fuel determines the amount of carbon released per mole of the fuel during combustion. As a result, the concept of “decarbonisation” has risen to evaluate the decrease of the carbon content in the fuel supply [2]. Wood, consisting of 80% cellulose ($(C_6H_{10}O_5)_n$) and 20% lignin ($(C_{10}H_{13}O_4)_n$), was first used as the primary energy source in human history, claiming a carbon-to-hydrogen ratio of about ten after subtracting the component of $(H_2O)_n$ [3]. Among fossil fuels, coal has the highest carbon contents at one or two times that of hydrogen. Oil is a little better, consisting of one carbon atom for each two hydrogen atoms, while natural gas, which is of growing importance in industry, contains one carbon atom for each four hydrogen atoms. Nevertheless, the amount of greenhouse gases keeps increasing all the time, which means that the decarbonisation effects of fuels on emission reduction are not yet sufficient to compensate for the increase in emissions due to growing energy consumption, resulting in the acceleration of global warming. Non-carbon fuels would be the

ideal answer to this serious environmental question, making hydrogen a very promising solution.

Hydrogen is widely favoured as an energy carrier for next generation energy systems due to its zero emissions and the large reserve of chemical energy, 142 MJ/kg, over three times that of hydrocarbon fuels [4]. Hydrogen is the most abundant element in the universe, making up 75 mass percent of the universe and 90 percent of its molecules [3]. Hydrogen is also the ideal fuel for many fuel cell systems, which could achieve high efficiency. Its wide distribution in materials, notably organic matter, hydrocarbons and obviously water, provides the possibility of it being produced from both renewable methods, such as the photolysis of water, and highly efficient chemical mass-production techniques, such as the reforming of natural gas.

However, there are obstacles to hinder the prosperity of the hydrogen economy. It is currently difficult to achieve mass production of hydrogen without any carbon footprint in its lifecycle. Notwithstanding that renewable methods, such as photolysis and wind powered reactions, still retain problems of low efficiency and high cost, some highly efficient techniques to produce hydrogen, such as the reforming of water using a nuclear-powered reactor, have proved feasible on a laboratory scale [5]. In comparison with the progress in hydrogen production, the remaining question of hydrogen research is the controversial storage techniques, for which there seems to be a lack of substantial development. Hydrogen gas is usually considered as a dangerous chemical due to the high risk of explosion when it is mixed with oxygen. High-pressure hydrogen tanks are currently the most common method to store and carry hydrogen, and they have proven to be safe enough for long distance transport and the distribution of hydrogen into stationary hydrogen stations [6]. Toyota introduced the world's first commercially sold hydrogen fuel cell car, Toyota Mirai, with a carbon fibre reinforced tank built in to store 700-bar pressurised hydrogen gas in 2014 [7]. Hyundai and Honda have also introduced their fuel cell cars with the similar technologies in recent years [8], [9]. Despite of these successes in research and commercial applications, the high pressure itself is difficult to be controlled, which requires costly pressure control units and expensive reinforced coatings on the storage tanks. Additionally, the safety concerns of the real hazards to passengers, from the potential release of intensively pressurised hydrogen

during collision, have also encouraged researchers to study alternative low-pressure techniques to store hydrogen in automobiles.

With the objective of reducing the risk of storing hydrogen at high pressure, either reducing the storage pressure of hydrogen gas or transferring the hydrogen into its liquid state could sufficiently meet the target, while both have their own restrictions in terms of feasibility and cost. In the next section, most of the common materials used for hydrogen adsorption and absorption, such as metal hydrides, metal-organic frameworks (MOFs), carbon nanoforms and other porous materials, will be reviewed in terms of their gravimetric uptake of hydrogen (wt%), applied pressure (*p*) and operating temperature (*T*).

2.2 Hydrogen storage techniques

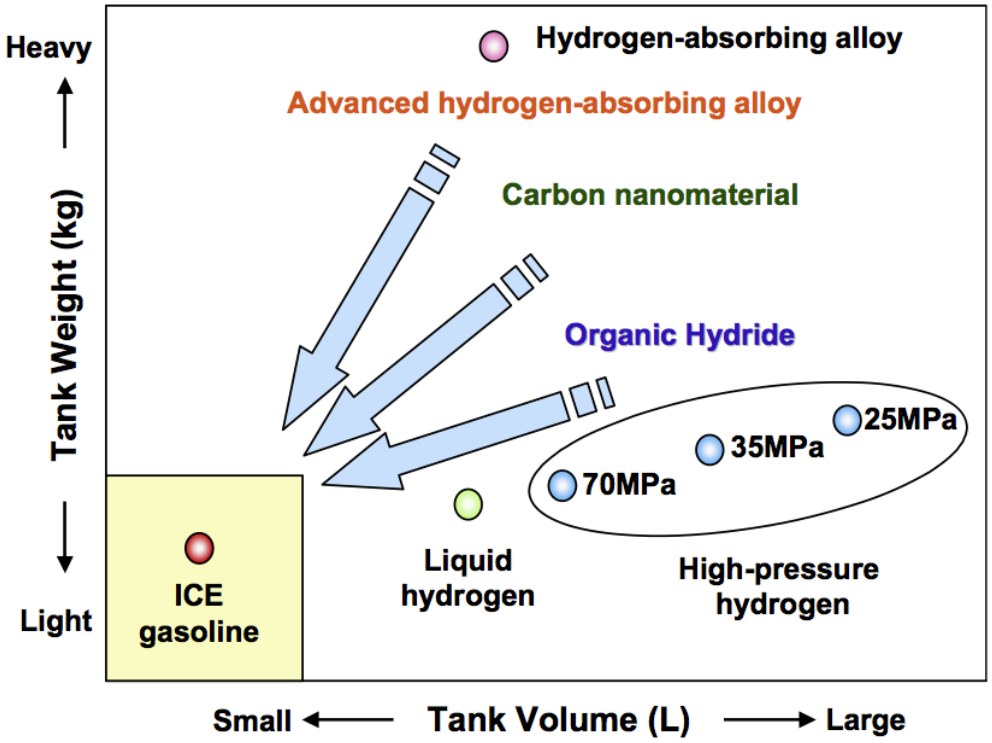

Figure 2.2.1 *Techniques and targets of hydrogen sorption [10].*

As indicated in x-axis and y-axis of Figure 2.2.1, the energy density of a storage system can be explained by both the volumetric uptakes and the gravimetric uptakes. According to the 2015 update of hydrogen storage section in "multi-year research, development, and demonstration plan", issued by Department of Energy (DOE), USA, the systematic target of hydrogen storage for light-duty fuel cell vehicles by 2020 is 5.5 wt% by mass or 40 kg/m^3 by

volume [6]. It is noted that the targets are for the complete storage and delivery system, including tank, material, valves, insulation, cooling and other components [6].

Since the equipment specifications (e.g. weight, material, volume, etc.) required to handle H_2 and sorbents depend mainly on the conditions, such as the pressure and temperature, of each storage system, researchers generally evaluate the wt% of hydrogen sorbed in respect of either the mass of sorbent or the total mass of sorbent and hydrogen contained. In this study, the former expression was adopted for consistency. It is noted that the hydrogen uptakes in respect of sorbent mass are generally the excess hydrogen uptake, because both the micro-balance methods and the pressure-rated methods only measure the hydrogen uptake adsorbed onto the pore surfaces of sorbents by either the weight changes or the pressure variance during the sorption, which is irrelevant to the surrounding gaseous hydrogen molecules. The total hydrogen uptake is often used to evaluate the capacity of a storage system, when both the excess uptakes and the compressed hydrogen gas should be considered. All sorption results reported in this study are excess hydrogen uptakes, which aims to illustrate the performance of sorbent itself.

By comparison with the gravimetric storage (wt%), the volumetric storage (kg/m^3) is difficulty to define a consistent and applicable expression for all studied sorbents, since the volume of porous sorbents is impossible to acquire an accurate measurement, especially for amorphous sorbents, like activated carbons. Some researchers used the apparent density to calculate the volumetric storage capacity, which was based on the method similar to ISO60 standard [11]. However, the measured results of lightweight porous materials via this method cannot be reliable, as whether the power or particles is packed loosely or tightly, as well as the handling in the test, can significantly influence the results. The other method applies the crystallographic volume that is theoretically calculated from the crystallographic structure of materials like metal-organic frameworks (MOFs), as described in reference [12], which is not applicable for amorphous materials or sorbents that is hard to identify their crystallographic structures.

Neither the volume of sample chamber nor the volume of sorbents excluding the pores that is measured through gas intrusion method can represent the right generic volumes of the porous sorbents. But it is possible to estimate the rough range of volumetric uptakes of

samples tested in this thesis. The sample vial used in this study is 2 ml in volume. The maximum hydrogen uptake measured for carbon samples is about 0.02 g, and the maximum uptake for tested zeolites is about 0.025 g. The estimated volumetric hydrogen uptakes (in respect of the container volume) are roughly 10 kg/m^3 for carbons and 12.5 kg/m^3 for zeolites, which is far from the systematic storage target of 40 kg/m^3. As the volumetric filling ratio of sorbent powders in the vial varies in each loading, the volumetric uptake estimated in respect of the vial volume cannot be used for evaluating the storage capacity of each sorbent. Instead, the gravimetric uptakes in wt% is more consistent and comparable to represent the H_2 uptake for each sorbent, no matter whether it is crystalline or amorphous. Thus, the gravimetric uptakes (in wt%) are widely applied in this thesis to represent the H_2 storage capacity of different sorbents.

Many new alloys, ceramics and composites have been reported for hydrogen sorption, such as metal hydrides, carbon structures, metal-organic frameworks (MOFs) and zeolites [10], [13]–[15]. Both the weight and the volume of storage systems for hydrogen storage need to approach the energy density of gasoline systems in automobiles prior to its wide applications. However, the energy densities of reported hydrogen storage methods still have a certain distance from the gasoline as described in **Figure 2.2.1**. In this section, most of the popular methods will be mentioned and analysed for advantages and disadvantages.

Three major evaluation parameters – pressure (*p*), temperature (*T*) and hydrogen weight percentage (wt%) – are considered in this analysis while commercial concerns are not imperative because most of the storage methods are still being studied in the laboratory. The U.S. Department of Energy (DOE) has reduced the previous target of 9.0 wt% hydrogen uptake to 5.5 wt% by 2020 because of the limited progress on recent hydrogen storage research for mobile applications [6]. For the crystalline sorbents, such as MOFs, the volumetric uptakes are also reviewed to compare with the DOE target of 40 kg/m^3. According to the calculation stated in reference [4], an automobile combustion engine with same efficiency requires 8 kg hydrogen, in comparison with 24 kg of petrol, to cover the same 400 km distance. BMW produced a limited amount of “hydrogen 7” model cars, which have a bivalent combustion engine built-in to use both gasoline and hydrogen as the fuel, from 2005 to 2007 [16]. The hydrogen fuel is stored in its liquid state at 20 K temperature, which was claimed by BMW to

offer 75% more volumetric energy density than a 700-bar compressed tank [17]. However, the liquid hydrogen started to boil after 17 hours of non-use, and was emptied completely in 10 - 12 days during the road test [17]. For a fuel cell system assumed to have the doubled efficiency of combustion engine, only 4 kg hydrogen is necessary to achieve the same distance, which means that about 10 wt% systematic hydrogen storage capacity can reach a similar energy density per unit mass with the petrol system if the storage equipment is assumed to take 30 – 40% of the total systematic weight. It is worth noting that the storage target set by DOE is regarded as systematic storage which means the weight of storage equipment is taken into considerations, although some carbon sorbents have proved to have gravimetric uptakes over 7 wt% in respect of the sorbents weight that cannot represent the storage systematic weight.

2.2.1 Metal hydrides

As early as 1974, the group of Wiswall [18] developed the metal-hydrogen reaction of FeTi and H_2, displaying remarkable hydrogen storage ability. Molecular hydrogen can be dissociated into two individual hydrogen atoms at the surface of the metal alloys; the metal alloys and hydrogen atoms are combined together to form metal hydrides, which could liberate H atoms reversibly in a thermodynamic process, as shown in **Figure 2.2.2** [4].

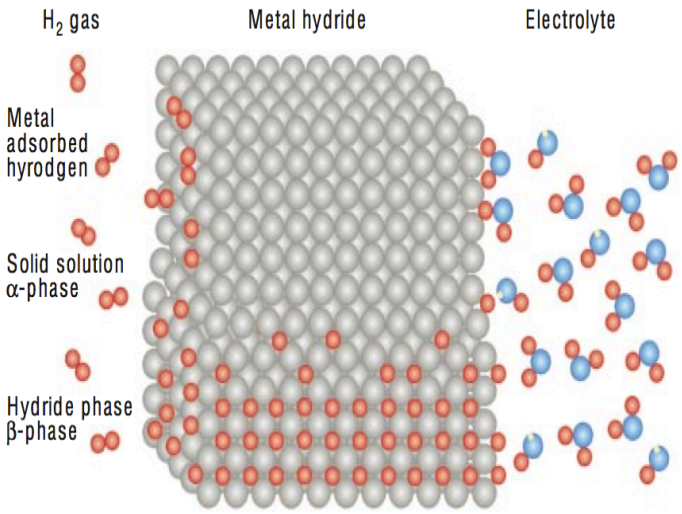

Figure 2.2.2 *A schematic diagram of the sorption mechanism in metal hydrides [3].*

In contrast with pressurised gas tanks, metal hydrides could store hydrogen reversibly in lower pressure conditions, e.g. temperatures of 77 K to 373 K and pressures of 1 - 10 bar. It is

reported that one of the popular metal alloys, $LaNi_5$, has the ability to store 1.37 wt% H_2 at 2 bar and 298 K, and for the A_2B type of metal hydrides, the operating conditions for 3.59 wt% of H_2 uptake are 1 bar at 555 K [19].

As shown in the overview of the materials discussed in **Figure 2.2.3** [4], where the horizontal axis represents the system weight percentage of stored hydrogen in the whole weight of the storage system, the hydrocarbon fuels generally have a system hydrogen weight percentage of over 15 % (marked as green rectangles in **Figure 2.2.3**), as does the liquid hydrogen method (blue), while metal hydrides (red) hold less than 5 system wt%. The metal alloys labelled in orange can store a weight percentage larger than the DOE target of 5.5 system wt%, but they usually have very poor performances in reversibly releasing hydrogen because of the hysteresis of their sorption and desorption of hydrogen, which is not compatible with the target for applications despite they achieve high gravimetric uptakes in overall adsorption [4]. Although these materials can store large quantities of hydrogen in proper pressure and temperature conditions, they are still far from commercial applications.

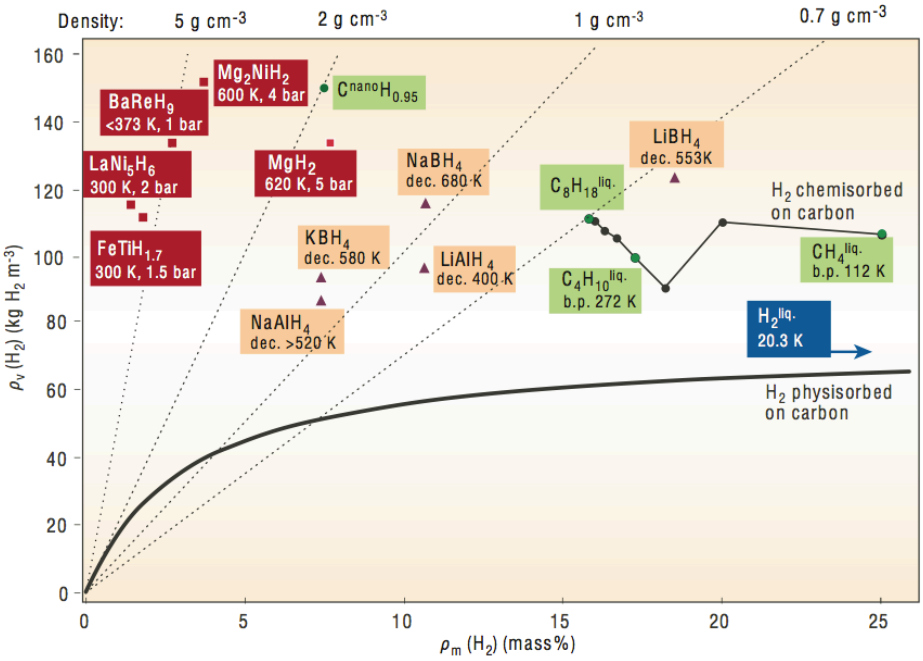

Figure 2.2.3 *Stored hydrogen in volumetric uptake versus mass percentage. Comparison among metal hydride, carbon nanotubes, petrol and other hydrocarbons [4].*

Except for the metal hydrides discussed that exhibits high hydrogen uptakes, another metal, palladium, can also exhibit a certain amount of hydrogen adsorption and absorption at room temperature reversibly. With the consideration of its high cost, palladium is rarely used as a

sole sorbent for hydrogen storage. Instead, palladium is commonly used as a catalyst for many industrial applications. As the palladium is studied as an additive to carbon sorbents in this study, the hydrogen absorption and spillover of palladium are reviewed here.

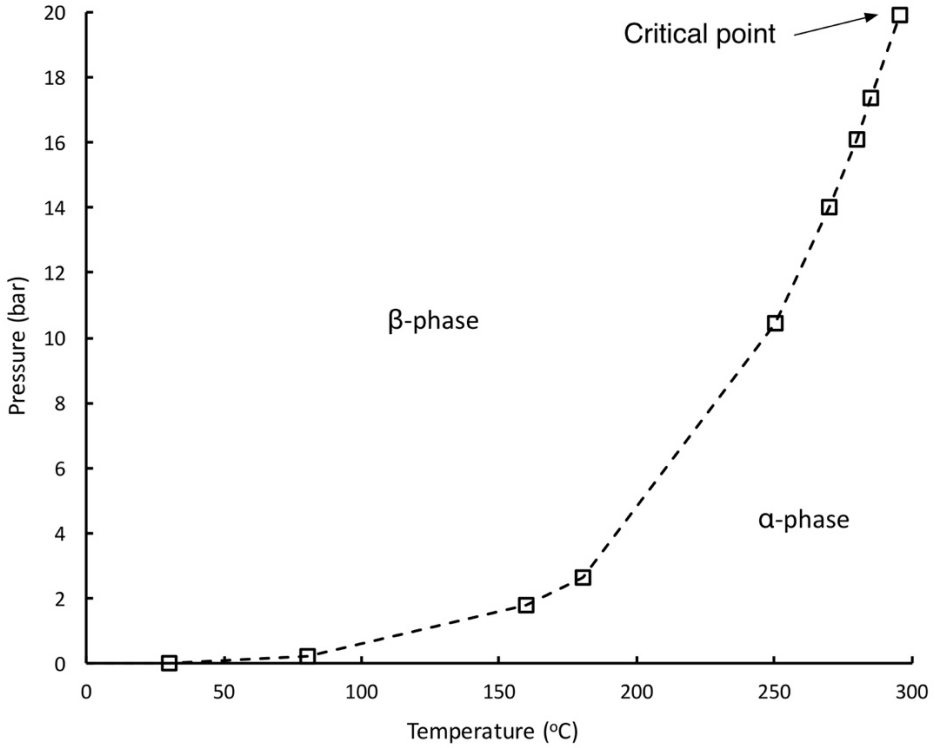

Figure 2.2.4 *Pressure-temperature phase diagram for the H:Pd system [20].*

Similar to many other metal hydrides, the sorption of palladium consists of the α-phase absorption and β-phase absorption. In a hydrogen-palladium system, hydrogen readily dissociates on the surface of palladium, and the hydrogen atoms diffuse into sublayers to form the palladium hydride [20]. The absorption of hydrogen in palladium does not change the lattice structure of pallidum metal, which is different with other metal hydride [20], [21]. The α-phase is a solution phase, in which the lattice constants are close to palladium metal with a hydrogen:palladium ratio (H:Pd or H/Pd) less than 0.03 at room temperature, while the lattice constants increase linearly with pressure to introduce the β-phase absorption with the H/Pd of approximate 0.6 at room temperature [20]. The α-phase and β-phase is found to coexist at certain pressures and in temperatures under around 300 ^{o}C [20]-[23]. The reduction of temperature and increase of pressure normally promotes the formation of β-phase palladium hydride [22], [23], which is also indicated in **Figure 2.2.4**. Above a critical point, as

described in **Figure 2.2.4**, the coexistence (dash line) of α- and β-phase no longer occurs. The palladium hydride will be either in α-phase or β-phase, depending on the actual condition.

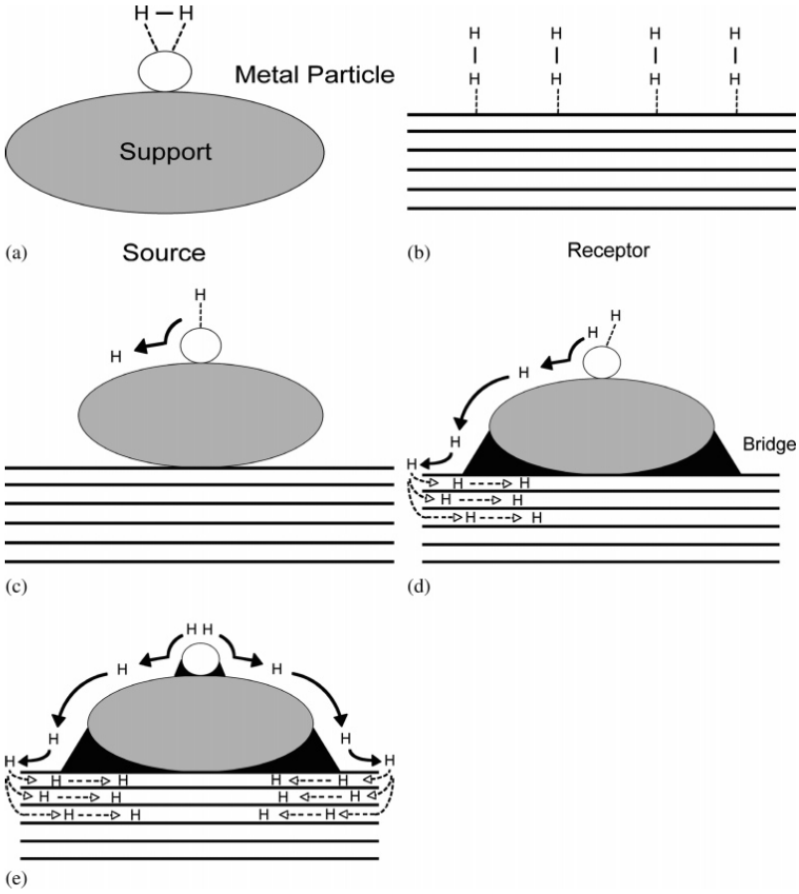

Figure 2.2.5 *Hydrogen spillover in a supported catalyst system: (a) adsorption of hydrogen on a supported metal particle; (b) the low-capacity receptor; (c) primary spillover of atomic hydrogen to the support; (d) secondary spillover to the receptor enhanced by a physical bridge; (e) primary and secondary spillover enhancement by improved contacts and bridges [24].*

Despite the continued work and research on the hydrogen spillover effect after its first introduction in 1960s [25], [26], the detailed mechanism are still not well understood [24]. Spillover was defined as the transport of adsorbed species from one site to another site that would not typically adsorb the species at normal conditions [27]. A brief description of hydrogen spillover process is shown in **Figure 2.2.5**. The hydrogen molecules are dissociated on the metal site, then diffuse to the support, which is called the primary spillover, as described in **Figure 2.2.5 (c)**. The hydrogen atoms further diffuse through the "bridges", as described in **Figure 2.2.5 (d)**, to the receptor, which is named as the secondary spillover. In this process, the "bridges" is crucial to reduce the barrier for hydrogen atoms to diffuse from

the support to the receptor, which were theorised to be created by pre-treament techniques or carbonisation of a precursor [24], [28]. The spillover effect is of particular interests for the graphite-like receptor, since the inter-planar spacing of graphitic layers restricts the access of molecular hydrogen [24]. Palladium has proven to be an excellent candidate to spillover hydrogen molecules [24]. The spillover effect introduced by palladium particles in palladium-AX21 mixtures has been verified experimentally to be able to increase the hydrogen capacity of AX21 receptor, a type of activated carbon, at room temperature [24]. Platinum, in the same group of palladium, was also found to have the similar hydrogen spillover effects [25], [26], [28].

2.2.2 Metal-organic Frameworks (MOFs)

Metal-organic frameworks (MOFs) are defined as a type of crystalline solid formed by the connection of metal ionic groups or clusters with molecular bridges [29]. MOFs draw significant attention because of their outstanding properties, such as high porosity, re-designable structure and straightforward modification for targeted properties. One model for the mechanism [29] (as shown in **Figure 2.2.6**) is that polymeric clusters act as bridges extending from metal crystalline centres, inducing the formation of voids surrounded by the frameworks. As the diameter of the hole is controllable, a large range of gas molecules with low molecular weight could be collected by this method, making MOFs a potential candidate for gas adsorption.

The kinetics of hydrogen sorption by microporous materials is generally very rapid, and cryogenic temperatures, such as 77 K, are normally required to achieve significant capacities at low pressures [30]. In terms of the sorption results shown in **Table 2.2.7**, the tests were conducted at relative low pressures (20 – 70 bar) and relatively low temperature (77 K), both of which are achievable. The high porosity achieved in MOFs sometimes results in large pores, which leads to a low volumetric storage, because the hydrogen gas is simply compressed within the empty pores [31]. For instance, in **Table 2.2.7**, MOF-210 and MOF-177, which had higher gravimetric excess uptake than NU135, exhibited worse volumetric densities. Although the excess volumetric density of MOF-210 is below the DOE target of 40 kg/m^3, the total volumetric density with the compressed hydrogen gas in pores considered is 44 kg/m^3 [32], which exhibits a great potential to fulfil the volumetric target with appropriate storage system

designs. As described in **Table 2.2.7**, it is obvious that high porous MOFs with high surface areas can achieve promising hydrogen uptakes in both gravimetric and volumetric densities. However, most of the high-performance MOFs reported are still in laboratory scale, and their mass production remains problematic.

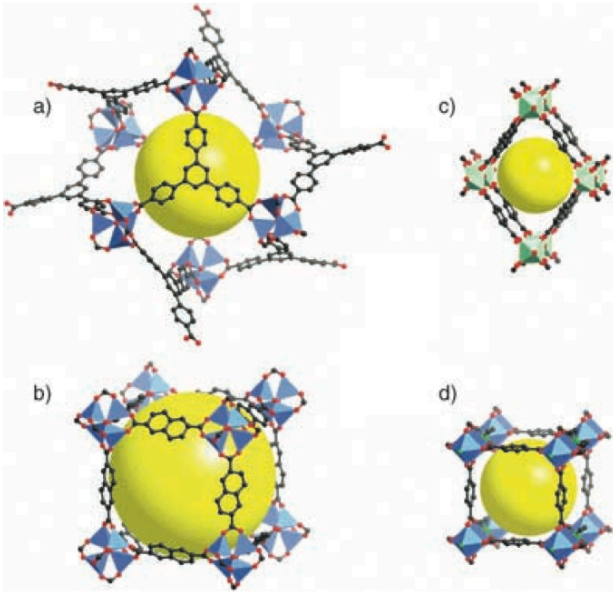

Figure 2.2.6 *Examples of MOFs: a) MOF-177, b) IRMOF-8, c) MIL-53 and d) Zn2-(bdc)2(dabco) (dabco = 1,4-diazabicyclo[2.2.2]octane) [29].Yellow balls represent the voids inside.*

Table 2.2.7 *Gravimetric hydrogen uptakes of MOFs at 77K, 1 atm.*

Material	Excess H_2 Uptake (gravimetric wt%)	Excess H_2 Uptake (volumetric, kg/m^3)	Apparent Surface Area (m^2/g)	Pore Volume (cm^3/g)	Conditions
NU-135 [33], [34]	5.1	49	2600	1.02	77 K, 55 bar
UiO-66 [35]	3.35	-	1358	-	77 K, 18 bar
NJU-Bai12-ac [36]	5.53	-	3038	1.135	77 K, 20 bar
NU-100 [37]	9.95	-	6143	2.82	77 K, 70 bar
MOF-210 [32]	8.6	21.5	6240	3.60	77 K, 60 bar
MOF-5 [12]	5.1	-	3100	-	77 K, 40 bar
UMCM-1 [38]	6.88	-	5200	-	77 K, 46 bar
MOF-177 [39]	7.6	32	4750	1.69	77 K, 66 bar

2.2.3 Conventional compressive tanks

High-pressure hydrogen tanks are designed to store hydrogen gas in pressure resistant tanks from 300 bar to 700 bar, and it is the most widely used technique nowadays. Hua et al. [40] made a technical assessment of compressive hydrogen storage systems, of which the results indicated that the gravimetric capacity of usable hydrogen in 350 bar tanks could reach 5.5 wt%. Considering the efficiency of the system and the chemical energy of the fuels, a combustion engine burns about 24 kg of petrol to cover a range of 400 km, while hydrogen fuel cell cars could use only 4 kg hydrogen to drive a similar distance. To store 4 kg of hydrogen at a pressure of 350 bar, around 150 litres of volume needs to be reserved, while a family-use car has a typical fuel capacity of approximately 80 litres: the extra space of 70 litres needed to install a 350-bar tank is clearly impractical.

Carbon Fibre Reinforced Plastic (CFRP) tanks have been introduced with the outstanding pressure resistance of nearly 700 bar. Nevertheless, this new type of tank needs a special and expensive reinforced coating to prevent corrosion, and it is also environment sensitive. Experimental tests indicated that the fatigue strength of CFRP reinforced tanks was influenced by temperature [41]. In spite of these disadvantages, the CERP tanks have proven to be feasible in commercial automobiles by car manufactures, such as Toyota [7], Hyundai [8] and Honda [9]. For instance, in Toyota Mirai, two triple-layer CEFR tanks with a total volume of 122.4 L are placed inside the vehicle to achieve a normal operating pressure of 700 bar, which results in a systematic storage density of 5.7 weight% and storing approximate 5 kg hydrogen in total [7]. However, high pressure itself increases the risk of explosion especially during crashes, and extra pressure control devices are needed to deal with the huge pressure difference between the high storage pressure and the low application pressure [4], which needs a lot of effects to reduce public concerns and reduce the cost to further increase its popularity.

2.2.4 Zeolites and Activated Carbons

Thanks to the microporous structure of zeolites, the surface areas of zeolite samples are generally large, varying from 400 m^2/g^{-1} to 1000 m^2/g depending on the types [15], [42]. The hydrogen sorption on zeolites is generally examined at 77 K, since the cryogenic adsorption can achieve large quantities of hydrogen uptakes of 1 – 2 wt% at relatively low pressures of

several MPa [15], [42]–[45]. Although different metal ions are contained in various types of zeolite structures, the hydrogen uptakes of different zeolites are dominated by the ideal adsorbent-adsorbate adsorption. Notwithstanding the fact that pores of faujasite framework zeolites, such as X type and Y type zeolites, are similar to each other, zeolite X was revealed to have a greater hydrogen uptake than zeolite Y, with similar surface areas, which was believed to correlate with enhanced binding effects of more cations sites in the X type zeolite [45]. As surface areas on zeolites are rarely over 1000 m^2/g, the maximum hydrogen uptakes are limited to the quantity around 2 wt%.

Activated carbons are normally prepared from carbonaceous materials, such as wood and coal, through an activation process of exposing them to oxidizing atmospheres, for instance, oxygen or steam at high temperatures [46]. In comparison with zeolites, activated carbons have been reported to have much larger surface areas, for instance, over 3000 m^2/g for AC-K5, giving a hydrogen uptake about 7 wt% at 77 K and 20 bar pressure [46], and carbon B for 4.5 wt% at 77 K and 10 bar pressure [47]. For commercial products of activated carbon, the surface areas are normally below 1500 m^2/g, about half of the reported highest surface areas for activated carbons. Although the 7 wt% excess uptake has great potential to meet the DOE systematic target of 5.5 wt%, there are still challenges remaining to produce activated carbons with higher surface areas than 3000 m^2/g in mass-production and cost-effective methods.

2.2.5 Carbon materials: nanoforms, graphane and graphene

When grain sizes are decreased to nanoscale, or even atomic scale, the Van der Waals force dominates surface forces instead of gravity. Owing to intermolecular forces, the most stable position for an attached molecule is about one molecular radius away from the surface.

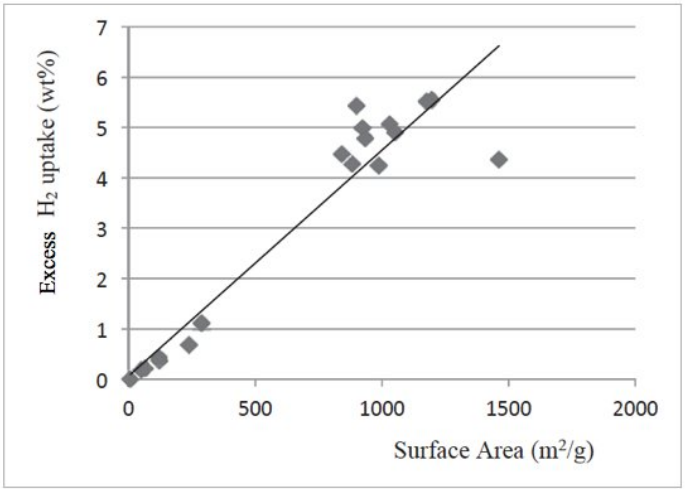

Figure 2.2.8 *Hydrogen excess gravimetric uptake versus the specific surface area of the carbon structures at 77 K and 1 bar. Based on the data reported by Nijkamp et al. in 2001 [48].*

In 2004, Novoselov et al. first found and produced a stable graphene sheet [49], proving the existence of single sheet molecules in ambient conditions. Unlike other nanoscale materials, graphene has an enormous surface free energy because of its high area/volume ratio, and better attraction performance due to its free valence electron and π-π stacking force (sp^2 C-C bonding) compared with normal graphite, which could be beneficial for increasing hydrogen uptake. As shown in **Figure 2.2.8**, Nijkamp and his colleagues ran many tests to discover the relation between hydrogen gravimetric percentage and surface area of popular carbon structures, such as activated carbon, carbon nanotubes and graphene [48]. Graphene sheet has been reported to have a specific surface area of 2630 m^2/g [50], [51]. With the relationship presented by **Figure 2.2.8**, the gravimetric uptake of hydrogen in graphene sheet is expected to be about 5 wt% at 77 K at 1 bar pressure in theory.

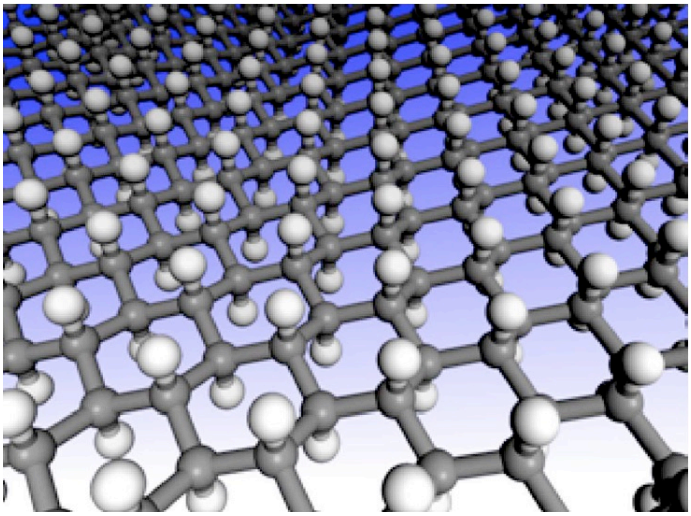

Figure 2.2.9 *Structure of graphane in the chair conformation (carbon atoms are shown in grey, and hydrogen atoms in white) [52].*

In 2007, a new concept of two-dimensional hydrocarbon was introduced with the name of graphane that consists of one layer of carbon backbone, like graphene, but saturated with hydrogen atoms [52], as shown in **Figure 2.2.9**. There are two favourable conformations of this new compound: the chair-like structure with hydrogen atoms alternating on both sides as shown in **Figure 2.2.9**, and the boat-like structure with the hydrogen atoms alternating in pairs [52]. These materials develop an sp^3 hybridisation and, it is claimed, form the most stable hydrocarbon compound, with 1:1 C:H ratio theoretically [52]. Although graphane has proven to perform a good reversible storage performance with hydrogenation by an atomic hydrogen treatment and de-hydrogenation by annealing at 450 °C in argon atmosphere [53], presenting a maximum hydrogen composition of 7.7 wt% in theory with considering that each carbon atom is bonded to a hydrogen atom in average [52], an efficient method to produce graphane is still unclear, which means this interesting material is far from practical applications at this moment.

Experiments have been further conducted to study curved graphene sheets and single-walled or multi-walled carbon nanotubes [54]. Because the curvature creates an overlap of molecule space, influenced by gyration and other factors of molecular movement, many researchers assumed that the weight percentage of hydrogen storage might have the potential to rise. Although it was claimed that the hydrogen storage capacity of single-wall carbon nanotubes could reach 4.2 wt% at room temperature under a modestly high pressure

(about 100 bar) [55], which was often considered to be unrealistically high recently [56], one thing seems to be clear: the perfect graphite nanostructure, whether in the form of carbon nanotubes or graphene sheets, could not provide competitive results compared with the DOE target experimentally.

The group of Pradhan [57] tried to modify the structures and create defects, reporting that perfect SWNTs stored only 0.52 wt% with 270 m^2/g specific surface area (SSA) at 77 K and 1 atm, while the hydrogen uptake after a sulphurisation and oxidation process dramatically increased to 6.4 wt% without much difference in SSA. Although it is realised that the structural features of carbon forms might have the potential to influence the hydrogen uptake, there is still a lack of systematic study.

2.2.6 Summary

For the purpose of storing hydrogen in mobile applications, the conventional high-pressure tanks are the most popular method in recent commercial applications among all reviewed techniques, but the high pressure itself can be a risk and is expensive to handle. Metal hydrides can reversibly store around 1 – 2 wt % of hydrogen at room temperature and low pressure conditions. 5 wt% uptake can be reached for some types of metal hydrides, but the reversibility is questionable. MOFs can have large surface areas, over 4000 m^2/g, and high porosity, which is favourable for hydrogen adsorption. The saturated uptakes of MOFs per unit surface area have matched the activated carbons, but the high cost of MOFs production restricts its prosperity. Zeolites are another type of porous sorbents that are favourable for gas adsorption, but the surface areas of zeolites cannot compete with high surface area carbons, which further restricts the overall hydrogen uptakes of zeolites. The high degree of ordering in the structures of zeolites is valuable for analysing the adsorption mechanism on microporous structures. The activated carbons can have surface areas over 3000 m^2/g and achieve uptakes over 7 wt% at 77 K and moderate pressures of 20 bar, but most of reported high performance carbons are in lab scale, which can take some time to boost their commercial production and application. Some new types of carbon nanoforms, such as carbon nanotubes, graphene and graphane, exhibit exciting potential for large quantities of hydrogen uptake in theory, but the experimental results failed to match with predictions.

The physical adsorbent-adsorbate adsorption is the dominant effect of hydrogen adsorption on carbon materials, zeolites and other inactive structures in general. Higher surface areas normally result in a larger amount of hydrogen uptakes. For achieving over 1 wt% of uptake, cryogenic temperatures are inevitable for both activated carbons and zeolites at low pressures. It is understood that the limitation of surface area sizes on some sorbents restricts the maximum hydrogen uptake. Modified porous structures, such as modified carbon nanotubes with extra structural defects and chemical radicals [57], experimentally prove to have a significant improvement of overall uptakes. Although it is still unclear, whether the improvement is related to structural effects or chemical effects, it provides a possibility of improving the saturated adsorption by introducing additional modifications on carbon materials.

2.3 Adsorption theories

2.3.1 Physisorption and chemisorption

Adsorption is a surface based phenomenon in which atoms, ions, molecules of a gas, liquid or solid can adhere to the surface. In this report, gas-solid adsorption was studied primarily. Notwithstanding that some parts of the theoretical analysis can also be applied for other types of adsorption mechanism, the explanations and discussions in this report were worked out and verified only on the basis of gas-solid adsorption. There are two kinds of adsorption involved in gas-solid adsorption: the physisorption and the chemisorption. Physisorption is similar to the condensation of vapours and those behaviours explained by gas laws, which only exhibits pure physical adsorption, while chemisorption interactions are responsible for the formation of chemical bonds.

Physisorption is usually related to the porous properties of materials, such as specific surface areas (SSA) and pore volumes of solid sorbents, but has very low specificity to material compositions. The chemisorbed molecules are generally linked to the surface with chemical reactions, which includes distinctive reactions for different chemical compositions of sorbents. With physical sorption, desorption behaviour can be achieved by modifying the temperature or pressure conditions, and the adsorbed molecules return to their original forms reversibly, whereas chemisorbed materials desorb with chemical dissociation. The thermodynamics of the physical and chemical sorption are opposite to each other. Physisorption tends to reach

a lower energy level with an exothermic process and can be promoted with low temperatures, while chemisorption requires additional energy, and so high temperature conditions are normally needed. In this study, carbon-based sorbents are the primary materials analysed, in which the adsorption is dominated by physisorption. The apparatus designed in this project focused only on adsorption behaviours and overall hydrogen uptakes, while desorption behaviours are not the priority of this study. Although chemisorption is less involved at 77 K in comparison with the physisorption, the catalytic effects of doping materials that are typically related to chemical mechanisms were also involved in this project.

2.3.2 Van der Waals equation of state and compressibility factor

Generally, at cryogenic temperatures and high pressures, a compressibility factor Z is used to modify the ideal gas law in order to account for real gas behaviours:

$$Z = \frac{p\overline{v}}{RT} \tag{2.1}$$

where p is the pressure, $\overline{v}$ is the specific volume, R is the gas constant and T is the temperature. To clarify the values of the compressibility Z, the Van der Waals equation of state is applied.

$$p = \frac{RT}{\overline{v} - b} - \frac{a}{\overline{v}^2} \tag{2.2}$$

The constant b is intended to account for the finite volume occupied by the molecules, and the term $\frac{a}{\overline{v}^2}$ accounts for the forces of attraction between molecules. It is noted that the ideal gas law applies when the both constants a and b are equal to zero.

At the critical point, the following relations can be written:

$$p_{\mathrm{c}} = \frac{RT_{\mathrm{c}}}{\overline{v}_{\mathrm{c}} - b} - \frac{a}{\overline{v}_{\mathrm{c}}{}^2} \tag{2.3}$$

$$\left(\frac{\partial^2 p}{\partial \overline{v}^2}\right)_T = \frac{2RT_{\mathrm{c}}}{(\overline{v}_{\mathrm{c}} - b)^3} - \frac{6a}{\overline{v}_{\mathrm{c}}{}^4} = 0 \tag{2.4}$$

$$\left(\frac{\partial p}{\partial \overline{v}}\right)_T = -\frac{RT_{\mathrm{c}}}{(\overline{v}_{\mathrm{c}} - b)^2} + \frac{2a}{\overline{v}_{\mathrm{c}}{}^3} = 0 \tag{2.5}$$

Solve the three equations (2.3), (2.4) and (2.5), and the following relations are obtained.

$$a = \frac{27}{64}\frac{R^2 {T_c}^2}{p_c} \tag{2.6}$$

$$b = \frac{RT_c}{8p_c} \tag{2.7}$$

To acquire the $\overline{v}$ of the gas, the equation 2.2 needs to be reformed into a polynomial in $\overline{v}$.

$$\overline{v}^3 - \left(b + \frac{RT}{p}\right)\overline{v}^2 + \frac{a}{p}\overline{v} - \frac{ab}{p} = 0 \tag{2.8}$$

Since the constants a and b have been acquired with equations (2.6) and (2.7), the equation (2.8) could be solved in computer programming for a defined set of pressure and temperature, and only one solution is real, which is the determined specific volume $\overline{v}$. The compressibility Z can be then solved in equation (2.1) with the determined specific $\overline{v}$. There are several other values defined prior to the computation. The critical temperature of hydrogen T_c is 33.19 K, and the critical pressure of hydrogen P_c is 12.98 bar [58]. According to Newton's publication in 1935 [59], for the special gases of hydrogen, helium and neon, both the critical temperature and critical pressure required a correction to obtain accurate values of the compressibility when the Van der Waals equation of state was applied, ($T_c = (33.19 + 8)\ \mathrm{K}, P_c = (12.98 + 8)\ \mathrm{bar}$ in calculation). For the hydrogen cryosorption experiments in this study, the compressibility calculation was performed programmatically.

The calculated curves for compressibility versus pressure at 77 K and 298 K are displayed in **Figure 2.3.1**. As shown in **Figure 2.3.1 (a)**, the compressibility factors in different temperatures exhibit differential behaviours with the increasing pressures. For the curve at 298 K, the compressibility has a linear growth with pressure for the full range up to 300 bar, while the compressibility at 77 K decreases at low pressures up to 70 bar, where the compressibility reaches a minimum, then increasing afterwards. For low pressures at 298 K (below 15 bar), the variance caused by pressure shifts is very small, as shown in **Figure 2.3.1 (b)**. During the experiments in this study, the gas at room temperature has two states in terms of compressibility (see **Figure 6.6.1** in section 6.6): the gas with loading pressure at step 2, and the gas after connection to the sorbent chamber in step 3, which has a pressure drop of maximum 3 bar (at the maximum pressure condition of the experiments). According to **Figure 2.3.1 (b)**, the compressibility difference of 3 bar pressure is negligible. Thus, both of states

would be assigned the same compressibility value of Z_1 based on the pressure condition in step 3 (see **Figure 6.6.1** in section 6.6). For the region kept in 77 K liquid nitrogen bath, the compressibility has a significant difference of nearly 3 % at a pressure of 11 bar in comparison with zero pressure. A second compressibility value, Z_2, was therefore assigned to the gas under liquid nitrogen bath via the mathematical relation discussed. The compressibility factors Z_1 and Z_2 are applied in the derivation of the mathematical relations for uptake measurements in section 6.7.

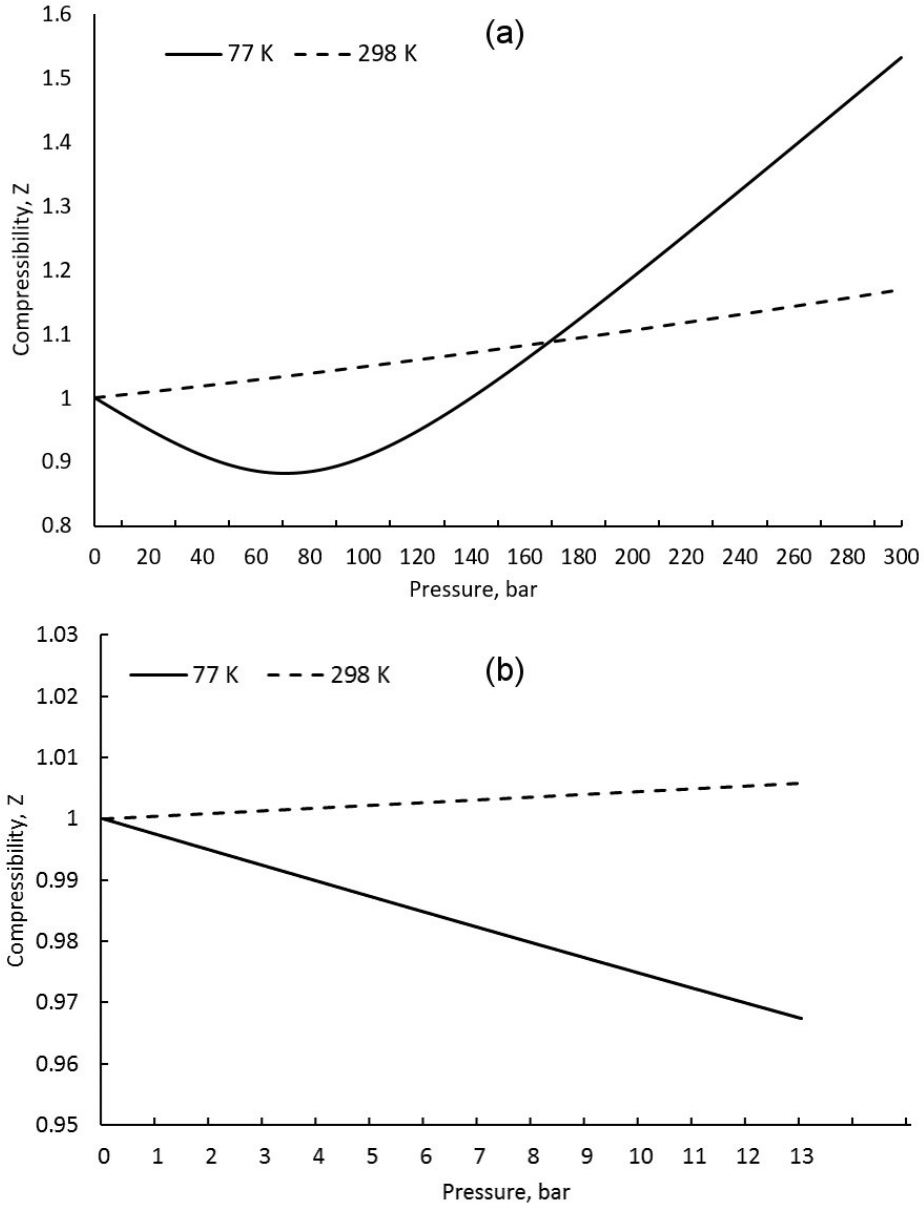

Figure 2.3.1 *The compressibility of hydrogen for 77 K and 298 K at pressures: (a) 0 – 300 bar and (b) 0 – 13 bar.*

2.3.3 Types of adsorption isotherms

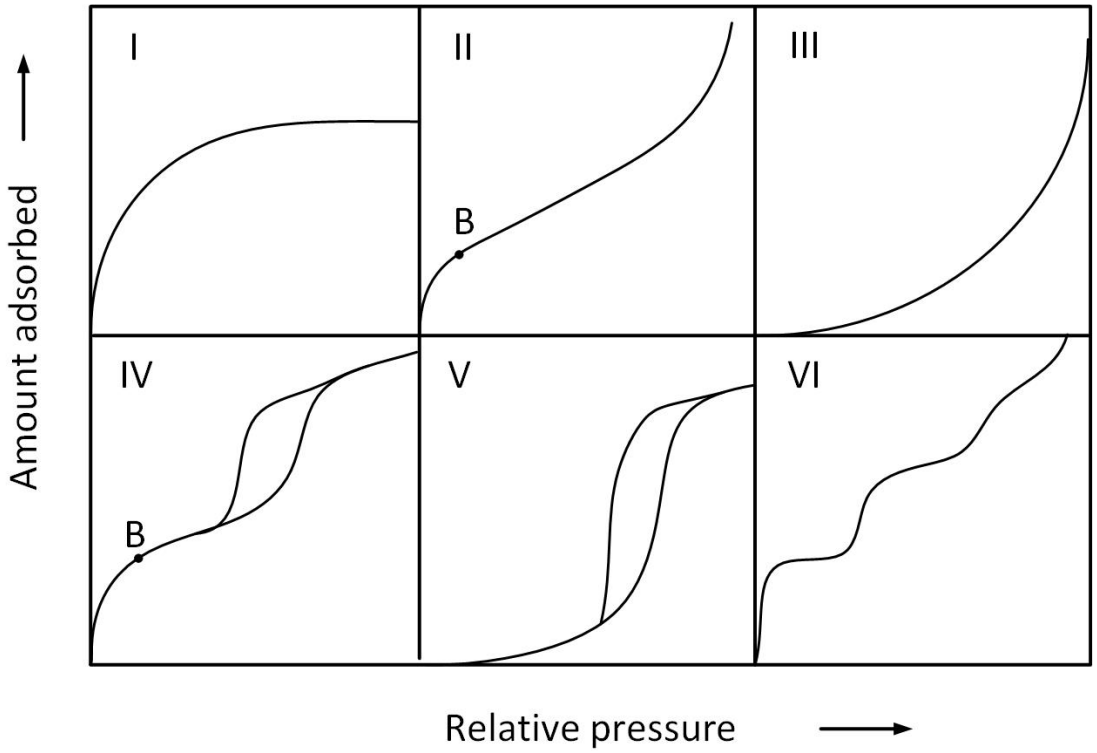

Figure 2.3.2 *Six types of physisorption isotherms below atmosphere pressures according to International Union of Pure and Applied Chemistry (IUPAC) classifications [60].*

In terms of IUPAC classifications [60], the majority of physisorption isotherms can be identified as one of the six types described in **Figure 2.3.2** for pressures below atmospheric pressure. The reversible type I isotherms are generally given by microporous solids with a relatively small external surface but large micropore surface areas, e.g. activated carbon, in which the uptake is governed by the accessible micropores to the probe gas molecules [60], [61]. The reversible Type II isotherm is normally achieved by non-porous or macroporous materials, in which unconstrained monolayer-multilayer adsorption occurs. Point B, as described in **Figure 2.3.2,** is regarded as the start of the linear progression section, which indicates the completion of monolayer packing of gas molecules on the surface. The reversible type III is concave to the relative pressure smoothly over the entire pressure range, which is not commonly observed, and it is believed to be caused by strong adsorbate-adsorbate interactions. The hysteretic type IV isotherm is related to the capillary condensation in mesopores, and its initial part follows the type II isotherm with monolayer-multilayer adsorption. Type V happens only rarely: it is similar to type III but with weaker adsorbate-

adsorbate interactions and a significant amount of mesopores. Type VI, in which the step sharpness relies on the systems and temperatures, describes stepwise multilayer adsorption on a uniform non-porous surface. The heights of steps are related to the monolayer capacity of each adsorption layer. Although the classification is clear for most situations, it was also noticed that some systems have a combination of more than one system [61]. The isotherms classified above are normally obtained via the BET measurements of sorbents. For a larger pressure range above atmosphere, the isotherms in **Figure 2.3.2** are normally impossible to acquire due to the lack of values in the low pressure range. In terms of the isotherm over the large pressure range, the isotherms are generally similar to the shape described for type I isotherms.

2.3.4 Gas/Solid interface and Gibbs representation

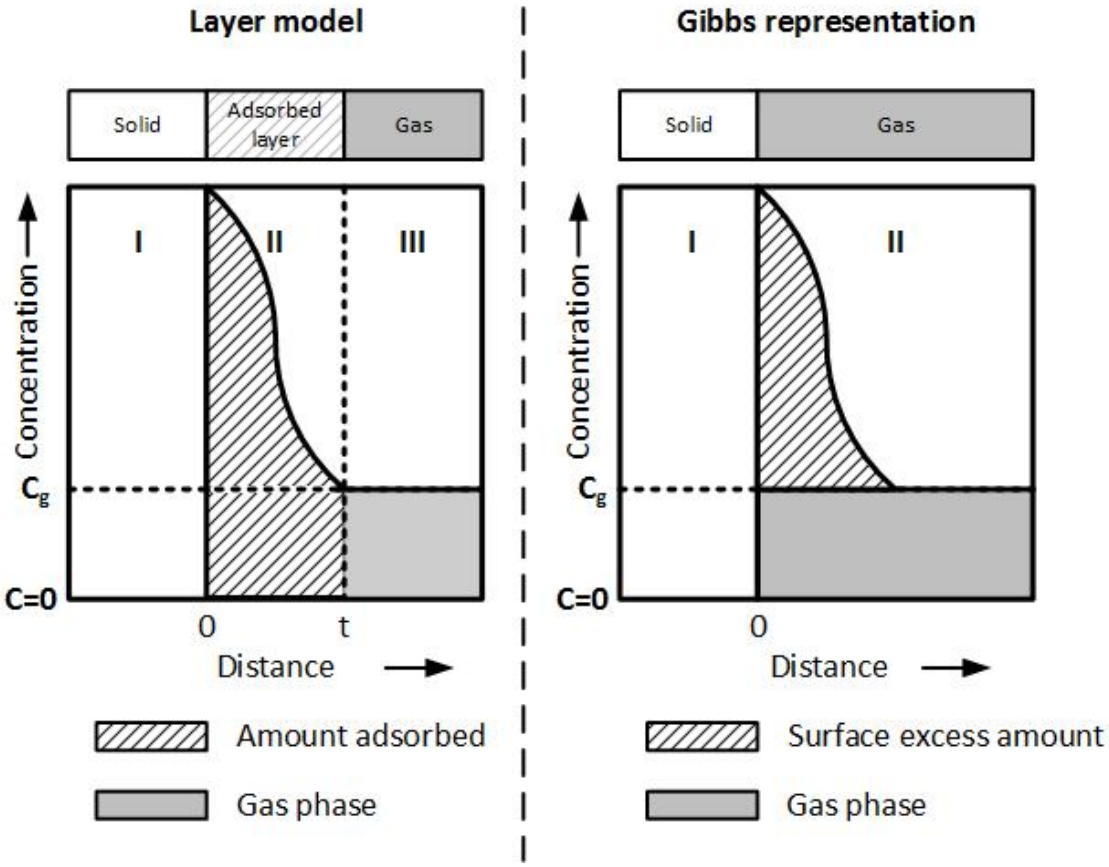

Figure 2.3.3 *The layer model and the Gibbs representation of surface excess amount (concentration* $C = \frac{dn}{dV}$ *of the adsorbed gas, the distance is from the solid surface) [61].*

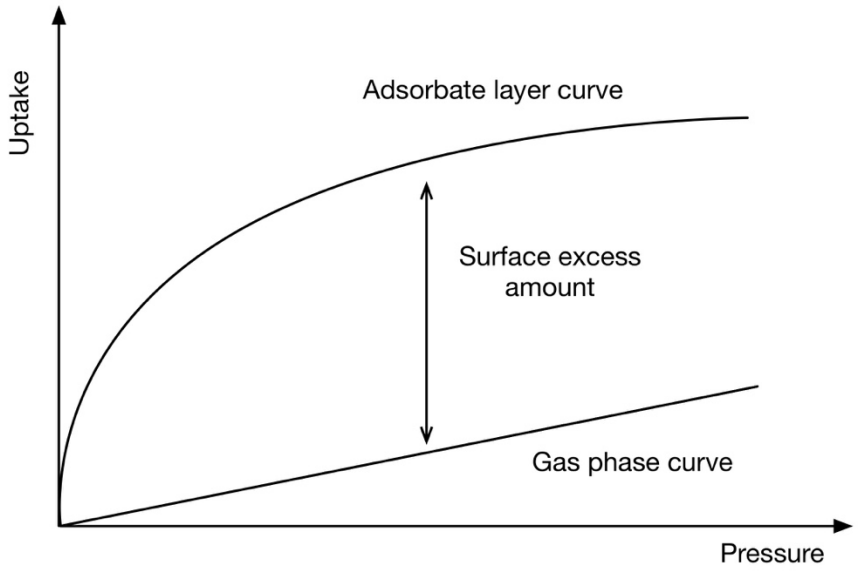

Figure 2.3.4 *Illustration of adsorbate layer (layer model in Figure 2.3.3), gas phase and surface excess amount in gas uptake – pressure isotherms at positive pressures [61].*

For the general layer model [61], the adsorbed gas phase has a certain distance *t* away from the solid surface, assuming that the adsorbed gas had no penetration inside the solid, as shown in **Figure 2.3.3**. As described in Zone III, the gas phase with sufficient distance away from the surface is presumed to have a uniform concentration. The amount of gas in the adsorbed layer labelled in the layer model in **Figure 2.3.3** is sometimes measured, especially when the measured volumes of sorbents include the pore volumes. However, there is always a portion of the gas in the adsorbed layer existing in the same concentration as the gas phase, of which the amount increases with pressure, as confirmed in **Figure 2.3.4**. Furthermore, the exact volume of this part of gas is difficult to determine, which results in difficulties in identifying the exact amount of gas adsorbed except the gas phase in the adsorbed layer, especially for porous sorbents with irregular surfaces.

A concept of "surface excess amount", referring to the amount of gas adsorbed which subtracts the portion at the gas phase concentration, was introduced in the Gibbs representation in **Figure 2.3.3** [61]. The surface excess amount is the portion of gas uptake that is irrelevant to the variances of pressure conditions, which is simpler to define and more related to the properties of sorbents. During the hydrogen cryosorption experiments in this thesis, a helium intrusion density measurement was performed for each sorbent, that determines the real sorbent volumes by subtracting pressure-sensitive pore volumes.

Because the volume during the helium intrusion test was measured with the pressure adjustments upon a certain amount of gas flow, it has avoided the influence of the pore volumes that vary with different pressure conditions. Therefore, the gas uptakes measured in our system were the surface excess amount as defined in the Gibbs representation. It should be aware that the helium can be adsorbed to the sample in the helium density measurement. According to the research in reference [62], the density of an activated carbon with surface area of 1030 m^2/g is 2 cm^3/g measured at 400 ^oC in comparison with 2.3 cm^3/g measured at 0 ^oC, of which the difference is due to the adsorption of helium [62]. In our experiment, a typical sample weight is 1 gram, which means the potential volume difference can be about 0.065 cm^3. Upon the testing condition of 10 bar pressure at 77 K, the hydrogen uptake difference caused by 0.065 cm^3 is 0.0002 gram, i.e. 0.02 wt% in respect of 1 gram sorbents, about 1 % error introduced to 2 – 3 wt% hydrogen uptakes as measured in our study on the activated carbons with similar size of surface areas, which is not significant. The amount of helium adsorbed in density measurement is also related to the surface area of samples [62], of which the systematic analysis has not been clearly defined yet.

2.3.5 Brunauer-Emmett-Teller (BET) method for surface area assessments

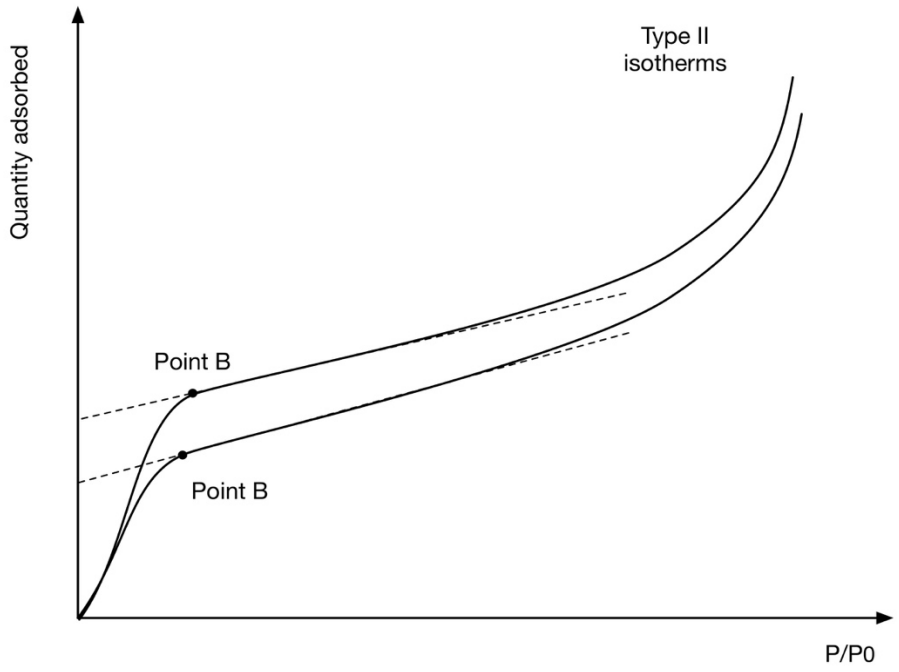

Figure 2.3.5 *The point B locations in type II adsorption isotherms.*

Adsorption isotherms with probe molecules, such as nitrogen gas at 77 K, are generally utilised for determining the specific surface areas (SSA) of porous solids and fine powders [61], [63], [64]. It is well recognised that the SSA is a vital material property for studying gas physisorption, and the research related to hydrogen adsorption is no exception [4], [65]. In the 1930s, Brunauer, Emmett and Teller (BET) first introduced that the point B (see **Figure 2.3.5**) from which the linear increase region started indicated the completion of monolayer packing, based on their previous empirical studies [66]–[70], which was further applied to calculate the surface area of solids, widely known as the BET theory [61]. The BET method has been exceptionally popular for evaluating the SSA of porous materials during the past eighty years.

There are two stages involved in the BET method: the derivation of the monolayer capacity, n_{m}, and the specific surface area, a_{BET}. The BET equation is expressed with the following linear form:

$$\frac{p/p_0}{n(1-p/p_0)} = \frac{1}{n_{\mathrm{m}}C} + \frac{C-1}{n_{\mathrm{m}}C}(p/p_0) \tag{2.9}$$

where n is the amount of gas adsorbed in moles per gram, n_{m} is the specific monolayer capacity of adsorbate, C is the BET parameter, p is the pressure of the adsorptive in equilibrium with the adsorbate and p_0 is the saturation vapour pressure of the adsorptive [61], [63], [70]. Equation 2.9 can be further plotted linearly with $\frac{p/p_0}{n(1-p/p_0)}$ on the y-axis and p/p_0 on the x-axis within the standard relative pressure range around 0.05 - 0.3 for mesoporous and non-porous materials as shown in **Figure 2.3.6**. Then n_{m} and C can be expressed in terms of the slope S and the intercept I, and a positive intercept I is required for the effective implementation of BET method.

$$n_{\mathrm{m}} = \frac{1}{S+I} \tag{2.10}$$

$$C = 1 + \frac{S}{I} \tag{2.11}$$

The specific surface area per mass of the adsorbents, a_{BET}, is calculated from the monolayer amount using the average area occupied by each molecule, a_{m}.

$$a_{\mathrm{BET}} = n_{\mathrm{m}} a_{\mathrm{m}} N_{\mathrm{A}} \tag{2.12}$$

where N_{A} is the Avogadro constant equal to 6.022 × 10^{23} mol^{-1}, and $a_{\mathrm{m}} = 0.162\ \mathrm{nm}^2$ is recommended for nitrogen at 77 K [63].

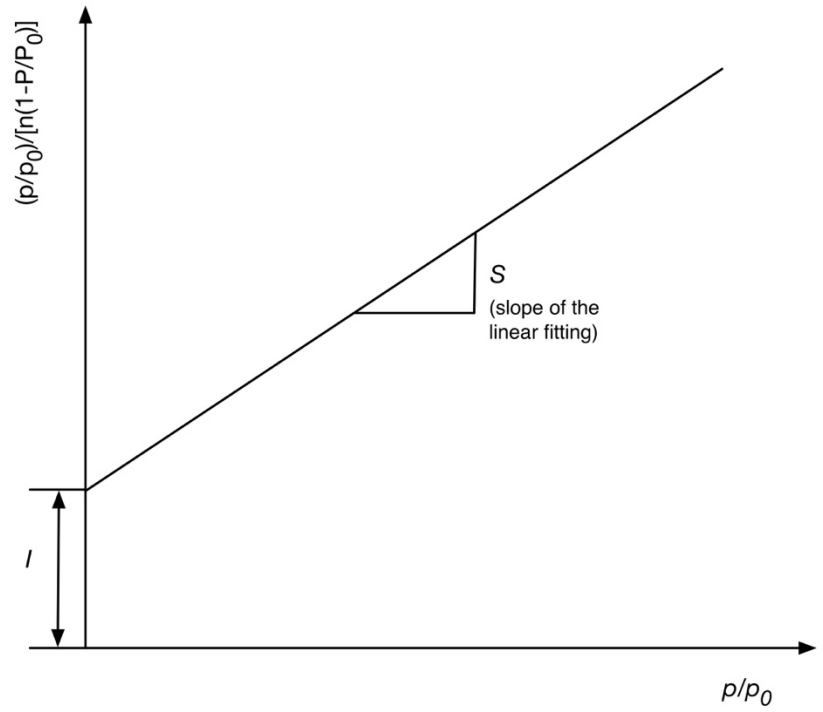

Figure 2.3.6 *An example of a typical BET linear plot.*

It is noted that the BET theory has its own limitations in spite of its great success and wide applications. Therefore, the implementation of the BET method is essentially an empirical process which requires additional validation of the results. As mentioned above, the BET linear plot is usually situated at $p/p_0 = 0.05 - 0.3$ with n_{m} located at ~ 0.1, which is regarded as the standard BET range. The BET method is not applicable if a straight-line fit is not obtained or if the intercept is negative. The BET parameter C should fit in the range of 100 – 200 in most mesoporous materials and non-porous materials. For $C > 200$, it may indicate the presence of micropores or the strong localised adsorption [61], [63], and type I isotherms are normally clear evidence for micropore filling. For $C < 100$, there is appreciable overlap of monolayer and multilayer adsorption due to relatively weak adsorbent-adsorbate interactions, which results in an indistinct B point in the isotherm [61]. The value of C can indicate the force of adsorbent-adsorbate interactions qualitatively [63]. The BET area

derived from a nitrogen isotherm of type II or type IV at 77 K can be considered as an effective result, while the BET method is strictly not applicable to type III and type V isotherms.

As the micropore filling happens during monolayer adsorption, the implementation of BET methods on type I isotherms of microporous materials requires extra verification to identify the approximate region for BET linear plots [63], [71]. A simple verification is recommended to locate the linear region as demonstrated in **Figure 2.3.7 (b)**, according to reference [71]. The trend of the BET plot (**Figure 2.3.7 (a)**) certainly deviates from initial linearity at a relative pressure of 0.1 for the AC Norit ROW that has been confirmed with the existence of a large composition of micropores (see section 7.1). The corresponding deviation point can be recognised at the maximum point in **Figure 2.3.7 (b)**. By contrast, the GNPs-500 that has fewer micropores diverges at a higher relative pressure of 0.2. The verification of the linear range of relative pressures is crucial for conducting effective BET methods, which prevents the occurrence of negative C values. The measured BET surface area of microporous materials is considered as the equivalent BET surface area instead of the true values, because of micropore filling effects during monolayer adsorption.

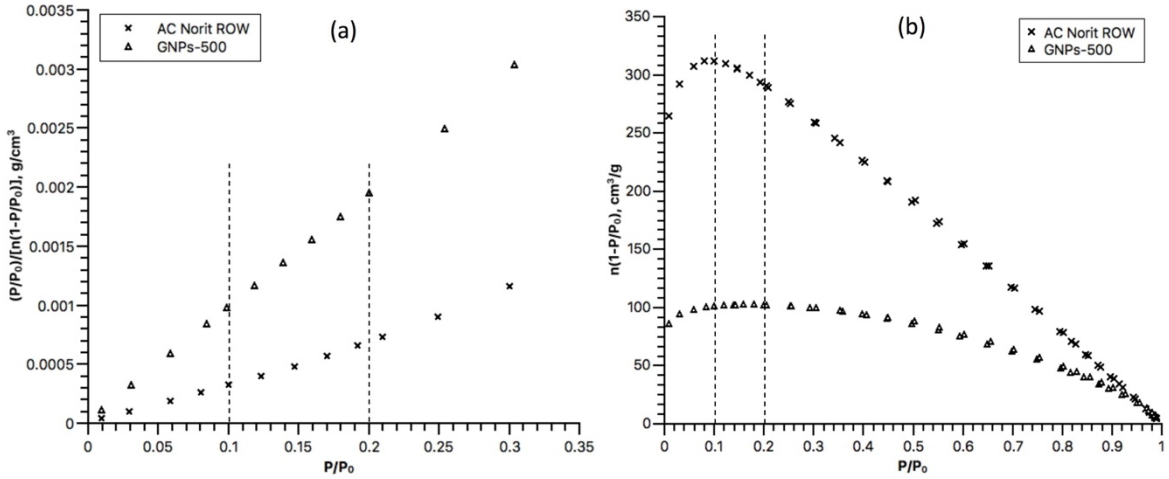

Figure 2.3.7 *(a) BET plots and (b) the verification plots of AC Norit ROW and GNPs-500 (characterisation of these samples has been discussed in section 7.1).*

2.3.6 Kelvin equation and mesopore analysis

The mesopore generally refers to pore sizes in the approximate range of 2 – 50 nm [72], of which the existence is indicated by the existence of type IV isotherms in **Figure 2.3.2**. It has

been reported that some type IV isotherms showed physisorption hysteresis of their adsorption-desorption loops [60], [61], [73]–[76], which was also found with some of the samples discussed in this study. The hysteresis effects are caused by capillary condensation that creates local vapour condensation in non-uniform mesopores below the saturated pressure of liquid [60], [61]. To describe the mechanical equilibrium condition of interfaces, the Young-Laplace equation was introduced in equation 2.13:

$$p^{\mathrm{l}} - p^{\mathrm{g}} = \frac{2\gamma}{r_{\mathrm{m}}} \tag{2.13}$$

where p^{l}, p^{g} are the pressures in liquid phase and gas phase respectively, r_{m} is the mean radius of the curvature and γ is the surface tension of the liquid. At the equilibrium state with a constant temperature, the relation can be further derived as:

$$dp^{\mathrm{l}} - dp^{\mathrm{g}} = d\left(\frac{2\gamma}{r_{\mathrm{m}}}\right) \tag{2.14}$$

Another expression of the equilibrium states at a constant temperature can be written as:

$$v^{\mathrm{l}} dp^{\mathrm{l}} = v^{\mathrm{g}} dp^{\mathrm{g}} \tag{2.15}$$

where v^{l} is the molar volume of the liquid and v^{g} is the molar volume of the vapour phase. By assuming that v^{l} can be neglected in comparison with the v^{g} and combining the equations (2.13), (2.14) and (2.15) with the ideal gas equation, the following expression can be obtained:

$$d\left(\frac{2\gamma}{r_{\mathrm{m}}}\right) = \frac{RT}{v^{\mathrm{l}}}\frac{dp^{\mathrm{g}}}{p^{\mathrm{g}}} \tag{2.16}$$

where R is the gas constant and T is the temperature. The above relation can be integrated from the flat interface ($1/r_{\mathrm{m}} = 0$, $p^{\mathrm{g}} = p^{0}$ the saturated pressure of liquid) to the real state condition ($1/r_{\mathrm{m}}$, p^{g}) with v^{l} kept constant.

$$\int_{0}^{1/r_{\mathrm{m}}} 2\gamma d\left(\frac{1}{r_{\mathrm{m}}}\right) = \int_{p^{0}}^{p^{\mathrm{g}}} \frac{RT}{v^{\mathrm{l}}}\frac{1}{p^{\mathrm{g}}} dp^{\mathrm{g}} \tag{2.17}$$

$$ln\frac{p^{\mathrm{g}}}{p^{0}} = \frac{2\gamma v^{\mathrm{l}}}{r_{\mathrm{m}} RT} \tag{2.18}$$

The integrated equation 2.18 is named as the Kelvin equation as it was first proposed by Lord Kelvin [61]. For $p^{\mathrm{g}} < p^{0}$, the negative value of concave curvature radius ($r_{\mathrm{m}} = -|r_{\mathrm{m}}|$) is presented as described in equation (2.18). In terms of Kelvin equation, the relative pressure of p^{g}/p^{0} is required be high enough for the occurrence of capillary condensation on large pores with a large $|r_{\mathrm{m}}|$. For a flat gas-liquid interface with an infinite $|r_{\mathrm{m}}|$, p^{g} is equal to the saturated vapour pressure of p^{0}. When the p^{g}/p^{0} increases during the adsorption process, the pores with small radii are filled firstly because of the vapour condensation in the low-pressure range.

There are two popular simplified theories based on capillary condensation for hysteresis explanations. The Kraemer and McBain “bottle-neck” model, also known as the “ink-bottle” model, assumes that larger mesopores are constrained with smaller neck tunnels [61], [74]. During desorption, the condensed neck tunnels of large pores are required to evaporate at a lower p/p^{0} range before the constrained large pores are available to desorb, resulting in the hysteresis loop. The other theory describes a cylindrical pore with both ends open [61]. As illustrated in **Figure 2.3.8**, the condensation on cylindrical pores occurs at high relative pressures due to the flat surfaces on which the gas molecules attach from monolayer to multilayer, then filling the whole pores corresponding to the increase of relative pressure during adsorption. When the relative pressure decreases gradually during desorption, the release of condensation starts at a much lower relative pressure because of the small diameters of the cylinder ends, which results in the hysteresis loop in the adsorption isotherms. It is noted that complex hysteresis effects are amongst outstanding problems in the field of adsorption study and each theory has its limitations.

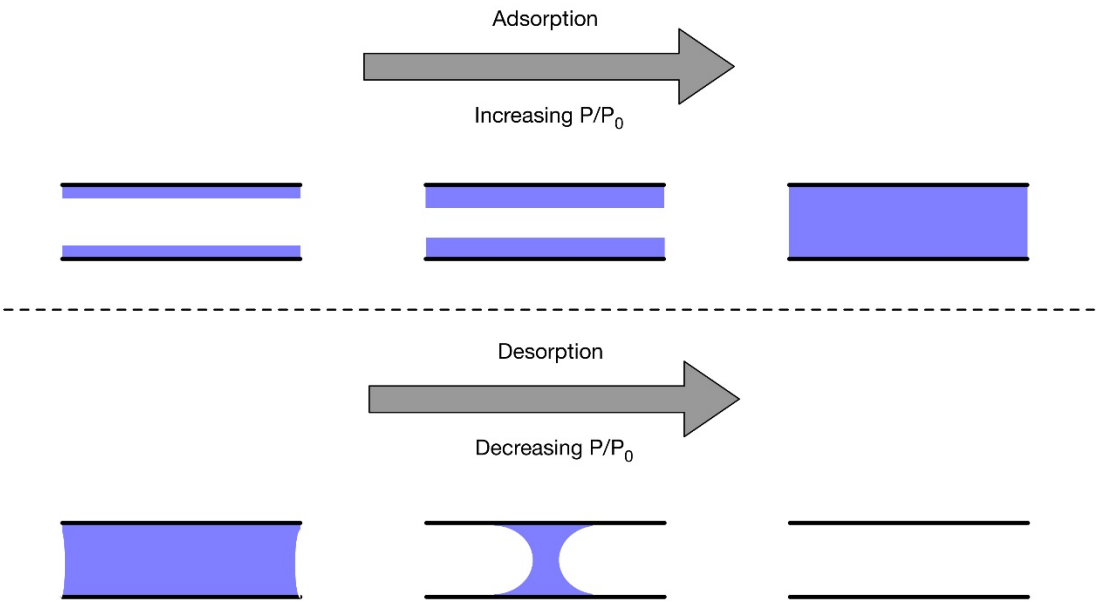

Figure 2.3.8 *Illustrations of the formation and release of vapour condensation in cylinder-like or slit-like pores.*

There are four major types of hysteresis loops classified by the IUPAC [60] as shown in **Figure 2.3.9** with the labels H1, H2, H3 and H4. H1 exhibits nearly a vertical and parallel-sided desorption hysteresis loop over a narrow range of p/p^0, while the H4 loop cycles horizontally between the adsorption and desorption isotherms for a wide range of p/p^0. Both are considered as extreme cases, with types H2 and H3 being regarded as combinations of these two extreme situations. The pressures at which hysteresis loops abruptly close on desorption are sometimes dependent on the nature of adsorptive [61]. For example, it occurs at a value of $p/p^0 \sim 0.42$ for hydrogen at its boiling point [61].

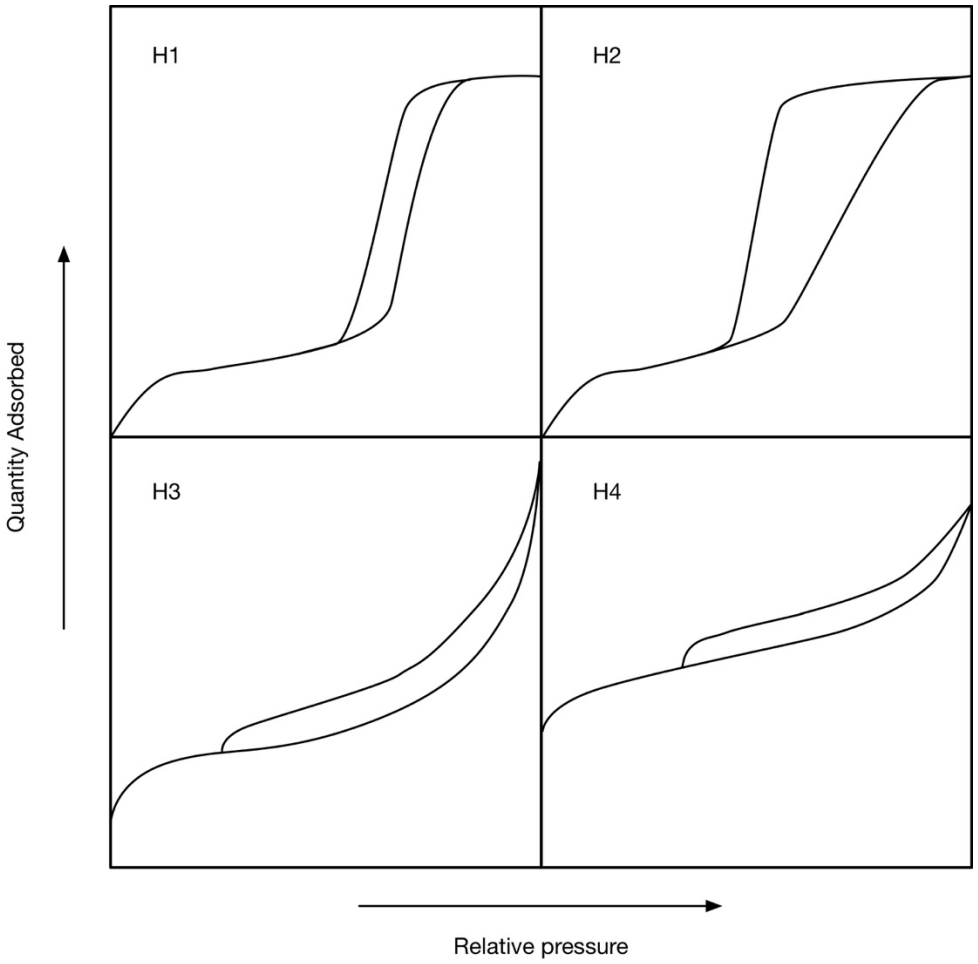

Figure 2.3.9 *Types of adsorption hysteresis referring to IUPAC classifications [60].*

The type H1 loop is generally observed for porous materials with a uniform distribution of pore sizes as it covers a small range of relative pressures. By contrast, the pore size distribution of materials with type H2 behaviours can be complex and difficult to identify. This behaviour was sometimes attributed to interconnected pore networks with necks and wide pores, such as the “ink-bottle” structure [60]. Type H3 loops, which have no limitation of the hysteresis loop at high p/p^0, is observed with the existence of plate-like particles which result in slit-shaped pores. Type H4 is often related to narrow slit-shaped pores in conjunction with type I isotherms of microporous materials, as obtained with some types of activated carbons [60], [61].

In terms of equation 2.18, the mean radius of curvature r_{m} can be obtained at a certain point of p/p^0. However, molecular simulations have suggested that the Kelvin equation was invalid to evaluate the r_{m} if the fluid-wall interactions are involved, in which the acquired pore

sizes are likely to be underestimated [61], [77]–[79]. For the analysis of pore size distribution of mesopores, the method of Barrett, Joyner and Halenda (BJH) can be expected to provide better assessments of r_{m} by contrast with Kelvin equation [61], [80], [81]. The BJH analysis is widely conducted simultaneously with the BET measurements in commercial equipment, such as the "Micromeritics" branded system that was used in this research.

2.3.7 Analysis methods for microporosity

Micropore (of sizes < 2 nm) filling normally occurs in the very low p/p^0 range, caused by enhanced adsorbent-adsorbate interactions [61]. The long horizontal plateau of type I isotherms indicates adsorption on micropores. The amount absorbed at the plateau represents the ultramicropore (of sizes < 0.7 nm) capacity for a well-defined type I isotherm as shown in **Figure 2.3.10 (a)**. For a more realistic condition, the size distribution of the micropores is not perfectly uniform due to the existence of wide micropores (or supermicropores with the sizes in 0.7 – 2 nm range, which is reflected in **Figure 2.3.10 (b)**. In the cases with micropore existed, the analysis of micropore properties should be attempted with the empirical methods discussed below.

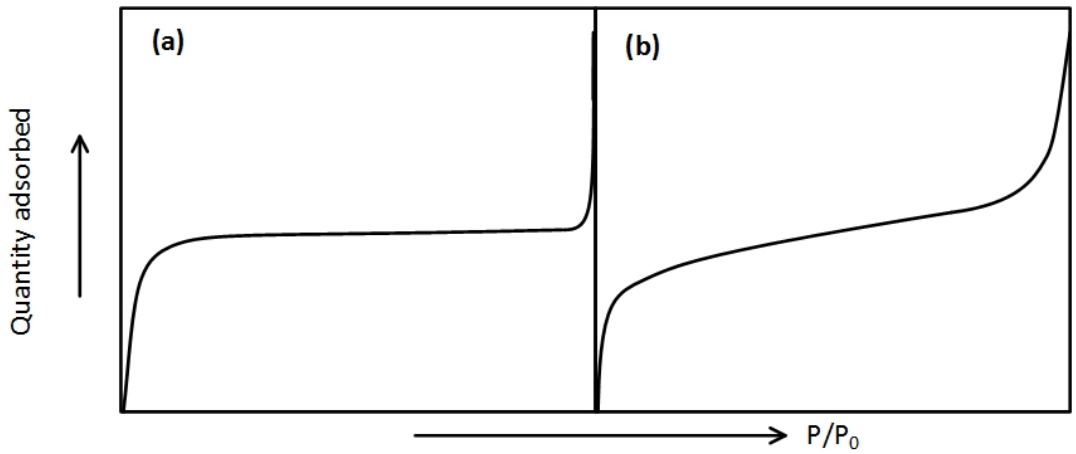

Figure 2.3.10 *The typical adsorption isotherms: (a) narrow micropores (or ultramicropores of pore sizes < 0.7 nm) and (b) wide micropores (or supermicropores of pore sizes 0.7 – 2 nm) [61].*

According to the BET equation 2.9, the total amount of gas adsorbed n and the monolayer capacity n_{m} can be obtained during BET measurements. The thickness of the multilayer packing can be calculated with:

$$t = 0.354 \frac{n}{n_{\mathrm{m}}} \tag{2.19}$$

which was firstly used by Lippens and de Boer (1964) to plot a "t-curve" [82]. The value of 0.354 is roughly the kinetic diameter of liquid nitrogen molecules. As the Lippens and de Boer method is simplified, without considering the micropore filling effects, the equation for deriving the thickness was further developed by Harkins and Jura (1944) with the following mathematical relation (HJ-equation) [83].

$$t[\text{Å}] = \left(\frac{13.99}{0.034 - \log_{10}(P/P_0)} \right)^{1/2} \tag{2.20}$$

Upon the application of Harkins and Jura (HJ) t-method, it was assumed that multilayer coverage on mesopore walls behaves in the same manner as that of the open surfaces [61], and the micropores are filled prior to the multilayer adsorption. The following linear dependence is present at a certain relative pressure range.

$$n = n_{\mathrm{micro}} + k \cdot a_{\mathrm{ext}} \cdot t \tag{2.21}$$

where t follows the HJ-equation 2.20, n is the total amount of gas adsorbed, n_{micro} is the amount of gas adsorbed in micropores, a_{ext} is the external surface area of mesopores, macropores and open surfaces, k is a constant given by the expression $k = 1/(4.3532 \cdot t_{\mathrm{mono}})$ for adsorbed amounts in cm^3/g under STP conditions, and t_{mono} is 0.354 nm for the monolayer thickness of a nitrogen adsorbed layer [84], [85]. To apply HJ t-plot methods, the adsorbed quantity is plotted against the HJ-thickness. Then the external surface area can be obtained from the slope of a linear fit, and the micropore surface area a_{micro} can be obtained by subtraction of external surface areas a_{ext} from the overall BET surface areas. The intercept of the linear plot illustrates the micropore volume, but in the gaseous STP units. Since the nitrogen adsorption at 77 K is assumed to be the liquid phase, the transformation of STP conditions into the real liquid phase volume can be achieved with the following relation.

$$v_{\mathrm{micro}} = \frac{n_{\mathrm{micro}} \cdot \rho_{\mathrm{nitrogen,STP}}}{\rho_{\mathrm{nitrogen,liq}}} \tag{2.22}$$

where the density of nitrogen in the STP condition, $\rho_{\mathrm{nitrogen,STP}}$, is 1.251×10^{-3} g/cm^3, and the density of liquid nitrogen $\rho_{\mathrm{nitrogen,liq}}$ is 0.807 g/cm^3.

The t-plot methods are introduced based on the existing nitrogen isotherms with the thickness range of 0.35 nm to 0.5 nm. Thus, the t-plot methods sometimes are not able to provide reliable results if the nitrogen isotherms cannot provide sufficient linearity in that range.

By analogy to the t-method, instead of reducing n by n_{m}, a lot of researchers suggested to reduce n by an uptake $n_{\mathrm{ref}\,(0.4)}$ at a pre-selected p/p_0 (usually = 0.4) based on reference data [61], [73], [86]–[88]. For instance, Carrott et al. selected the sooty silica adsorption data as the standard [87], [88]. The α_s (fulfilling a similar role as t in the t-method) can be defined as:

$$\alpha_s = \frac{n_{\mathrm{ref}}}{n_{\mathrm{ref}\,(0.4)}} \tag{2.23}$$

where n_{ref} is the reference data of gas adsorbed and $n_{\mathrm{ref}\,(0.4)}$ is the amount of gas uptake in the reference data at $p/p_0 = 0.4$. Then the surface area of the test sample, a_{test} can be written as:

$$\frac{a_{\mathrm{test}}}{a_{\mathrm{ref}}} = \frac{n_{\mathrm{test}}/n_{\mathrm{ref}(0.4)}}{n_{\mathrm{ref}}/n_{\mathrm{ref}(0.4)}} \tag{2.24}$$

$$a_{\mathrm{test}} = \frac{a_{\mathrm{ref}}}{n_{\mathrm{ref}(0.4)}} \frac{n_{\mathrm{test}}}{\alpha_{\mathrm{s}}} \tag{2.25}$$

where n_{test} is the adsorbed amount for the tested sorbent. The α_{s}-plot can be drawn with n_{test} on the y-axis and α_{s} on the x-axis. The surface area a_{test} can be calculated from the slope using equation 2.25.

As shown in **Figure 2.3.11**, for ideal monolayer and multiplayer adsorption on mesopores and large pores, the slope should be constant at low range (type II (a)). Type II (b) indicates the existence of strong adsorbent-adsorbate interactions in the monolayer adsorption, while Type II (c) demonstrates relatively weak adsorbent-adsorbate interactions. The initial linear part of type IV corresponds to monolayer-multilayer adsorption on the mesopore walls, followed by an upwards turn due to capillary condensation [88]. If the linear section can extrapolated back to the origin, there is unlikely to be micropore filling in the type IV isotherm [61].

The appearance of linear regions in α_s-plots as shown in **Figure 2.3.12** indicates the occurrence of multilayer adsorption. The intercept of the linear fit represents the specific micropore capacity n_{micro}. Then the specific micropore volume v_{micro} can be expressed in equation 2.26.

$$v_{\mathrm{micro}} = \frac{M}{\rho} n_{\mathrm{micro}} \tag{2.26}$$

where M and ρ are the molar mass and the average density of the adsorbate, for instance, the related values of liquid nitrogen for isotherms tested at 77 K.

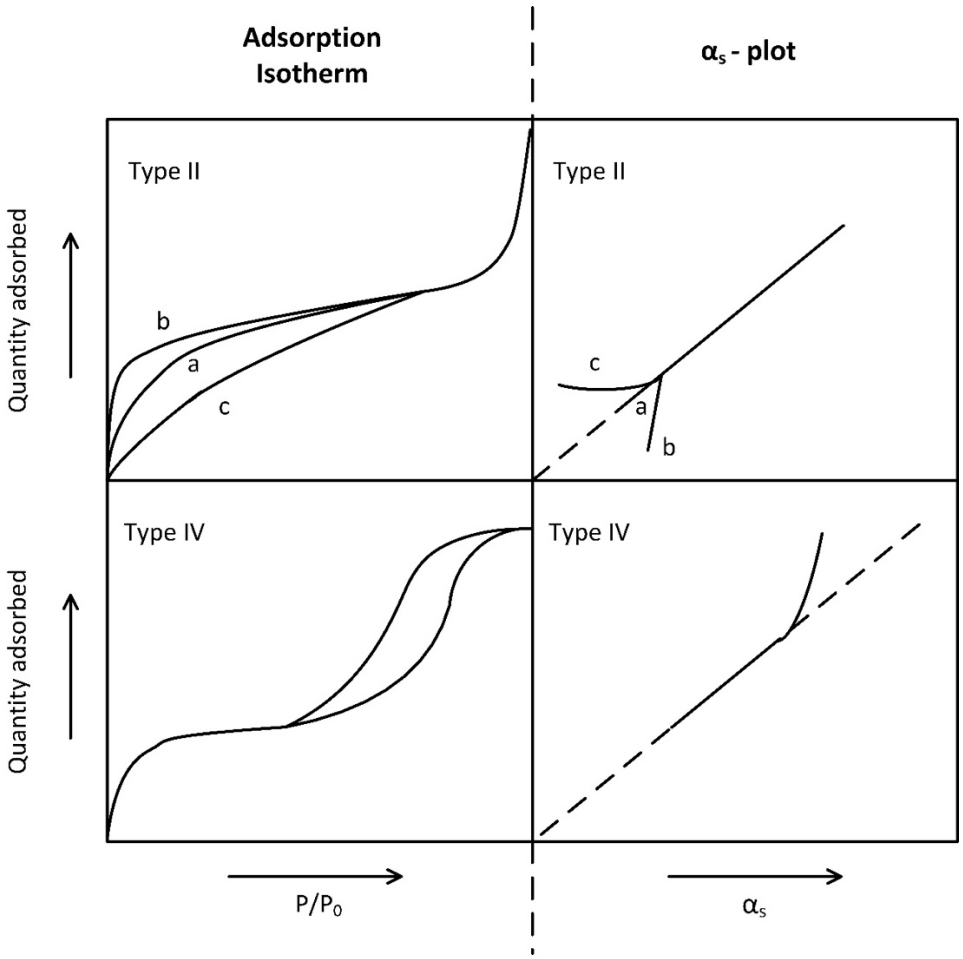

Figure 2.3.11 *Examples of adsorption isotherms and related α_s-plots [61].*

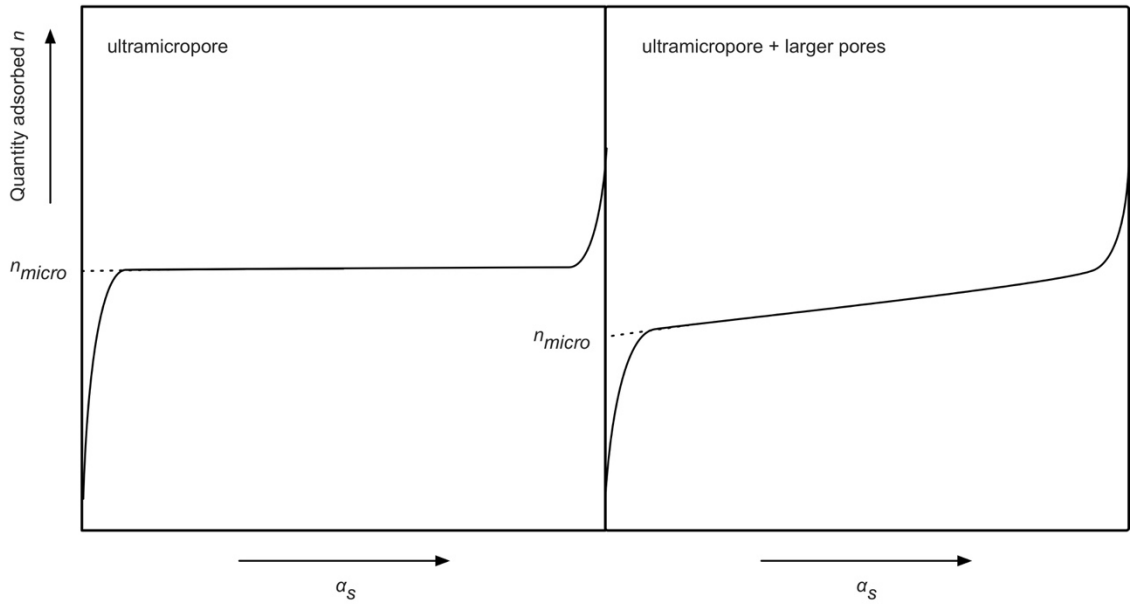

Figure 2.3.12 *An example of using the α_s-method to measure micropore capacity [61].*

2.3.8 Isosteric heat of adsorption

Isosteric heat of adsorption is the molar enthalpy variance of adsorbate transforming from gaseous phase to the adsorbed phase, which is used to describe the thermal property of a storage system [89]. There are two well established methods to measure the isosteric heat of adsorption: the first method is named as the “adsorption calorimetry” which directly measures the heat with the coupled calorimetric-volumetric system; the second method is called the “sorption isosteric method” which indirectly calculates the isosteric heat from a series of adsorption isotherms at various temperatures, using Calusius-Clapeyron thermodynamic relations [89]. The latter method is comparably much more popular than the other one due to its simplicity in implementation [89]–[92].

The value of isosteric heat at a given temperature is found to be related to the coverage of adsorption that is defined as the ratio between the adsorbed amount in comparison with the maximum uptake [89], [93], which means the isosteric heat reaches the maximum at zero coverage, and it then gradually decreases with the increase of adsorption coverage. Pore sizes and unsaturated metal centres which exist in MOFs are reported to have significant influences on the isosteric heat [94], which makes the isosteric heat a significant term for analysing the performance of both MOFs and porous carbons in adsorption. Higher isosteric heat is generally favourable for better hydrogen uptakes at a certain temperature and pressure

condition. In terms of the results in reference [93], the higher adsorption heat was confirmed to result in a larger H_2 wt% uptake per unit SSA for carbide-derived carbons at 77 K and 1 atm. The isosteric heat values for MOFs were reported to be in 3 – 7 KJ/mol [89], [94], and some zeolites were reported to have the isoteric heat around 5 – 6 KJ/mol [95]. The isosteric heat of activated carbons is expected to be 5 – 6.5 KJ/mol [93].

2.4 General designs for adsorption measurements

2.4.1 Simple adsorption volumetry

The expression ”gas adsorption volumetry” generally refers to the type of apparatus to measure gas adsorption based on the volumetric uptake, which was firstly applied to investigate adsorption isotherms between vacuum and atmospheric pressure [61]. A mercury burette system (as shown in **Figure 2.4.1**) was originally used by Brunauer et al. in 1930s to study their well-known multi-layer adsorption theory, also referred to as the Brunauer-Emmett-Teller (BET) theory [66], [67], [70]. With the development of laboratory electronics, the mercury burettes were gradually replaced by pressure transducers. Thereafter, the volume of gas sorption was then measured by monitoring the pressure variations instead of volume change directly [61]. Although many early published isotherms stuck to the expression of hydrogen uptakes in adsorbed volume of STP conditions even though the adsorption uptakes were actually measured by manometers, the gravimetric expressions of adsorbed gas quantities, such as weight percent “wt%”, became increasingly popular.

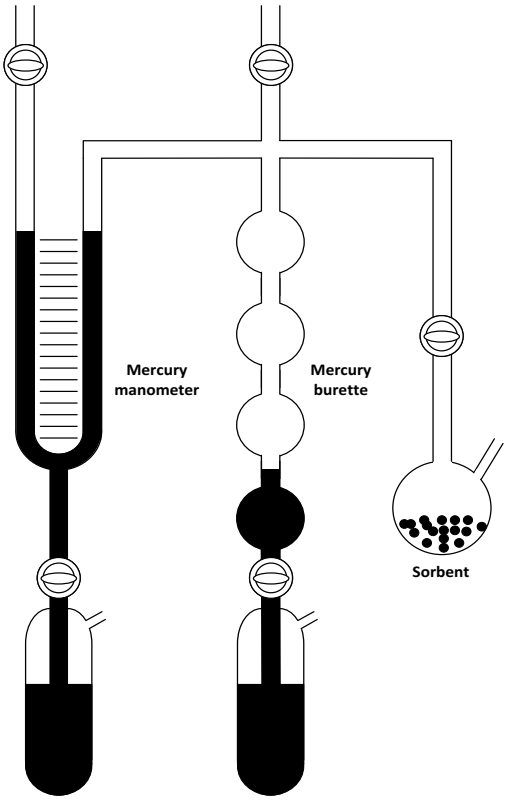

Figure 2.4.1 *A typical design of an adsorption volumetric system at lower pressures than one atmosphere, based on the equipment used in reference [66].*

Following the remarkable efforts from Brunauer et al. to advance the BET theory [70], scientists started to study adsorption behaviour on a great variety of sorbents over a broadened range of pressures. Since the glass based system was not suitable for high-pressure tests, stainless-steel tubing and containers were gradually introduced to replace glassware for constructing sorption measuring systems for more universal applications. A type of volumetric measuring system is described in **Figure 2.4.2**, in which an additional intermediate reservoir was introduced to store the gas before ejection to the sorbent. The volume of the reservoir was significantly larger than that of the sorbent chamber, which could reduce the pressure drop when the sorbents chamber was connected in the experiment. Sometimes, there were two static pressure transducers, fitted on both the reservoir side and the sorbent side. These two transducers were separated with a controlled leak valve so that the adsorption equilibrium pressure during experiment could be adjusted via controlling the flow rate through the valve [61]. This type of volumetric manometry is the most widely used equipment for high pressure adsorption tests nowadays, and is known as Sievert's type apparatus [61], [96], [97].

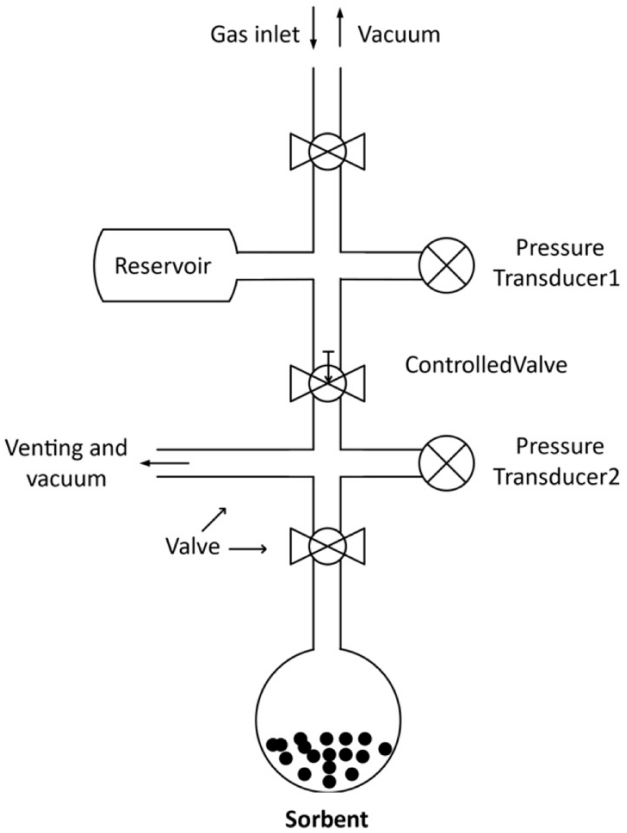

Figure 2.4.2 *A typical design of Sievert's type volumetric systems [61].*

Despite the popularity of the Sievert's type design, there are several disadvantages to consider. The volume of the reservoir and the sorbent chamber can be identified straightforwardly before they are fitted to the system. However, the dead volume of the tubing sections is difficult to measure, which results in uncertainties of measurements. Additionally, the measurement accuracy is governed by the accuracy of the pressure transducers applied. For high pressure tests, the measured pressure variation caused by gas sorption is relatively small in comparison with the static pressure of gas loading prior to the test. However, the measurement uncertainties are related to the static pressure range of the transducer, which can result in obvious uncertainties of measured minor uptakes that are calculated from small pressure variations. For instance, in order to measure a gas uptake, which induces a 1 bar pressure variance at 200 bar absolute pressure, 200 bar static pressure transducers are required. By assuming that the accuracy of transducer is 0.1% of full scale, the error is 0.2 bar, which is significant in comparison with the 1 bar pressure difference.

2.4.2 Differential gas adsorption manometry

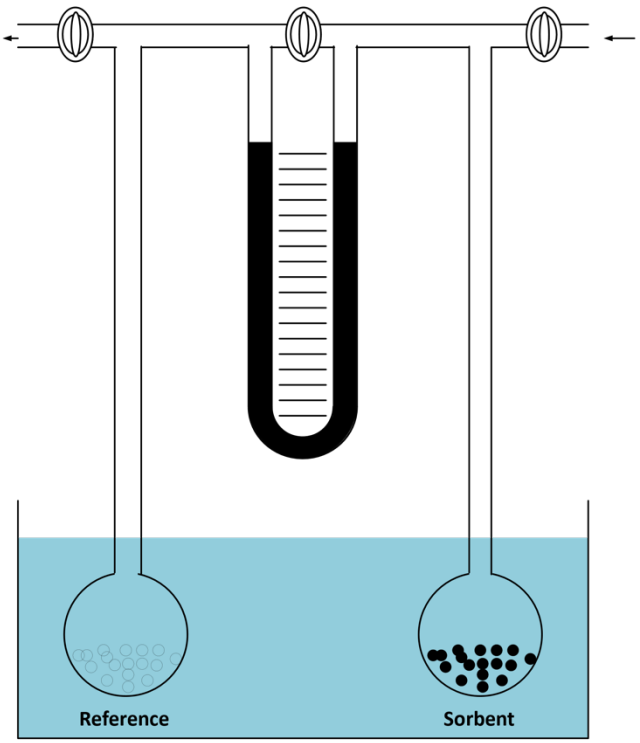

Figure 2.4.3 *A differential manometry designed for tests below one atmosphere [98].*

To overcome the drawbacks in a Sievert's type apparatus, the method of using two identically designed systems, in which one system was filled with sorbents while the other

held a certain amount of glass beads to eliminate the volume difference between two systems, has drawn a lot of attention from researchers [99]. Haul and Dümbgen introduced a simple differential adsorption manometry method in 1960 for nitrogen adsorption under atmospheric pressure, as shown in **Figure 2.4.3** [98]. After the system was filled with nitrogen at a certain pressure, all valves were closed, and both the sorbent chamber and reference chamber were immersed in a liquid bath to achieve a targeted temperature. The recorded pressure variations induced by nitrogen adsorption in sorbents were utilised to calculate the adsorbed quantity. Because of the lack of a vacuum pumping prior to test, the adsorption results did not fall within the BET range of pressures below atmosphere for analysing the sizes of surface areas [99].

With further development of the differential manometry design, more sophisticated differential systems were introduced with the ability to conduct the experiment at various pressures [61], [100]–[104]. As shown in **Figure 2.4.4**, two differential pressure transducers are separated with a control valve with adjustable flows, providing the possibility of continuously modifying the testing pressures. Additionally, the degassing of sorbents could be conducted with the built-in vacuum ports, which is essential to improve the measurement accuracy. Thanks to the stainless steel construction of the system, the measurement can be conducted in a wide pressure range from vacuum to several hundred bars. Because the amount of gas sorption is indicated mainly by the pressure difference between the reference part and the sample part, the selection of the differential transducer can merely consider the maximum pressure difference between two identical systems in adsorption instead of the significantly larger absolute pressures, therefore contributing to high measurement accuracies for small gas uptakes. Since it is more difficult to construct both the sorbent system and the reference system with identical volumes and more pressure transducers are required than Sievert's type apparatus, differential manometry is not so popular as the simple Sievert's type apparatus. It is also worth noting that it is difficult to maintain negligible flow rate differences between two sides using control valves for continuous adjustment of pressures if the induced differential pressure by sorption is small, which is usually the case for hydrogen adsorption.

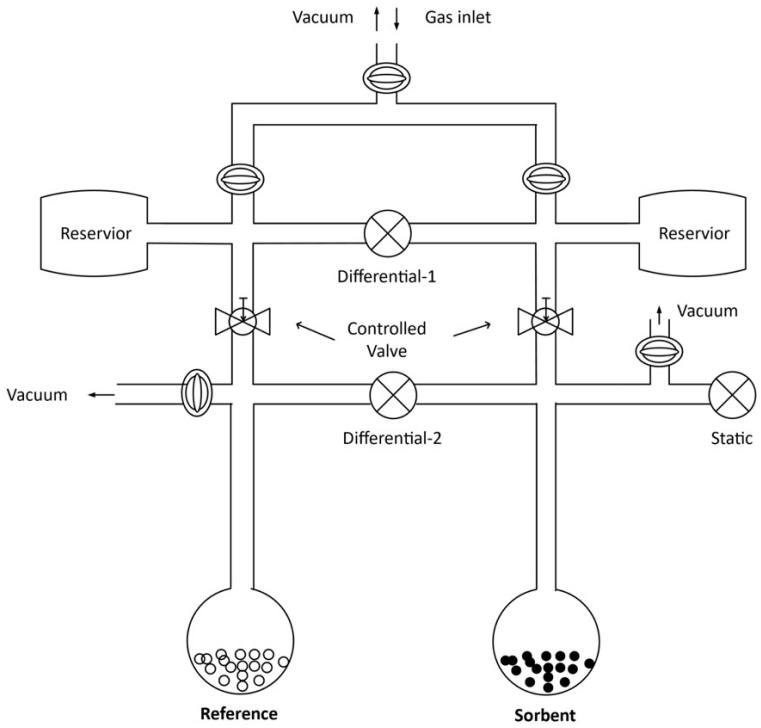

Figure 2.4.4 *A modern design of differential manometry for measuring gas adsorption [61].*

2.4.3 Gravimetric methods

a. <u>From vacuum to atmospheric pressure</u>

The sorption balance was used in laboratories as early as in 1926, when McBain and Bakr reported a detailed description of a sorption balance design that targeted gases sorption below atmospheric pressure [105]. As shown in **Figure 2.4.5**, the spring was made from a fine silica fibre, hanging a sorbent container at its bottom end. A glass tube shielded the spring and the container from the heating zone. When the sorption experiment reached equilibrium, the weight of obtained gas could be measured by determining the extended length of the silica spring. As with the volumetric apparatus in the 1930s in **Figure 2.4.1**, this type of balance could only measure uptake at pressures below 1 atm. Although the loading and calibration of the silica springs costed a lot of time and efforts, the spring balances were an excellent option to study sorption mechanisms with slow equilibriums, such as the hysteresis phenomena.

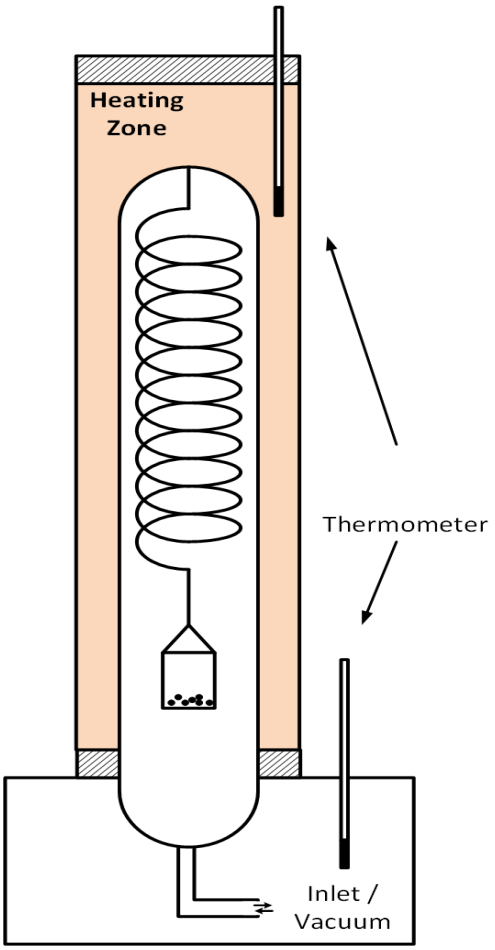

Figure 2.4.5 *A sorption balance designed by McBain and Bakr for gas adsorption below atmosphere pressure [105].*

In recent years, spring balances have been replaced with electronic microbalances [61], [106], for the purpose of avoiding condensation on springs that could contribute to a larger result of the measurement than the real value [107]. With the development of electronics, the gravimetric apparatus was the first available technique that generated an automated recording of adsorption-desorption isotherms [61]. Rouquerol and Davy further developed the design by introducing high-stability leak valves, which allowed the adsorption-desorption isotherms of quasi-equilibrium sorption to be measured at a continuously increasing pressure [108]. The gravimetric method is especially productive for studying condensable gases since the condensation on chamber walls that usually happens in volumetric systems does not affect the measured adsorbed amount in gravimetric apparatus with a microbalance [61].

b. Above atmospheric pressures

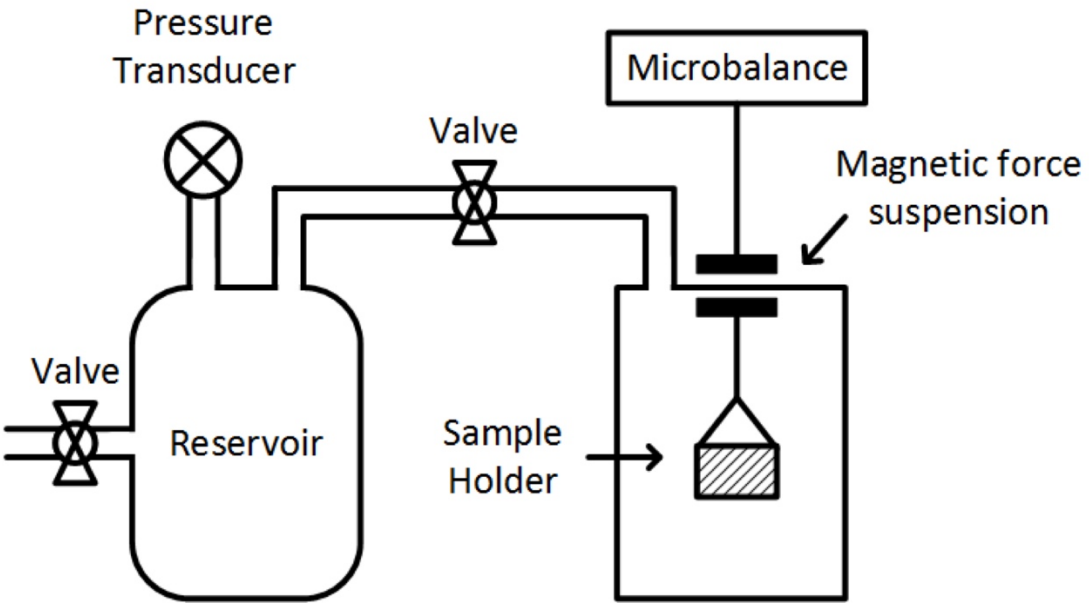

Figure 2.4.6 *Schematic diagram of a gravimetric system with magnetic force suspension [109].*

The techniques reviewed for pressures below atmospheric pressure were based on the application of vacuum microbalances with quartz tubes. For high pressure experiments, stainless-steel vessels are highly recommended instead of glasses for constructing the apparatus. A lot of scientists have made great efforts to modify the vacuum microbalance to be capable for high pressure applications [61]. More recently, magnetic suspension balances have matched the performance of standard analytical microbalances [109]. Instead of installing the microbalance inside the sorption chamber, the balance was situated outside the pressurised chamber, connected to the sorbent container via magnetic suspension, which is well suited for high-pressure tests. In high-pressure gravimeters under constant flows, the evaluation of buoyancy effects is critical to acquire accurate results [61], which can be achieved with the introducing samples with known volumes and determining their weight losses in high pressures.

2.4.4 Summary

Volumetric and gravimetric designs are the most popular methods for characterising gas adsorption. The Sievert's type volumetric design is more commonly adopted in laboratories due to its low-cost and versatility but involving multiple pressure transducers and temperature sensors to obtain gas uptakes in a less direct way, which leads to complicated

combinations of uncertainties from different variables; while the gravimetric method has significant advantages in measuring uptakes more accurately from direct measurements of weight variations caused by gas adsorption, but it requires precise microbalances that costs far more than pressure transducers.

With the consideration of constructing testing equipment for hydrogen adsorption at 77 K, the volumetric method has substantial benefits in comparison to gravimetric methods. Firstly, the stainless-steel vessels and fittings can stand both high pressures and cryogenic temperatures with metal-metal sealing, while it is difficult to implement a microbalance for high pressure adsorption due to significant buoyancy effects. Secondly, the pressure transducers and mass flow controllers for a volumetric system that are specifically rated under European ATEX directives are more convenient to find, compared with the rated microbalances for gravimetric systems. Furthermore, the volumetric systems that consist of transducers and flowmeters are more resistant to harsh conditions, for instance, vibrations during transport, than gravimetric systems with precise microbalances: this factor is potentially significant for mobile applications.

Since hydrogen adsorption uptakes are generally in small quantities, as little as 0.1 wt% or less at room temperatures and hardly more than 2 – 3 wt% at 77 K, the sensitivity for small uptakes is crucial for constructing the system. Therefore, the concept of differential manometry was adopted for building the hydrogen adsorption testing system involved in this study. Although there have been many attempts to implement differential manometry on hydrogen adsorption at high temperatures and pressures, there was a lack of experience in using differential manometry to study hydrogen cryosorption at cryogenic temperatures, such as 77 K. Differential manometry to examine hydrogen uptakes at 77 K and up to 11 bar pressure are discussed in detail in section 6 upon our experiences during the construction.

3 Hypotheses in this study

In this study, the following hypotheses were postulated:

I. A reliable and practical hydrogen adsorption measurement system can be constructed affordably based on differential manometry in order to rapidly characterise the adsorption abilities of sorbents at 77 K.

II. Differential manometry for adsorption measurement can reduce "dead volume effects" and deliver more precise measurements on small adsorption uptakes than Sievert's type apparatus.

III. Medium vacuum degassing, which is easier and cheaper to implement in comparison with high-vacuum pumping, should be sufficient to provide accurate results for mesoporous sorbents for fast tests in 1 – 2 hours at 77 K.

IV. The combination of BET method, Harkins-Jura t-method, α_s-method and BJH method can effectively and systematically evaluate both microporous and mesoporous properties of mesopore-dominant porous carbons.

V. It should be possible to apply the "amorphisation trajectory" primarily based on Raman spectroscopy for rapid assessment of the degree of graphitisation for amorphous carbons and nanocrystalline carbons that might be potential sorbents for hydrogen adsorption, such as pyrolysed biomass and the carbons produced from the microwave plasma splitting of methane.

VI. High surface area graphene nanoplatelets (GNPs) containing slit-like pores and ordered graphitic flakes are better candidates as carbon substrates for producing a metal-decorated carbon composite for gas adsorption, in comparison with activated carbon AC Norit GSX with amorphous structures and pores.

VII. The decoration of palladium on porous carbons might be able to accelerate the sorption kinetics and enhance the overall maximum uptakes for hydrogen cryosorption.

4 Experimental: sample preparation

4.1 Carbon production by the microwave plasma splitting of methane

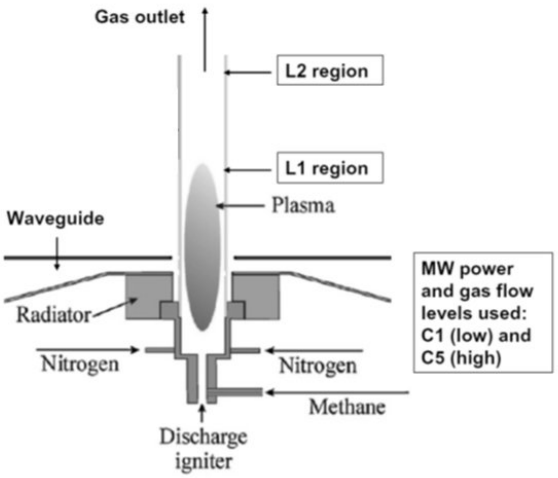

Figure 4.1.1 *Schematic of the microwave plasma reactor (C1 with 1.5 kW power; C5 with 5 kW power) showing the sample collection L1 and L2 [110], [111].*

The microwave plasma splitting of methane was originally developed by GasPlas for hydrogen production, and it was gradually realised to have potential for the synthesis of carbon nanoforms. The plasma carbons are by-products of the microwave splitting of methane to produce pure hydrogen. An atmospheric microwave reactor is described schematically in **Figure 4.1.1**. In the active glow of the plasma source, the high-energy electrons activated split the methane molecules into mobile ionic and neutral radicals [112]. These active species compactly spread in the glow and collide with each other. Some of the carbonaceous products stick to the inner wall of the quartz tube around the glow region (L1 region, **Figure 4.1.1**), while others were located at the tube walls at a cool-down region downstream (L2 region, **Figure 4.1.1**). The carbon products were in the form of small particles but were observed to agglomerate together to form large particles [112].

Table 4.1.2 *The classification of plasma carbons [110].*

Sample name	Plasma reactor power	Gas flow L/min	Location
C1L1	1.5 kW	3	Active glow (L1)
C1L2	1.5 kW	3	Downstream (L2)
C5L1	5 kW	21	Active glow (L1)
C5L2	5 kW	21	Downstream (L2)

According to the power inputs of the plasma reactors and the residence time of the active species for constructing the carbon by-products (reflected in collection regions of carbons on tube walls as illustrated in **Figure 4.1.1**), four groups of carbons were identified in terms of different plasma powers and collection locations of samples, as described in **Table 4.1.2**. Based on previous research [112], the gas flow rate was discovered to have a negligible influence on the structural formation of carbon by-products. As shown in **Table 4.1.2**, the low power plasma input (1.5 kW) was marked as C1 so that the carbon collected from L1 region with the 1.5 kW input was labelled as C1L1, and the carbon situated in L2 region with the same power was C1L2. Analogously, the plasma carbon C5L1 was collected from L1 region with the input power of 5 kW, while C5L2 was collected from the L2 region with the same power input as C5L1.

In addition to the carbon products, there were traces of polycyclic aromatic hydrocarbons (PAH) observed, which can be recognised by their strong smells. These additional components were removed by cleaning with a mixture of solvents, e.g. hexane, chloroform, acetone and ethanol. Then the purified samples were dried prior to any further adsorption examinations.

4.2 Pyrolysis of *Miscanthus*

Miscanthus is a genus of perennial grasses, native to some regions such as Africa and Asia, but growing in many other places including the UK and Ireland. Because of its broad distribution and economical acquisition, *Miscanthus* was selected the start material of biochar production for this project. The collection of raw materials and the pyrolysis of *Miscanthus* were conducted by Dr Kwapinski in University of Limerick. The collected plants

were firstly dehydrated and shredded into small pieces of 5 – 10 mm length prior to further heat treatments. During the pyrolysis process, the compressed *Miscanthus* materials were carbonised for 20 minutes at the temperatures from 200 °C to 1000 °C in a protective nitrogen flow. A rate of 25 °C/min for increasing the heating temperature was set for optimised bio-char yield. The carbonised samples were thereafter cooled down within a similar protective nitrogen environment to prevent the sample from contacting with moistures in the air.

4.3 The Pd-decoration of carbons

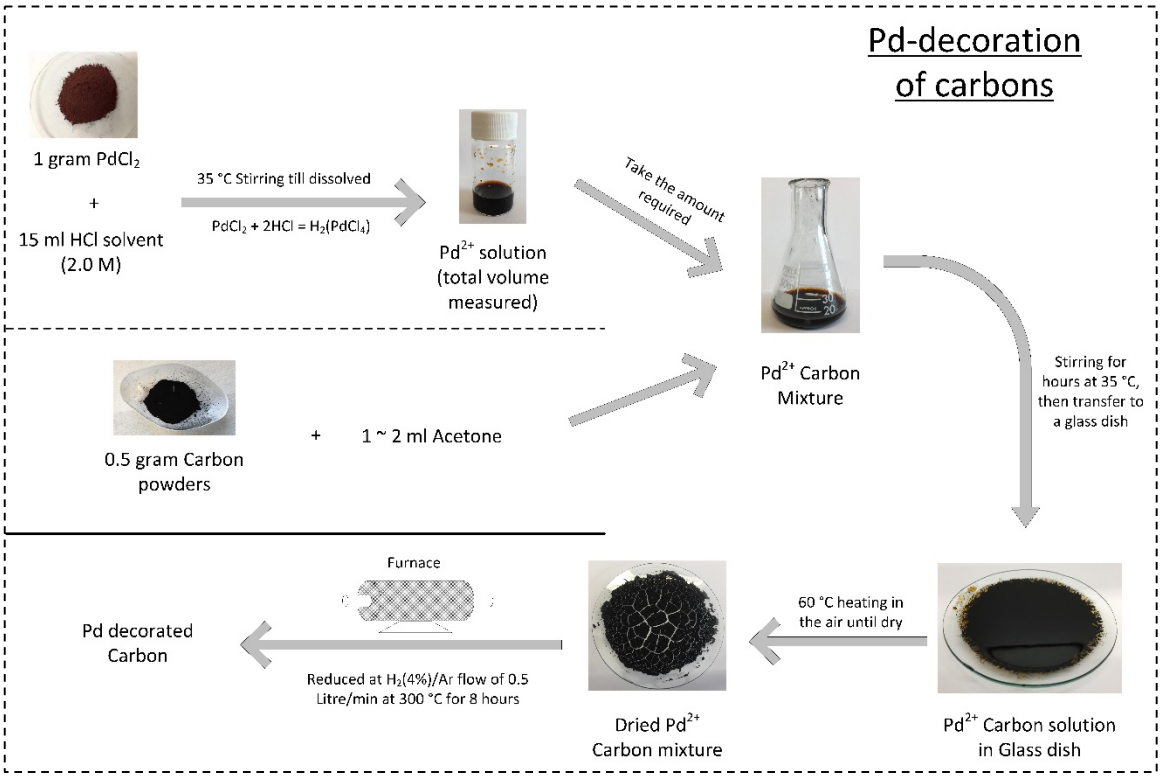

Figure 4.3.1 *The procedure for palladium (Pd) decoration on carbon materials.*

Palladium on carbon is widely adopted as a versatile catalyst for industrial applications, for instance, dehydrogenation, petroleum cracking, etc. [113], [114]. For hydrogen storage, palladium itself is an excellent sorbent to absorb hydrogen due to the formation of hydride, as previously discussed in section 2.2.1. Moreover, the introduction of hydrogen spillover effect by palladium has been proven to improve the overall uptakes of carbon-based substrates, which is of particular interests to graphite-like materials [24]. Palladium decorated activated carbons can be purchased from many chemical suppliers, such as Sigma-Aldrich and Fisher Scientific. As the unique supply of some carbons studied in this thesis, a method of Pd

decoration was applied by the author as described in **Figure 4.3.1**, which was first published in the work of Campesi et al. [115]. With the aim of acquiring a targeted amount of decorated Pd and meeting our laboratory restrictions, the amount of solvents and carbons applied, as well as the flow rate of the reduction gas during heat treatment, were adjusted but the procedures followed the original work.

For accurately controlling the compositions of carbons and Pd^{2+} in the Pd^{2+} carbon mixtures, the total volume of the prepared Pd^{2+} solution with a certain amount of $PdCl_2$ dissolved was measured with a measuring cylinder. By assuming that the loss of carbons and solutions during the transfer between vessels is negligible, a target weight percentage of decorated Palladium could be obtained, if both Pd and carbons were assumed to be fully integrated with each other. The real composition of palladium in the carbons was discovered to be less than the expected percentage, which is discussed in the results section 7.5, based on thermal gravimetric analysis (TGA).

Two carbons, the activated carbon AC Norit GSX and graphene nanoplatelets with surface areas of 700 m^2/g (GNPs-700), were selected for the palladium decorations. The AC Norit GSX is a type of activated carbons with surface areas with over 800 m^2/g, while the GNPs-700 has a surface area over 700 m^2/g. The high surface areas of these materials are critically important for large uptakes of gas adsorption including hydrogen cryosorption. AC Norit GSX has a highly amorphous and porous microstructure, whereas the structures of GNPs-700 are more graphitic and better identified, in spite of the similar surface areas in between two carbons. The study of Pd decoration in these carbons is looking for their potential catalytic effects on adsorption kinetics and the formation of palladium hydride during hydrogen absorption in cryogenic temperatures.

Each of the carbons was doped with 20 wt% and 40 wt% of Pd in the total weight of the doped samples, resulting in four products: “20 % Pd – AC Norit GSX”, “40 % Pd-AC Norit GSX”, “20 % Pd-GNPs700” and “40 % Pd-GNPs700”. These four labels for Pd decorated carbons are utilised throughout this thesis for consistency, although the real compositions of Pd in the produced composites are estimated to be less than the assumed Pd deposition in the preparation procedure. Furthermore, the raw materials and the doped materials were analysed with XRD for determining the crystallite sizes of the Pd contents and SEM/EDS for

discovering the Pd particle distributions. BET measurements were also undertaken for evaluating the changes in surface areas and the pore properties in the presence of Pd particles compared to the raw carbons. The exact compositions of produced carbons were characterised with TGA, and both raw carbons and Pd decorated samples were tested for hydrogen cryosorption in the constructed system at 77 K and gauge pressures up to 10 bar.

4.4 Commercial sorbents

4.4.1 Graphene Nanoplatelets

The graphene nanoplatelets (GNPs) studied in this programme were supplied by DZP Technologies[1] with diverse surface areas, 20 m^2/g (GNPs-20), 500 m^2/g (GNPs-500) and 700 m^2/g (GNPs-700). According to the characterisation and analysis in section 7.4, the GNPs are able to provide high surface areas, which is crucial for gas adsorption without downgrading the ordering of graphitic structures. The high surface areas GNPs have mostly slit-shape mesoporous structures in which the pore volume is homogeneously distributed in the pore diameter range of 2 – 50 nm. The porous structures of high surface areas GNPs are attributed to the aggregation of small crystallites. The GNPs-700 was also decorated with palladium particles to form the Pd carbons as studied in section 7.5.

4.4.2 Activated carbons

Two branded activated carbons, AC Norit GSX and AC Norit ROW, were selected both as porous sorbents for adsorption and as reference materials for comparison with the GNPs. The microporous and mesoporous properties of AC Norit GSX and AC Norit ROW were characterised quantitatively with various analytical methods. AC Norit GSX was also used for palladium decoration for comparison with the GNPs-700.

4.4.3 Zeolites 13X and NaY

Both 13X and NaY are zeolites in the faujasite group, but with different silicon-to-aluminium ratios (Si/Al ratios). 13X, with a low Si/Al ratio, is a type of molecular sieve for industrial gas drying, purification and sweetening, while the zeolite NaY, with a high Si/Al ratio, is used as a catalyst due to its high activity and stability at elevated temperatures. Both zeolites have

[1] DZP Technologies Ltd, Future Business Centre, Kings Hedges Road, Cambridge, CB4 2HY, UK

ordered structures and uniform pore diameters around 1 nm. As the pore sizes of the two zeolites are close to the ultramicropore sizes (< 0.7 nm), the application of analysis methods, such as BET, requires high vacuum degassing for measuring nitrogen adsorption isotherms that is beyond the capacity of BET equipment used in this thesis. According to the specifications from the supplier, zeolite 13X has a specific surface area of around 720 m^2/g, while the zeolite NaY has a much larger surface area of 900 m^2/g. These values of surface areas for the two zeolites are used to compare with the surface areas of carbons that were measured from nitrogen adsorption isotherms.

4.5 Selection of samples

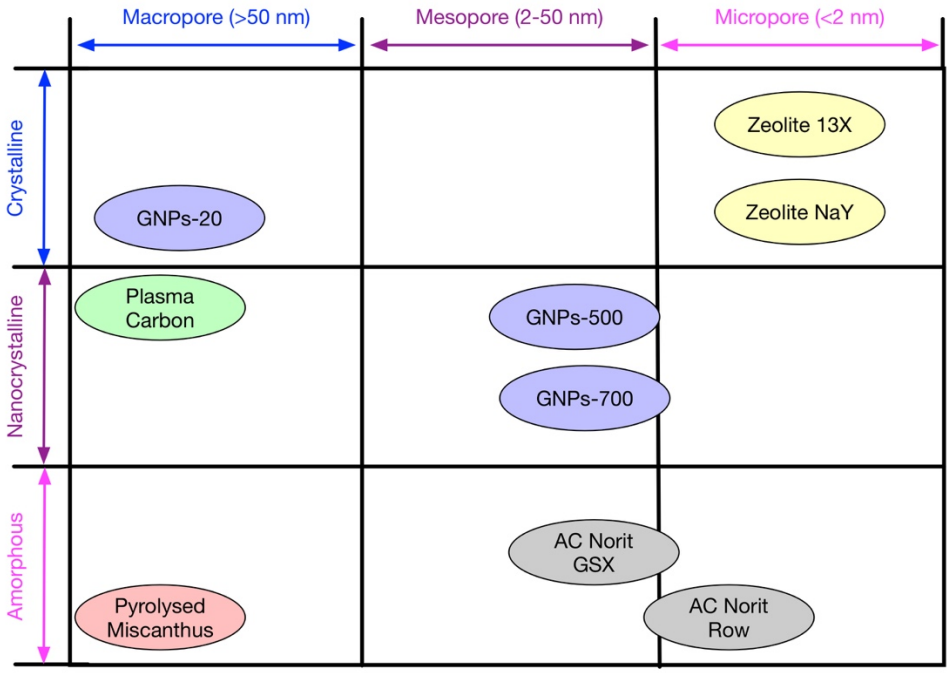

Figure 4.5.1 *The comparison of selected samples.*

There are two basic criteria to select the samples for this study: crystallinity and porosity. Higher crystallinity generally results in a more definable structure, and higher porosity is favourable for better gas adsorption. Different with zeolites and MOFs which can achieve a high porosity without losing a crystalline structure, activated carbons or carbon based materials except for graphene are normally in amorphous phase if they have a high porosity and a large surface area. Well defined crystalline sorbents are excellent candidates with no doubt if people would like to investigate how microstructures affect the adsorption behaviours of carbon sorbents, which is the one of main purposes of this thesis.

As shown in Figure 4.5.1, with the definition of both plasma carbons and prolysed carbons (*Miscanthus*) into a single category due to their similarity in properties, and with the fact that Palladium decorated carbons remain the similar porosity and crystallinity as their raw materal, there are nine types of materials studied in this thesis. Three graphene nanoplatelets (GNPs) with various surface areas, GNPs-20 (around 20 m^2/g), GNPs-500 (around 500 m^2/g) and GNPs-700 (around 700 m^2/g), remain a high crystallinity (either crystalline or nanocrystalline) with the increase of surface area, of which the structure is more definable than activated carbon with similar surface areas, making GNPs excellent candidates for studying structural effects of hydrogen adsorption. Activated carbons, AC Norit GSX and AC Norit ROW, which have high porosity and large surface areas, are the most popular and easy to obtain carbon sorbents for gas adsorption. Zeolites, 13X and ZaY, are chosen to be the reference sorbents to verify the functionality of newly-designed system and to be as references to other carbon materials in adsorption. Pyrolysed carbons from *Miscanthus* is used to investigate the carbonisation process of biomass, and plasma carbon is for exploring the structural formation of carbon by-products in the novel microwave plasma splitting of methane.

For hydrogen adsorption, the sorbents are normally either mesopore-dominated or micropore-dominated. As shown in Figure 4.5.1, six porous sorbents are well distributed not only evenly in porosity (three mesopore-dominated sorbents and three micropore-dominated sorbents), but also averagely in crystallinity (two crystalline sorbents, two nanocrystalline sorbents and two amorphous sorbents), which makes the chosen samples a convincing selection for this study.

5 Experimental: characterisation techniques

5.1 X-ray Diffraction (XRD)

X-ray diffraction (XRD) scans of carbon samples were performed using a Philips X'Pert PW1820 diffractometer with Cu-Kα radiation. A step mode scan was conducted in the range of 5 - 90° in general with a step size of 0.1° and a counting time of 2 – 30 seconds per step depending on the noise level. It is noted that comparable results in each figure presented in this thesis were obtained with identical XRD settings. A 1/2° divergence and a 0.2 mm receiving slit were generally adopted. Diffraction data was analysed and fitted in PANalytical HighScore Plus software.

The quantitative study of sample structures via X-ray diffraction can be performed according to the Bragg and Scherrer equations. Bragg's law is described as below:

$$n\lambda = 2d_{\mathrm{hkl}} \sin\theta \tag{5.1}$$

where θ is the angle of incidence to the lattice plane, n is the order of reflection, λ is the wavelength, and d_{hkl} is the lattice plane spacing.

Scherrer's equation is generally applied to relate the broadening of an hkl peak to the crystallite size, and it is presented below:

$$\beta = \frac{K_{\mathrm{c}}\lambda}{L\cos\theta} \tag{5.2}$$

where β is the full width at half maximum (FWHM), L is the crystal size, and K_{c} is a shape factor with a value of 0.9 in general. In calculating the crystal size of graphitic structures along the a-axis from a (10) peak (assuming the growth of the graphitic layer is isotropic), K_{c} is defined as 1.84 [116], [117].

5.2 Brunauer-Emmett-Teller (BET) assessment

A Micromeritics TriStar 3000 machine was used to measure the nitrogen adsorption isotherms of sorbents and to apply the BJH method for analysing mesopore size distributions at 77 K. The machine can conduct the pressure measurements with a resolution of up to 0.05 mmHg and an accuracy of up to 0.5% of full scale, in the range of 0 to 999 mmHg (1.33 bar).

Since the vacuum pump can only reach the medium vacuum of 20 μm Hg (2.67 Pa), the minimum relative pressure of nitrogen isotherms was about 0.01. Although this vacuum is not high enough to characterise microporous materials, such as zeolites, it is sufficient to characterise mesoporous materials, such as the carbon materials studied in this report. As the applied BET range by the machine is fixed to the relative pressure range of 0.01 – 0.2, which is appropriate for sorbents containing a certain amount of micropores, the BET analysis of all studied carbons was further verified with the method discussed in section 2.3.5.

5.3 Raman spectroscopy

For Raman measurements, a Renishaw Ramascope-1000 was used, with a 50 mW 633-nm HeNe excitation laser, calibrated against a silicon standard. Spectra were normally collected in the range of 600 – 3500 cm^{-1} Raman shift. Some points on the powder surface gave extremely high intensities of scattered irradiation due to sample fluorescence, and these spectra were discarded. The spectra background determination and peak fittings were conducted using Origin Pro software.

5.4 Scanning electron microscopy (SEM)

FEI Nova NanoSEM, an analytical FEGSEM designed for high-performance imaging, was used for SEM characterisation. In addition to the secondary electrons (SE) detector for SE imaging, a Bruker electron backscatter diffraction camera was used for backscattered electron imaging (BSE), and a silicon Drift Detector energy-dispersive X-ray (EDX) spectrometer was used for chemical mapping and chemical composition analysis.

5.5 Thermogravimetric analysis (TGA)

A TA Instruments Q500 was used to carry out thermogravimetric analysis (TGA) on Pd decorated carbons and their raw carbons. About 10 mg samples were tested under an air flow of 60 ml/min from room temperature to 1000 °C at the ramp rate of 10 °C per minute. The TGA results will be discussed in section 7.5 for determining the Pd content of decorated carbons.

5.6 Density measurement

An AccuPyc 1330 pycnometer with helium gas intrusion was used to measure the density of sorbents for hydrogen adsorption. The weights of samples were measured with an analytical balance, and the volumes of samples that were inaccessible to the probing gas molecules were measured by the pycnometer. Then the density of sorbents can be obtained with dividing the mass by the volume of the sample.

5.7 Transmission electron microscopy (TEM)

The TEM images of the graphene nanoplatelets (GNPs) studied in this thesis were taken by our collaborators in the University of Limerick. The facility used for TEM characterisation is JEOL JEM-2100F, a multipurpose, high resolution electron microscope with a field emission source. The fast Fourier transform (FFT) analysis of graphitic layer pictures in some carbons were conducted with ImageJ software.

5.8 Other techniques

The characterisation of plasma carbons and biochars using X-ray photoelectron spectroscopy (XPS) and Fourier transform infrared spectroscopy (FTIR) was conducted by our collaborators in the University of Limerick. The XPS equipment used is Kratos AXIS-165, and the FTIR equipment applied is Perkin Elmer Spectrum 100 with Universal attenuated total reflection (ATR).

6 Experimental: the design and development of differential manometry system

6.1 Hydrogen cryosorption conditions

As discussed in section 2.4, there are a range of possible apparatus designs suitable for gas sorption measurements. It is worth noting that the risk assessments of experiments involving hydrogen gas are considerably different from those applying only inert gases such as nitrogen and helium. With the concern of hydrogen safety, some precautions need to be considered during the construction of system. With the intention of building a cost-effective and practical system to handle fast and accurate measurements, we cautiously examined every possible aspect of the experimental design. Among these concerns, there are several key points to be clarified in detail:

I. Hydrogen molecules are small and light, which means that the chambers containing hydrogen under pressures need better sealing than those for dealing with nitrogen gas. Additionally, the consequences of a hydrogen leak are more severe than inert gases. It is worth noting that the hydrogen is lighter than air. Thus, it is essential to have ventilation systems fitted above the adsorption system to prevent local accumulation of hydrogen.

II. Electronics are highly recommended to meet industrial European ATEX directives, which were issued for electronics used in explosive gas environments, although the ATEX directives are not compulsory for lab environment. Additional safety precautions are required, such as isolating the parts that have the possibility to leak hydrogen in emergency circumstances from users.

III. Hydrogen-air mixtures are highly explosive, so attached devices, for instance, the vacuum pump and the power supplies that can potentially introduce local hydrogen-air accumulations or generate electric sparks, require careful consideration in the experimental design. Experimental procedures need to be optimised to reduce the risk to a minimum and controllable level.

To confront these safety concerns, the apparatus was entirely constructed with stainless-steel tubing and bottles, and all components were attached with metal-metal fittings, for example, the Swagelok tube fittings and Swagelok VCR fittings, so that the equipment can achieve leak tightness and withstand cryogenic temperatures. Besides, the equipment was housed in a concrete cell equipped with extraction fans to provide high flowrate extraction, which was discussed in detail in the section 6.5.5. In addition, for the safety of users, the equipment was controlled by a combination of pneumatic valves, which were further regulated by a set of solenoid valves situated outside the hydrogen cell. The experiment was run remotely via computer software by managing the states of the solenoid valves, which prohibited the exposure of users to hydrogen gas during operation.

6.2 Selection of volumetric design

Each type of apparatus design for sorption measurement has its own advantages and disadvantages. The gravimetric type of equipment has the capability to record both the adsorption and desorption isotherms in a single test straightforwardly but involving precise fabrications and costly components, while the volumetric devices are more affordable to construct, and are better suited to future modification by amending the combinations of sensors, but require meticulous assessments of volumes and elaborate calculations of uncertainties among a lot of parameters.

Since the main purpose of this thesis is to study the hydrogen cryosorption at conditions for mobile applications, the proposed equipment is required to deliver rapid and affordable tests upon sorbents. For instance, in a refuelling station or an automobile service garage, a measuring equipment should be able to monitor the degradation of storage capacity in sorbents caused by hydration and contamination cost-effectively and quickly. The equipment shall also be small and robust if it needs to be implemented into a vehicle. The specially rated pressure transducers used in volumetric systems are more common than suitably rated microbalances in the market. With the consideration of the cost of construction and the testing environment (e.g. 77 K), the volumetric type design was the better option to implement.

Although Sievert's type apparatus, which contains only one set of reservoir and sorbent volumes, has been widely used for adsorption, it has a serious accuracy concern for small uptake measurements, especially for hydrogen adsorption measurements, because of the accuracy limitations of high-pressure static pressure transducers on small pressure changes induced by gas uptake. The quantity of hydrogen uptake was reported to be less than 1 wt% for carbon materials at room temperature and several hundred bar pressures, and less than 7 wt% of uptakes at 77 K and tens of bar pressure [4], [14], [46], [48], [118], which is much less than the amount of nitrogen adsorbed under the same condition. By contrast with the application of a static pressure transducer, differential manometry consists of one differential pressure transducer that is only responsible for monitoring the induced pressure difference by gas adsorption between the two identically designed systems, and a pair of static pressure transducers that are implemented to measure the static pressure condition during tests. As the sorption uptake is mostly decided by the differential pressure transducer with a small measuring range, differential manometry is far more sensitive for small uptakes of hydrogen sorption than the Sievert's type apparatus using high-pressure static pressure transducers.

6.3 Design criteria and parameters

- Sample quantity: 1 gram for carbons, or 2 cm^3 volume

  In most cases, the samples available for testing are in small quantities. Since we targeted our research mainly on carbon-based materials, the density of most porous carbons with high specific surface areas (SSA) is around 2 g/cm^3. For sufficient measurements, a 1 gram sample size was the standard quantity for testing.

- The targeted sorption amount: maximum 10 wt% of hydrogen uptake in respect of the sorbent weight of 1 gram

  The US Department of Energy (DOE) set the gravimetric target of 5.5 wt% systematic hydrogen uptake by 2020 for on-board automobile applications [6]. Since the published hydrogen adsorption capacity of sorbent generally referred to the weight percent of adsorbed hydrogen in respect of the weight of sorbent, which ignores the mass contribution from storage system, the targeted hydrogen excess uptake of sorbent is expected to be much higher than the systematic target of 5.5 wt%. Since it

has been reported that some activated carbons with surface areas over 3000 m^2/g were able to store hydrogen more than 7 wt% [46], 10 wt% will be a good compromise for both evaluating the storage abilities of current sorbents and providing enough room for future improvements.

- The quality of outgassing (vacuum): typically better than 10^{-4} bar, ideally better than 10^{-7} bar depending on tested materials, at room temperature

  The vacuum degassing quality can be improved conveniently by switching between the medium-vacuum rotary pump and high-vacuum diffusion pump depending on the porous structure of samples.

- The pressure range: -1 – 10 bar gauge pressures (0 – 11 bar absolute pressure)

  The experimental design of this thesis mainly focused on hydrogen sorption abilities for mobile applications. There are two main methods to use hydrogen as the fuel to power automobiles: internal combustion engines (IEC) and fuel cells. The application of cryogenic temperature 77 K in hydrogen storage aims to significantly reduce the storage pressure condition for achieving a large quantity of uptake, in which the expensive and complicated pressure reduction (control) system is no longer needed. For a IEC power system, the supply pressure is similar to that of a natural gas combustion engine which requires the supply pressure below 11 bar [119]. The operating pressure of a fuel cell was reported to be about 1 – 3 bar pressure [120], and the corresponding delivery pressure from the storage system should be 3 – 12 bar in terms of DOE targets for light-duty fuel cell vehicles [6]. Therefore, the 11 bar is a comprised pressure range for both ICE and fuel cell applications using hydrogen fuels. It is noted that the system was tested at the pressure of 15 bar, and it can also deliver slightly higher pressures than 11 bar.

- The temperature: liquid nitrogen temperature, 77K

  It was widely recognised that hydrogen uptakes at 77K was significantly higher than that at room temperature even with pressure at hundreds of bars. Besides, thanks to the development of thermal insulation technique, 77 K is inexpensive to achieve and

maintain for a long period of time, which has been widely approved in industrial applications.

- The approximate number of points required: 15 points per isotherm

  The equipment is built for single measurements instead of a continuous measurement with the consideration of difficulties in delivering the same flow controls between two systems. Each isotherm covers 2 - 4 points below atmospheric pressure depending on the sorbents and over 11 points above atmospheric pressure, which is sufficient to monitor the variations of uptakes versus small pressure steps.

- The conditions of equilibrium: < 0.001 wt% per minute variation

  As the measured uptakes is observed to gradually approach the equilibrium maximum uptake asymptotically, it is impossible to identify an exact time of maximum uptake. Instead, an equivalent maximum uptake was defined for the sorption measurement as the stage at which the variation of points during the last minute has an average value less than 0.001 wt% per minute. The average of the last 20 uptake values was then taken as the maximum uptake at that pressure.

- The volumes of chambers for each system: 300 cm^3 for the reservoir bottle and tubing at room temperature; 20 cm^3 for sorption chambers submerged in liquid nitrogen

  Although the reference system and the testing system are identically designed, small volume deviations are inevitable during construction. The volume difference between the two system is considered in the calculation of ultimate adsorption uptake, as discussed in section 6.6. To minimise the pressure drop when the sample chambers under vacuum are connected to the reservoir volumes, the reservoir volumes are much larger than those of the sample chambers. All volumes are calculated to achieve the full range of a 1 bar differential pressure transducer at 10 wt% uptake for a 1 gram sample.

- Sealing type and materials: metal-metal sealing, stainless steel

  In order to meet the safety requirements of hydrogen experiments, metal-metal sealing was implemented for building the system. Swagelok tube fittings were

selected for non-amendable joints, and Swagelok VCR fittings were applied for most replaceable and re-openable sections.

- Data Acquisition: 0.5 – 100 times per second

  A National Instruments X series USB card (NI USB-6351) was fitted for measuring and digitising the voltage signals from the sensors. Each recorded point had been averaged with 100 continuous measurement points. The sampling rate depended on the purpose of the experiments. For instance, high frequency recording is required for a kinetics study of the sorption experiment at a certain pressure.

6.4 The schematic diagram and pictures of constructed system

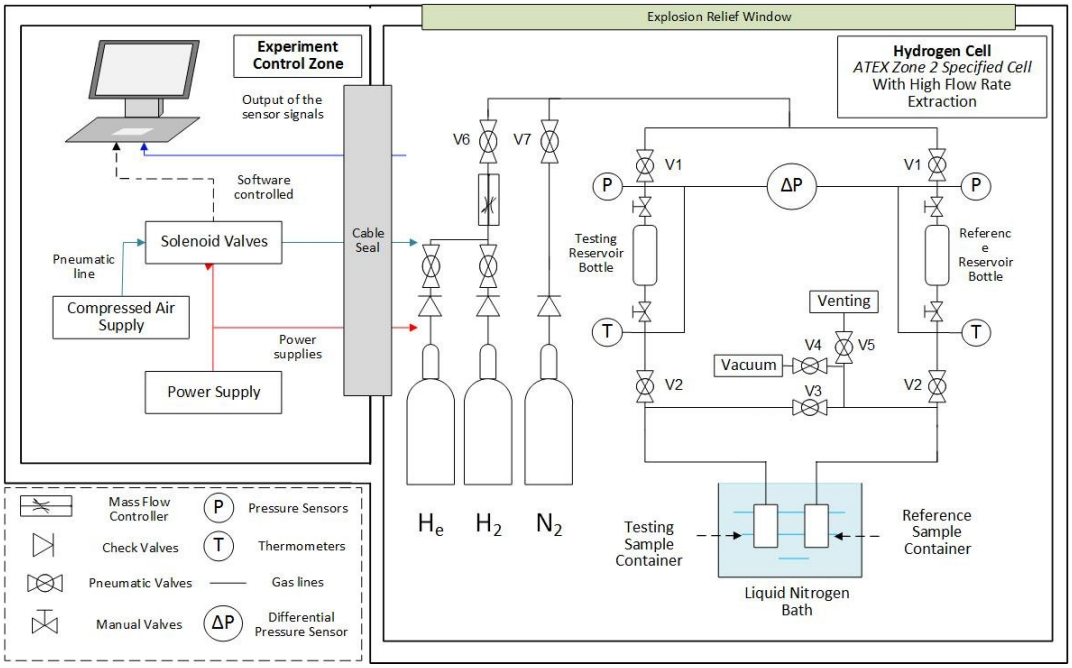

Figure 6.4.1 *A schematic diagram of the constructed volumetric apparatus for hydrogen cryosorption measurement at a temperature of 77 K and pressures up to 11 bar. Connections to individual sensors and valves are omitted for clarity.*

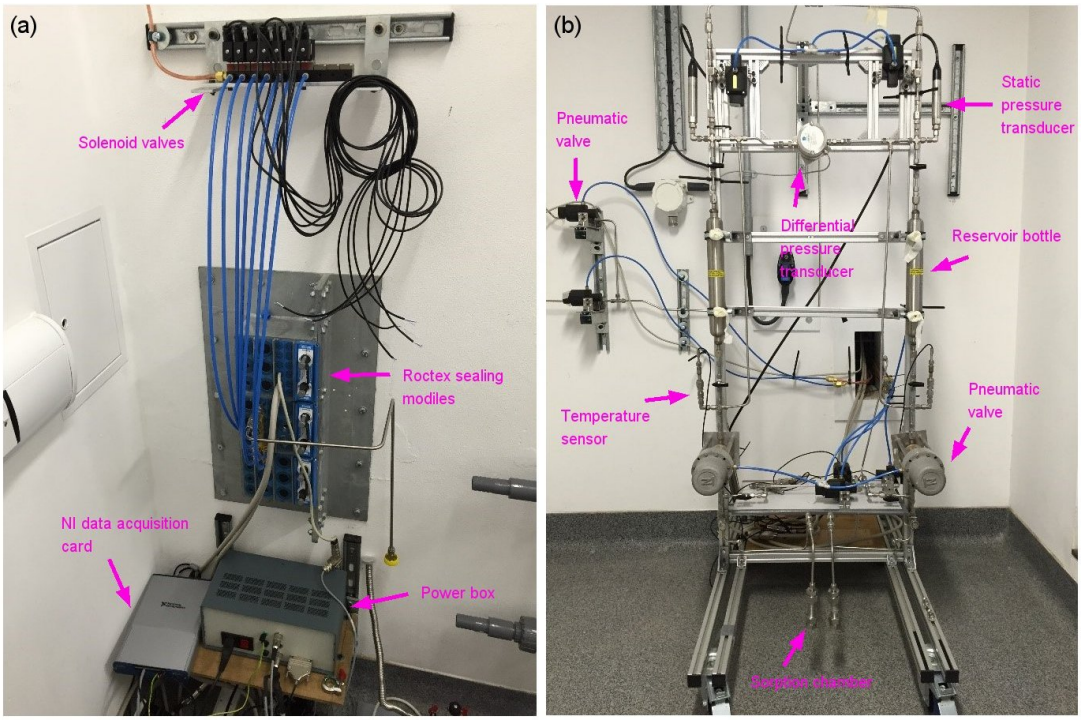

Figure 6.4.2 *(a) Electronics and pneumatic control system. (b) The part of sorption system situated inside the hydrogen cell.*

6.5 Key components and designs

6.5.1 Differential pressure transducers

The selected model of differential pressure transducer was from the GE Druck LPM 9000 series with a measurement range up to 1 bar. The rated temperature condition was between -4 °F to 180 °F (253 – 355 K). The related combined accuracy caused by non-linearity, hysteresis and repeatability is 0.1% of full scale. The sensor required zero offset adjustment for each test, which had been taken into consideration in the design of experimental procedures.

The selected 1 bar range was targeted for 10 wt% uptake on 1 g sorbents. In practice, 0.1 – 0.6 bar of differential pressures were generally reached depending on the amount of loading and the type of sorbent, which was in good accordance with the original design. The resolution of the sensor was well suited to logging short bursts of readings, which was also confirmed with the actual operation.

6.5.2 Mass flow controller and gas supply

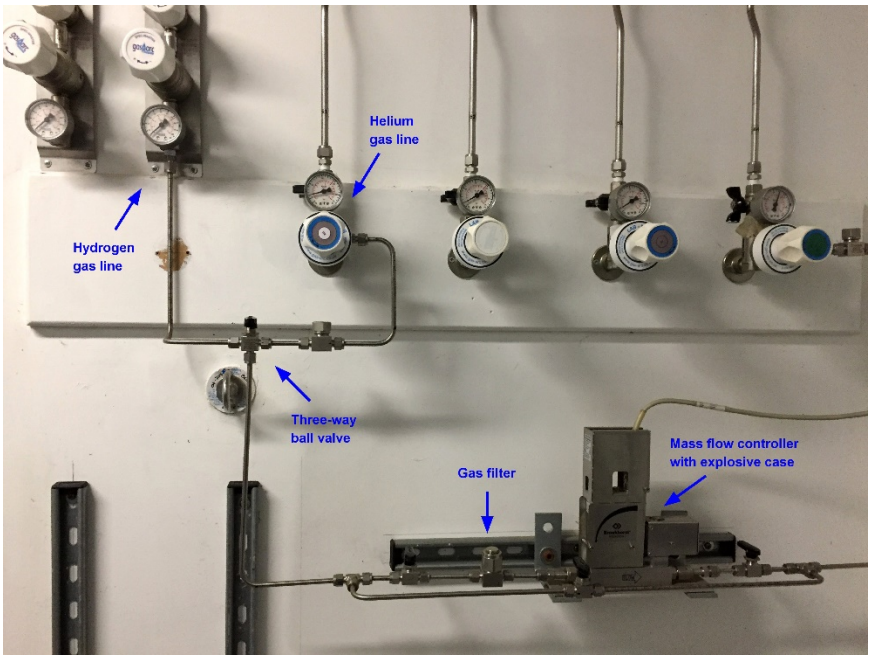

Figure 6.5.1 *The picture of layout of mass flow controller and connected gas lines.*

Apart from pressure transducers and temperature sensors, which were implemented with extra electrical insulation, the mass flow controller was the only device situated inside the

hazardous atmosphere cell (ATEX zone 2 rated environment). The installed Bronkhorst IN-FLOW model was rated for a ATEX Zone 2 atmosphere by the manufacturer, and it could control the flow rate of hydrogen gas at up to 2 normal litres per minutes.

There were two premeditated applications for the fitted flow controller. Firstly, it was used to adjust the loading pressure in the reservoir volumes at the initial step of sorption experiments. The other function of the mass flow controller was to conduct the volume measurement of some chambers in the system, which could be carried out by monitoring the pressure variations via introducing a constant flow rate to a targeted volume. The built-in multi-gas interface of the flow controller allowed us to conduct initial tests under helium prior to the application of hydrogen gas.

6.5.3 Pneumatic system for remote gas control

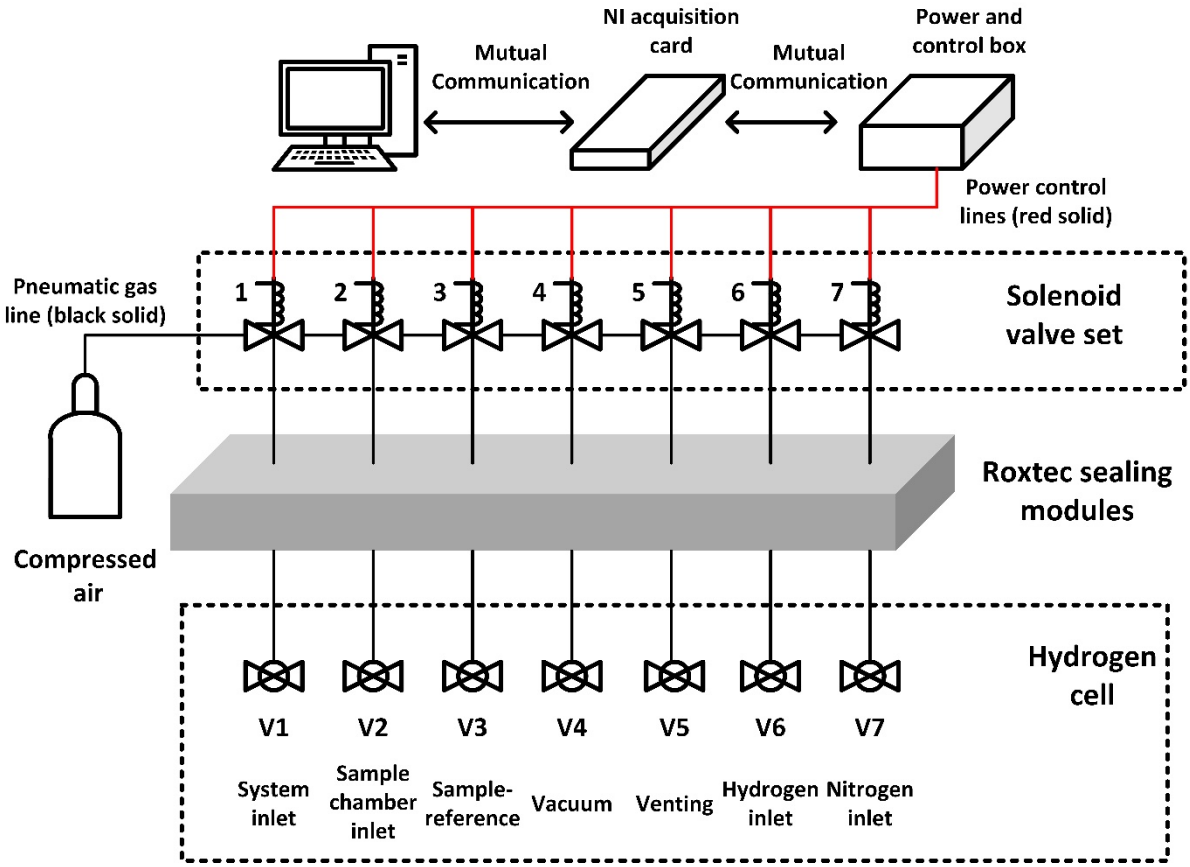

Figure 6.5.2 *Details of the design and implementation of the pneumatic control system. V1-V7 are corresponding labels of valves described in Figure 6.4.1. The full name of each valve is in accordance with the software interface in Figure 6.5.3.*

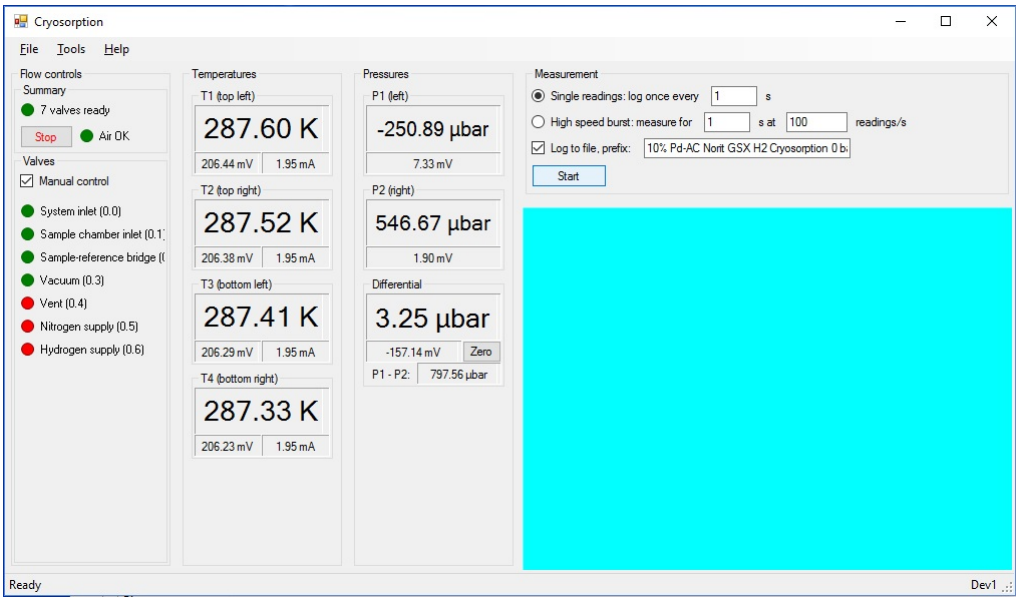

Figure 6.5.3 *The software interface for hydrogen cryosorption measurement.*

The pneumatic remote control system was one of the vital design choices for minimising the hydrogen safety risks to users. By controlling the valves that were built into the system with compressed air lines, the electrical sources need not be present inside the hydrogen cell. As shown in **Figure 6.4.2** and **Figure 6.5.2**, the key component of the control system is the NI data acquisition card that is used for delivering signals to the solenoid valve controller ("power and control box") that further regulates the gas lines to power pneumatic valves located inside the hydrogen cell. There is a set of relay switches built into the power box for powering on and off the solenoid valves, and current monitors for each solenoid were also included to provide verification that each solenoid valve had switched correctly. The pneumatic valves are normally closed if the pressure was absent, which means that the hydrogen gas can be fully sealed in the chamber if any emergency happens. In addition, for monitoring the pressure status of the compressed air line feeding the pneumatic values, a pneumatic pressure switch which can deliver an electrical signal if the air supply pressure drops below a certain level (5 bar for our system) was installed. Only if all the checks mentioned above confirm normal conditions can the software controls for regulating the experimental procedures be operated. Otherwise, alerts would be activated and the system would require further examination.

6.5.4 Data acquisition and software

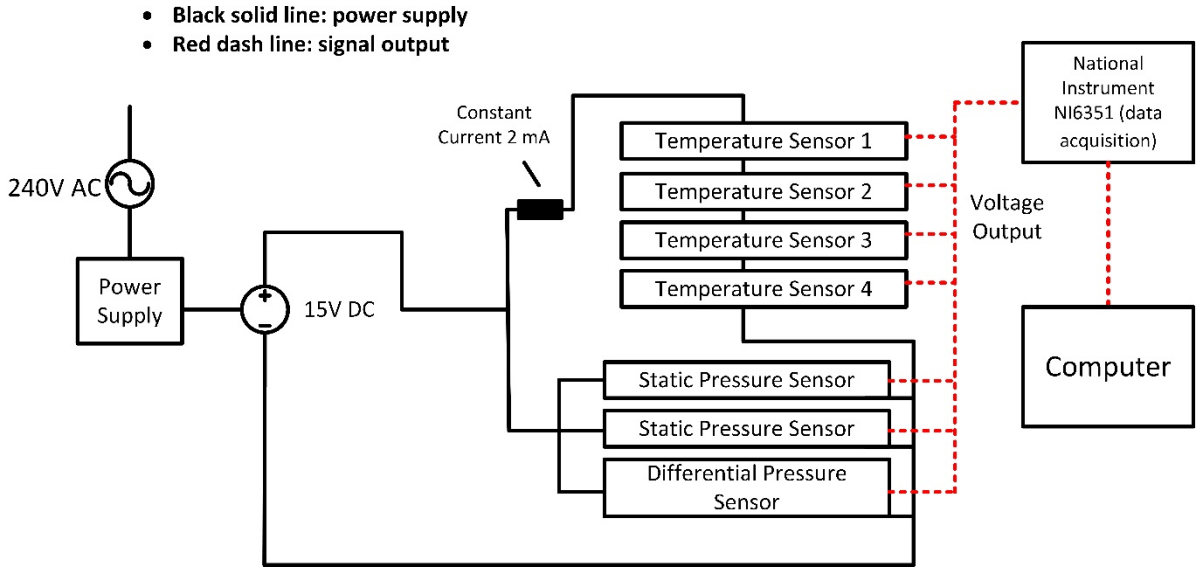

Figure 6.5.4 *The design of power supplies and connections for sensors (temperature sensors 1 and 2 are built into the testing system, while temperature sensors 3 and 4 are placed inside the hydrogen cell for monitoring air flow temperatures).*

All four temperature sensors are PT100 platinum resistance thermometers, which were powered with a constant current of around 2 mA in series. The pressure transducers have built-in voltage regulation and signal conditioning so that they can be supplied with 15 V DC power. The output voltages were measured differentially using the National Instruments X Series Data Acquisition card, NI6351, as shown in **Figure 6.5.4**. This instrument can measure 8 differential inputs, multiplexed to a 16-bit analogue-digital converter, at an aggregate sampling rate of 1 MHz, which is vital for evaluation of the sorption kinetics in burst mode.

Software was developed by Dr Simon Hopkins to record the data, including the control of sampling rate and a moving average procedure to reduce noise and the measurement uncertainty. As shown in **Figure 6.5.3**, the software has a graphical user interface, which can plot a live chart of voltage outputs versus time in accordance with the experimental progress. The data were logged, including the raw voltages of all sensors and the results of conversion to the actual pressures and temperatures. The raw data were recorded in a comma-separated values (csv) file, thereafter analysed by a self-written Python program to obtain the final uptake amounts and measurement uncertainties.

6.5.5 Hydrogen cell and safety considerations

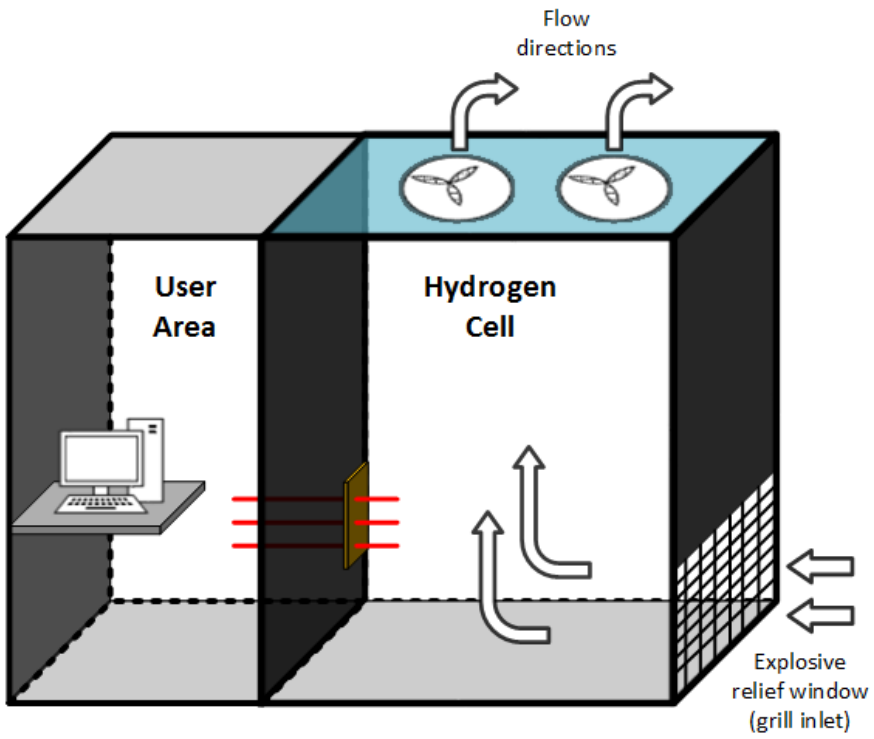

Figure 6.5.5 *Schematic diagram of the hydrogen cell construction.*

With the consideration of handling hydrogen gas in an insulated space, a hydrogen cell was designed and constructed to meet the European ATEX directives (Zone 2). The extraction system was built to manage the extreme condition of 2 litres liquid hydrogen leakage at its maximum working power. The air flows into the hydrogen cell via an explosive relief window with mesh grill, and brings any hazardous gases out of the cell rapidly. The hydrogen cell is separated by thick concrete walls from the user area. As described in **Figure 6.5.5**, it is worth noting that the electric connections and pneumatic pressure lines were sealed with Roxtec sealing modules when passing through the insulation wall. All power supplies and electronics which were not rated for ATEX zone 2 were placed in the user area. Thanks to the remote pneumatic controlling system discussed in section 6.5.3, the entire experimental procedure can be fully operated without the presence of users in the hydrogen cell.

The user is only allowed to access the hydrogen cell when the experiment is not operating and the hydrogen gas is properly sealed inside the vessels. Additionally, there were several alarms installed inside and outside the cell to detect the gas concentrations in addition to the hydrogen alarm. The oxygen alarm is essential for the safe handling of the liquid nitrogen

coolant. Finally, the venting port of the measurement system was located at a height close to the extraction fans, and hydrogen has minimised contact with electronics inside the hydrogen cell under normal conditions.

6.5.6 Vacuum degassing

It is recommended that an outgassing vacuum better than 10^{-5} bar (~ 1 Pa) is necessary to conduct reliable BET measurements for microporous materials, according to the ISO standard [63]. The main purpose of high vacuum is to remove the trapped gases in the microporous structures of sorbents [60], [63], which is no doubt important to identify the accurate pore volumes and specific surface areas of the materials. For a practical and fast evaluation of the sorption ability of materials, especially mesoporous carbon materials, the medium vacuum degassing (better than 10^{-4} bar)) is preferred with the following considerations in terms of the analysis presented in section 7.2.1:

I. The uptake differences between high and medium degassing are very tiny for hydrogen cryosorption. The condensation of residual nitrogen shows no significant local concentration on mesoporous in comparison with large open surfaces.
II. The reason for the degassing procedure in the sorption experiment is to create a pure hydrogen environment by removing unrelated gases, such as nitrogen, and for the convenience of the mathematical calculations of uptakes. A proper drying process of removing moisture was sometime more supportive for a better uptake compared with high vacuum degassing if there are moisture trapped in the sorbents, based on the experimental experiences in this study.
III. In terms of the implementation cost of the equipment, the medium vacuum system, like a rotary pump, is generally ten times cheaper than high vacuum equipment, for instance, a diffusion pump. Meanwhile, the time required for reaching high vacuum can be as long as several hours, while the medium vacuum can be achieved in only minutes. Additionally, the medium vacuum system is typically lightweight and far more portable, which makes it more adaptable for targeted mobile applications.

It is worth noting that high vacuum is required for microporous sorbents (pore diameters < 2 nm), like zeolites, because the residual nitrogen can preferably condense in micropores, further resulting in significant reductions of micropore surface area. Regarding the design

discussed in this thesis, a rotary vane vacuum pump with a self-built foreline trap was introduced for medium vacuum degassing, which can achieve a pressure of 0.1 mbar in several minutes, as measured using a Pirani vacuum gauge (Edwards APG100XN). The high vacuum of 10^{-7} bar (0.01 Pa) for the measured zeolites was achieved by attaching the vacuum port to a diffusion pump system.

A high temperature vacuum degassing is favourable, since it is not only capable to increase the energy level of adsorbed gas molecules and promote them to separate from the sorbent surface, but also able to remove the water vapour prior to the sorption test without the risk of exposing to the environment. However, the time saved because of elevated temperature in degassing to reach the required vacuum is very limited, as the medium vacuum degassing for mesoporous materials discussed in this study has already taken only 15 minutes or so. The effect is more significant for a high vacuum or ultra-high vacuum degassing. Besides, it is very difficult to introduce a heating unit inside the hydrogen cell with ATEX zone approved, since it unavoidably introduces potential sources of electric sparks and a high electric current, which is normally tried to be prevented for an explosive atmosphere. Therefore, at the current stage of the designed measuring system used in this study, the degassing procedure is always conducted at room temperature.

6.5.7 Others

Because hydrogen gas forms an explosive mixture with air at approximate concentrations between 4 and 75 percent by volume, it is important that any fittings sealing against, or in contact with, hydrogen are carefully selected and handled. Metal-metal sealing is preferred in piping and connections of hydrogen gas. Two Swagelok branded types of fitting were used in this reported system: VCR fittings and Swagelok tube fittings. VCR fittings are more convenient to re-assemble with the replacement of a gasket, but have much higher costs, while Swagelok tube fittings are simpler to install due to the ferrule type sealing, but more difficult to disassemble due to the continuous deformation of the tube ends and ferrule contacts on the surface by reassembly. For the sorption tests taken in this study, reassembly is not necessary for most of the components once the system is established. Swagelok tube fittings were implemented for most connections, but VCR fittings were applied for the joints

that needed to be reopened during sample exchange and for parts with the potential to be upgraded in the future.

In order to prevent tested samples from contaminating the system, a Swagelok particulate filter with the pore size of 40 microns is placed between V2 valves (see **Figure 6.4.1**) and the sample chambers in both systems. Furthermore, a 0.5-micron gasket was fitted on the caps of the sorbent vial. Although the filters could restrict the gas flow rate to the sorbents to some extent, the influence is negligible for determining the equilibrium uptakes of sorption.

6.6 Experimental procedures for sorption tests

Most of the porous samples contained a certain proportion of moistures when they firstly arrived in the lab, for instance, around 5% for the activated carbons. It is also known that some materials, such as zeolites, have great affinity for polar molecules, such as water vapours from the air, which has a considerable influence on the adsorption uptakes. Thus, the sorbents tested were dried under a pure argon flow at 400 °C for 5 hours before they were loaded into cryogenic vials for hydrogen cryosorption measurements. The sample weight was measured prior to the operation of sorption experiment. The hydrogen gas and the nitrogen gas used in the experiment are technically graded with high purity (Air Products BIP cylinders) so that the sorbents can be kept in dry conditions between tests. Meanwhile, the characterisation methods were operated with the dried samples instead of the original samples for accuracy and consistency.

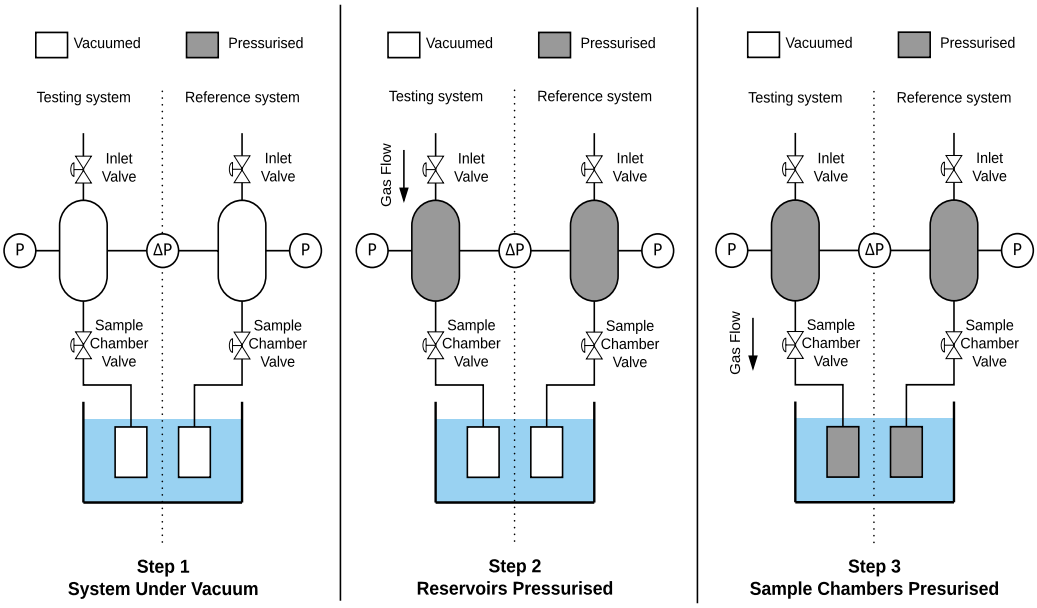

Figure 6.6.1 *Illustration of experimental procedures in cryosorption measurements. All temperature sensors and some parts of the system are omitted for clarity.*

In step 1, all chambers were pumped to vacuum as shown in **Figure 6.6.1**. Once the vacuum condition reached the targeted vacuum, the reservoir bottles of both subsystems were gradually pressurised to the set pressure under the control of the mass flow controller (step 2 in **Figure 6.6.1**). Then the sample chamber valves of both subsystems were opened simultaneously, and the containers submerged in the liquid nitrogen bath were pressurised with hydrogen gas (step 3). The software recorded the voltage signals of all sensors in small time segments during all three steps. The adsorption of hydrogen on the sample results in a pressure difference, which was measured by the differential pressure sensor.

It is worth noting that there were two offset adjustments in each test. The first offset adjustment is the zero offset of all pressure transducers before step 1, by connecting the system to atmosphere through the vacuum port. The other adjustment is the zero offset of the differential pressure transducer before step 3, as the pressure transducer has a small offset as the function of static pressure.

The venting procedure requires the system chambers to be flushed to below the lower flammability limit of 4 % hydrogen composition of residual gas prior to the next experiment. Although pure nitrogen gas was utilised for flushing the system, there were the possibility of a hydrogen-air mixture before the next vacuum pumping procedure, such as replacing the

tested samples. After the pressurised residual hydrogen at the end of each experiment was vented to the atmospheric pressure level, the system would be pressurised with the nitrogen gas supply up to 4 bar pressure, then flushed again to atmospheric pressure, which was named as a nitrogen flushing cycle. Five cycles of nitrogen flushing were required to be completed prior to the vacuum pumping procedure (Step 1 in **Figure 6.6.1**) for the next experiment.

6.7 Derivation for sorption uptakes

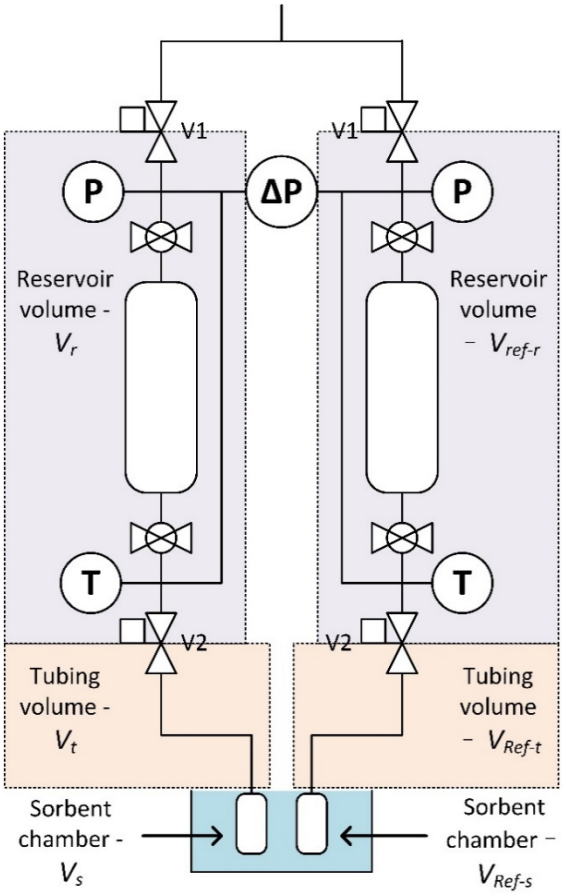

Figure 6.7.1 *A simplified schematic diagram of the involved volumes and parameters in constructed system.*

Prior to detailed mathematical derivations, all volumes described in **Figure 6.7.1** are defined as following (all tubing volumes have been combined within the related chamber volumes):

- ΔP: the induced differential pressure in sorption experiment
- V_{r}: the reservoir volume in the testing system where the adsorbate is located before it is released into the sorbent chamber under vacuum during the experiment
- V_{t}: the tubing volume below the sample-inlet valve (V2 valve in **Figure 6.7.1**) at room temperature
- V_{s}: the revised sample chamber volume submerged in liquid nitrogen with the sorbent volume (mass/density) subtracted in the testing system
- T_{r}: room temperature as measured by the average of two temperature sensors
- T_{c}: the cryogenic temperature – approximate 77 K achieved with liquid nitrogen bath
- $V_{\mathrm{ref-r}}$: analogous reservoir volume to V_{r} in the reference system

- $V_{\mathrm{ref-t}}$: analogous tubing volume to V_{t} in the reference system
- $V_{\mathrm{ref-s}}$: the sample chamber volume in the reference system
- P_{i}: the initial static pressure in the reservoir bottles of both systems at the beginning of the experiment, which was obtained by averaging the readings from two static pressure transducers
- R: the gas constant for the real gas law
- Z_1: the compressibility factor of hydrogen gas at the measured room temperature
- Z_2: the compressibility factor of hydrogen gas at 77 K

The amount of gas n_{t} in the reservoir volume of the testing system in step 2 (as described in **Figure 6.7.1)** is given by the following relation.

$$n_{\mathrm{t}} = \frac{P_{\mathrm{i}} V_{\mathrm{r}}}{Z_1 R T_{\mathrm{r}}} \tag{6.1}$$

By analogy with n_{t}, the amount of gas n_{r} in the reservoir volume of the reference system in step 2 is expressed by the following equation.

$$n_{\mathrm{r}} = \frac{P_{\mathrm{i}} V_{\mathrm{ref-r}}}{Z_1 R T_{\mathrm{r}}} \tag{6.2}$$

Then the equilibrium states of hydrogen gas in step 3 of **Figure 6.7.1** are analysed. Each system is divided into three volumes in respect of three zones.

A. <u>Testing system:</u>

After the hydrogen gas is released into the sample chamber, the amount of gas left in the reservoir volume n_{t1} is:

$$n_{\mathrm{t1}} = \frac{P_{\mathrm{t}} V_{\mathrm{r}}}{Z_1 R T_{\mathrm{r}}} \tag{6.3}$$

where P_{t} is the static pressure at the equilibrium state of sorption.

The amount of gas contained in volume V_{t} can be presented as:

$$n_{\mathrm{t2}} = \frac{P_{\mathrm{t}} V_{\mathrm{t}}}{Z_1 R T_{\mathrm{r}}} \tag{6.4}$$

The amount of gas trapped in volume V_{s} after sorption is:

$$n_{t3} = \frac{P_t V_s}{Z_2 R T_c} \tag{6.5}$$

If the adsorbed amount of gas is labelled as n. Then the total amount of gas in the testing system after sorption should be equal to the initial amount of gas loaded:

$$n_t = n + n_{t1} + n_{t2} + n_{t3} \tag{6.6}$$

The pressure P_t can be derived by combining the equations (6.1), (6.3), (6.4), (6.5) and (6.6).

$$P_t = -\frac{n - \frac{P_i V_r}{R T_r Z_1}}{\frac{V_s}{R T_c Z_2} + \frac{V_r}{R T_r Z_1} + \frac{V_t}{R T_r Z_1}} \tag{6.7}$$

B. Reference system:

By analogy to the derivation in the testing system, the amount of gas left in the reservoir volume V_{ref-r} of the reference system is:

$$n_{r1} = \frac{P_r V_{ref-r}}{Z_1 R T_r} \tag{6.8}$$

where P_r is the equilibrium static pressure in the reference system.

The amount of gas in the tubing volume V_{ref-t} is:

$$n_{r2} = \frac{P_r V_{ref-t}}{Z_1 R T_r} \tag{6.9}$$

The amount of gas, n_{r3}, contained in the sample chamber of the reference system is:

$$n_{r3} = \frac{P_r V_{ref-s}}{Z_2 R T_c} \tag{6.10}$$

The sum of the amounts of gas left in all three volumes, n_r, should be equal to the initial loaded amount of gas in the reference system, since there is no gas sorption occurred with the sorbent absence.

$$n_r = n_{r1} + n_{r2} + n_{r3} \tag{6.11}$$

The pressure P_r can be derived with combining equations (6.2), (6.8), (6.9), (6.10) and (6.11).

$$P_{\mathrm{r}} = -\frac{P_{\mathrm{i}} V_{\mathrm{ref-r}}}{RT_{\mathrm{r}} Z_1 \left(\frac{V_{\mathrm{ref-s}}}{RT_{\mathrm{c}} Z_2} + \frac{V_{\mathrm{ref-r}}}{RT_{\mathrm{r}} Z_1} + \frac{V_{\mathrm{ref-t}}}{RT_{\mathrm{r}} Z_1}\right)} \tag{6.12}$$

The differential pressure between the two systems as measured by the differential pressure transducer is:

$$\Delta P = P_{\mathrm{r}} - P_{\mathrm{t}} \tag{6.13}$$

Then the amount of gas adsorbed n can be expressed with the measured parameters by combining the equations (6.7), (6.12) and (6.13).

$$n = (\Delta P - \frac{P_{\mathrm{i}} V_{\mathrm{ref-r}}}{RT_{\mathrm{r}} Z_1 \left(\frac{V_{\mathrm{ref-s}}}{RT_{\mathrm{c}} Z_2} + \frac{V_{\mathrm{ref-r}}}{RT_{\mathrm{r}} Z_1} + \frac{V_{\mathrm{ref-t}}}{RT_{\mathrm{r}} Z_1}\right)} + \frac{P_{\mathrm{i}} \cdot V_{\mathrm{r}}}{RT_{\mathrm{r}} Z_1 \left(\frac{V_{\mathrm{s}}}{RT_{\mathrm{c}} Z_2} + \frac{V_{\mathrm{r}}}{RT_{\mathrm{r}} Z_1} + \frac{V_{\mathrm{t}}}{RT_{\mathrm{r}} Z_1}\right)}\Bigg)\left(\frac{V_{\mathrm{s}}}{RT_{\mathrm{c}} Z_2} + \frac{V_{\mathrm{r}}}{RT_{\mathrm{r}} Z_1} + \frac{V_{\mathrm{t}}}{RT_{\mathrm{r}} Z_1}\right) \tag{6.14}$$

Equation (6.14) can be further rewritten as follows:

$$n = \Delta P \left(\frac{V_{\mathrm{s}}}{RT_{\mathrm{c}} Z_2} + \frac{V_{\mathrm{r}}}{RT_{\mathrm{r}} Z_1} + \frac{V_{\mathrm{t}}}{RT_{\mathrm{r}} Z_1}\right) + K \tag{6.15}$$

where K is the correction coefficient of the system based on the volumetric difference between the two systems, which is calculated as shown below:

$$K = \left(\frac{P_{\mathrm{i}} V_{\mathrm{r}}}{RT_{\mathrm{r}} Z_1 \left(\frac{V_{\mathrm{s}}}{RT_{\mathrm{c}} Z_2} + \frac{V_{\mathrm{r}}}{RT_{\mathrm{r}} Z_1} + \frac{V_{\mathrm{t}}}{RT_{\mathrm{r}} Z_1}\right)} - \frac{P_{\mathrm{i}} V_{\mathrm{ref-r}}}{RT_{\mathrm{r}} Z_1 \left(\frac{V_{\mathrm{ref-s}}}{RT_{\mathrm{c}} Z_2} + \frac{V_{\mathrm{ref-r}}}{RT_{\mathrm{r}} Z_1} + \frac{V_{\mathrm{ref-t}}}{RT_{\mathrm{r}} Z_1}\right)}\right)\left(\frac{V_{\mathrm{s}}}{RT_{\mathrm{c}} Z_2} + \frac{V_{\mathrm{r}}}{RT_{\mathrm{r}} Z_1} + \frac{V_{\mathrm{t}}}{RT_{\mathrm{r}} Z_1}\right) \tag{6.16}$$

According to equation (6.16), the correction coefficient K is related to the volumetric symmetry between two systems. For an ideal situation, K would be zero if the systems were

constructed with identical volumes to each other. But there are always small variations of the volumes and K is required to be evaluated in the result calculations, especially for small uptake experiments. It is worth noting that the amount of gas uptake is mainly related to the differential pressure instead of the static pressure in differential manometry if a good symmetry of the apparatus is achieved, which results in better sensitivity and accuracy thanks to the smaller range of the differential pressure transducer in contrast with static pressure transducers.

6.8 Volume measurement and error analysis

The error of an experiment consists of the uncertainties of random measurements and the systematic errors caused by the manufacturer of the devices or other features of the experimental design. There are mathematical rules for evaluating the uncertainties of measurements, while the systematic errors, which can be related to temperature effects and offset adjustments of sensors, have no exact method to follow. In this study, the uncertainties have been discussed in detail. An analysis of the systematic errors was conducted as well relying on the knowledge of the specifications of the electronics involved.

The volumes of the system were measured by determining the pressure differences at a constant flow rate. As shown in **Figure 6.8.1**, the pressure versus time isotherm at a constant flow rate yielded near-perfect linear regressions with an R^2 value (coefficient of determination, i.e. in this case the square of the correlation coefficient) of almost 1. In comparison with other measurement uncertainties, the measured slope value is far more accurate and its uncertainty was neglected in the following calculations. As the flow rate is rated as the normal flow rate, the measured volume at the normal volume condition (0 °C and 101.325 kPa) can be written as:

$$V_{\mathrm{n}} = \frac{P_0 f}{S} \tag{6.17}$$

where P_0 is 1.01325 bar which is a constant value for one atmosphere pressure, f is the set flow rate from the mass flow controller, of which the uncertainties were provided by the manufacturer, and S is the measured slope from linear regression, with a negligible uncertainty.

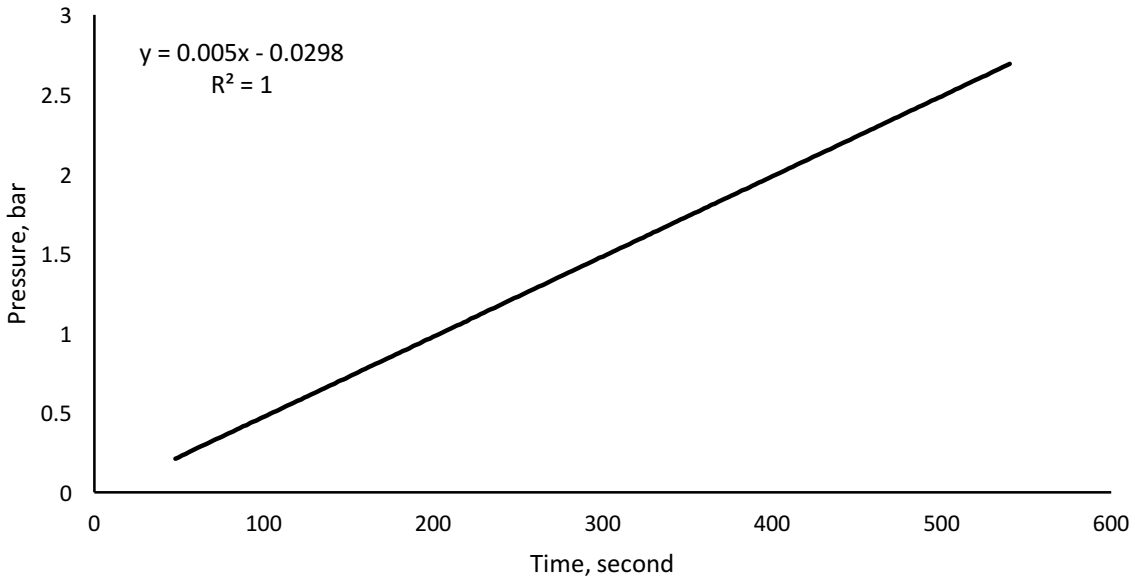

Figure 6.8.1 *An example for the volume measurements (for measuring the total volume above both sample inlet valves).*

The normal flow rate is with the condition of atmospheric pressure and 0 °C temperature, while the volume was measured at around room temperature. As a result, the normal volume equation can be further adjusted to give the real volume expression:

$$V = \frac{T}{T_0}\frac{P_0 f}{S} \tag{6.18}$$

where V is the real volume measured, T is the testing temperature and T_0 is 273.15 K.

As each reservoir bottle, as shown in **Figure 6.4.1**, is isolated with two manually controlled valves, the exact volume can be obtained by subtracting a volume without the bottle attached from the volume with the reservoir bottle attached. For measuring the left reservoir bottle volume, the total volume V_{sum} of the reservoir volumes in both systems as marked in **Figure 6.7.1**, was first measured. The following relation was obeyed (assuming the same flow rate for both tests):

$$V_{\mathrm{sum}} = \frac{T_{\mathrm{sum}}}{T_0}\frac{P_0 f}{S_{\mathrm{sum}}} \tag{6.19}$$

The T_{sum} is the average temperature in the test.

For the volume $V_{\mathrm{no-LBot}}$ that is obtained by subtracting the left reservoir bottle from the V_{sum} (see **Figure 6.7.1**), the related expression was written as:

$$V_{\mathrm{no-LBot}} = \frac{T_{\mathrm{no-LBot}}}{T_0}\frac{P_0 f}{S_{\mathrm{no-LBot}}} \tag{6.20}$$

The $T_{\mathrm{no-LBot}}$ is the related temperature condition.

Then the left bottle volume can be derived as:

$$V_{\mathrm{L-Bot}} = \frac{P_0 f}{T_0}\left(\frac{T_{\mathrm{sum}}}{S_{\mathrm{sum}}} - \frac{T_{\mathrm{no-LBot}}}{S_{\mathrm{no-LBot}}}\right) \tag{6.21}$$

As discussed above, the uncertainties of the slope identifications were negligible, and T_0 is a constant temperature value. Accordingly, there are three random variables involved, the temperature conditions T_{sum} and $T_{\mathrm{no-LBot}}$, and the flow rate f.

The combined uncertainty of the measurements can be described with the following equation:

$$\delta V_{\mathrm{L-Bot}} = \sqrt{\left(\frac{\partial V_{\mathrm{L-Bot}}}{\partial T_{\mathrm{sum}}}\delta T_{\mathrm{sum}}\right)^2 + \left(\frac{\partial V_{\mathrm{L-Bot}}}{\partial T_{\mathrm{no-LBot}}}\delta T_{\mathrm{no-LBot}}\right)^2 + \left(\frac{\partial V_{\mathrm{L-Bot}}}{\partial f}\delta f\right)^2} \tag{6.22}$$

The volume of the right reservoir $V_{\mathrm{R-Bot}}$ bottle can be measured by the same method as the left reservoir bottle. For the left and right reservoir volume including the tubing (V_{r} and $V_{\mathrm{ref-r}}$) as described in **Figure 6.7.1**, the volumes can be obtained by connecting the bottle volumes at a certain pressure ($P_{\mathrm{L-Bot}}, P_{\mathrm{R-Bot}}$) to the connected tubing volume which was previously evacuated (at the same temperature condition).

$$V_{\mathrm{r}} = \frac{P_{\mathrm{L-Bot}} V_{\mathrm{L-Bot}}}{P_{\mathrm{r}}} \tag{6.23}$$

$$V_{\mathrm{ref-r}} = \frac{P_{\mathrm{R-Bot}} V_{\mathrm{R-Bot}}}{P_{\mathrm{ref-r}}} \tag{6.24}$$

The bottom volumes of the system can be measured with the same method. For instance, the total bottom volume of the testing system including both V_{t} and V_{s} (see **Figure 6.7.1**) can

be measured by connecting to preloaded reservoir volume V_{r} at a certain pressure. Since the sorption chamber volumes of both subsystems were fitted with VCR fittings, V_{s} and $V_{\mathrm{ref-s}}$ were measured by monitoring the added weight on filling the volumes with deionised water: i.e. the volumes can be obtained by dividing the added weight by the density of deionised water at the testing temperature. The calculation of combined uncertainties can be conducted with the random variables equation as in equation (6.22). In addition, it is worth noting that each measurement was repeated several times to reduce the uncertainty in accordance with expressions (6.25) and (6.26) for the standard deviation of mean $\sigma_{\overline{\mathrm{x}}}$.

$$\sigma_{\mathrm{x}} = \sqrt{\frac{1}{N-1}\sum (x_{\mathrm{i}} - \overline{x})^2} \tag{6.25}$$

where σ_{x} is the standard deviation of the individual measurements x_1, x_2, x_3, ..., x_{n}, N is the number of measurements, and $\overline{x}$ is the mean values of measurements. The standard deviation of mean $\sigma_{\overline{\mathrm{x}}}$ further follows the equation below.

$$\sigma_{\overline{\mathrm{x}}} = \frac{\sigma_{\mathrm{x}}}{\sqrt{N}} \tag{6.26}$$

Table 6.8.2 *The measured volumes and related errors (systematic errors of V_{s} and $V_{\mathrm{ref-s}}$ are negligible).*

System	Symbol	Volume/ml	Volume uncertainty / ml	Volume systematic error / ml	Volume combined error / ml
Testing	V_{r}	322.99	1.31	1.21	1.78
	V_{t}	21.96	0.16	0.85	0.86
	V_{s}	16.67	N/A	0.1	0.1
Reference	$V_{\mathrm{ref-r}}$	321.74	1.29	1.20	1.76
	$V_{\mathrm{ref-t}}$	23.12	0.16	0.84	0.86
	$V_{\mathrm{ref-s}}$	17.13	N/A	0.1	0.1

The evaluation of systematic errors followed a similar method to that described above for uncertainties. The systematic error of each device was initially analysed either by its

manufacturer's calibration or depending on its specifications. The combination of random measurement uncertainties and system errors are calculated approximately with the square-root rule.

$$\sigma_{\text{total}} = \sqrt{\sigma_{\text{ran}}{}^2 + \sigma_{\text{sys}}{}^2} \tag{6.27}$$

where σ_{total} is the total error of the measurement, σ_{ran} is the random uncertainty combined from the uncertainties of all variables, and σ_{sys} is the estimated systematic error merged from the systematic errors of all electronic sensors by assuming that all errors are independent. It should be noted that the error of a single sorption measurement is specific to its unique combination of variable measurement uncertainties and systematic errors.

In addition to the errors in the volume measurements, there are other variables, such as ΔP, P_{i} and T_{r}, to be considered in the error analysis, while the liquid nitrogen temperature T_{c}, the gas constant R and the compressibility values of Z_1 and Z_2 are constant. The measurement uncertainties of the variables were calculated from the raw logging data, for which various results are obtained in different measurements. The systematic errors of these measurements are constant, depending on the sensor accuracies. In terms of the specifications of related sensors, the ΔP has a 0.1 % systematic error of the full scale of the differential sensor, and the P_{i} has a 0.04% error of the full scale. The accuracy of the temperature sensor for T_{r} is 0.1 °K. The uncertainty and the systematic error of the gas amount can be obtained using the uncertainty equation for independent variables, equation (6.28).

$$\delta n = \sqrt{\left(\frac{\partial f(n)}{\partial \Delta P}\delta \Delta P\right)^2 + \left(\frac{\partial f(n)}{\partial P_{\text{i}}}\delta P_{\text{i}}\right)^2 \cdots \left(\frac{\partial f(n)}{\partial V_{\text{ref-s}}}\delta V_{\text{ref-s}}\right)^2 + \left(\frac{\partial f(n)}{\partial T_{\text{r}}}\delta T_{\text{r}}\right)^2} \tag{6.28}$$

The combined error of the uncertainty and the systematic errors obeys the same equation (6.27). Thus, the results of the uptake can be presented with a measured (average) uptake curve, as well as a lower error limit curve and a higher error limit curve, as shown in **Figure 6.8.3**. The relative error in respect of the uptake amount (1.9 wt% at 11 bar) varies from 2.5 % to 8 % with increasing pressure. The absolute errors were discovered to be nearly unchanged for the measurements performed in a similar pressure range, which means that the relative

errors were approximately from 0.5% to 1.6 % with the same absolute error as in **Figure 6.8.3** if the uptake could reach the full range 10 wt%. For the samples tested in this study, the relative uptake errors were about 2 – 5 %.

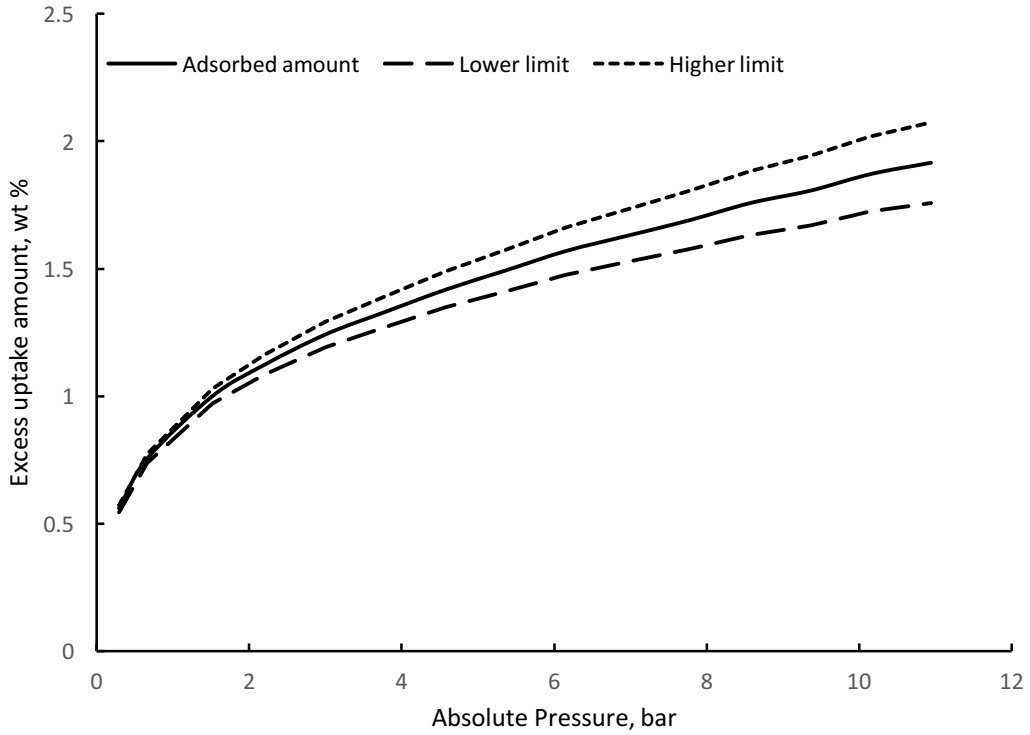

Figure 6.8.3 *An example of adsorption isotherms on an activated carbon (SSA: 700 m^2/g).*

6.9 Additional words and summary

An differential manometry system was constructed and reported by Dr Ghoman for measuring hydrogen uptake at high pressures up to 200 bar and room temperature about ten years ago in Polymer Group, Department of Materials Science & Metallurgy, University of Cambridge [121]. The system was then soon abandoned because low uptakes of high-pressure hydrogen physisorption at room temperature struggled to compete with hydrogen cryosorption at 77 K and many other methods reviewed in section 2.2. During the construction of the present hydrogen cryosorption system, some parts of the previous construction were reused, such as the differential pressure transducers with 1 bar range and some reservoir chambers. Except for these reused parts, the whole cryosorption was entirely

redesigned and rebuilt from as little as a single fitting to the whole electrical wiring and connections, as well as safety precautions for handling hydrogen gas.

In this section, the key designs of cryosorption measurement system, such as major components, safety designs and electrical connections, were discussed thoroughly. It is worth noting that the method of implementing the pneumatic control system, as well as the mathematical derivations and error evaluations, can be applied more generally for building differential manometry systems for gas sorption, especially for some explosive gases, like methane. With the consideration of providing enough room for improvements in the hydrogen sorption abilities of future sorbents, the system was built for analysing up to 10 wt% of hydrogen uptake. The hydrogen cryosorption measurements presented in this report were entirely tested in this newly constructed system. Related results have been discussed and studied later in section 7.

7 Results and discussion

In this section, the nitrogen adsorption isotherms of common sorbents studied, including zeolites, activated carbons and graphene nanoplatelets, are utilised to characterise their surface areas and pore properties, based on BET, HJ t-method, α_s-method and BJH method, in section 7.1. The hydrogen cryosorption measurements for these studied sorbents are discussed in section 7.2. Section 7.3 studies the structural formation of the plasma carbon and the biochar during their carbonisation process depending on the characterisation with XRD, Raman, XPS and FTIR. The graphitic structures and pore properties of graphene nanoplatelets with various surface areas are investigated in section 7.4. The Pd decoration on AC Norit GSX and GNPs-700 are discussed for their influence on both the porous structures of raw carbons and the hydrogen cryosorption behaviours in section 7.5.

7.1 The analysis of adsorption isotherms and porous properties of general sorbents

7.1.1 Nitrogen adsorption isotherms at 77 K and BET results of sorbents

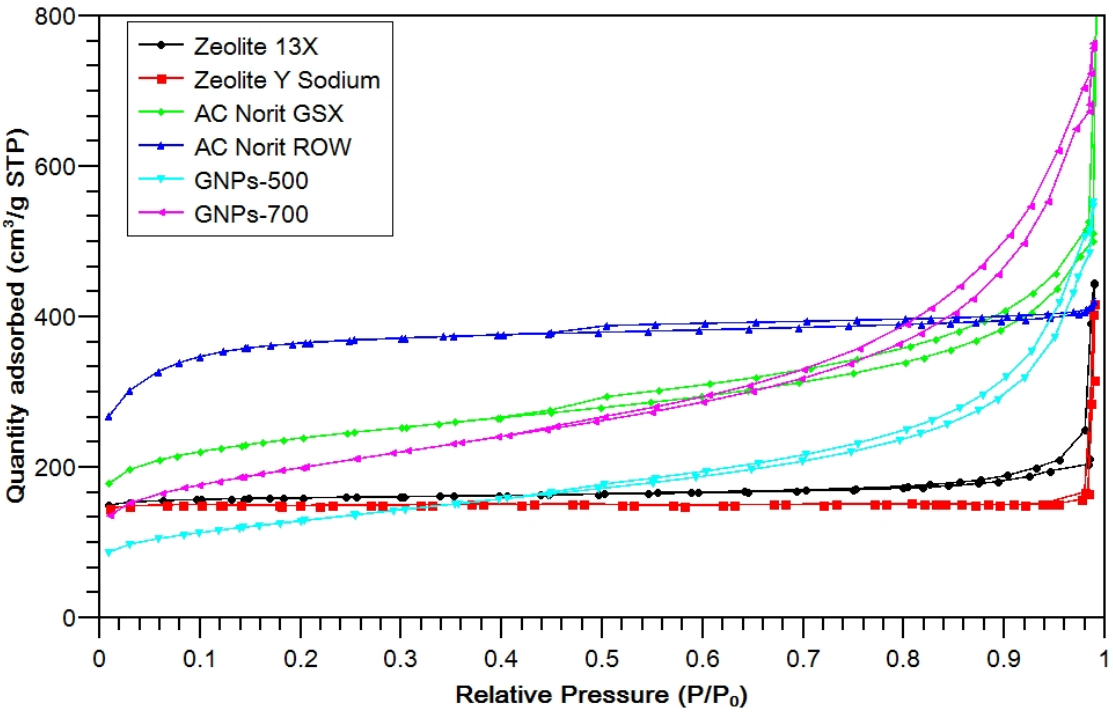

Figure 7.1.1 *Nitrogen isotherms of tested sorbents at 77 K: zeolite 13X, Zeolite Y Sodium, AC Norit GSX, AC Norit ROW, GNPs-500 and GNPs-700.*

Nitrogen adsorption isotherms at 77 K, which were characterised by a Micromeritics TriStar 3000 apparatus (BET assessment), are generally used as the first attempt in characterisation of surface areas and porosities of porous structures. Although there are many limitations of BET theory as discussed in section 2.3.5, BET method is still the most standardised and widely adopted method. The nitrogen isotherms of the selected sorbents, such as activated carbons and zeolites, and the unique high-surface-area graphene nanoplatelets (GNPs), GNPs-500 and GNPs-700, are plotted in **Figure 7.1.1**.

The primary analysis based on the nitrogen adsorption data is to identify the type of isotherm for each material that explains qualitatively whether its pore structure is micropore dominated or mesopore dominated. This can also verify the applicability of BET method, and determine the type of hysteresis loop if a type IV isotherm appears (see **Figure 2.3.2** in section 2.3.3). According to the classification of physisorption isotherms discussed in section 2.3.3, the two types of zeolite are typical type I isotherms that have the long flat plateaus and point B lying in the extreme low relative pressure range, which indicates the dominance of micropores (pore diameters < 2 nm). Zeolite 13X is an X-type molecular sieve with uniform pore sizes of 1 nm, and zeolite Y is another type of faujasite with aperture sizes less than 1nm [15], which agrees well with the micropore features of type I isotherms. The isotherm of AC Norit ROW as shown in **Figure 7.1.1** has a complex combination of a type I isotherm with a long plateau, which is caused by the existence of micropores, and a type IV isotherm exhibiting an obvious hysteresis loop, which is caused by capillary condensation in mesopores.

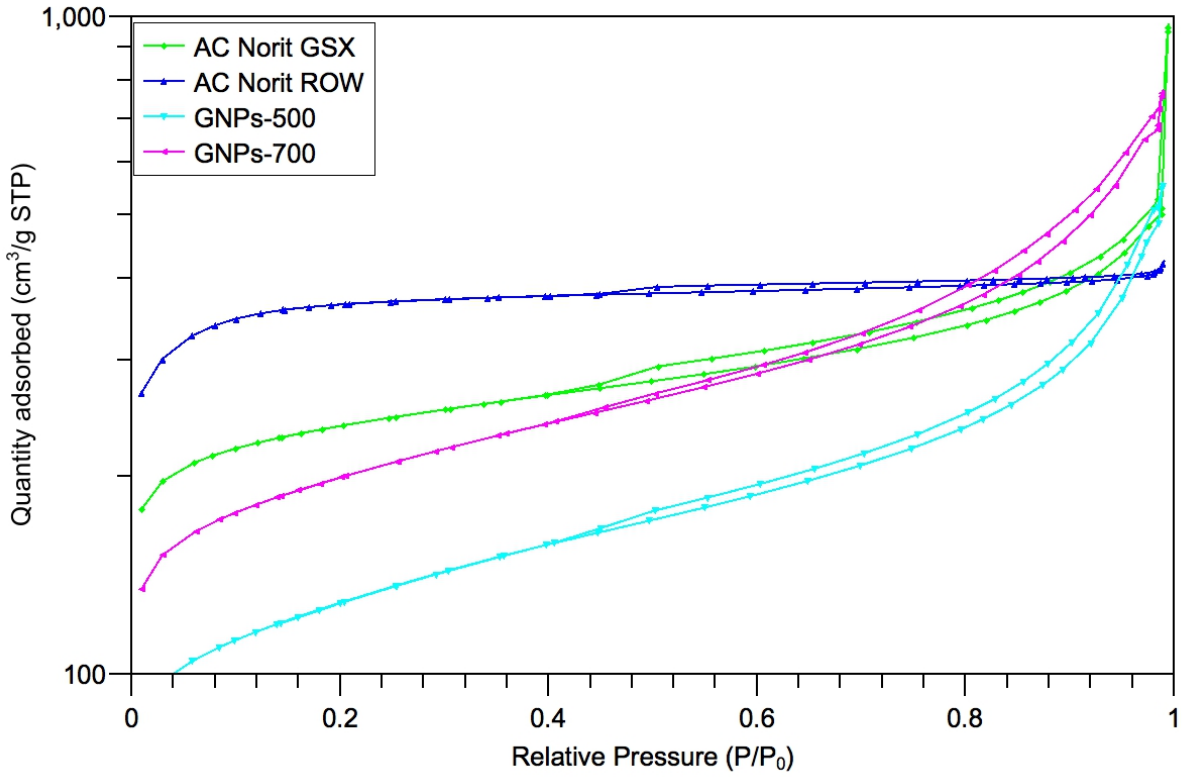

Figure 7.1.2 *Isotherms of sorbents with hysteresis loops. The quantity adsorbed is presented on a common logarithmic scale to aid comparison.*

The isotherms of AC Norit GSX, GNPs-500 and GNPs-700 are observed to match type IV isotherms but displaying diverse types of hysteresis loops. The type IV isotherm shows a similar shape to the type II isotherm at low relative pressure range up to the B point (see **Figure 2.3.2** in section 2.3.3) that is related to completion of monolayer adsorption, followed by a linear progression at a certain slope instead of a flat plateau with increasing relative pressure, which is connected to multilayer adsorption. As described in **Figure 7.1.2**, the hysteresis loops of AC Norit GSX and AC Norit Row refer to the typical H4 type of hysteresis loop according to the classification represented in section 2.3.5. The H4 hysteresis loops (see **Figure 2.3.9** in section 2.3.6) of activated carbons show a steeper drop in the desorption isotherms at low p/p_0 than the GNPs-500 and GNPs-700, and the adsorption and desorption isotherms re-join together at very high p/p_0. The H4 loops that are often observed in some types of activated carbons are related to the existence of narrowly shaped pores in conjunction with micropores [61]. The GNPs-500 and GNPs-700 exhibit a similar shape of hysteresis loop, dominated by H3 type, which indicates the existence of slit-shaped pores

formed by the aggregation of plate-like particles, but with traces of H2 type hysteresis at low relative pressure that is initiated by cylindrical-shaped pores and interconnected “ink-bottle” structures. The “ink-bottle” pores are possibly induced by both the folded soft GNPs layers and the bended plate-shaped flakes, following the structural analysis discussed later in section 7.4.

Ideally, to apply the BET method to calculate surface areas, a linear BET plots should be obtained over an approximate p/p_0 range of 0.05 – 0.35, with point B located at $p/p_0 \sim 0.1$. An important rule that needs to be considered is that the standard p/p_0 range is only valid for non-porous structures and pure mesopores, because micropore filling of microporous structures can happen at p/p_0 lower than 0.1, which will eventually affect the evaluation of monolayer capacity in the BET method. For ultramicropores (< 0.7 nm), the measured BET surface area likely under-estimates the real surface area as the large probe molecules, like nitrogen, cannot reach pore channels with extreme curvatures; on the contrary, the BET surface area can be an overestimate in wider supermicropores (0.7 – 2 nm) since some of the probe molecules stay in the centre of the pore without contacting the surfaces (so called “micropore filling”) [63]. As a result, the application of BET methods to micropore materials (type I isotherm), such as the zeolite samples in this study, require the evaluation of BET plots locating at p/p_0 lower than the standard p/p_0 range, and the measured surface areas are considered as the equivalent BET surface areas instead of the true surface areas.

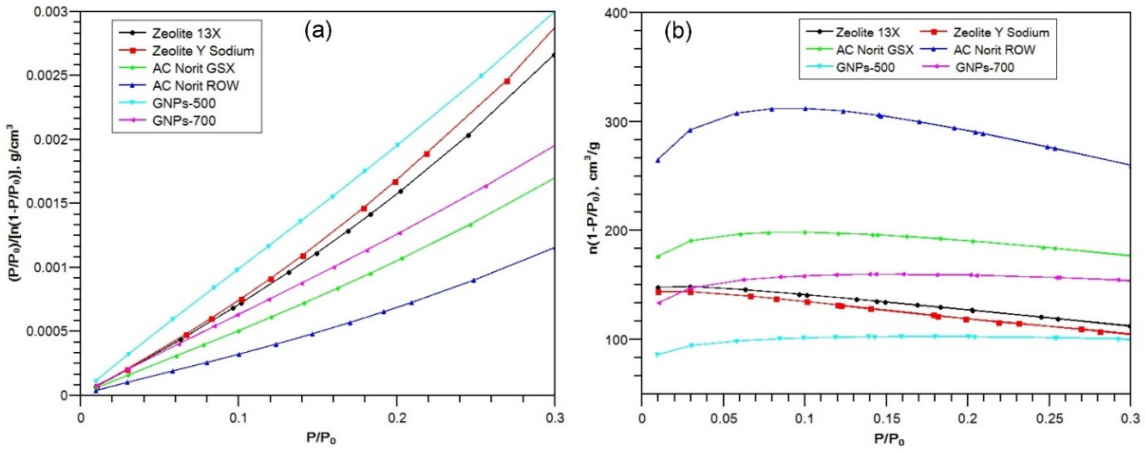

Figure 7.1.3 *(a) The BET linear plots of sorbents at the standard p/p_0 of 0 – 0.3. (b) The modified BET plot of sorbents for evaluating the linear range.*

The equipment used (see section 5.2) for characterising the nitrogen adsorption isotherms was discovered experimentally to apply a relative pressure range of 0.01 – 0.2 in the calculation of the BET surface area, which resulted in negative C values and invalid results. As shown in the BET linear plots of **Figure 7.1.3 (a)**, all sorbents apart from GNPs-500 obviously demonstrate significantly curved plots in the p/p_0 range of 0 – 0.3, and linear plots are difficult to identify for zeolites even at a relative pressure below 0.1. According to references [63], [71], a modified BET plot is recommended to be applied for determining the effective linear regression range, as described in **Figure 7.1.3 (b)**. An effective linear range requires that the values of $n(1 - p/p_0)$ increase with the growth of p/p_0 [63], [71]. As described in **Figure 7.1.3 (b)**, the BET linear ranges of zeolites are expected to be found at a relative pressure below 0.01 that is beyond the capacity of the applied apparatus and requires higher vacuum degassing. Therefore, the nitrogen isotherms obtained for zeolites cannot be used to calculate their BET surface areas. The BET surface areas for 13X and NaY used in this thesis are therefore the specified values provided by material suppliers.

For the activated carbons, AC Norit GSX and AC Norit ROW, the linear plot range is reduced to 0.01 – 0.1, in which each has five points available to achieve a decent linear regression, while the GNPs-500 and GNPs-700 have sufficient data in the relative pressure range of 0.01 – 0.2. **Table 7.1.4** lists the measured BET surface areas and related parameters for four carbon materials, in which the STP molar volume is defined as 22.414 dm^3/mol at 0 °C and 101.325 kPa, according to the IUPAC standard and the specifications of the BET machine. The *C* values of these carbons are higher than 200, which is indicative of the strong adsorbent-adsorbate interactions. GNPs-500 and GNPs-700 have surface areas of 453 m^2/g and 705 m^2/g respectively, which meets the expectations for their highly porous structures. Two activated carbons have higher surface areas, 875 m^2/g for AC Norit GSX and 1387 m^2/g for AC Norit ROW.

Table 7.1.4 *The measured BET values for AC Norit GSX, AC Norit ROW, GNPs500 and GNPs700.*

	AC Norit GSX	**AC Norit ROW**	**GNPs-500**	**GNPs-700**
Slope (10^{-3} g/cm^3 STP)	4.97	3.13	9.58	6.15
Intercept (10^{-6} g/cm^3 STP)	7.41	7.17	28.00	17.10
n_m (cm^3/g)	200.96	318.65	104.03	162.08
C	671.39	437.99	343.33	360.91
a_{BET} (m^2/g)	875	1387	453	705

7.1.2 Mesopore and micropore analysis

Referring to the BET analysis discussed in section 7.1.1, the BET method has restricted effectiveness for micropore-dominant materials, and it is also not able to evaluate micropore properties. The Harkins-Jura (HJ) t-method was then developed to characterise micropore sizes and volumes based on standard nitrogen isotherms. It is worth noting that the effectiveness of HJ t-methods is also restricted by the efficacy of BET method, since the micropore surface area is obtained from deducting the external surface area, which is measured by t-method, from the overall BET surface areas. The initiation of t-methods started from the Lippens and de Boer (LdB) model [82], stating that the thickness *t* of the multilayer coverage can be obtained by dividing the total amount adsorbed n by the monolayer capacity n_{m} if the mesopores are assumed to have the same adsorption behaviour as the open surface in non-porous and mesoporous materials. However, the hypothesis cannot be applied for materials in the presence of micropores, because micropore filling, which happens during monolayer packing, complicates the identification of the appropriate monolayer capacity n_{m}. The Harkins and Jura equation [83] was a better option for evaluating the thickness of adsorbed molecules compared to the LdB theory (see section 2.3.7). The amount of gas adsorbed shows a short linear increase with thickness during the multilayer packing of probe molecules for the approximate thickness range of 0.35 – 0.5 nm. As shown in **Figure 7.1.5 (d)**, linear plots are obviously observed for the GNPs at the standard p/p_0 range of 0.35 – 0.5 nm, but the linear sections for activated carbons are found at a slightly higher thickness of 0.4 –

0.5 nm. The slope of the linear fit represents the external surface areas of mesopores and open surfaces, while the positive intercept illustrates the pore volume of micropores.

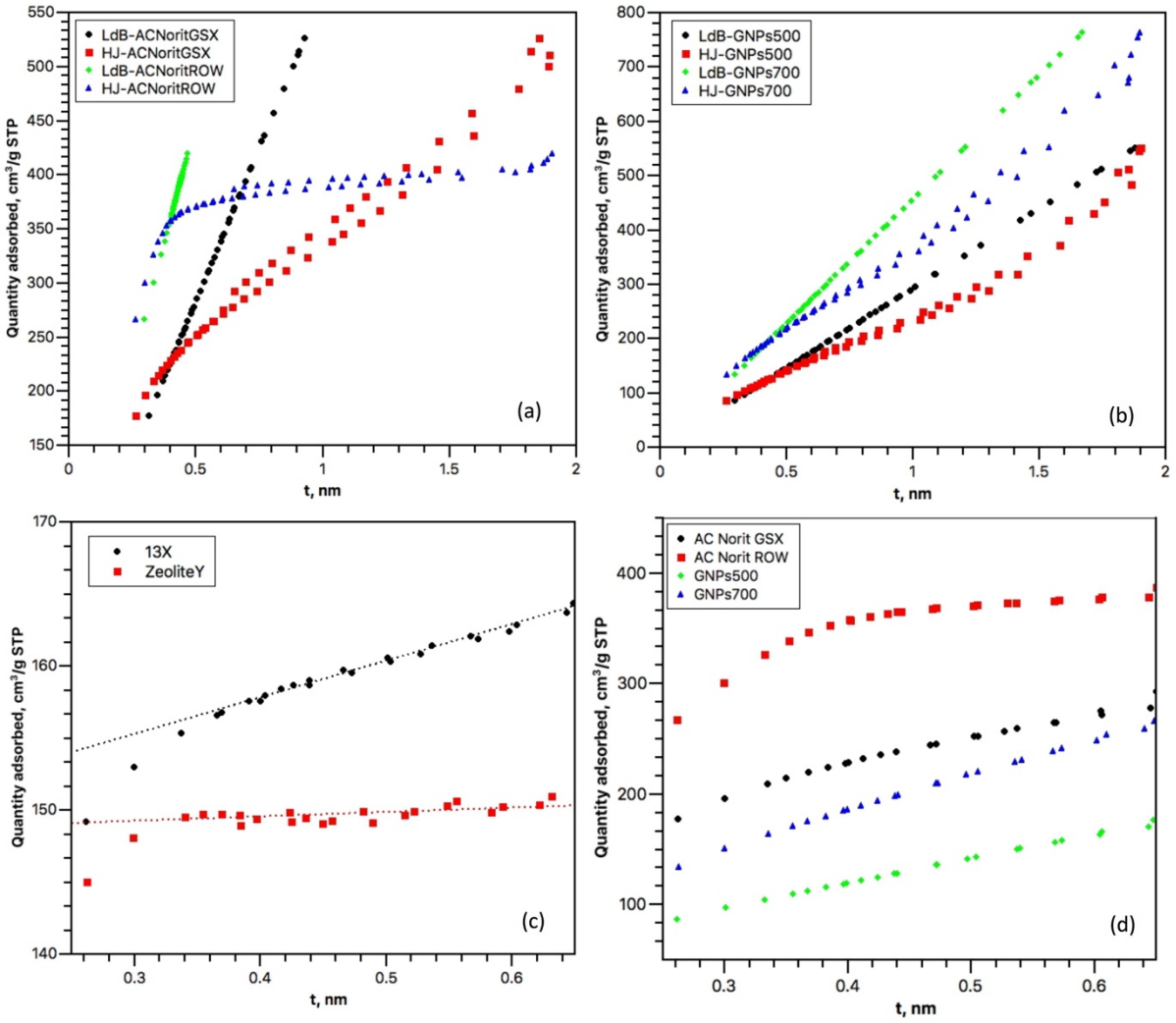

Figure 7.1.5 *(a) The Lippens – de Boer model (LdB) and Harkins – Jura model (HJ) t-plots of AC Norit GSX and AC Norit ROW. (b) The LdB and HJ t-plots of GNPs-500 and GNPs-700. (c) The HJ t-plots of zeolite 13X and zeolite Y over the adsorption thickness of 0.25 – 0.65 nm. (d) The HJ t-plots of four carbon samples over the adsorption thickness of 0.25 – 0.65.*

As shown in **Figure 7.1.5 (a)** and **(b)**, the Lippens and de Boer (LdB) model is simplified, with the linear regions starting from the origin. The HJ t-plots of four carbons are observed to deviate into a higher slope from the linear section at a thickness less than 0.35 nm, which is caused by the combination of monolayer adsorption and micropore filling in these materials. The hysteresis loops at thicknesses above 0.65 nm for the activated carbons and 1 nm for the GNPs correlate with capillary condensation in mesopores [61]. In terms of the Kelvin equation

that has been discussed in section 2.3.6, the adsorbed phase will accumulate quickly by the filling of mesopores at high p/p_0 thanks to capillary condensation if the volume of mesopores is large, which explains the higher adsorbed quantity of the desorption isotherm than the adsorption isotherm over the thickness range of the hysteresis loop.

The hysteresis loop is absent in the adsorption isotherms of pure microporous sorbents, like zeolites, so that only micropore filling and multilayer adsorption on external surfaces exist in these materials [61], which agrees with the results for two zeolites in **Figure 7.1.5**. As shown in **Figure 7.1.5 (c)**, the occurrence of micropore filling during monolayer adsorption is indicated by the long plateau in zeolite Y, while 13X has a higher slope of the linear section, indicating a larger external surface area than the zeolite Y. The further quantitative implementation of the HJ t-method on zeolites is restricted by their invalid BET analysis. As indicated in **Figure 7.1.5 (d)**, the implementation of a linear fit on GNPs is in the range of 0.35 nm – 0.5 nm, while the HJ t-method analysis of activated carbons is based on the thickness range of 0.4 nm – 0.5 nm. The mathematical relations in the HJ t-method have been discussed in section 2.3.7, and corresponding results are delivered in **Table 7.1.6**.

Table 7.1.6 *The Harkins-Jura (JH) t-method results for AC Norit GSX, AC Norit ROW, GNPs500 and GNPs700.*

	AC Norit GSX	**AC Norit ROW**	**GNPs500**	**GNPS700**
Slope (cm^3/g, STP)	225.08	114.65	228.71	329.81
Intercept (cm^3/g, STP)	139.57	313.93	28.32	54.57
a_{ext} (m^2/g)	347	177	352	508
a_{micro} (m^2/g)	528	1210	101	197
V_{micro} (cm^3/g)	0.22	0.49	0.044	0.085

In addition to the Harkins - Jura (HJ) model of characterising the micropore properties of sorbents, the α_s-method, analogous to the t-method, has also been acknowledged to be effective for evaluating the micropore properties [86]–[88]. Instead of using the nitrogen isotherms to calculate the adsorption thickness, a reference isotherm, for which the sorbent has only macropores, is introduced to perform as a reference standard for comparison with the measured isotherms. α_s is defined as the ratio of the quantity adsorbed n_{ref} at each p/p_0

to the quantity adsorbed at a relative pressure of 0.4 (hypothetical monolayer capacity), $n_{\mathrm{ref}}/n_{\mathrm{ref}\,(0.4)}$, in a reference isotherm. Since the reference material is a pure macroporous structure, in which the ideal multilayer adsorption is expected, the α_s curve, which is plotted with the quantity adsorbed of the tested sorbent on the y-axis versus α_s on the x-axis, can provide a linear region at an α_s range around 0.5 – 1 if ideal multilayer adsorption happens. The mathematical relations for the α_s-method have been discussed in section 2.3.7.

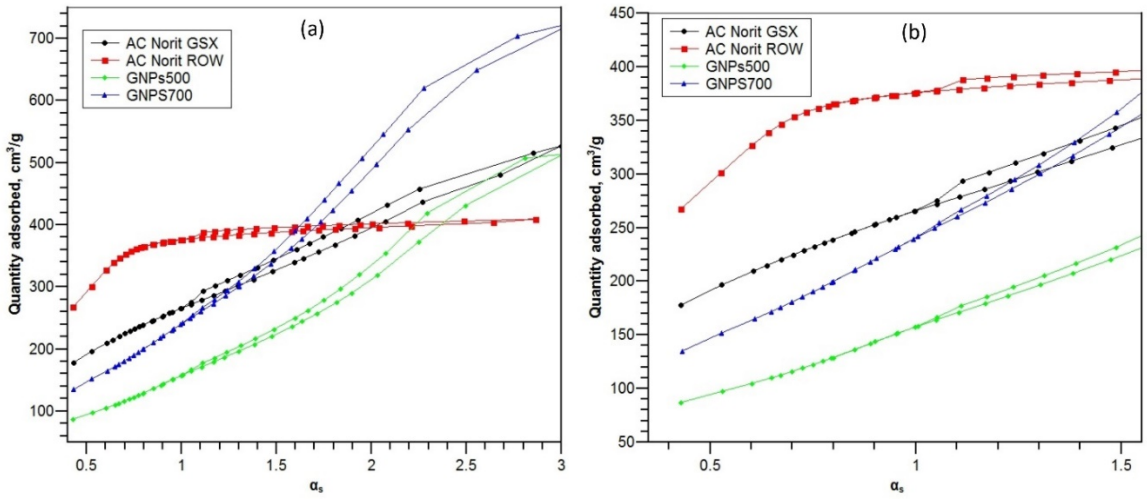

Figure 7.1.7 *The α_s plots of four carbons – AC Norit GSX, AC Norit ROW, GNPs-500 and GNPs-700 – at different α_s ranges: (a) the full range, (b) the localised range for the implement of α_s calculations.*

The α_s plots of the studied carbons, as shown in **Figure 7.1.7**, are drawn in reference to the nitrogen adsorption isotherm of the macroporous silica LiChrospher Si-1000 [86]. The acquisition of α_s values from the reference data involves a linear interpolation between two discrete values. As shown in **Figure 7.1.7 (a)**, the α_s plots display a similar shape to the HJ t-method plots (**Figure 7.1.5 (a)** and **(b)**). The deviation to a higher slope at an α_s values less than 0.7 for AC Norit GSX suggests the strong adsorbate-adsorbent interactions in micropores, and the hysteresis loops of all carbons at α_s larger than 1.0 indicates capillary condensation of liquid nitrogen in mesopores, which agrees with the results obtained from HJ t-method. The linear region that illustrates multilayer adsorption is revealed in the magnified α_s plots of **Figure 7.1.7 (b)**, demonstrating that the linear range of all four carbons is for an α_s of 0.8 – 1. The calculated external surface areas, a_{ext}, and micropore volumes, v_{micro}, from both α_s – methods and HJ t-methods are compared in **Figure 7.1.8**. The results between the two

methods are in good agreement, and the implementation of both methods is confirmed to be effective.

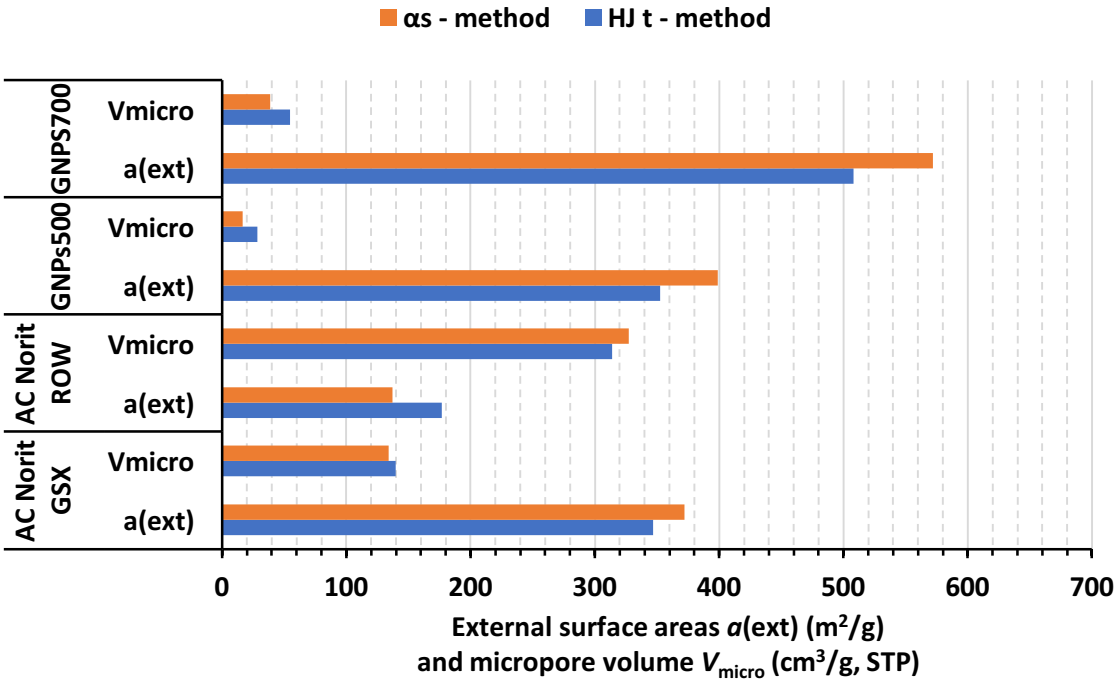

Figure 7.1.8 *The comparison of results between the α_s-method and the HJ t-method for four carbon samples.*

By contrast with the micropores, with diameters less than 2 nm, the mesopores cover a broad range of pore sizes in from 2 to 50 nm. The pore size distributions of mesopores can be characterised with Barrett-Joyner-Halenda (BJH) method. The BJH plots were measured with the BET measurement equipment mentioned in section 5.2. In **Figure 7.1.9**, the pore size distribution is represented by a plot of the specific pore volume against the logarithm of the pore size. It is discovered that zeolite 13X has very limited amounts of mesopores, which is in accordance with the lack of hysteresis loop in its nitrogen adsorption isotherm. By comparing the adsorption and the desorption plots, both AC Norit GSX and AC Norit ROW exhibit a significant extra amount of pore volume at around 4 nm in the desorption isotherms, which is caused by the release of condensed liquid nitrogen in large pores that is trapped by the smaller “neck” pores. The capillary condensation in these large pores also contributes to the sudden drop at the lower end of the hysteresis loops in the desorption adsorption isotherms.

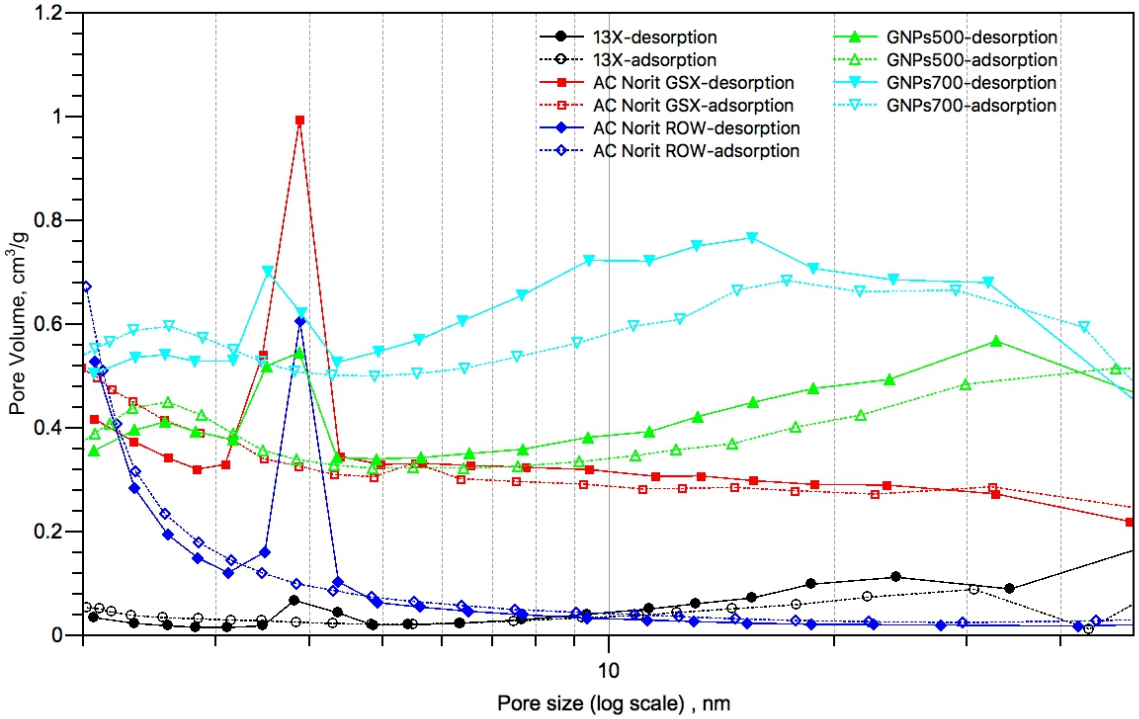

Figure 7.1.9 *BJH adsorption and desorption plots of 13X, AC Norit GSX, AC Norit ROW, GNPs-500, GNPs-700 covering mesopore sizes of 2 – 50 nm.*

As shown in **Figure 7.1.9**, GNPs-500 and GNPs-700 exhibit a larger amount of mesopores more uniformly distributed across the entire range of mesopore sizes in contrast with the activated carbons. The total volume of mesopores and macropores can be obtained by integrating the pore volume over the whole range of the BJH assessments, and a similar method can also be applied to obtain the external surface area across the mesopore range. These integrated values between the BJH adsorption and BJH desorption are similar to each other. Since the adsorption isotherm has more evaluated points than the desorption isotherm, the BJH accumulated values quoted in this study are based on the BJH adsorption data for consistency. As shown in **Figure 7.1.10 (a)**, the external surface areas integrated from BJH adsorption over pore diameters of 2 – 200 nm exhibit consistent values with the external surface areas measured in HJ t-method; the BJH values are slightly lower because the few pores larger than 200 nm are not included in the BJH integration. Since the surface areas contributed by pores larger than 200 nm is small and negligible, it is assumed that the surface areas covering mesopores and macropores from the BJH assessment can be treated as the same external surface areas that are obtained from the HJ t-method. The total pore volumes

of the sorbents can be considered to consist of the micropore volume evaluated in the HJ t-method and the meso-macropore volumes measured in the BJH method. The volumetric composition of micropores in the total pore volume can be further calculated quantitatively.

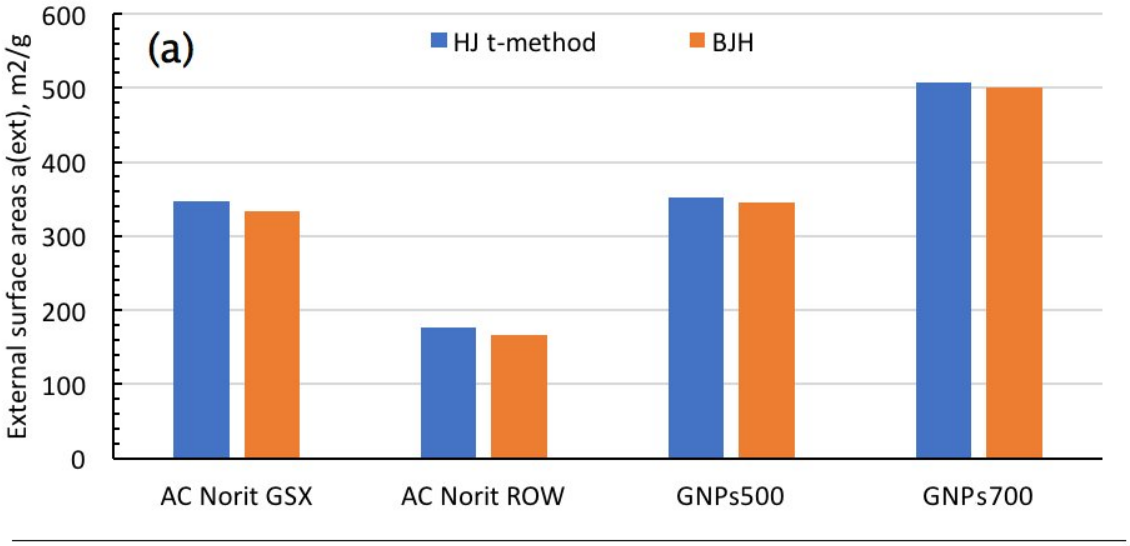

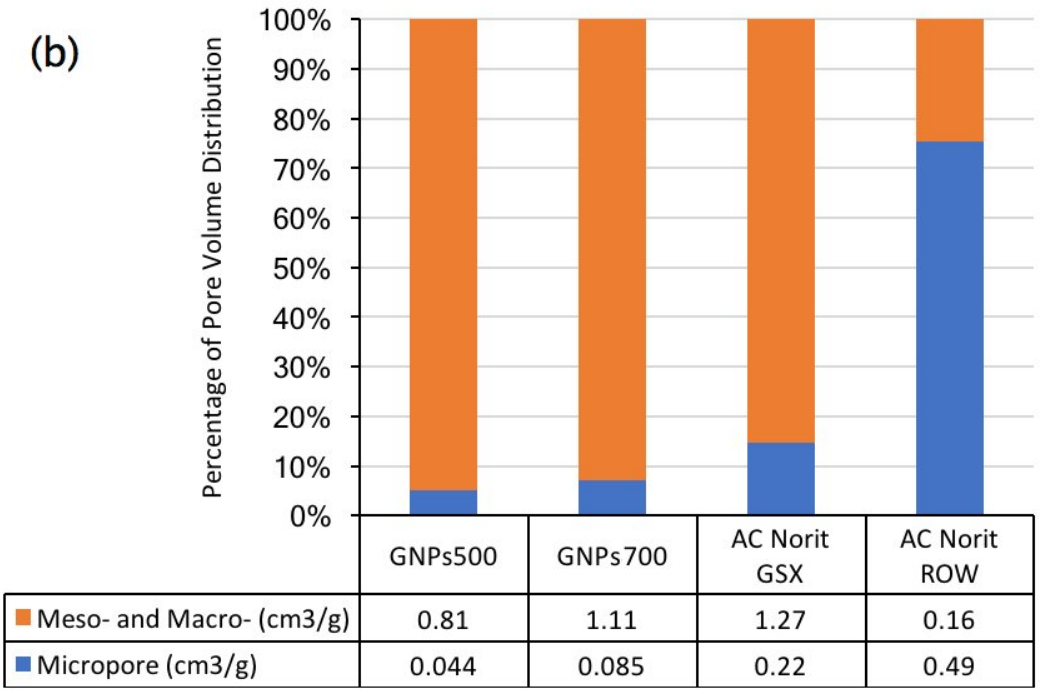

	GNPs500	GNPs700	AC Norit GSX	AC Norit ROW
Meso- and Macro- (cm3/g)	0.81	1.11	1.27	0.16
Micropore (cm3/g)	0.044	0.085	0.22	0.49

Figure 7.1.10 *(a) The comparison of measured external surface areas* a_{ext} *between the BJ t-method and the BJH accumulated meso- and macropore surface areas. (b) The pore volume comparison between the micropore and meso-macropores evaluated from the HJ t-method and BJH-method respectively.*

Figure 7.1.10 (b) shows that both GNPs-500 and GNPs-700 have a micropore composition of less than 10% by volume, which confirms the lower micropore contribution in the HJ t-plots than for activated carbons. The slightly larger micropore fraction of GNPs-700 than GNPs-500 is due to the smaller crystallite size of GNPs-700, of which aggregations lead to smaller pores. Although AC Norit GSX has a micropore volume occupying 15 % of the total pore volume, the mesopore structures still dominate the pore properties, which is consistent with similar trends at the low range of both t-plots and α_s-plots to the GNPs. Unlike the other carbons, micropores dominate (75 % of micropore contents by volume) for AC Norit ROW. The high micropore composition of AC Norit ROW results in a significant micropore filling effect and enhanced adsorbent-adsorbate interactions, which turns the t-plots and α_s-plots in the range below monolayer adsorption to higher slopes than the other carbons.

7.1.3 Summary

Four porous carbon structures, AC Norit GSX, AC Norit ROW, GNPs-500 and GNPs-700, and two zeolites, zeolite 13X and zeolite NaY, are studied in this section. The zeolites exhibit type I adsorption isotherms, indicating the full dominance of micropore structures. BET measurements were discovered to be inapplicable for the zeolite samples, because the vacuum degassing is not high enough to provide sufficient information during the examination. The same argument also applies to HJ t-methods and α_s-methods. According to the specifications from the suppliers, zeolite 13X has a surface area of 720 m^2/g and the surface area of zeolite NaY is 900 m^2/g. The BET methods were thoroughly implemented on four porous carbons for determining their surface areas. With the purpose of discovering the microporous structures of materials, HJ t-methods and α_s-methods were conducted for measuring the micropore volumes and the external surface area. BJH analysis was performed to analyse the pore size distribution and pore volumes of mesopores, as well as the external surface areas.

Zeolite 13X and zeolite NaY are X-type and Y-type of faujasites with different ratios of Al:Si. The faujasite type zeolites (illustrated in **Figure 7.1.11**) have caves with a size around 1 nm. Thanks to the uniform pore sizes distributions, zeolites generally have pure microporous structures. The microporous structures of both zeolites, 13X and NaY, were confirmed by the

presence of type I adoption isotherms and BET linear plots at the extreme low range of relative pressure. AC Norit ROW has micropore-dominated structures with the micropore volume taking up 75 % of the total pore volume. The high proportion of micropores is also confirmed by the micropore surface areas, contributing 1210 m^2/g of the total 1387 m^2/g BET surface area based on the HJ t-method calculation. The large pores are interconnected with smaller pores, as indicated in **Figure 7.1.11**, which leads to enhanced capillary condensation. In the BJH desorption isotherms, the evaporation of capillary condensation in large pores depends on the sizes of connected small pores in the "neck". On referring to Kelvin equations, the condensation in small pores evaporates at lower relative pressures than large pores. When the condensate in small pores desorbs, the condensate in the connected large pores evaporates rapidly, resulting in the steep drop of the hysteresis loop in the nitrogen isotherm.

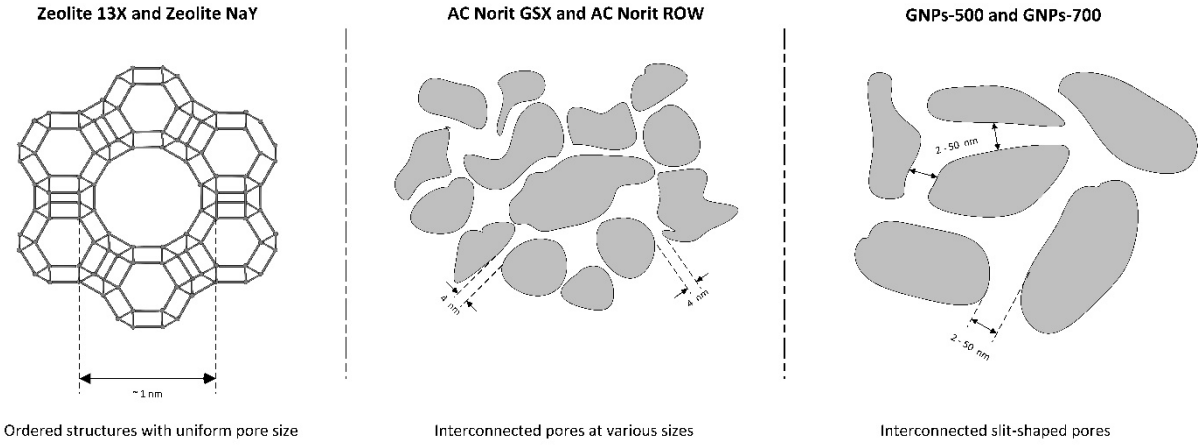

Figure 7.1.11 *Illustrations of pore shapes and sizes for zeolites, activated carbons and GNPs.*

By contrast with AC Norit ROW, AC Norit GSX has a pore structure dominated by mesopores but with a certain amount of micropores present (15% by volume). The steep drop of the hysteresis loop at the lower end is also observed in AC Norit GSX, indicating the presence of interconnected small and large pores. The evaluated BET surface area of AC Norit GSX is 875 m^2/g, in which the micropore surface area contributes 528 m^2/g.

The pores of GNPs-500 and GNPs-700 are primarily in mesoporous structures, which is similar to the case for AC Norit GSX. But the mesopores in GNPs are suggested to have slit-shaped pores, resulting from the aggregation of plate-like crystallites. The slit-shaped pores are evidenced by the absence of steep drops at the lower end of hysteresis loops, due to the lack of significant pore size variations in connected pores. The formation of mesopores can

be caused by both trapped spaces in between adjacent stacked graphitic flakes and the aggregation of small crystallites.

In summary, four carbon samples were intensively studied both qualitatively and quantitatively in this section. The measured pore properties, such as the pore volume and the surface area, are valuable parameters for further analysing the hydrogen cryosorption behaviour. The results from the BET method, t-method, α_s-method and BJH analysis are in good accordance with each other. The application of these methods together can systematically provide a reliable analysis for both the microporous structures and the mesoporous structures of the sorbents.

7.2 Hydrogen cryosorption on carbon samples and zeolites

7.2.1 High-vacuum and medium-vacuum degassing for hydrogen cryosorption measurements

As early as the design stage of the manometry system, it was considered whether the degassing of sorbents in the hydrogen cryosorption measurement needed ultra-high vacuum. The primary consideration of outgassing volumetric chambers under vacuum pumping is to remove gas residues so that the clean surface is created to adsorb hydrogen. In several references [13], [122], it was pointed out that the measurement of hydrogen adsorption essentially requires a degassing vacuum better than 10^{-10} bar (10^{-5} Pa), while BET adsorption measurements are recommended to reach a vacuum of 1 Pa for achieving the sufficient analysis, referring to the ISO standard [63]. The ultra-high vacuum (UHV) of 10^{-5} Pa is unrealistic for volumetric manometry designed for measuring hydrogen adsorption in positive pressures. The volumetric design, consisting of multiple transducers and diverse sizes of volume chambers, requires a large quantity of fittings, which are not designed for ultra-high vacuum applications. The more fittings built into a volumetric system, the worse the vacuum that might be expected. Secondly, the capital cost and the time required to achieve ultra-high vacuum are challenges to the practicability and mobility of measuring systems in commercial applications. Although UHV is unattainable with this equipment design, a high vacuum of 10^{-7} bar (0.01 Pa), which is sufficient to ensure rigorous surface cleanliness for determining porous properties in most cases [60], can be achieved with a diffusion pump; and it provides enough of a margin in vacuum quality over the medium vacuum of 10^{-4} bar (10 Pa) to evaluate whether the higher vacuum is strictly essential for hydrogen cryosorption measurements.

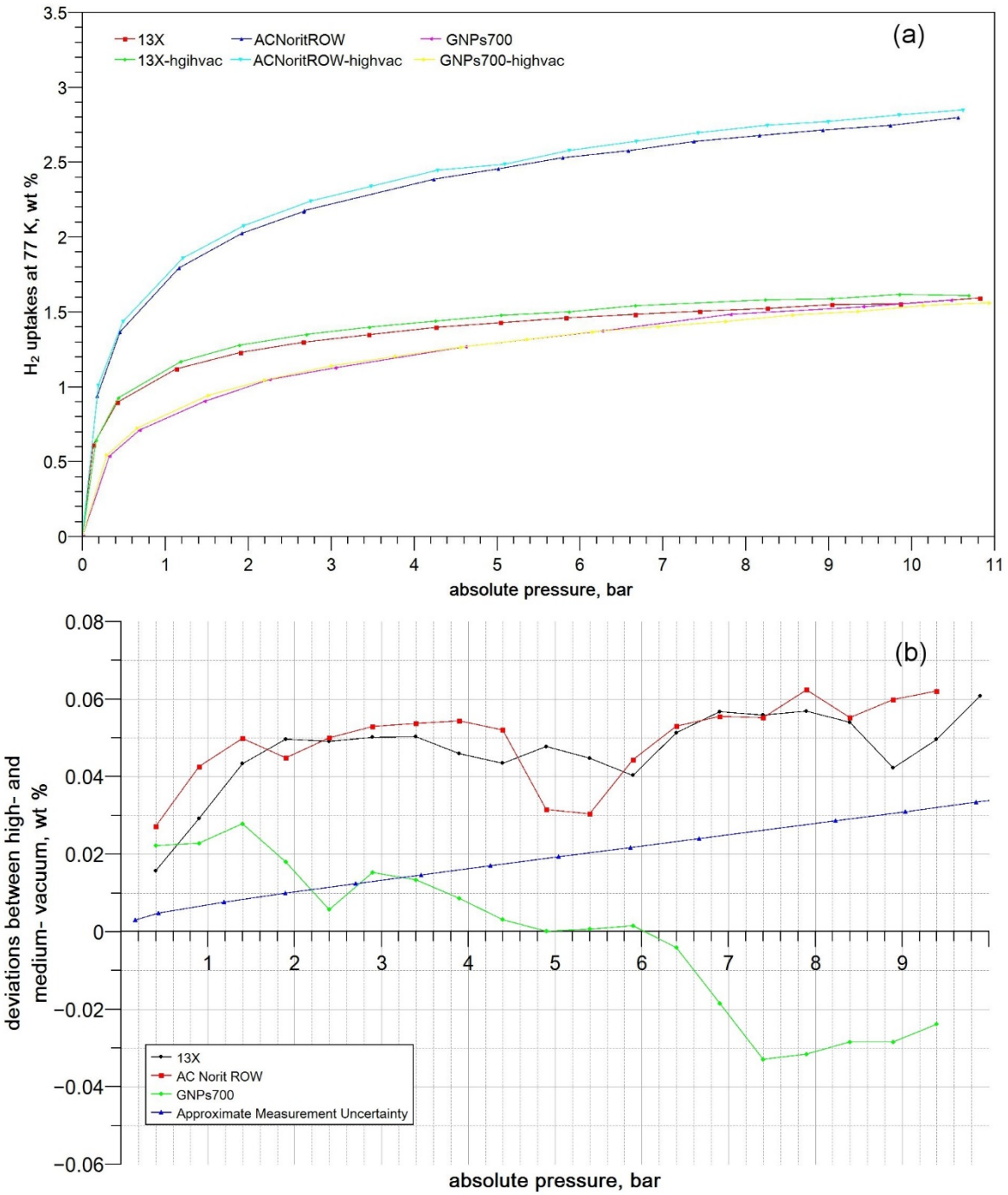

Figure 7.2.1 *(a) Comparison of hydrogen cryosorption uptakes on 13X, AC Norit ROW and GNPs700 between high vacuum degassing (10^{-7} bar, at room temperature) and medium vacuum degassing (10^{-4} bar = 0.1 mbar, at room temperature); (b) the deviations between the high-vacuum degassing uptakes and medium-vacuum degassing uptakes of the tested carbons (points by the linear interpolation; the approximate measurement uncertainty plotted in blue line).*

In order to determine the hydrogen uptake differences between high vacuum degassing and medium vacuum degassing, the systems were connected with two different vacuum pumps, a portable rotary pump for achieving 10^{-4} bar (10 Pa) vacuum and a diffusion pump for reaching 10^{-7} bar (0.01 Pa). The designed testing system has a self-built cold trap for preventing any oil vapour from entering the system. Three sorbents, zeolite 13X, AC Norit ROW and GNPs-700, were selected to represent microporous structures with uniform pore sizes, micropore dominated structures with varied pore sizes and mesoporous structures, respectively.

The hydrogen cryosorption isotherms of the three sorbents at 77 K are presented in **Figure 7.2.1 (a)** with both high-vacuum degassing and medium-vacuum degassing. The cryosorption isotherm of GNPs-700 with high-vacuum outgassing is in accordance with the medium vacuum uptakes; and the positive and negative deviations result in an average fluctuation over the 11 bar pressure range close to zero in **Figure 7.2.1 (b)**. In contrast with GNPs-700, both zeolite 13X and AC Norit ROW exhibit slightly higher uptakes with high-vacuum degassing than low-vacuum degassing. This difference is noticeably larger than the approximate measurement uncertainty. By comparing the porous structures analysed in section 7.1, the difference between the mesoporous GNPs-700 and the microporous zeolite 13X and AC Norit ROW is mainly the proportion of micropores. Therefore, it is supposed that the observed higher uptakes in AC Norit ROW and 13X with high-vacuum outgassing is associated with the condensation of nitrogen on micropores that reduces the micropore surface area on which hydrogen can be adsorbed. It should also be noted that the deviations between high and medium vacuum outgassing in 13X have similar values and trends to those for AC Norit ROW, as shown in **Figure 7.2.1 (b)**, although the two microporous samples have significantly different surface areas, 720 m^2/g for the 13X and 1387 m^2/g for the AC Norit ROW.

To further analyse the observed uptake differences between different vacuum conditions, several assumptions are proposed for simplification. Firstly, the amount of hydrogen adsorbed is assumed to correlate only with surface area. Furthermore, the residual nitrogen gas after vacuum degassing is condensed in micropores preferentially in comparison with mesopores, based on the Kelvin equation. The surface area covered by condensed liquid nitrogen in micropores at 77 K is supposed to be unable to adsorb hydrogen. The following

analysis is based on AC Norit ROW because of its well-understood porous properties in section 7.1. Since the hydrogen cryosorption uptakes of AC Norit ROW, with high vacuum degassing at 77 K and 11 bar pressure, is around 2.85 wt%, the reduced 0.05 wt% uptake for medium vacuum degassing would correspond to 1.7% of the total surface area being blocked, equal to 25 m^2/g micropore surface area that is only 2 % of the total micropore surface of 1210 m^2/g. It means that the micropores of AC Norit ROW cannot be fully filled with condensed residual nitrogen. If it is assumed that micropore surface areas are uniformly distributed within micropore volume in approximation, 25 m^2/g micropore surface areas take up 2 % of the total micropore volume of 0.14 cm^3 (for 0.89 g of sorbent), equal to 2.8×10^{-3} cm^3 of liquid nitrogen condensed in the micropores. The amount of condensed nitrogen is calculated to be 2.26×10^{-3} g (8.07×10^{-5} mol) in respect of the liquid nitrogen density of 0.807 g/cm^3. Therefore, the theoretical residual pressure of 0.05 wt% uptake deviation is calculated to be around 5 mbar in average based on the ideal gas law at room temperature and the chamber volumes of the apparatus if the pressure is evenly distributed inside the volume chamber and the pores of sorbent.

In practice, the small pores in the sorbent can hold local residual pressure higher than 5 mbar due to the strong adsorbate-adsorbent interactions, while the pressure in volume chambers is expected to be smaller. Considering that the vacuum pump and the vacuum gauge are remote from the sample chamber, the actual residual pressure inside the system is expected to be higher than the measured vacuum of 0.1 mbar by the vacuum gauge. The 5 mbar estimated residual pressure is perhaps a reasonable approximation of the achieved 0.1 mbar gauge pressure at the inlet of vacuum pump. Thus, it is a logical hypothesis that the condensation of residual nitrogen in micropores at 77 K contributes to the slightly reduced amounts of hydrogen uptakes in microporous sorbents, and the similar values of deviations between 13X and AC Norit ROW is due to the small fractions of micropores filled by condensed residual nitrogen. For mesoporous structures like GNPs-700, the majority of pores have large diameters so that the adsorbate-adsorbent interactions in mesopores have no significant difference from those on open surfaces. In the case of mesoporous materials, the condensed nitrogen is distributed homogeneously on the surface of the volume chambers and the sorbents, which results in no specific reduction of mesoporous volumes and surface areas.

In summary, high-vacuum degassing can increase the uptakes of hydrogen cryosorption to some extent with a volumetric testing system for micropore-dominated sorbents: by 2 – 3 % in this study in relative to medium-vacuum degassing. It is difficult to judge whether high-vacuum is necessary in practice, considering the expense and time required to implement a high vacuum system for a small uptake improvement. The deviation could possibly be reduced with smaller chamber volumes, and it is also possible that this could be quantified with a large amount of experimental data so that an appropriate model could be built to obtain accurate results with medium vacuum degassing (approximately 0.05 % absolute deviation in this study for microporous sorbents). For evaluating mesoporous materials, medium-vacuum pumping seems sufficient, probably due to the lack of nitrogen condensation on mesopores.

7.2.2 Hydrogen cryosorption isotherms of highly porous carbons and zeolites

In each hydrogen cryosorption measurement, the reservoir chambers filled with pure hydrogen at a pre-set pressure are connected to the evacuated sample chambers by opening the corresponding valves, exposing the sorbents to hydrogen, and at that moment (labelled as time zero) the amount of hydrogen uptake starts to be recorded. **Figure 7.2.2** illustrates the progress of uptake in each measurement versus time, in which the pressure is the equilibrium pressure at the saturated uptake. In this study, the hydrogen cryosorption measurements generally reached the maximum saturated uptake at a certain pressure within 10 – 15 minutes. The sorption isotherm exhibits a sharp increase in the first 50 seconds, followed by a curved corner after which the increase of uptake slows gradually until the maximum is reached. If the entire isotherm is separated by a rough mid-point of the curved corner section as shown in **Figure 7.2.2**, the majority of the uptake is achieved in the first section within a hundred seconds.

By comparing the microporous sorbents in **Figure 7.2.2**, like 13X and AC Norit ROW, and the mesoporous sorbents, such as AC Norit GSX and GNPs-700, the mesoporous sorbents take less time (< 300 seconds) to approach the maximum uptake than the microporous materials (> 400 seconds). It is difficult to conclude whether the prolonged adsorption time is due to the higher proportion of micropores in 13X and AC Norit ROW depending solely on the profiles of isotherms, but the decreased pore sizes can potentially restrict the hydrogen gas from flowing into the pores. As the uptake maximum is approached with a gradually reducing rate in each cryosorption isotherm, it is impossible to identify a single, precise time point at which the maximum uptake is reached. Instead, a series of specific sorption uptakes were defined as 40%, 50%, 60%, 70%, 80% and 90% of the rough maximum uptakes, i.e. those values reached at 400 seconds for mesoporous materials, GNPs-700 and AC Norit GSX, and 600 seconds for microporous materials, 13X and AC Norit ROW, as shown in **Figure 7.2.3**. The times corresponding to these relative uptakes can be obtained by linear interpolation between adjacent discrete points.

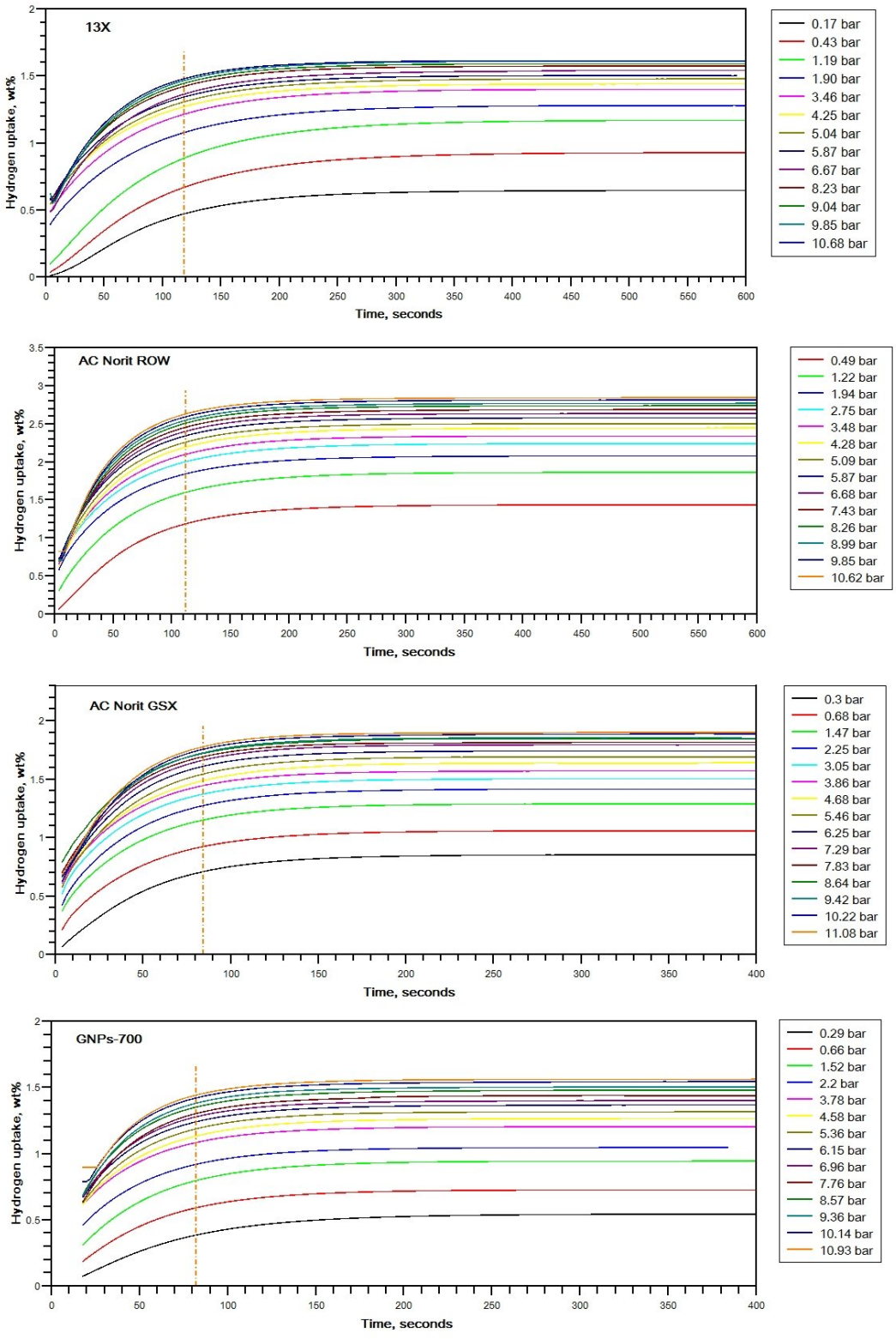

Figure 7.2.2 *H_2 cryosorption uptakes versus time at various equilibrium pressures for microporous sorbents, zeolite 13X and AC Norit ROW, and mesoporous sorbents, AC Norit GSX and GNPs-700.*

As illustrated in **Figure 7.2.3**, high pressures are favourable for more rapidly arriving at a similar level of hydrogen uptake than low-pressure tests among all four samples. For reaching 90 % specific uptake, the time required at 10 bar pressure is noticeably 20 % - 30 % less than that at 1 bar, which might be due to enhanced adsorbent-adsorbate interactions because of high pressures and high molecular densities accelerating the adsorption kinetics. However, the pressure-dependent kinetics of adsorption are observed to saturate in the pressure range of 3 – 11 bar for the plots of 40 %, 50 % and 60 % specific uptake in all samples: the time to reach a targeted sorption level is approximately constant for pressures in the 3 – 11 bar range. The times required to reach 70 % and 80 % were also discovered to be less dependent on pressure than the 90 % isotherms. Thus, it is supposed that a type of saturated kinetic state that is not pressure dependent is reached at 3 – 4 bar pressure for a certain material. And it is also postulated that the time spent for achieving the maximum at higher pressures than 10 bar might reach a similar type of saturation for 90 % specific uptake. The trends in the time required to reach a certain uptake intensity with pressure have no significant variations among diverse types of materials, indicating the pressure-dependent performance is likely to be associated with the adsorption mechanism instead of specific material properties.

According to the results in **Figure 7.2.3**, the 90 % specific uptake at 10 bar pressure takes a similar 80 seconds to be achieved in GNPs-700 compared with AC Norit GSX; while the other microporous materials, zeolite 13X and AC Norit ROW, take ~120 seconds to fulfil the similar uptake level that is obviously longer than the mesoporous sorbents. These differences can hardly be considered to be the sole effect of microporous properties, since the adsorption isotherm is in a non-equilibrium state except at the maximum uptake, which means that both the fluctuation of molecule-molecule interactions and the instability of testing conditions can potentially influence the adsorption kinetics. As the maximum pressures studied in this report are 10 – 11 bar absolute pressures, the hydrogen uptakes are not expected to have reached the saturated values as a function of pressure, in reference to the works conducted for sorption higher than 11 bar pressures [15], [42], [45], [123]; but the significance of low-pressure H_2 cryosorption tests is in discovering possible ways to enable rapid measurements and simulate the practical conditions for potential mobile applications.

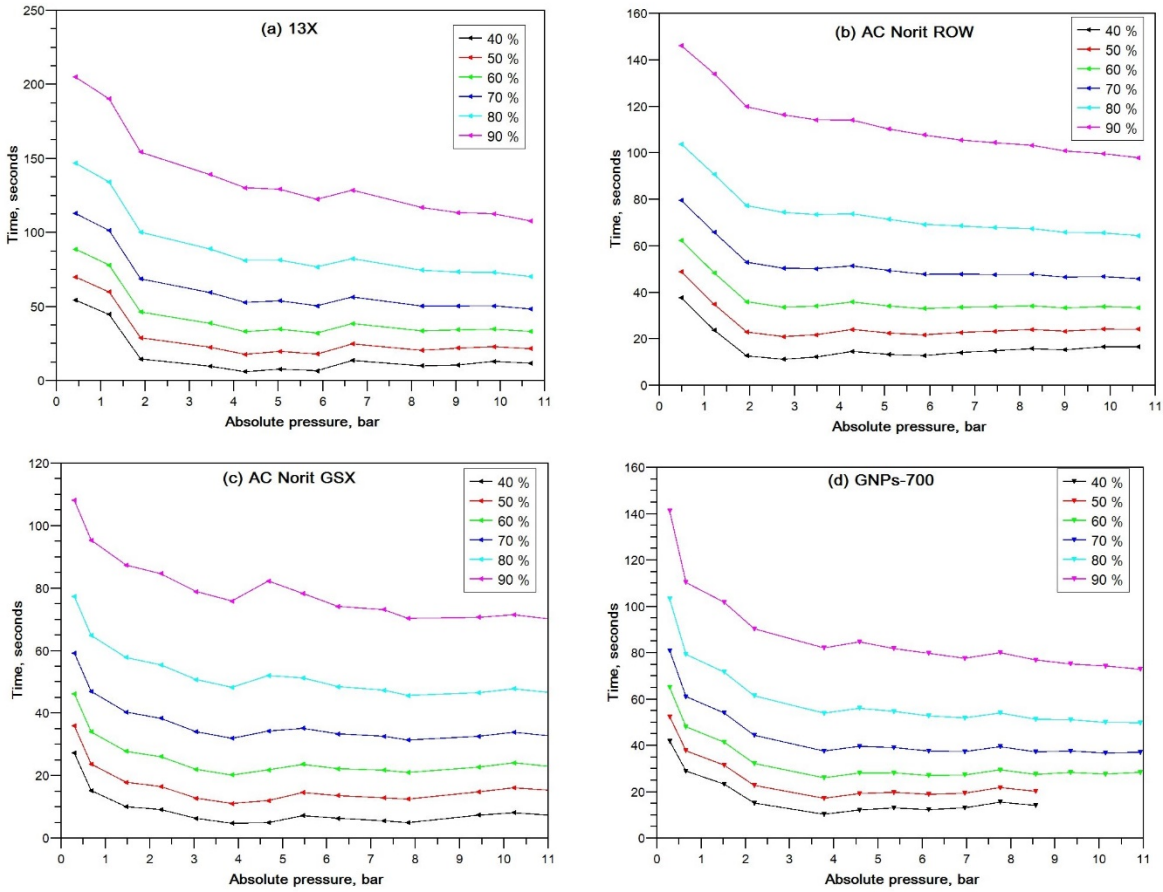

Figure 7.2.3 *The time required to reach specific H_2 uptakes of 40%, 50%, 60%, 70%, 80% and 90% of the maximum uptakes at various pressures: (a) 13X, (b) AC Norit ROW, (c) AC Norit GSX and (d) GNPs-700.*

7.2.3 Hydrogen cryosorption uptakes analysis

Hydrogen uptakes are generally plotted against their equilibrium pressures. The hydrogen cryosorption of different zeolites has been studied by Langmi et al. in a similar pressure range and at 77 K using a gravimetric adsorption analyser [15], [45]. The results of hydrogen cryosorption measurements for the six samples presented in section 7.1 are plotted in comparison with Langmi et al.'s published results [45] for zeolites NaX with surface area of 662 m^2/g and zeolite NaY with surface area of 725 m^2/g in **Figure 7.2.4 and Figure 7.2.4b**. It is also worth noting that the surface areas obtained from the supplier for the zeolites in this study cannot be reliable enough to compare with the published results quantitatively. Although the published results of selected zeolites have differences in uptake compared with the same types of zeolite tested in this study, which can be explained by the different

suppliers and the various surfaces areas of the materials, both isotherms exhibit a similar range of overall uptake and the similar plot shapes/trends. The X type zeolites (13X and Zeolite NaX*) exhibit a rough saturated uptake at lower pressures than the Y types zeolites (Zeolite NaY and Zeolite NaY*) and the carbon sorbents, for which the reason is difficult to judge as the detailed porous properties of these zeolites are not known. The hydrogen uptakes at 10 bar for all the measured samples, as well as the BET surface areas, are listed in **Table 7.2.5**.

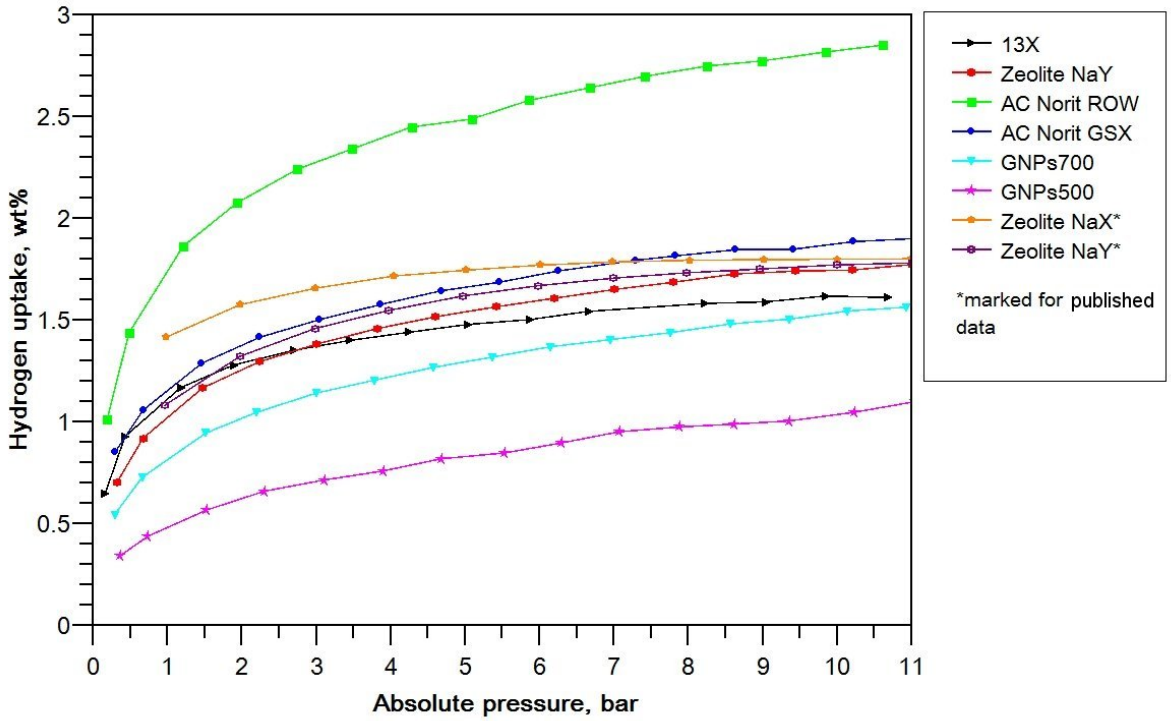

Figure 7.2.4 *The H_2 cryosorption isotherms of measured six samples and two zeolites referring published results [45].*

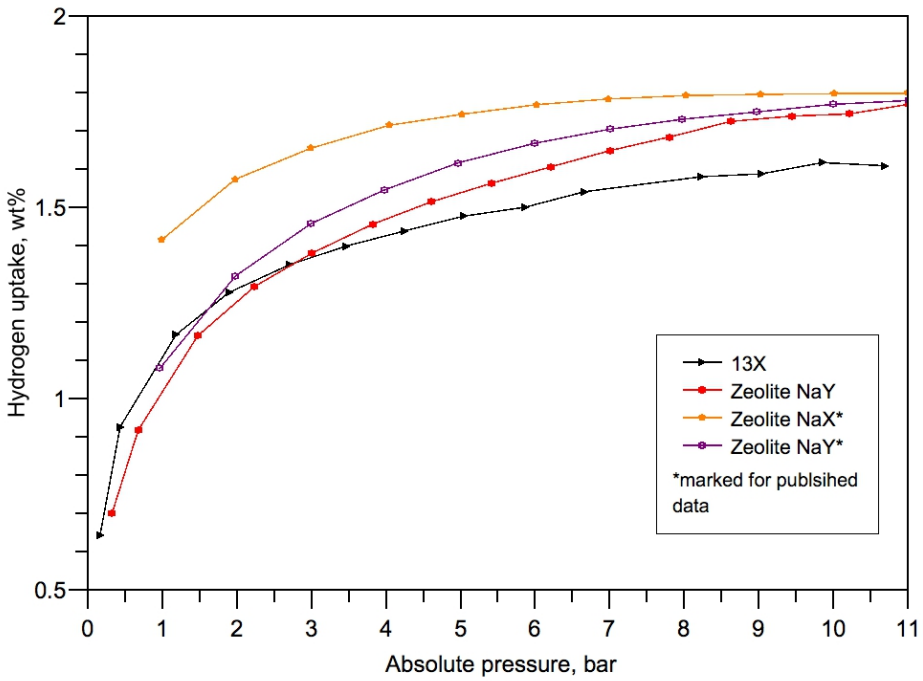

Figure 7.2.4b *The H_2 cryosorption isotherms of two zeolites measured and two zeolites from published results [45].*

Table 7.2.5 *The hydrogen uptakes at 10 bar and 77 K, BET surface areas and monolayer capacity based on Langmuir model.*

	H_2 uptake at 10 bar, 77 K (wt%)	**BET surface area (m^2/g)**	**Monolayer capacity (Langmuir model) (wt%)**
13X	1.62	720	1.68
Zeolite NaY	1.84	900	1.88
AC Norit ROW	2.82	1387	2.96
AC Norit GSX	1.87	875	1.99
GNPs700	1.53	705	1.66
GNPs500	1.03	453	1.16

It is generally agreed that the surface area is a critical parameter for achieving high uptakes of hydrogen physisorption [14], [15], [65], [124]–[127]. By contrast with nitrogen adsorption isotherms at 77 K, the hydrogen molecules attach to the surface as gaseous molecules, i.e. without condensation that happens in nitrogen adsorption at 77 K. When the temperature decreases to 20K, the boiling point of hydrogen, hydrogen adsorption isotherm has been proven to follow the BET theory, and the measured BET surface area of MOFs based on hydrogen adsorption isotherm is slightly larger than that based on nitrogen adsorption

isotherm, which is due to the smaller size of hydrogen probe molecule that can reach smaller pores [128]. However, at 77 K, the BET theory is no longer valid, since multilayer adsorption is unlikely to occur in hydrogen adsorption at 77 K and 10 bar pressure. The Langmuir model, by contrast, can potentially be applied for studying hydrogen adsorption, considering its assumptions of only one kind of adsorbent system and no lateral interactions between the adsorbed molecules [61]. As a result of the small sizes of hydrogen molecules and the lack of liquid hydrogen condensation at low pressures and 77 K, the hydrogen molecule is expected to independently attach to the adsorbent surface, so that lateral interactions are weak and negligible. The Langmuir model has been applied in analysing various zeolite sorbents [45], which achieved good agreements between theoretical expectations and the measured results. The linear expression of the Langmuir equation 7.1 [61] is:

$$\frac{P}{n} = \frac{1}{n_{\mathrm{m}} b} + \frac{1}{n_{\mathrm{m}}} P \tag{7.1}$$

where P is the equilibrium pressure, n is the amount of uptake, n_{m} is the monolayer capacity of uptake and b is the "adsorption coefficient" that is exponentially related to the adsorption energy. In terms of the Langmuir equation, a linear plot can be obtained by plotting P/n as a function of P if ideal adsorption is dominant.

The Langmuir plots of the measured sorbents, as well as two series of published results [45], are presented in **Figure 7.2.7**. The Langmuir plots of the sorbents show acceptable linear agreement, which indicates the occurrence of ideal adsorption behaviour of hydrogen cryosorption at 77 K and 10 bar pressure. The reciprocal value of the monolayer capacity n_{m} is equal to the slope of the linear regression of Langmuir plot, and the calculated monolayer capacity is discovered to correlate linearly with the BET surface area in **Figure 7.2.8 (a)**. The fitted slope on the monolayer capacity plot is 0.0021 wt%·gram/m^2, equal to 1.05 × 10^{-5} mol/m^2. Considering one layer of hydrogen molecules in which both atoms attach to the surface with the closest possible spacing, as illustrated in **Figure 7.2.6**, the area that is covered by each hydrogen molecule can be estimated from the covalent distance and the Van der Waals distance. The single hydrogen molecular area is 7.536 × 10^{-20} m^2. Thus, 1 m^2 of surface area can take up to 1.327 × 10^{19} hydrogen molecules, equal to 2.2 × 10^{-5} mol. Based on the linear fit of Langmuir monolayer capacities n_{m} in respect of the equilibrium pressure, the

saturated hydrogen molecule adsorption of 1.05 × 10^{-5} mol/m^2 takes up nearly 50 % of the maximum adsorption amount of 2.2 × 10^{-5} mol/m^2 in theory. As the attached hydrogen molecules are in the gaseous state at 77 K and far from saturated adsorption on the surface, both atoms of the molecule are more likely to attach to the surface for achieving the enhanced adsorbent-adsorbate interactions than the molecule attached to the surface via only one atom (see **Figure 7.2.6**).

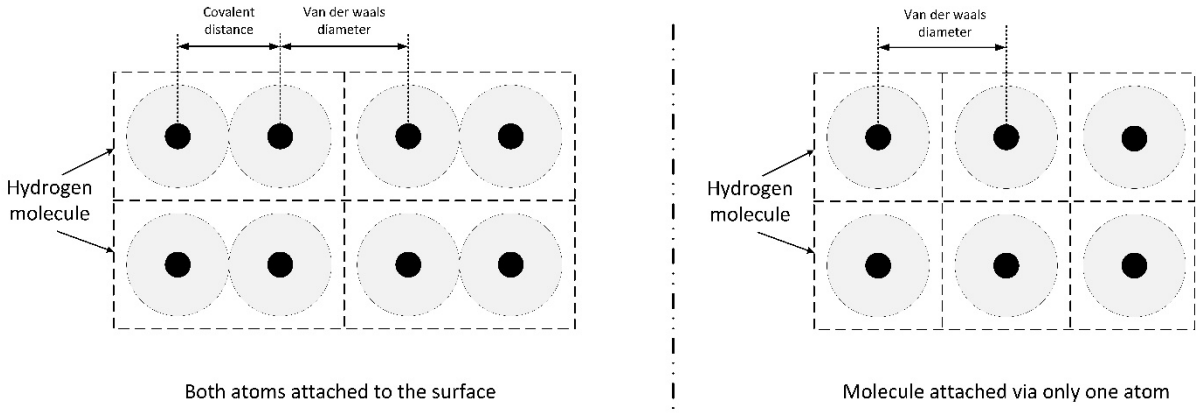

Figure 7.2.6 *The theoretical model of maximum monolayer adsorption of molecules.*

For nitrogen adsorption at 77 K, the monolayer capacity n_{m} has been calculated with the BET method for each carbon sorbent (see **Table 7.1.4**). As shown in **Figure 7.2.8 (b)**, good linear fitting is expected for evaluating nitrogen monolayer capacities, since the BET theory is based on homogeneous adsorption on surfaces. The monolayer capacity per unit surface area is obtained from the slope of the linear plot, 0.2297 cm^3 STP/m^2, equal to 1.02 × 10^{-5} mol/m^2. The theoretical maximum uptake of nitrogen adsorption at 77 K is 1.18 × 10^{-5} mol/m^2 with both atoms of each molecule attached on the surface and 1.75 × 10^{-5} mol/m^2 for attachment of each molecule via a single atom, based on the same calculation method as the hydrogen adsorption discussed above. By comparing the measured monolayer capacity with the theoretical calculations, the condensed liquid nitrogen molecules are mostly likely to display double atom attachment on the surfaces. The calculations of monolayer adsorption for nitrogen at 77 K based on BET methods are in good accordance with that of the hydrogen adsorption at 77 K based on the Langmuir model, which justifies the application of the Langmuir model to hydrogen cryosorption. A detailed development of the potential applications of the Langmuir model on hydrogen adsorption would require a large amount of

hydrogen cryosorption data of different sorbents at various temperatures and a wider range of pressures, which is a prospective target for future research.

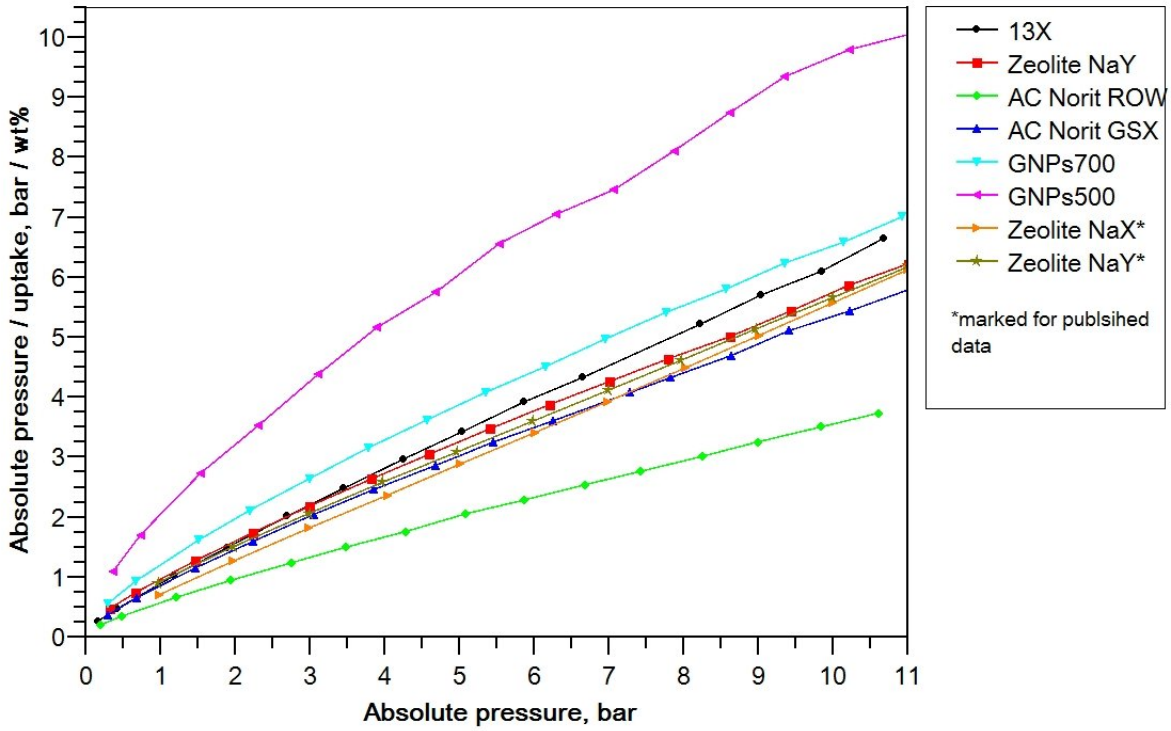

Figure 7.2.7 *Langmuir plots of measured sorbents and two reference samples [45].*

By analogy to the Langmuir analysis of liquid nitrogen adsorption, the monolayer capacity of hydrogen at its liquefaction temperature 21 K could also correspond to the saturated double-atom attachment on the surface, in which the monolayer capacity is close to the 2.2 × 10^{-5} mol/m^2. The coverage of adsorbed hydrogen molecules on monolayer adsorption at 77 K is around 50 % as measured. For the same combination of adsorbent and adsorbate, the temperature-dependence of hydrogen uptakes is probably due to the variations in adsorption coverage. It is not clear whether the 50:50 composition ratio of ortho-hydrogen to para-hydrogen at 77 K is similar to the hydrogen molecule coverage on surface by coincidence, but exploring any correlation between ortho-para conversion of hydrogen and adsorption energy variations would be an interesting direction for future analysis.

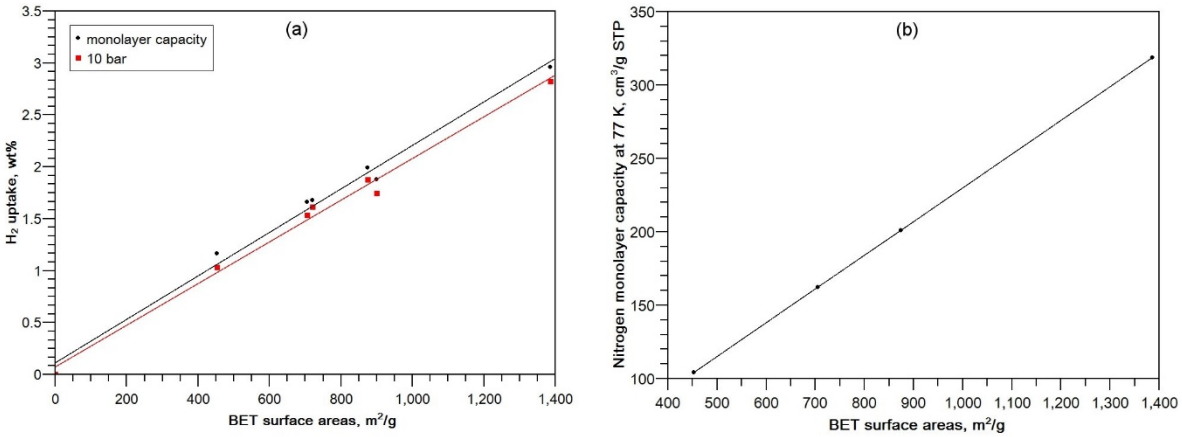

Figure 7.2.8 *(a) The monolayer capacity obtained from Langmuir plots and H_2 cryosorption isotherms at 10 bar pressure versus BET surface areas. (b) The nitrogen monolayer capacity at 77 K from BET methods versus BET surface areas.*

The correlation between the hydrogen uptakes at 77 K and the surface areas at various pressures is presented in **Figure 7.2.9**. The points deviate from linearity more significantly at low pressures than high pressures, which suggests that a better linear correlation between hydrogen uptake and surface area for higher pressures. The fluctuations of the low pressure adsorption might be caused by the locally concentrated adsorption on small pores and curved surfaces that is less obvious at higher pressures. The slopes of the linear regressions increase with pressure, gradually approaching the monolayer capacity plot as described in **Figure 7.2.8 (a)**.

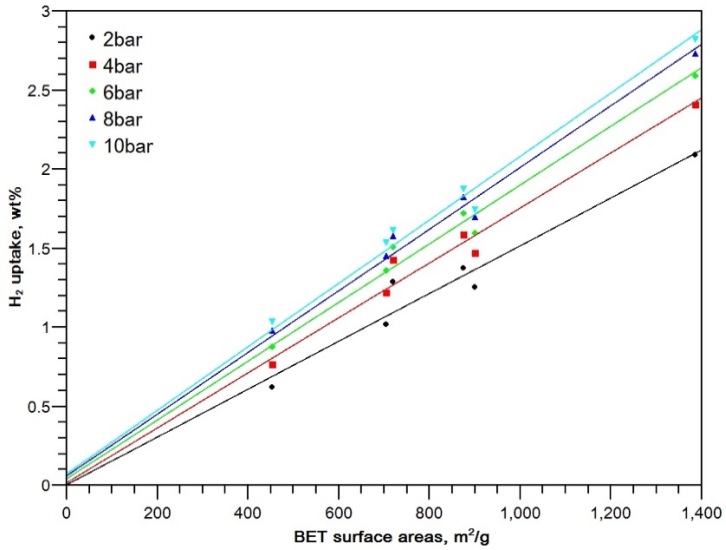

Figure 7.2.9 *The measured hydrogen uptakes versus BET surface areas at various pressures.*

7.2.4 Summary

In this section, the question of whether high-vacuum degassing is essential for providing accurate measurements was reviewed. The hydrogen cryosorption measurements of microporous materials, such as zeolites, require high-vacuum pumping, as the residual nitrogen can result in liquid nitrogen condensation on micropores so that the surface areas available for adsorption of hydrogen molecules can be reduced. The mesoporous materials, such as some types of activated carbons and the graphene nanoplatelets (GNPs), can be accurately assessed for their hydrogen cryosorption uptakes with medium-vacuum outgassing achieved by cost-effective and lightweight rotary pumps, since the liquid nitrogen condensation is not significant in large mesopores. The offset induced by medium vacuum compared with high vacuum is constant with a certain chamber volume of the system, if the micropore volume is large enough to accommodate the entire amount of condensed liquid nitrogen. A complete analysis could allow a model to be built for correcting the measurement results with medium vacuum degassing to obtain accurate uptakes. Considering the prospective mobile applications, medium vacuum is preferable as a result of the significantly reduced capital cost and time requirements, and it is likely to have only an almost insignificant effect on storage capacity (2 wt% for AC Norit ROW with 2.82 wt% hydrogen uptake at 77 K and 10 bar in this study).

The hydrogen cryosorption isotherms of the zeolites 13X and NaY, the activated carbons, AC Norit ROW and AC Norit GSX, and the graphene nanoplatelets, GNPs-500 and GNPs-700 were compared with published results and reviewed in depth with the implementation of Langmuir model. The time required to reach a certain level of uptake is discovered to be independent of the equilibrium pressures. The Langmuir model was revealed to be in good agreement with the measured results. Hydrogen adsorption at 77 K is quite far from achieving saturated monolayer adsorption, taking up nearly 50 % of the maximum coverage. The measured hydrogen uptakes are linearly correlated with the surface areas at pressures ~10 bar, which is consistent with existing literatures reporting that the hydrogen uptakes of both zeolites and carbon sorbents at the same temperature and pressure are in an approximately linear correlation with surface areas [4], [45], [48], [65].

7.3 Study of the plasma carbon and pyrolysed biomass

Most of the results and discussions in this section have been published in a co-authored paper in reference [110]. The XRD patterns of plasma carbon and the knowledge of plasma reforming of methane were attributed to the previous work by Ms Juda [112]. We also acknowledge our collaborators in the University of Limerick for the FTIR and XPS characterisation of both the plasma carbon and the pyrolysed biochar from *Miscanthus*. The Raman spectroscopy of plasma carbon was performed by Dr Tsaneva, and the Raman and XRD characterisation on pyrolysed biochars were conducted by the author in this report. The analysis of XRD results in this section was conducted by the author primarily, and the Raman analysis was studied with the assistance of Dr Tsaneva. In order to present a complete and clear report of this topic, the published results from the previous paper, as well as some extra results, are presented and discussed in this section.

A detailed description of the production and characteristics of plasma carbons and biochars was discussed in section 4.1 and 4.2. The labels identifying the plasma carbons collected from differential plasma powers and sampling locations are presented in **Table 4.1.2** of section 4.1. The carbon collected from L1 region with the 1.5 kW input was labelled as C1L1, and the carbon situated in L2 region with the same power was C1L2. Analogously, the plasma carbon C5L1 was collected from L1 region with the input power of 5 kW, while C5L2 was collected from the L2 region with the same power input as C5L1. The plasma carbon was a product of microwave splitting of methane, and the biochar was acquired by the pyrolysis of *Miscanthus*, as described in sections 4.1 and 4.2. The production process of plasma carbon reduces CO_2 emissions by transforming the carbon content of methane into solid carbon materials, also yielding pure hydrogen gas, while the production of biomass was not only economical and sustainable because of using plants as raw materials, but also environmentally-friendly by introducing a way of capturing carbon to reduce the emission of carbon dioxide. The graphitic properties of both carbons were studied, and the possible applications related to these materials were briefly discussed.

7.3.1 Raman spectroscopy of plasma carbons

The Raman spectra of the four plasma-carbon samples are shown in **Figure 7.3.1**. It is observed that all plasma carbons exhibit sp^2 bonds, with the appearance of the graphitic "G peak" at around 1580 cm^{-1} [129]. The existence of a G peak in the Raman spectra is associated with E_{2g} modes (see **Figure 7.3.2**) of shear vibrations in graphitic six-fold rings [130]. The vibrations of atoms in E_{2g} modes can be either in phase or with opposite phase. As the energy levels of two vibration modes are very similar to each other due to the weak interlayer reactions of graphite [130], two vibration modes were combined to form the single G peak appearance in Raman spectra.

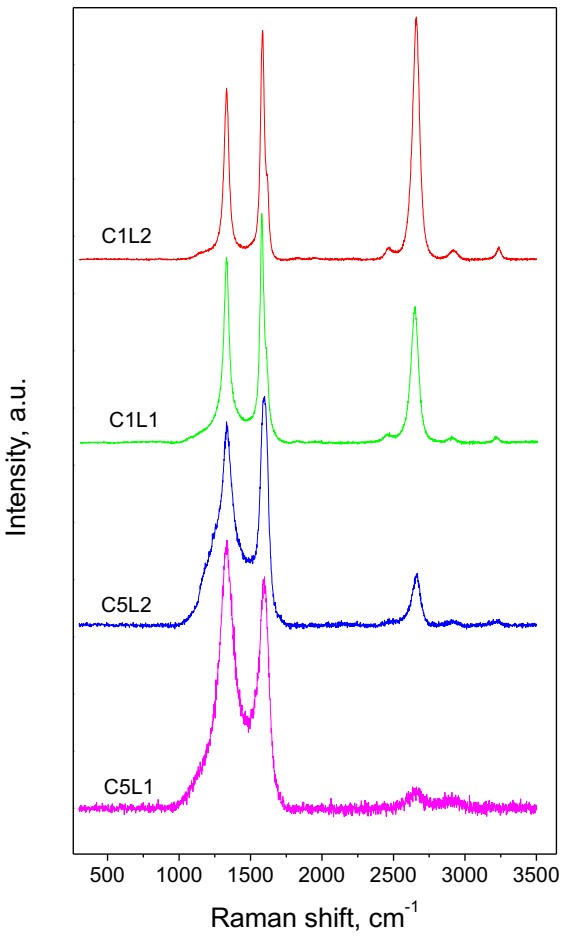

Figure 7.3.1 *The Raman spectra of plasma carbons: C1L1, C1L2, C5L1 and C5L2 (see Table 4.1.2 for sample details).*

In addition to the G peak, there is another 1st order peak located at around 1355 cm^{-1}, the "D-peak", which relates to disorder. It is also understood that diamond shows an intense peak with a narrow width at 1332 cm^{-1} [129], [131]. But the existence of diamond-like impurities is

highly unlikely in plasma carbons, since the non-equilibrium plasma glow can only reach a temperature of about 1000 K at atmospheric pressure [111], [112]. The existence of D peaks is believed to correlate with the increased degree of disorder due to the existence of small crystallites and the presence of mobile six-fold aromatic rings [129]–[131]. The breathing vibration of A_{1g} symmetry of the six-fold rings induces the D-peak in the Raman spectra, as illustrated in **Figure 7.3.2**.

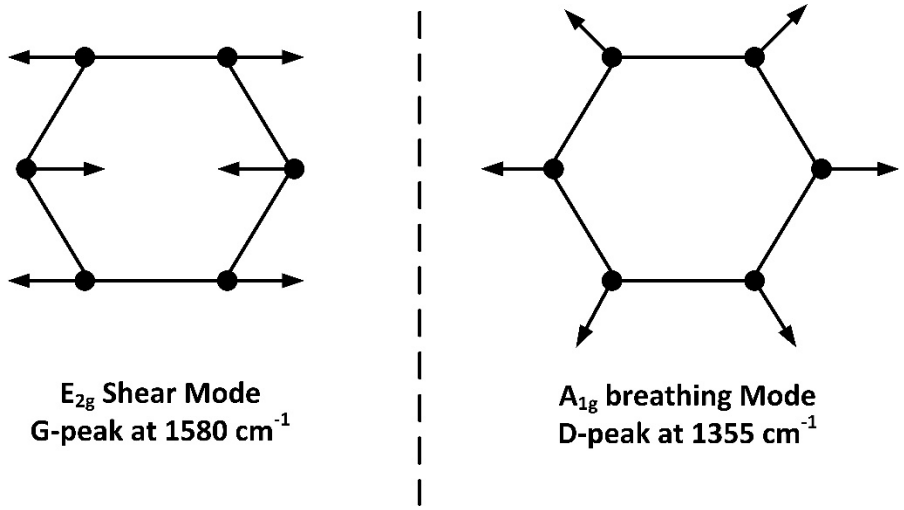

Figure 7.3.2 *Illustration of vibration modes of aromatic rings, associated with the corresponding Raman peaks [129].*

The Raman peaks are broadened by the introduction of defects, as the phonon modes take a wide range of vibrational energies in quantised states. The width of the graphitic G peak is related to the degree of bond angle disorder at sp^2 sites (or induced sp^3 by the distorted carbon rings) [129], while the FWHMs of the D peaks increases with the reduction of crystallite sizes [130]. The Raman G peaks and D peaks were deconvoluted as described in **Figure 7.3.3 (a)**.

Both C1 carbon samples from the low-power (1.5 kW) plasma have smaller FWHMs than the high-power (5 kW) plasma C5 carbons in first-order peaks, indicating the better crystalline construction of plasma carbons produced with a lower power input. The variations of FWHMs between different collection locations with the same plasma power are not significant, as described in **Figure 7.3.3 (b)**, which suggests that the collection location of carbons is not a major parameter in forming the carbon graphitic structures. The broadening of peaks for the sample produced with 5 kW microwave power is caused by the shrinkage of crystalline sizes,

which was confirmed by TEM micrographs from the previous work in reference [112] and was in good accordance with the analysis from Tuinstra and Keonig [130] that crystallites with small sizes contributed to so-called “boundary effects”. The defects induced by grain boundaries in polycrystalline materials led to a distribution of phonon energies corresponding to the different unit cell sizes, which further broadened the Raman peaks.

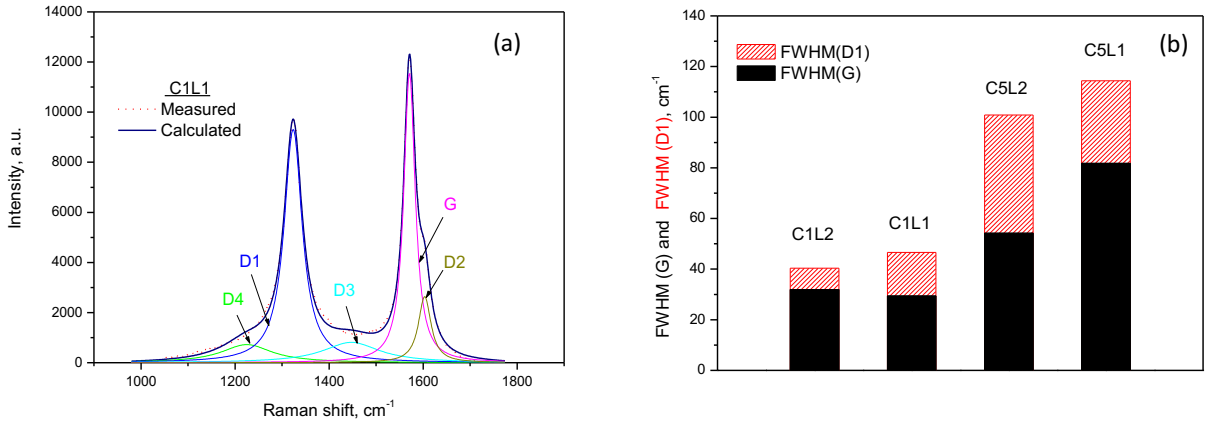

Figure 7.3.3 *(a) The deconvoluted first-order Raman peaks. Five peaks G, D1, D2, D3 and D4 were fitted according to reference [132]. (b) FWHMs of the G-peak (black) and D1-peak (red shaded).*

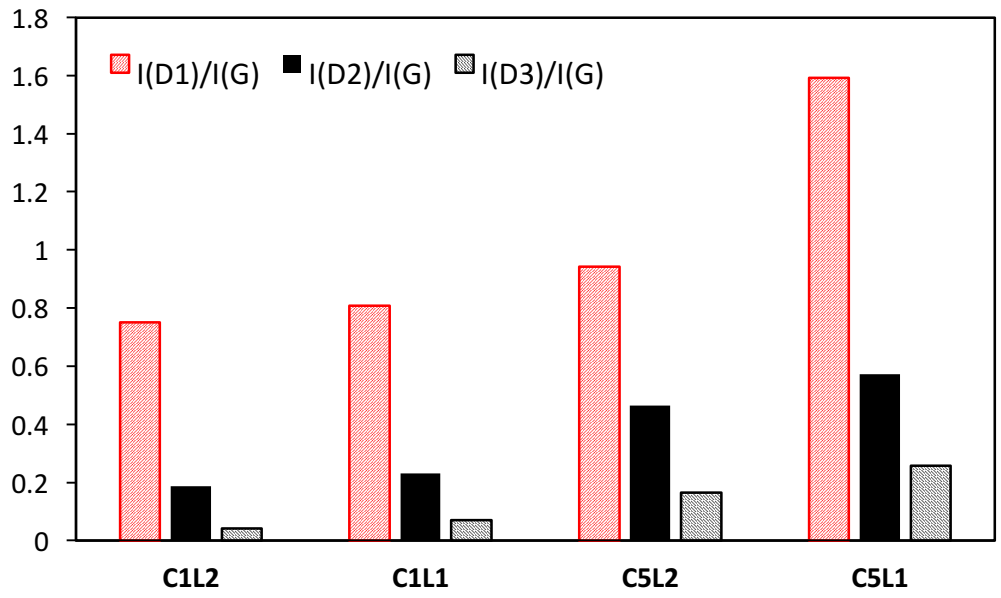

Figure 7.3.4 *The intensity ratios of D1-to-G peaks, D2-to-G peaks and D3-to-G peaks from the deconvoluted of Raman peaks.*

The D-to-G peak intensity ratio is a widely-used parameter for analysing graphitic structures, which has been applied in many references [129], [131]–[133]. As described in **Figure 7.3.4**, the highest *I(D1)/I(G)* is observed for the high-power plasma glow region carbons (C5L1) in comparison with the lowest intensity ratio for low-power downstream carbons (C1L2), of which the difference is caused by the diverse degrees of graphitic defects and various crystallite sizes based on the TK relation [129], [130]. In addition to the D1-peak and the G-peak, another Raman D2-peak at 1620 cm^{-1} is observed in **Figure 7.3.3 (a)** and **Figure 7.3.1**, especially for the C1L2 carbon. The appearance of this peak is related to the surface graphene layer of graphite with deformed E'_{2g} vibrations [134], and it is also believed to correlate with the distorted sandwich graphene layers by defects. Sze et al. [134] discovered that samples with more intense D2-peaks had higher surface-to-volume ratios, suggesting the composition of thinner graphitic domains. C1 plasma carbons have lower values of *I(D2)/I(G)* among the samples in **Figure 7.3.4**, signifying the less distorted graphitic structures and the larger crystallite sizes, which is in good accordance with the *I(D1)/I(G)* trend.

Figure 7.3.4 also describes a D3-peak that was found to be irrelevant to the graphitic structures [135]. The identification of the D3-peak is relevant to the impurity composition of bulk carbon samples, referring to the possible organic residues of oxidation or hydrogenation during the production; the occurrence of some such products is evidenced by the odour of the carbon-rich product. The C1 carbons are observed to have lower *I(D3)/I(G)* than the C5 carbons, which suggests that the low-power plasma reactor produces a higher proportion of graphitic contents. Of the two collection regions of carbon samples during the plasma production process, the downstream site L2 is preferred for better crystalline structures of carbon products. This is because the downstream collection results in a longer residence time and sufficient energy for activated species to react and combine, thus enhancing the formation of graphitic ordering. The D4-band at around 1200 cm^{-1} at lower phonon energy was reported to match the fingerprint of transpolyaceylene-like structures (TPA), such as the C-C and C=C stretching vibration modes, according to the work of Osipov et al. [132]. The TPA-band was also observed by Ferrari et al. [136], who found that related peaks were combined with the two peaks of 1150 cm^{-1} and 1450 cm^{-1} in nanocrystalline diamond into sp^2-bonded structures of trans-polyaceylene segments at grain boundaries and surfaces. The D4-peaks are observed to be more prominent in high-power *C5* carbons (see **Figure 7.3.1**), which is

because the higher energy plasma input bombarded the carbon into smaller grains, further enhancing the TPA effects at the boundaries.

The intensities of second-order *2D*-peaks at 2700 cm^{-1} were found to vary significantly among the four plasma carbons as described in **Figure 7.3.1**. Cuesta et al. discovered that the *2D*-peaks were less intense in nano-crystallite structures in contrast with highly ordered graphitic structures [135]. The 2*D*-peaks were further deconvoluted by Ferrari et al. into two 2D-peaks with another one located just at 50 cm^{-1} lower wavenumber that was intensely present in the spectra of a single graphene sheet [137]. Ferrari also observed that the 2D-peak at higher wavenumbers dominated the peak intensity and significance, when the stacking number of graphene sheets was over ten [137], indicating the larger sizes of crystallites in the c-axis by higher intensities, which is in accordance with the characterisation in **Figure 7.3.1**.

In summary, both the first-order and second-order Raman peaks show the consistent trend that C1 carbons produced with the low power input of 1.5 kW exhibit better graphitic structures, both in having larger crystallite diameters and enhanced c-axis ordering of stacked graphene sheets, than the high power (5 kW) C5 carbons. For the carbons produced from the plasma reactor with the same power input, downstream collection is preferred for better crystalline structures. C1L2 carbons evidently had the best degree of crystallinity among the plasma carbons, followed by C1L1, C5L2, C5L1 in order of decreasing degree of graphitic order.

7.3.2 X-ray diffraction of plasma carbons

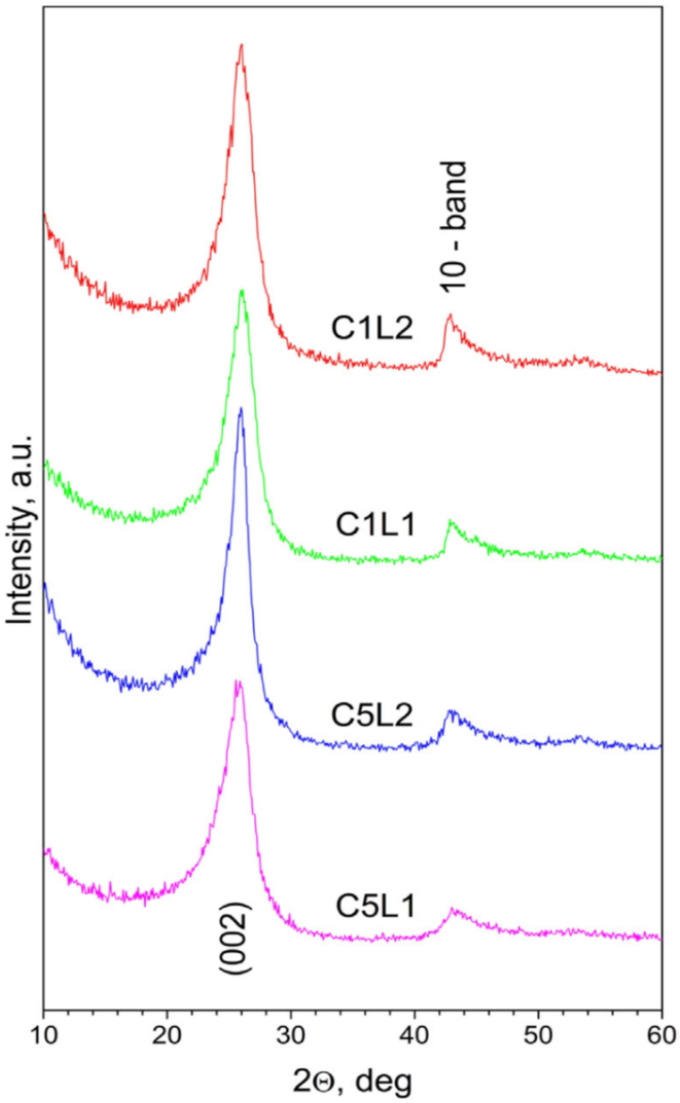

Figure 7.3.5 *The XRD patterns of plasma carbons: C1L1, C1L2, C5L1 and C5L2.*

Figure 7.3.5 shows the X-ray diffraction (XRD) patterns of the plasma carbons [112]. The appearance of (002) peaks at $2\theta{\sim}26°$ and (10) peaks at $2\theta{\sim}43°$ demonstrate the existence of graphite-like structures in plasma carbons. The width and relative intensities among peaks in comparison with reference patterns of graphite [138] suggest the lack of 3D crystalline ordering of the plasma carbons.

The average crystallite size $L_{\mathrm{a}}(XRD)$ of the graphitic planes is calculated from the profile fitting of the (10)-peak in XRD patterns. It is also understood that the mean crystalline size $L_{\mathrm{a}}(Raman)$ could be evaluated in terms of the TK relation [129], [130], with the coefficient stated in reference [130], based on the relative intensity ratio of *I(D1)/I(G)* in Raman spectra.

The $L_a(Raman)$ was plotted against $L_a(XRD)$ in **Figure 7.3.6**. Although the FWHMs of the (10)-peak applied in Scherrer's equation for $L_a(XRD)$ was not well defined due to the low peak intensities, it can be concluded that the $L_a(XRD)$ is correlated with the $L_a(Raman)$, which supports the validity of applying the TK equation to the Raman spectra of plasma carbons.

Although the quantitative analysis of the parameters, e.g. electron densities and energy distributions, are not available for plasma carbons, it can be speculated, in terms of the spectroscopic characterisations of both Raman and XRD patterns, that the low power input is advantageous to the formation of the crystalline ordering of plasma carbon particles and the large crystallites. The plasma carbons with more graphitic structures can be favourable for applications that require a high degree of crystallinity.

A higher power input for the plasma reactor leads to more nanocrystalline structures and a smaller particle size, especially for the carbons collected around the glow region (L1), because of the introduction of bond angle defects and graphitic sheet distortion. The potentially high surface-to-volume ratios of these carbons are preferred for applications that require high surface energies, e.g. water purification, catalyst substrates and gas adsorption.

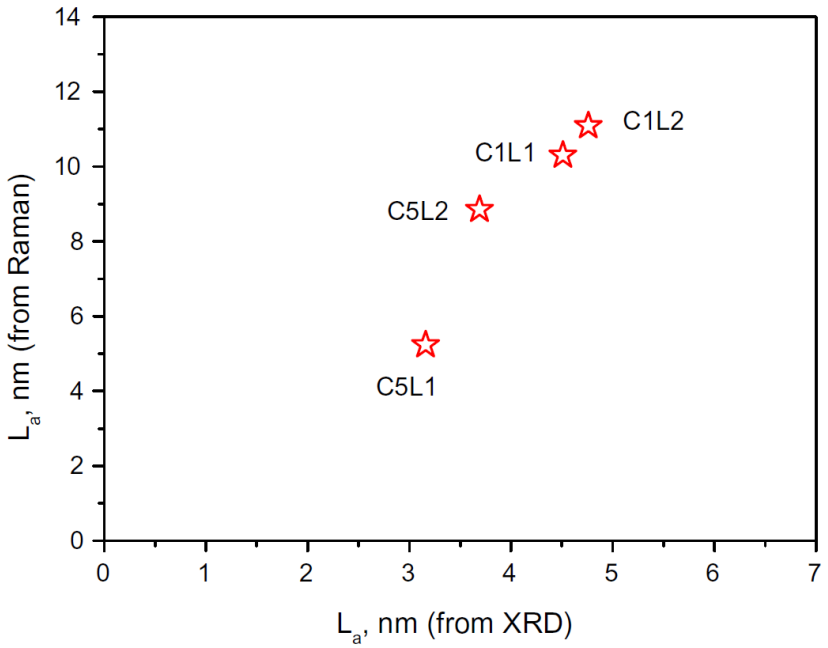

Figure 7.3.6 *The graphitic layer sizes (L_a) obtained from Raman results versus the graphitic layer sizes (L_a) obtained from XRD analysis.*

7.3.3 Raman spectroscopy of biochars

The dominant content of *Miscanthus* is cellulose, of which several vibrational modes are potentially Raman active [139], as described in **Figure 7.3.7**. The high composition of hydrocarbons in the raw materials leads to a fluorescent background as seen in **Figure 7.3.7**, which was also observed in reference [140]. Although the Raman spectra were taken with a reduced power and a short accumulation time, the fluorescence is hard to avoid. The significantly broadened Raman peaks of the raw materials indicate the lack of crystallinity and the heterogeneous composition. The peak at around 1095 cm^{-1} is induced by the carbonyl stretching mode and the glycosidic stretching (-C-O-C-) vibration in cellulose, and the broader peak at around 1600 cm^{-1} is related to the presence of amorphous lignin according to reference [141].

The carbonisation process with increasing pyrolysis temperature starts with dehydration and the removal of functional groups containing oxygen, which is reflected with the significant reduction of peak intensity of the -C-O-C- stretching band. The oxygen groups (-O-C-) are detached prior to hydrogen contents (-C-H) in cellulose [142]. The residual hydrogen content in 300 °C still results in high-level fluorescent backgrounds that diminish at temperatures above 500 °C, as indicated in the Raman spectra.

A small sharp peak at around 1600 cm^{-1} starts to appear from a temperature of 300 °C, which is likely to be related to the Raman peak of lignin at 1600 cm^{-1} becoming apparent after the reduction in the background. Although bulk graphitic structures are unlikely to appear in this range of temperatures, this could also be partially linked with small fragments of sp^2 carbon chains that develops with the increase of the pyrolysis temperature and the removal of oxygen in C-O groups, which brings E_{2g} vibrations at 1580 cm^{-1}. The peak at 1350 cm^{-1}, which is strictly connected to the breathing mode vibration of six-fold rings, starts to be detected from 400 °C. In terms of the pyrolysis model in reference [143], small stacks of aromatic molecules can form because of “polymerisation, dehydrogenation and condensation” in the early stages of carbonisation. These stacks can be graphitic-like, consisting of small size graphene-like layers possibly with five-fold or seven-fold rings [144].

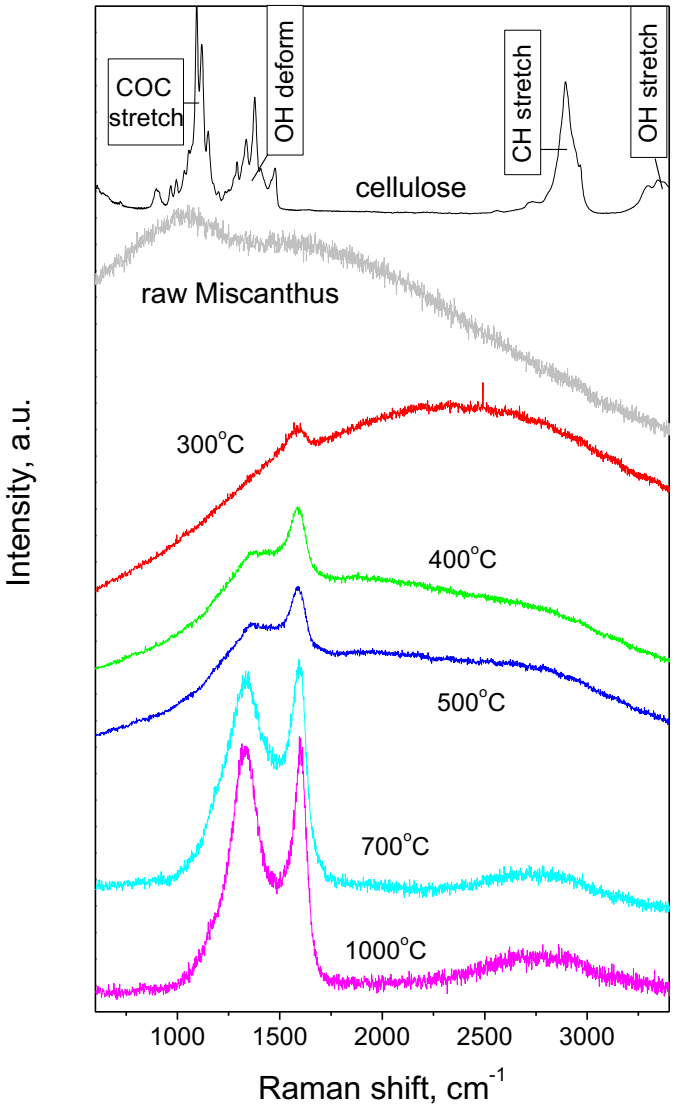

Figure 7.3.7 *The Raman spectra of biochars from pyrolysed Miscanthus at 300 °C, 400 °C, 500 °C, 700 °C and 1000 °C. A reference spectrum of pure cellulose is also presented [141].*

The growth of graphitic structures (sp^2 clusters) can be treated as an increasing number of hexagonal rings transformed from fused five or seven-fold rings as the pyrolysis temperature increases. This is further confirmed with the development of the intensity ratio of D-to-G peaks (see **Figure 7.3.4**), which was also observed in references [133], [144]. It is in opposite progression with the TK equation due to the high degree of amorphisation that introduces small crystallites, which has been studied by Ferrari and Robertson [129], since the TK equation is only capable for graphitic structures with crystallite size larger than 2 nm. The breadths of the D-peak and G-peak at low pyrolysis temperatures are broad and contributed by multiple phases, e.g. ~210 cm^{-1} for D-peak and ~90 cm^{-1} for G-peak at 500 °C. The degree of graphitic disorder decreases with higher carbonisation temperatures, e.g. ~150 cm^{-1} in

width for D-peak and ~50 cm^{-1} in width for G-peak at 1000 °C, which is in good accordance with the investigated behaviours of carbonised cellulose and lignin [142].

In summary, the Raman spectra of the biochars reveal an amorphous phase with highly disordered graphitic-like structures and a low degree of crystallinity. The intensity ratios of *D*-to-*G* peaks increases with the growing crystallinity and the growth of carbonisation temperatures, which is opposite to the TK equation due to the amorphisation of carbons but fits well with the "amorphisation trajectory" based on the work of Ferrari and Robertson [129], as discussed later in section 7.3.6.

7.3.4 X-ray diffraction of biochars

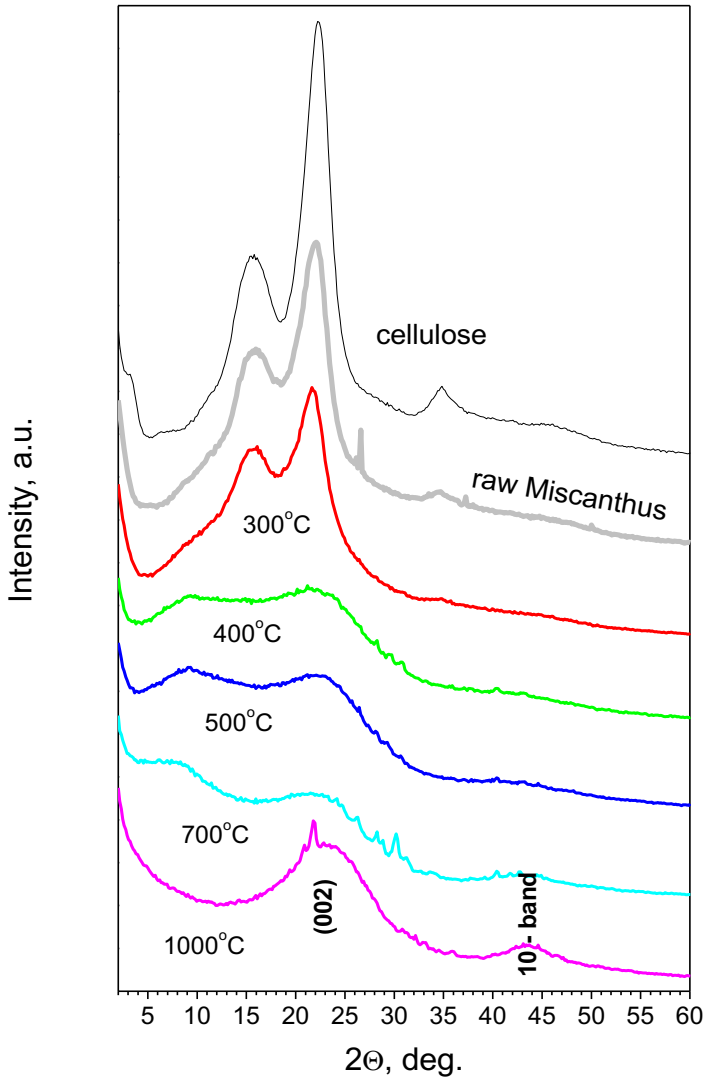

Figure 7.3.8 *The XRD patterns of biochars from pyrolysed Miscanthus at 300 °C, 400 °C, 500 °C, 700 °C and 1000 °C and pure cellulose.*

The X-ray diffraction patterns for raw Miscanthus, pure cellulose and biochar pyrolysed at temperatures from 300 °C to 1000 °C are plotted in **Figure 7.3.8**. The XRD pattern of raw *Miscanthus* is in accordance with the XRD pattern of the pure cellulose but with reduced peak intensities and increased peak breadth, suggesting the high proportion of amorphous phases. In a similar way to the Raman analysis, the graphitic (002) peak is hardly recognisable until the sample is pyrolysed at 400 °C, which suggests that graphitic layer stacking cannot occur below 400 °C. The broad (002) peaks at around 23° and (10) peaks at 43° of the biochars with low pyrolysis temperatures reflect highly disordered pre-graphitic materials in an amorphous matrix.

It is noticed that a peak at about 9° appears with the increase of pyrolysis temperature, reaching maximum intensity at 500 °C. Then the peak disappears with the further rise of temperature, becoming unrecognisable at 1000 °C. This phenomenon was also observed in references [145]. The occurrence of this small angle peak is related to the formation of discotic phases (also called turbostratic intermediate structures) that are formed as a precursor for graphitic structures during carbonisation [145], [146], which well explains its disappearance at high temperatures.

The heterogeneous background from the amorphous structures and the non-decomposed lignocellulosic contents makes the estimation of the peak positions and peak widths complicated. The XRD patterns were analysed with profile fitting, and the interplanar *d*-spacing was calculated based on Bragg's law. In terms of the deconvolution of the broad (002) peaks at 1000 °C in **Figure 7.3.9 (a)**, a γ-band peak with high intensity was characterised at 23° in addition to the typical (002) peak at 26°. According to reference [146], the γ-band is attributed to the presence of saturated phases like aliphatic size chains along the edge of the char crystallites [146].

The *d*-spacing of (002) planes reduces from ~0.4 nm at 500 °C to ~0.38 nm at 1000 °C as described in **Figure 7.3.9 (b)**. Furthermore, the (002) peaks were discovered to be sharper at higher pyrolysis temperatures, reflecting larger crystallite sizes along the c-axis. The crystallite sizes L_c of biochars pyrolysed from various temperatures are less than 2 nm. Thus, the biochars are regarded to have a low degree of crystallinity, which can also be concluded from the broad XRD peaks, even at 1000 °C.

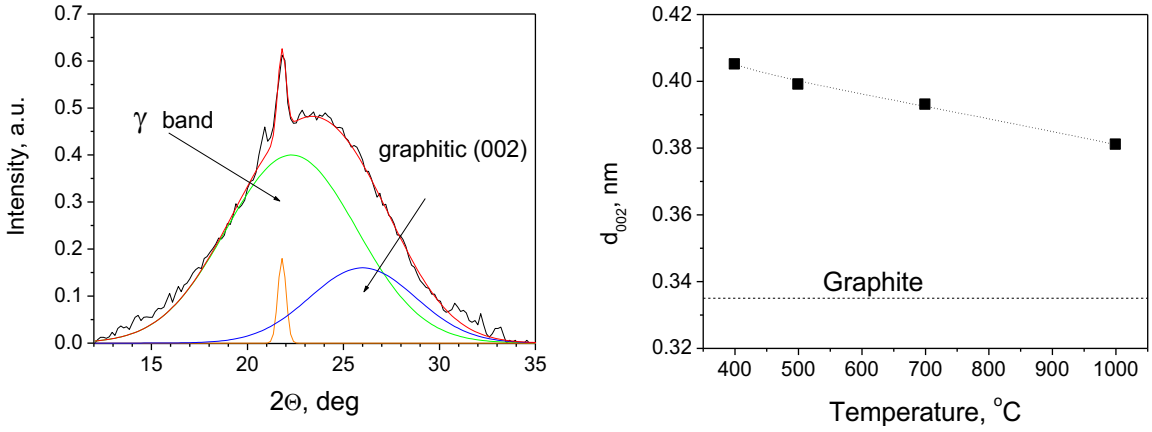

Figure 7.3.9 *(a) (002) peak deconvolution of 1000 °C biochar XRD. (b) The calculated (002) interplanar distances of biochars versus the pyrolysis temperature.*

7.3.5 FTIR and XPS analysis of biochars

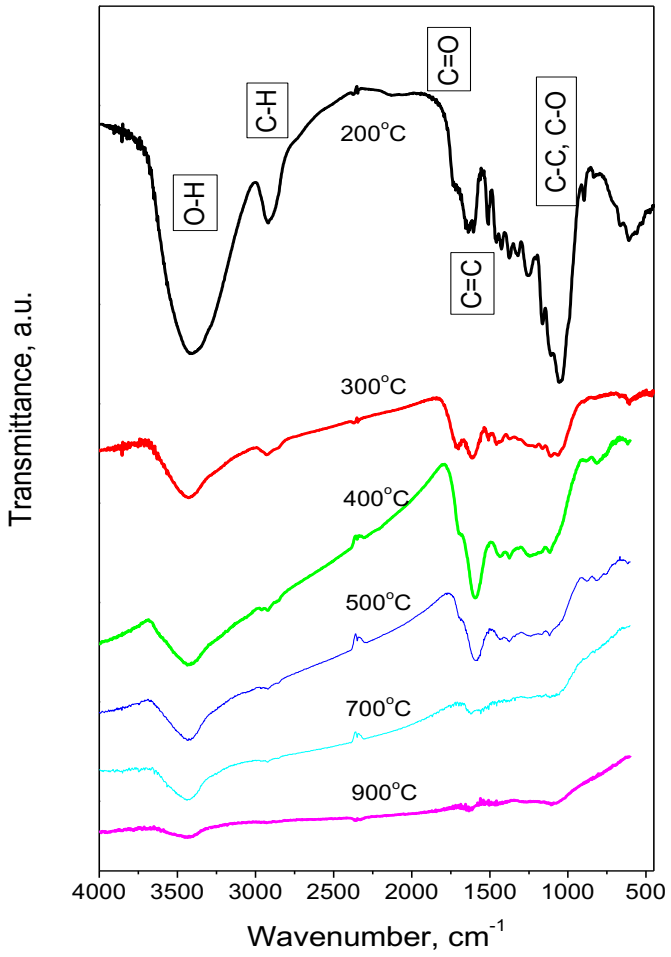

Figure 7.3.10 *The FTIR spectra of biochars pyrolysed in different temperature conditions.*

Infrared spectroscopy (IR), as presented in **Figure 7.3.10**, was applied to identify the existing stages of the functional groups, e.g. C-O, O-H, etc., during the carbonisation process. It is obvious that functional groups originating from the lignin and cellulose contents of the raw material dominate the IR transmission spectra at low temperatures. The significant band around 1600 cm^{-1} is attributed to the stretching vibration of the C=C bond which is polarised by the oxygen atoms attached. The carboxyl C=O groups are removed at low temperatures, while the hydroxyl and methylidyne radicals are more thermally stable. In addition, the C-O bonds are believed to be eliminated at early stages since their presence is not detectable at temperatures above 400 °C. These results provide substantial evidence to confirm the understanding from the previous Raman and XRD patterns. The carbonisation of the *Miscanthus* is basically a process of transforming the organic-dominated phases into better organised aromatic structures, then further into six-fold graphitic structures with increasing pyrolysis temperature.

The FTIR results also match well with the Krevelen diagram from the work of Ishmaru et al. [142] that the hydrogen and oxygen-rich contents are strongly removed during the pyrolysis process. The existence of O- and H- groups is beneficial to the construction of non-six-fold rings and distorted graphitic rings, which can potentially increase the surface areas and porosities of carbon products.

The high resolution C1s and O1s XPS spectra are displayed in **Figure 7.3.11**. A rapid reduction in the peak intensities of oxygen groups (C-O, C=O, C-O-H) is straightforwardly observed in C1s spectra at low pyrolysis temperatures in accordance with the assignment described in **Figure 7.3.12 (c)**, which further supports the previous analysis of the FTIR results. This aspect is also demonstrated in the O1s spectra with the faster decrease of C-O peak intensities at 533 eV relative to C=O peaks at 531.2 eV with increasing temperature. Along with the reduction in oxygen content with the increase of temperature, the peaks related to carbon-carbon groups (C=C, C-C at 285 eV) progressively become more prominent.

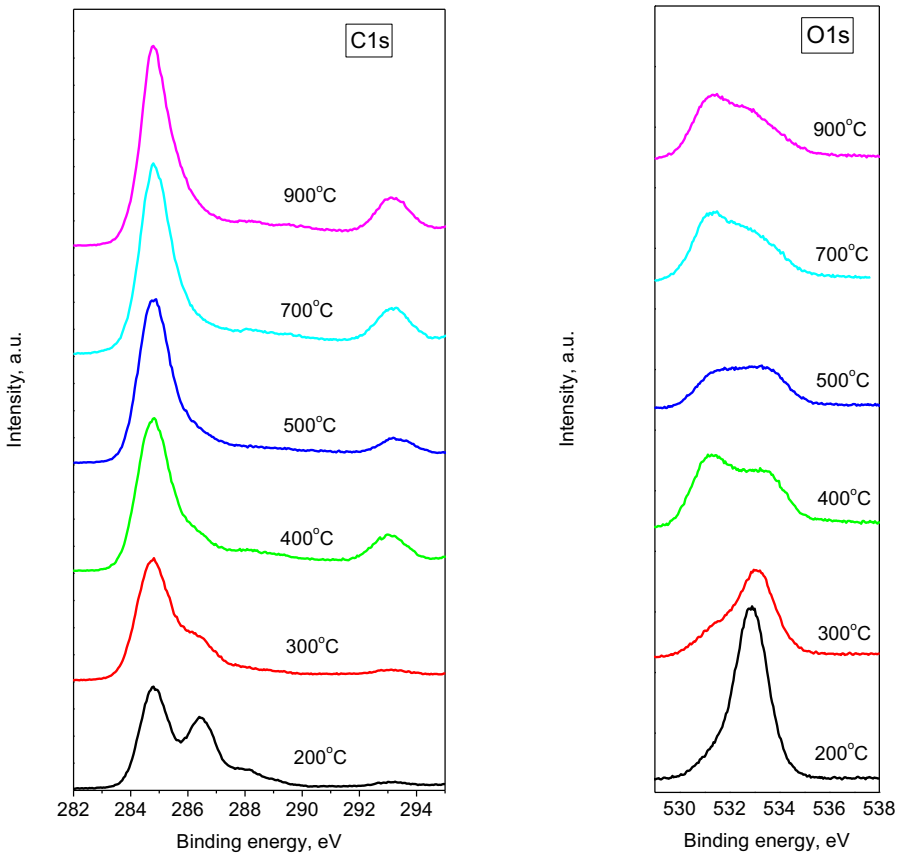

Figure 7.3.11 *High resolution XPS (a) C1s and (b) O1s spectra of biochars.*

7.3.6 Formation routes of plasma carbons and biochars based on the "amorphisation trajectory"

With the aim of discovering the differences between the two types of carbon structure studied, the comparative XRD patterns and Raman spectra for the plasma carbons and biochar pyrolysed at 1000 °C, as well as the XPS spectra (for biochar, at 900 °C), are exhibited in **Figure 7.3.12**. As shown in **Figure 7.3.12 (a)**, the XRD (002) peak of the biochar sample is not only shifted to a lower angle, indicating a larger *d*-spacing between graphitic layers, but also much broader as a result of the less degree of crystallinity, by contrast with the plasma carbon. Although the *I(D)/I(G)* of the Raman spectra are similar for the two carbons, the 2D-peak differs dramatically in both breadth and intensity, which reveals obvious differences in structural ordering, especially the c-axis stacking order.

The XPS spectra in **Figure 7.3.12 (c)** and **(d)** demonstrate the difference in surface bond chemistry, especially the traces of oxygen functional groups. The composition of oxygen is noticeably higher in the biochar, based on the C1s comparison. Furthermore, the peaks related to C-O groups in O1s also have clearly higher intensities for the biochars than the plasma carbons. The high oxygen content during carbonisation is not favourable for the formation of graphitic structures, as the existence of oxygen crosslinks within carbons can constrain both the layer growth and the layer stacking, thus preventing high degrees of graphitisation [147]. The high content of oxygen in the biochar is likely to be caused by an insufficient pyrolysis temperature, since it has been reported that a high degree of graphitisation is not expected at temperatures below 2000 °C [147], [148]. Additionally, the possible crosslinks introduced by oxygen contents also increase the difficulty of their removal.

In terms of the TK expression [129], [130], the intensity ratio of *D*-to-*G* peaks is inversely proportional to the crystalline size ($I(D)/I(G) \propto 1/L_a$) for nanocrystalline carbons, as illustrated in **Figure 7.3.13**. The plasma carbons are well explained by the TK equation in terms of the discussion in this study, while the biochars that are far less crystalline and graphitic exhibit a reverse tendency to the TK relation in accordance with the previous XRD and Raman results so that the TK equation is no longer valid in these situations. The substantial differences between the plasma carbons and the biochars (see **Figure 7.3.12**) in XRD, Raman and XPS confirm that the crystallinity differs significantly. This phenomenon coincides well

with the Ferrari and Robertson (FR) model [129], [131] that the TK relation cannot explain the amorphous carbons with crystallite sizes less than 2 nm. Instead, the intensity ratio was observed to be proportional to the square of crystallite size ($I(D)/I(G) \propto L_a^2$), as shown in **Figure 7.3.13** for amorphous carbons. Thus, the biochars are likely to be located in the region of amorphous carbons with smaller crystallite sizes, whereas the plasma carbons are nanocrystalline structured with larger lattice sizes.

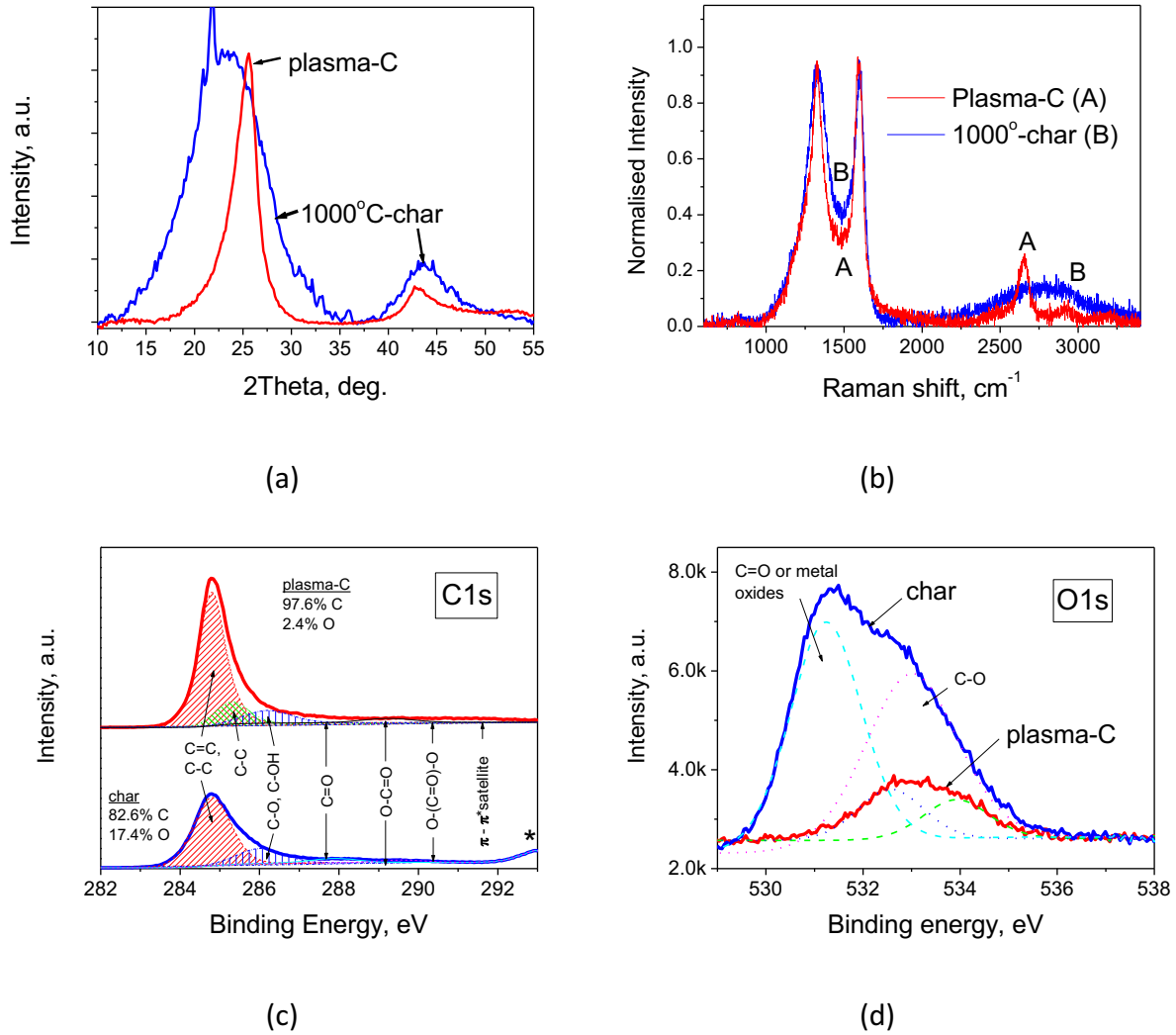

Figure 7.3.12 *Comparison of (a) XRD, (b) Raman, and XPS (c) C1s and (d) O1s spectra of plasma-carbon and biochar from 1000/900 °C – pyrolysis.*

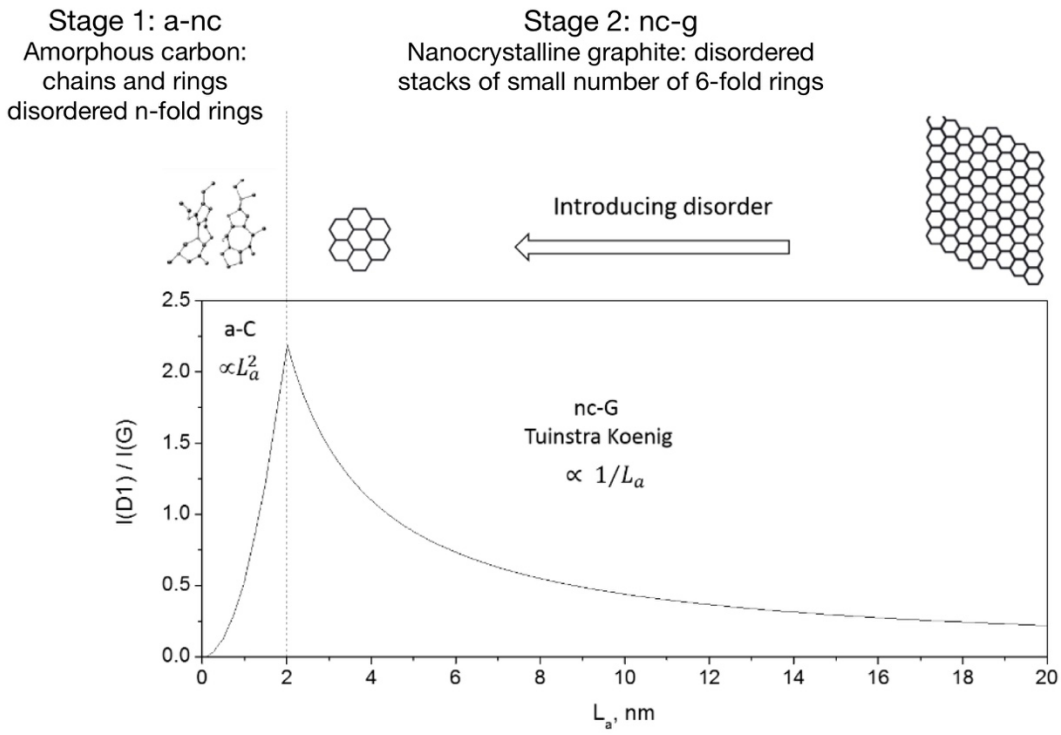

Figure 7.3.13 *Illustration of the concept of "amorphisation trajectory" [129], [130]. The structural transition in stage 1 from amorphous phase to nanocrystalline phase (a-nc) and in stage 2 from nanocrystalline phase to pure graphite (nc-g).*

As presented in **Figure 7.3.14**, the results for both plasma carbons and biochars can be compiled into a data set of $I(D)/I(G)$ versus L_a. The blue dashed line illustrates the theoretical curve from the FR model [129], [131], and the solid black line is based on the TK equation [130]. It is evident that both the plasma carbons and the biochars are in good agreement with the theoretical model, except the biochar at 1000 °C that is located on the "demarcation line" between the two regions. It is understood that carbons with L_a of around 2 nm is not organised with the FR theory of which the validity limit has been not clearly defined in this region. It is also worth noting that the calculation of L_a based on the XRD pattern can be less reliable and more complicated for small crystallite sizes and amorphous structures, since the peak intensity is lower and the profile is less recognisable [149], especially for non-graphitising carbons with misaligned defective layers and crosslinks [144], [147], [150].

The crosslinked structures are favourable for inducing porous structures in carbons, which can be beneficial for gas purification and storage. The contamination of inorganic materials

can catalytically induce graphitisation upon annealing to form non-porous carbons [151]. Sometimes, the polymer originated non-graphitising carbons can be activated into graphitising carbons under high temperature treatment, e.g. over 2000 °C, resulting in a heterogeneous phase of both pre-graphitic structures and non-graphitising structures [152].

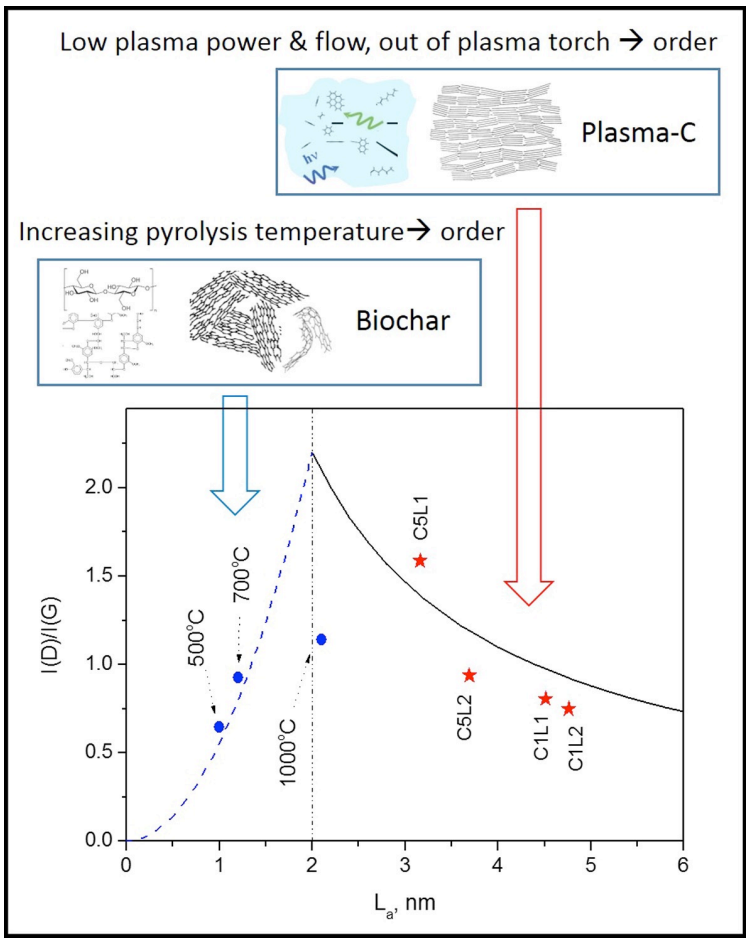

Figure 7.3.14 *Relation between the Raman D-to-G band intensity ratio and the graphitic layer diameter L_a of plasma-C (red stars) and biochar (blue circles). The solid line (black) represents the TK inverse proportionality dependence [130]; the dashed line (blue) follows the square root proportionality [129].*

It has been clear that the formation of plasma carbons under various conditions obeys the TK relation of the FR "trajectory theory" as shown in **Figure 7.3.14**. The mobile carbon and hydrocarbon ions and radicals tend to be activated intensively in the high-power plasma reactor (5 kW), of which the recombination results in highly defective and amorphous structures. The existence of sp^3-bonds induced by layer distortions and the small crystalline sizes caused by the short residence time in the plasma glow contribute to the reduced

graphitic ordering of carbon products. On the contrary, the carbon products are more ordered with reduced power input (e.g. 1.5 kW) due to the lessened ion bombardment and prolonged residence time (e.g. downstream collection), which allows the carbon atoms to reform into a more graphitic and well-organised structure.

For the other type of carbon, the biochars, the structures are amorphous instead of nanocrystalline, which follows the FR theory with a reverse trend to the TK equation. During the carbonisation process, organic molecules connected with carbon atoms are gradually transformed into intermediate states and gas species by thermal decomposition. At low temperature (< 500 °C for instance), the biochar is highly amorphous with distorted structures and the lack of six-fold graphitic rings. With further heat treatment at higher temperatures, the disordered amorphous state can either be transformed into more ordered graphitic structures with larger crystalline sizes and better stacking order, or producing more distorted phases with better porous structures due to the existence of oxygen crosslinks [147].

7.3.7 Summary

From the research and discussions in this section, it can be concluded that the method of plasma reforming of methane can reform activated radicals into more organised graphite-like carbon structures, while the carbonised biomass from pyrolysis of *Miscanthus* demonstrates less-organised structures as a result of the existence of organic groups and possibly the lack of sufficient heat treatment.

The formation routes of two carbons in terms of the intensity ratio of Raman first-order D-to-G peaks confirm the validity of the "amorphisation trajectory" theory introduced by Ferarri and Robertson [129]. The profile (e.g. the breadth and the intensity) of second-order Raman 2D peak is critical for clarifying whether the carbon is ordered and nano-crystalline or disordered and amorphous, when the first-order peaks show limited features. In terms of the results and discussions presented in this study, the Raman characterisation alone can provide sufficient information to characterise the carbon materials for their degree of graphitisation and crystallinity.

Considering the plasma carbons, the low-powered reactor and downstream collection are preferred for obtaining products with better graphitic structures and higher crystallinity. For the pyrolysed biochars studied, the carbons show reliable indications of the existence of a

certain amount of distorted graphitic fragments and non-six-fold rings, although they are highly disordered even at the highest pyrolysis temperature of 1000 °C.

Although the Raman analysis of distorted graphitic structures indicates the potential for porous structures because of the oxygen group impurities, the BET surface areas of the pyrolysed carbons are characterised to be smaller than 20 m^2/g. The appearance of the small surface area can be due to the lack of an activation process. In the physical activation process, after the carbonisation of biomass, the pyrolysed carbons are activated in the presence of appropriate oxidizing gases, such as carbon dioxide [153] and steam [154], at high temperatures from 600 °C to 900 °C for a duration up to 40 hours [155], [156]. Sometimes, the carbonisation and activation processes can be conducted simultaneously with the heat of steam (700 °C – 800 °C) [155]. The other method is named as the chemical activation that requires the biomass to be impregnated with chemicals, such as H_3PO_4 [157], KOH [158] and NaOH [157], followed by heating under a nitrogen flow at temperatures from 450 °C – 900 °C of which the selection depends on the impregnant applied [156]. The carbonation and activation are also simultaneously performed in the chemical activation, and the duration required is generally less than 2 hours, which is comparably much short than the physical activation [156].

The plasma carbons are also non-porous samples with surface areas around 60 m^2/g, although they are observed to be very lightweight in handling during the experiment. The lightweight particles of plasma carbons might illustrate the non-aggregated carbon particles that restrict the formation of pores in the interstitial spaces of packed small crystallites. H_2 cryosorption measurements of both the plasma carbon and the biochar pyrolysed at 1000 °C were also conducted, but the hydrogen uptakes were too small to be detectable above the measurement errors. As a result, the hydrogen adsorption isotherms of these carbons were not presented in this thesis.

7.4 The structural analysis of graphene nanoplatelets

7.4.1 X-ray diffraction analysis of graphene nanoplatelets

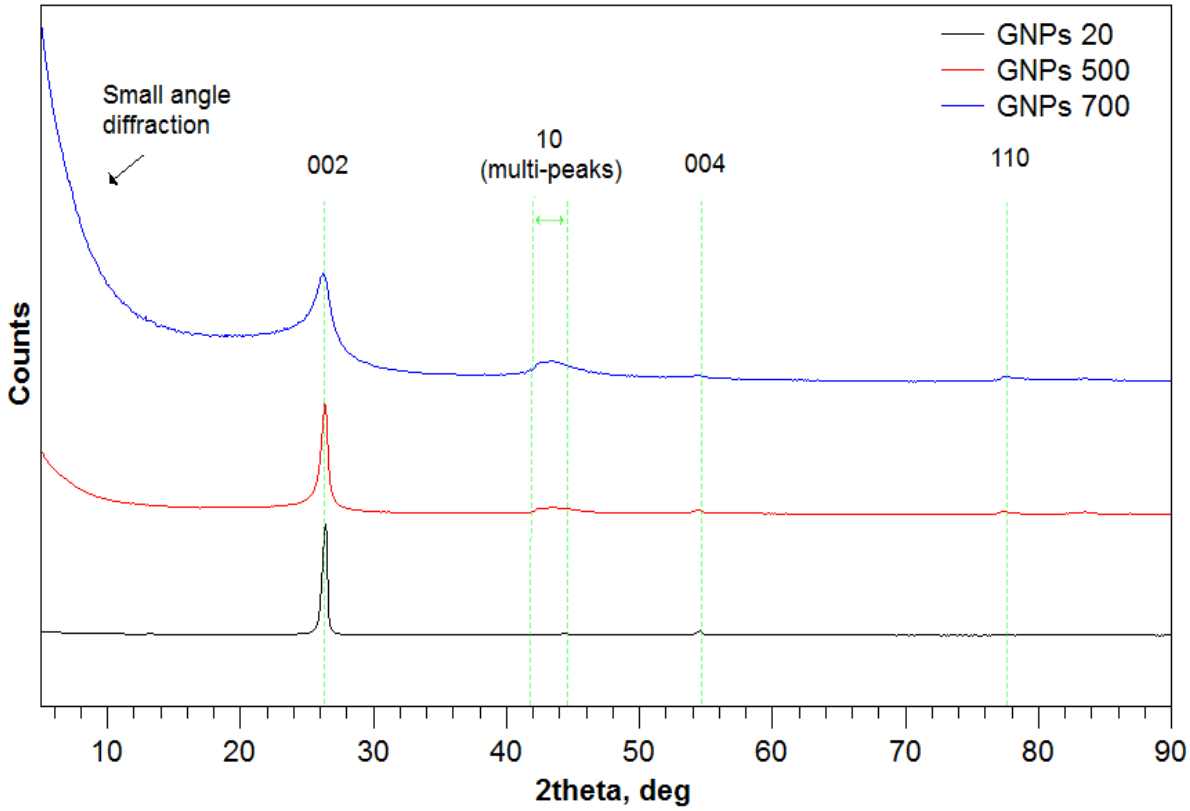

Figure 7.4.1 *X-ray diffraction patterns for graphene nanoplatelets GNPs-20, GNPs-500 and GNPs-700 with SSAs of 20 m^2/g, 500 m^2/g and 700 m^2/g, respectively.*

The graphene nanoplatelets (GNP) obtained from DZP Technologies have various surface areas (SSAs). As the available manufacturing details for the GNPs are limited, it is important to obtain a qualitative understanding of the materials prior to further quantitative analysis, such as the definition of crystallite sizes. According to the X-ray diffraction pattern shown in **Figure 7.4.1**, the GNPs-20 exhibits a dominant (002) peak, along with weak (10) peaks and a (004) peak, which is very similar to a type of two-dimensional turbostratic structure [116], [117], [138]. The sharp 002-peak is related to the high degree of graphitic structure in c-axis ordering. It is noticed that the 002 peaks of GNPs become broadened with increased surface area, indicating a reduced crystallite size in the c-axis. The broadened 002 peaks are commonly observed in turbostratic structures with small size layers obtained from ground pure graphite [159], [160]. The small-angle diffraction signal becomes intense with the

increase in surface area, and the intensity of small angle diffraction for GNPs-700 is even higher than the significant 002-peak, which is due to the increased dispersion of fine particles [161] and the presence of pores [162].

In contrast with the 002 peak shifting to a smaller angle, as in most ground graphite materials [159], [160] and low-rank coals [162], the 002-peak position of GNPs shows negligible variations with the decrease of crystallite sizes and the dramatic increase of surface area from 20 m^2/g to 700 m^2/g. The calculated interlayer spacing based on the 002-peak positions is ~ 0.338 nm, very close to the 0.3355 nm of single crystal graphite [163]. The non-shifting of 004 peaks further proves the uniform interlayer distances in GNPs.

The 10-band is deconvoluted into multiple peaks as shown in **Figure 7.4.2**. Three peaks are observed in all GNPs samples, including the graphitic 100 and 101 peaks. The appearance of a peak at ~43.3°, of which the breadth does not vary noticeably with different surface areas, is related to traces of silicon carbide (SiC) contents that is confirmed by analysis from Energy Dispersive X-ray spectroscopy (EDX) on isolated heavy particles in the bulk carbon materials. Additionally, a peak at ~46° only exists in GNPs-20 samples, which is related to the presence of oxygen and hydrogen contents during sample manufacturing, such as monobenzone structures. For the graphitic (100) and (101) peaks, the peaks are broadened with increasing surface area, which is a similar trend to the 002-peak, suggesting the simultaneous reduction of layer size with the shortened c-axis crystallite size.

The c-axis crystalline stacking dimension L_c and the graphitic layer dimension L_a are obtained using Scherrer's equation, which was also applied in references [117], [146], [164], as listed in **Table 7.4.3**. The L_a size of the GNPs are discovered to be larger than 5 nm, as shown in **Table 7.4.3**, further confirming the validity of Scherrer's equation in evaluating GNPs, according to reference [117]. The crystallite size of the GNPs reduces in both the intra-planar layer dimension and the c-axis crystallite size with the increase of surface area. Because single-crystal graphite has a very low surface area, which indicates that the interplanar spaces between adjacent graphitic layers cannot adsorb gas molecules, the increased surface areas of the GNPs-500 and the GNPs-700, in comparison with GNPs-20, are mainly due to the increased surface-to-volume ratio from the small crystallites and the interstitial pores formed

in the aggregation of fine particles, which are further revealed in the SEM pictures in section 7.4.3.

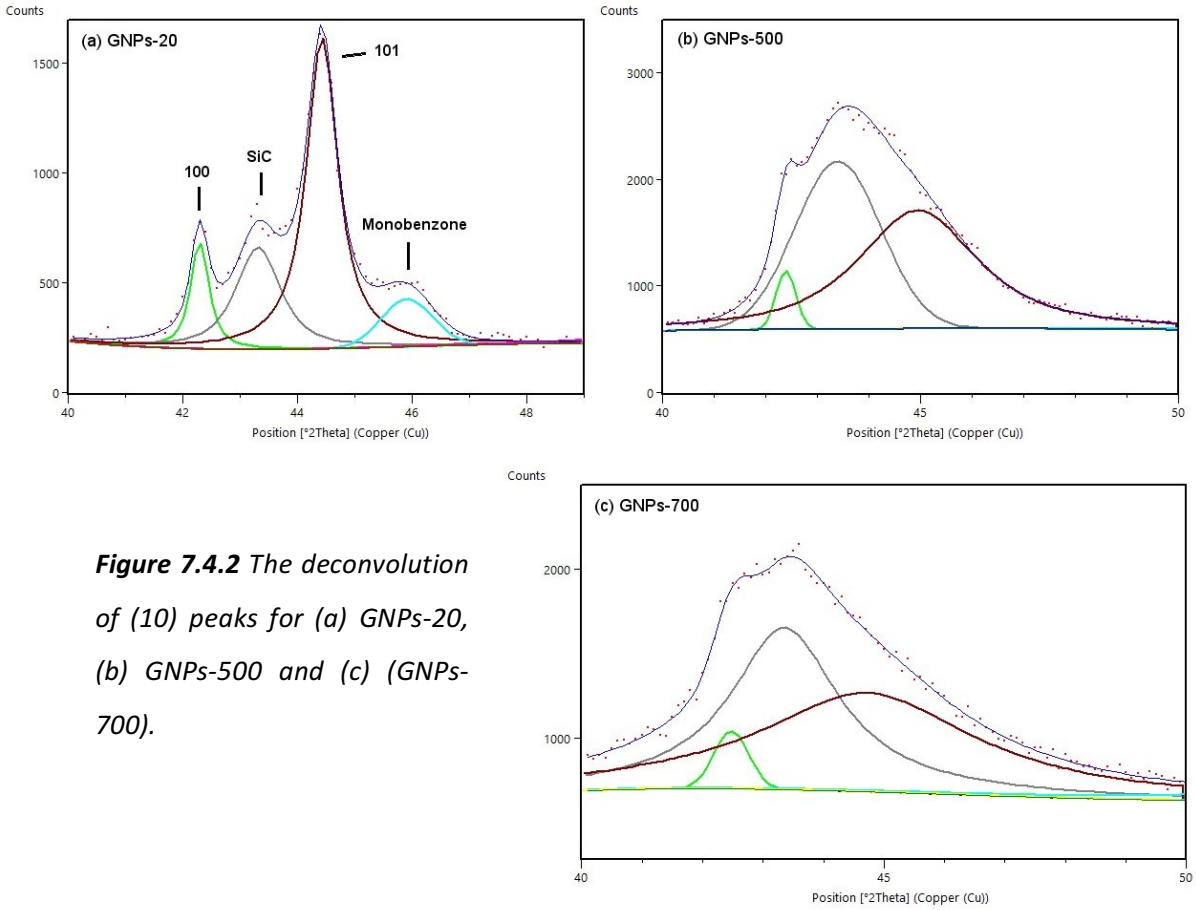

Figure 7.4.2 *The deconvolution of (10) peaks for (a) GNPs-20, (b) GNPs-500 and (c) (GNPs-700).*

In summary, the GNPs have significantly larger crystallite sizes and highly ordered layer stacking in comparison with amorphous carbons, such as activated carbons, and turbostratic structures, e.g. coals, but still displaying large surface areas. The reduced crystallite size of GNPs results in the increase of overall surface areas and the introduction of potential porous structures that were discovered in the previous BET measurements in section 7.1. By contrast with the amorphous porous carbons, such as activated carbons, the GNPs-500 and the GNPs-700 are far more crystalline, therefore having great potential as the substrate for doping catalytic groups to analyse related structural modification on the base carbon and as sorbents for gas adsorption due to their high surface areas.

Table 7.4.3 *The calculation of L_c sizes based on the 002-peak and of L_a sizes based on the 100-peak.*

	(002) position / ° 2θ	FWHM (002) / ° 2θ	L_c / nm	(100) position / ° 2θ	FWHM (100) / ° 2θ	L_a / nm
GNPs-20	26.35	0.42	19.3	42.27	0.25	56.8
GNPs-500	26.33	0.59	13.7	42.37	0.47	30.2
GNPs-700	26.2	1.52	5.3	42.5	0.81	17.5

7.4.2 Raman spectroscopy of graphene nanoplatelets

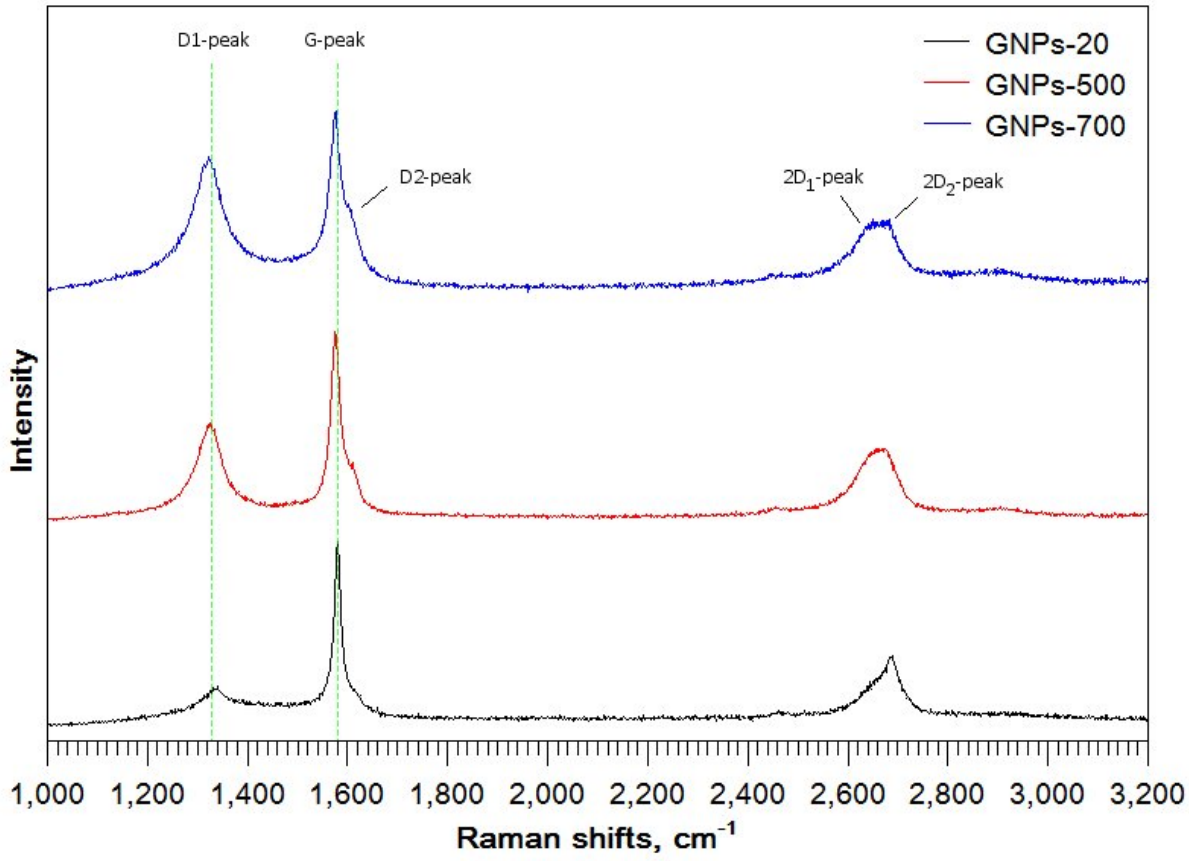

Figure 7.4.4 *Raman spectra of GNPs-20, GNPs-500 and GNPs-700.*

The Raman spectra of GNPs are presented in **Figure 7.4.4**. As the intensities of the first order G-peaks (1580 cm^{-1}) among GNPs samples have been adjusted to a similar level, it is clearly observed that the intensity ratio of D-peaks (1350 cm^{-1}) to G-peaks increases with the

enhanced surface areas. Referring to the previously discussed XRD patterns, the trend in the intensity ratios of D-to-G peaks follows the TK equation, in which the *I(D)/I(G)* increases with the reduction of graphitic layer dimension [129], [130]. The D2-peak, which has been observed in plasma carbons, can also be identified in the GNPs, and it is discovered to be more significant in the GNPs with higher surface areas. As shown in section 7.3.1, the presence of the D2-peak is related to the deformed E_{2g} symmetry in distorted graphene layers, e.g. some surface layers. It is also believed that some crystallite flakes in GNPs-500 and GNPs-700 contain bent graphitic layers, which is observed in the TEM pictures in section 7.4.3, further enhancing the deformed E_{2g} vibration.

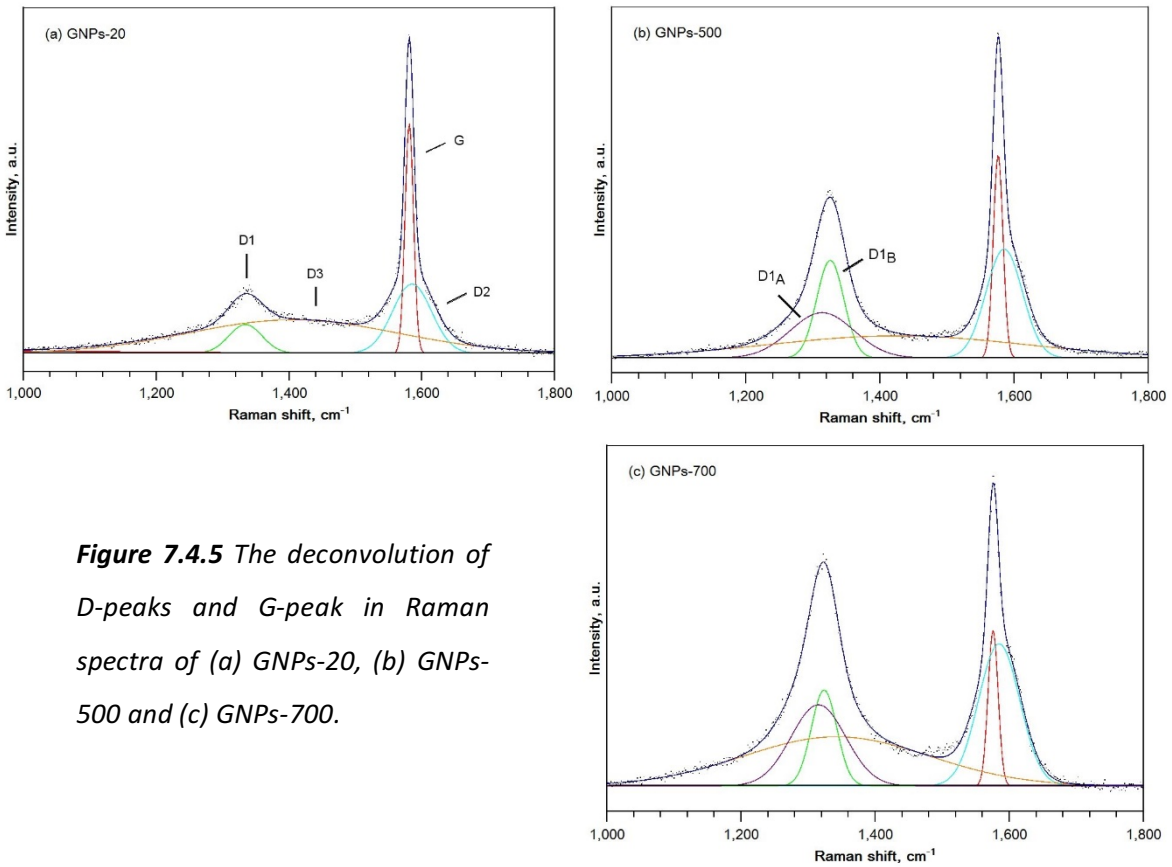

Figure 7.4.5 *The deconvolution of D-peaks and G-peak in Raman spectra of (a) GNPs-20, (b) GNPs-500 and (c) GNPs-700.*

The Raman spectra of GNPs around the D and G peaks region are deconvoluted in **Figure 7.4.5**. In addition to the intense D1-peak and G-peak, the D2-peak and D3-peak are exposed during profile fitting in the GNPs. Unlike the appearance of a single D1-peak in GNPs-20, a split in the D1-peak is observed in the high surface areas GNPs, which is caused by the presence of edge graphite around the grain boundaries of small crystallites [165]. These edge effects become progressively more apparent with the increased content of fine particles. The

D2 peak intensities are also enhanced with the growth in surface area by the boosted edge effects of distorted E_{2g} vibrations in surface layers. By contrast with the broadened peaks with increased disorder in biochars, the FWHMs of D-peaks and G-peaks show no substantial variation, indicating a similar structural ordering. The overall profile differences among GNPs are principally presented by the relative ratio deviations in between peaks, as indicated in **Figure 7.4.5**. The high surface areas of GNPs-500 and GNPs-700 are most likely created by the high surface-to-volume ratio of small crystallites. The high surface-to-volume ratios can also be illustrated by the growth in the D2-peak intensity in GNPs-500 and GNPs-700, according to Sze's research [134].

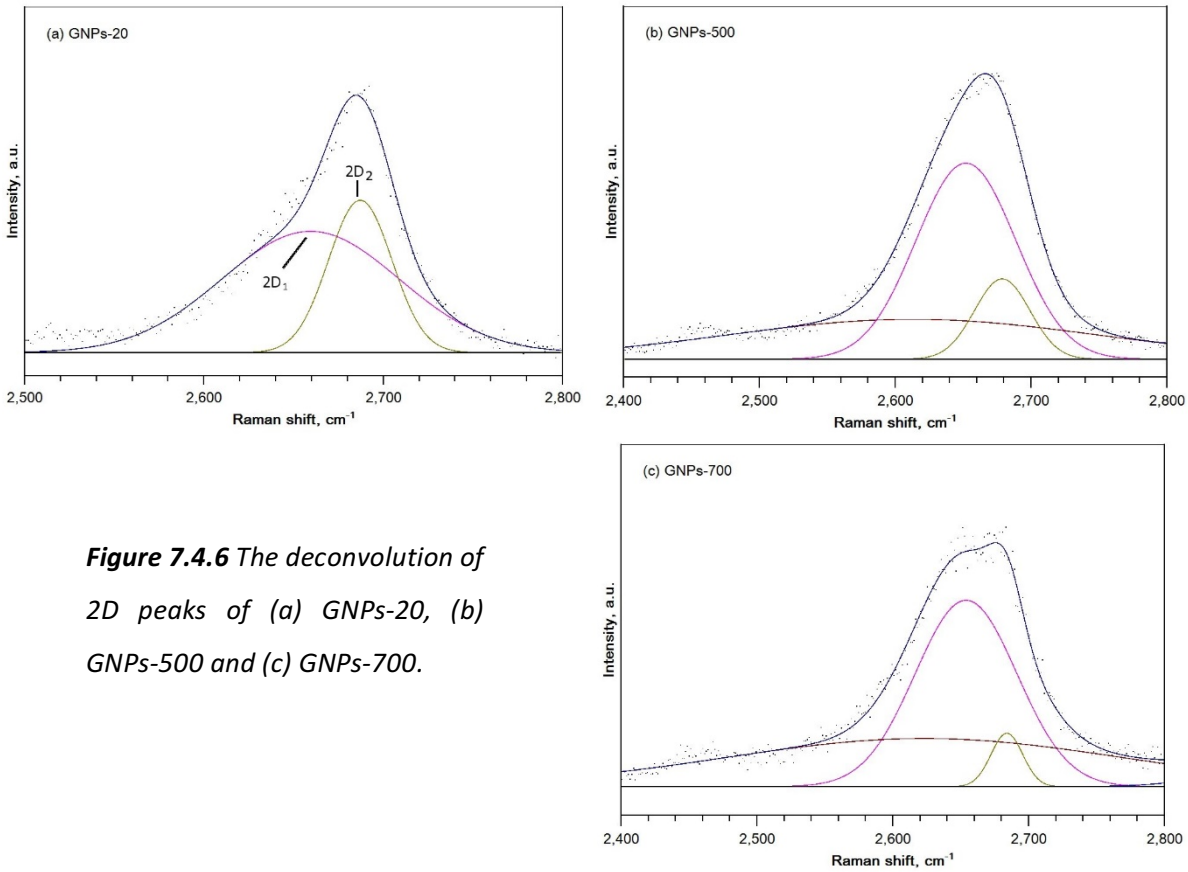

Figure 7.4.6 *The deconvolution of 2D peaks of (a) GNPs-20, (b) GNPs-500 and (c) GNPs-700.*

A distinctive characteristic appearance in the Raman spectra of the GNPs, by contrast with the previously studied plasma carbons and bio-chars, is the well-recognised doublet structures of 2D peaks at 2600 cm^{-1} – 2700 cm^{-1}, as shown in **Figure 7.4.6**. The doublet 2D-peaks occur in highly ordered graphene and graphite samples, but gradually disappear with the increase in disorder during the transition from the pure structure to the nanocrystalline

structure [165]. Thus, the appearance of doublet 2D-peaks clearly indicates the highly ordered graphitic structures of GNPs, which agrees with the XRD results that the interlayer distance is close to the value of pure graphite materials.

In previous works on graphene and graphite [165], a single layer of graphene was observed to have a single 2D peak at 2650 cm^{-1}, and the increased number of layers stacked from double layers will induce another peak with a growing intensity at a position 50 cm^{-1} higher. Exactly this type of overall profile variation is observed in the Raman spectra of GNPs, as interpreted in **Figure 7.4.6**. The broad peaks (wine colour) in both GNPs-500 and GNPs-700, which are not observed in GNPs-20 with large crystallites, are believed to be caused by the high content of fine particles and can be treated as a type of background. It is obvious that the $2D_2$-peak appears to be more intense and sharper than the $2D_1$-peak in GNPs-20, while both the GNPs-500 and GNPs-700 have a more intense and dominant $2D_1$-peak. The switch in dominance from the $2D_2$-peak to a $2D_1$-peak at lower wavenumber between the GNPs-20 and the GNPs with high surface areas is due to the reduced number of stacked graphitic layers. The further growth of the $2D_1$-peak in GNPs-700 is also noteworthy in comparison with GNPs-500, confirming a smaller number of staked graphitic layers in GNPs-700 crystallites than the GNPs-500.

The graphitic layer sizes L_a of GNPs can be calculated from the relative intensity ratio *I(D)/I(G)*. When the TK equation was first published in the 1960s, it was not clearly stated whether the deconvolution of Raman peaks was conducted in the early work. The peak intensities that were used in the derivation of TK equation were likely to be the overall intensity of all peaks at the rough position of D-peak and G-peak. For clarity, the calculations discussed in this study will include the raw intensities with background subtracted (*I(D1)/I(G)*), the intensity ratio of $D1_A$-peak to G-peak ($I(D1_A)/I(G)$) and the intensity ratio of $D1_B$-peak to G-peak ($I(D1_B)/I(G)$). Since no doublet D1-peaks are observed in GNPs-20, the same fitted D-peak intensity of GNPs-20 is implemented in the calculations of both $D1_A$ and $D1_B$ in **Table 7.4.7**.

Table 7.4.7 *List of calculated L_a sizes based on Raman results.*

	Raw		***D1$_A$***		***D1$_B$***	
	I(D1)/I(G)	*L_a* / nm	*I(D1$_A$)/I(G)*	*L_a* / nm	*I(D1$_B$)/I(G)*	*L_a* / nm
GNPs-20	0.20	21.84	0.13	35.18	0.13	35.18
GNPs-500	0.51	8.73	0.22	19.72	0.48	9.15
GNPs-700	0.75	5.90	0.52	8.44	0.62	7.15

By comparing the obtained results with the XRD analysis, it becomes clear that the differences among values acquired from different characterisation methods are significant. The XRD analysis of graphitic layer sizes is expected to be given an overestimate because of instrument broadening, which has not been subtracted. Since the peak intensity is very small for 100-peaks, the deconvolution of 100-peaks is considered to have an inherent amount of uncertainty, which makes the L_a calculations based on XRD analysis less reliable than those from Raman analysis. For the implementation of the TK equation on the Raman spectra, the results are more reliable, as the TK equation was calibrated with previous well-defined XRD results [130]. However, the method of obtaining the peak intensity is not clearly defined. **Figure 7.4.8** compares peak intensity definitions for all four derivations. The L_a obtained from the XRD analysis is roughly 2 – 3 times that from Raman spectra, which is also observed in the previous calculation for plasma carbons with similar difficulties in defining 10-peaks. Among these Raman calculations, the method of using raw intensities of peaks is likely to give the most accurate results, while both methods of using fitted D1$_A$-peaks and D1$_B$-peaks are noticeably inconsistent with each other except for GNPs-700. As the sizes of layers are unlikely to be uniformly distributed, the best compromise is to evaluate the layer sizes in a range of values. In conclusion, the GNPs-20 has the largest span of graphitic layer sizes of 20 – 35 nm, while GNPs-500 has a size in the range of 9 – 20 nm and the GNPs-700 has an approximate value of 6 – 8 nm.

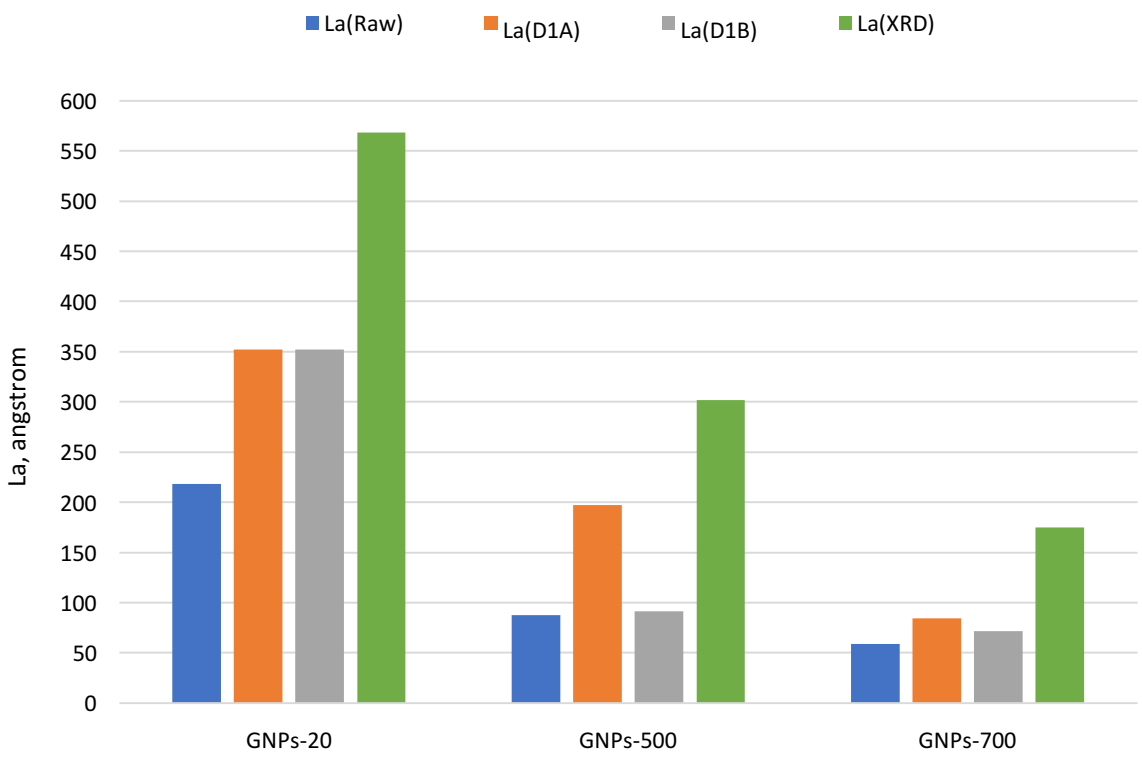

Figure 7.4.8 *The comparison of calculated L_a sizes using different characterisation methods.*

7.4.3 SEM and TEM micrographs of graphene nanoplatelets

It was concluded in the previous section that the GNPs with high surface areas have smaller crystallites, while GNPs-20 is expected to be more graphitic-like with larger grains, which is clearly confirmed by the SEM pictures in **Figure 7.4.9**. GNPs-20 seems to have glassy layers and fragments. On the contrary, the pictures of GNPs-700 reveal aggregations of fine particles on a nanoscale.

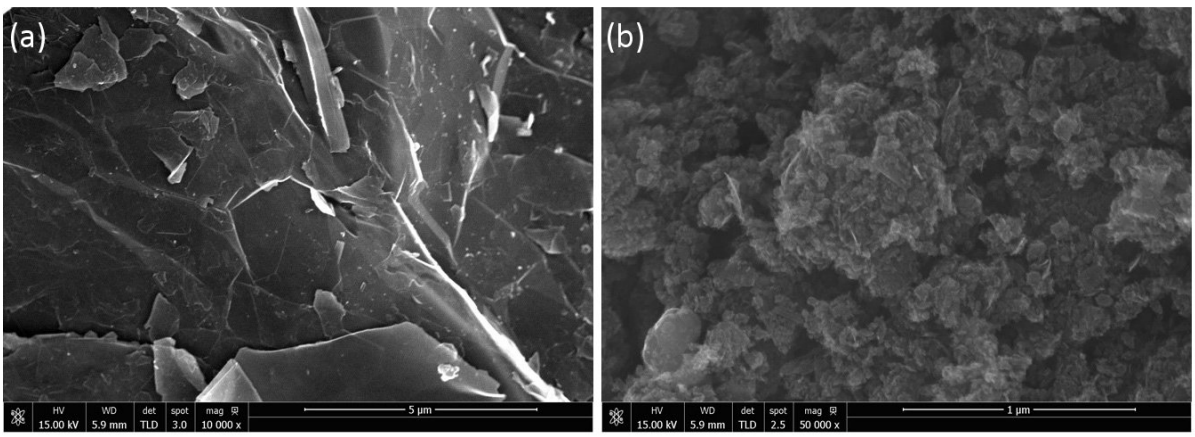

Figure 7.4.9 *SEM micrographs (secondary electron) of (a) GNPs-20 and (b) GNPs-700.*

High-resolution transmission electron microscopy (HRTEM) images of GNPs-20 is shown in **Figure 7.4.10 (a)**. Flat graphite ribbons with 100 nm – 150 nm in width and many larger flakes are clearly recognised. Since the number of stacked graphitic layers in GNPs-20 is expected to be several hundred according to the previous XRD analysis, the flakes are rigid, resulting in the absence of bent flakes, which agrees with the observation that the ribbon flakes display smooth edges and surfaces along the entire length. The stacking of graphene layers is further described as marked in **Figure 7.4.10 (b)**, and the ordered stacking can be as much as tens of nanometres in length, which is in similar order of magnitude as determined by XRD analysis. The ordered intra-planar distribution of carbon atoms is evident in high-magnification TEM images, as in **Figure 7.4.10 (c)**, which agrees with the results of mono-graphene layers [166], thin graphite flakes [167] and graphene nanoribbons [168]. According to the FFT analysis in **Figure 7.4.10 (d)**, the (100) planar distance is measured as 0.22 nm per cycle, very close to the (100) *d*-spacing of 0.24 nm in XRD patterns. The (110) is also less significantly indicated with roughly 0.13 nm per cycle, which is in good accordance with the position of weak (110) peaks in previous XRD analysis.

The estimation of hexagon dimensions and bond lengths of carbon atoms is conducted on the plot profile of **Figure 7.4.10 (f)** in regard to the red cross line (zigzag) through the hexagon centres as marked in **Figure 7.4.10 (c)**. In terms of the profile plot, the peaks of hexagon centres are periodically reached, and an accumulation of 13 cycles is obtained in the overall length of around 3.4 nm. The distance between the centres of two adjacent hexagons in the zigzag direction as described in **Figure 7.4.10 (e)** is estimated to be 0.26 nm. Considering the hexagonal geometry, the carbon-carbon bond length is around 0.15 nm, very close to the carbon bond length of 0.142 nm in graphite. The small variation of measured bond length in comparison with graphite can be explained by the resolution limit at high magnification, the possible non-flat arrangement of layers and local distortions in terms of the poorer crystallinity of GNPs-20 compared to graphite.

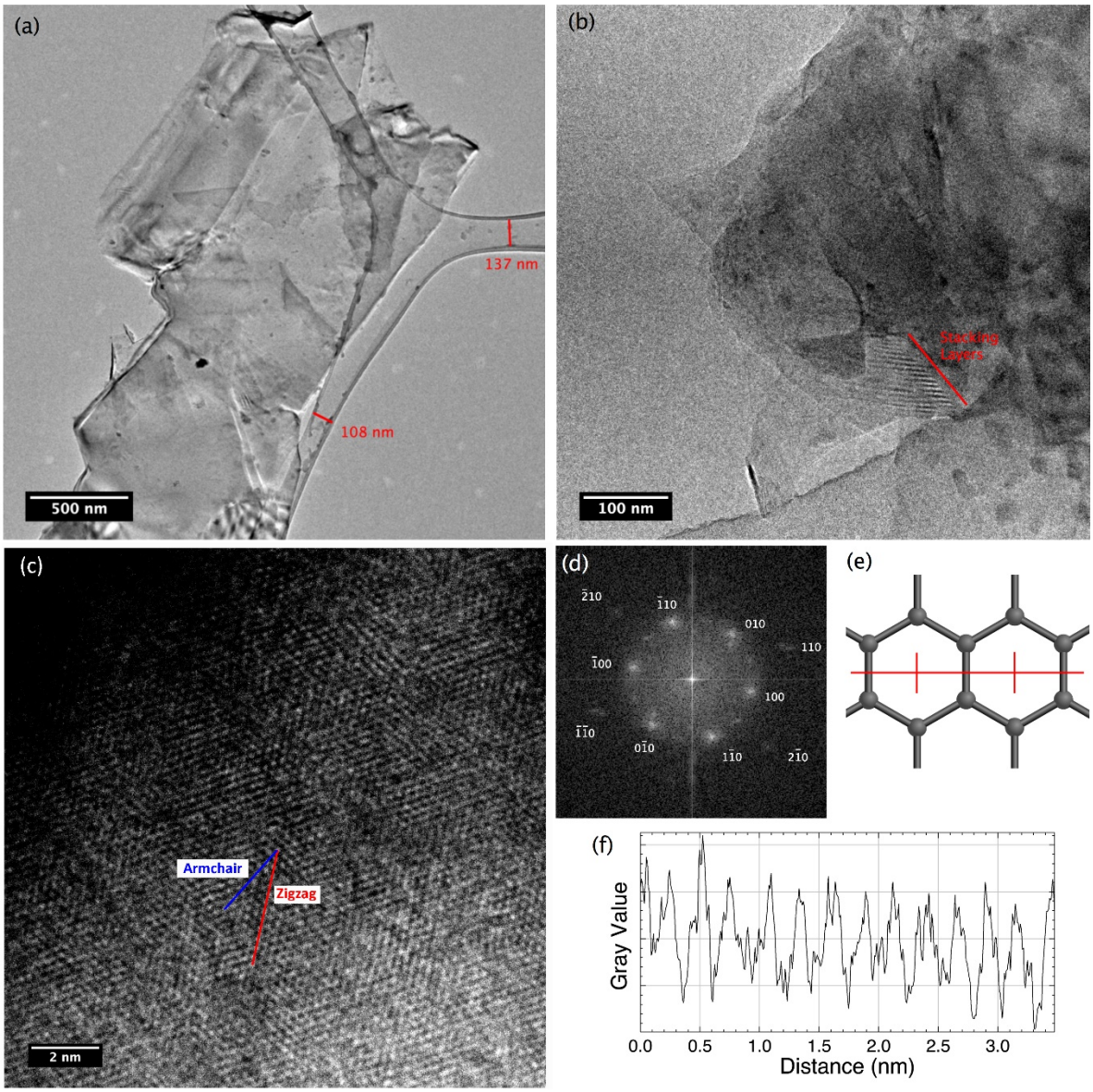

Figure 7.4.10 *TEM images of GNPs-20 focusing on (a) large layers, (b) stacking 002 layers and (c) hexagon atoms patterns of a graphene layer. The Fast Fourier Transform (FFT) of (c) is presented in (d). The plot profile of red line (zigzag direction) in (c) that crosses the centres of hexagons as shown in (e) was drawn in (f).*

Based on the discussion of XRD patterns, GNPs-20 has no significant differences in peak positions in contrast with pure graphite. Therefore, GNPs-20 is basically the reduced sizes of both the c-axis stacking and the graphitic layers from crystalline graphite, which has been clearly confirmed in the TEM pictures in **Figure 7.4.10**. For general carbon structures with surface areas over 500 m^2/g, the structures mostly become amorphous and distorted in both layer stacking and intra-planar ordering, e.g. activated carbons, which makes structural

characterisation problematic. Following the studies of XRD and Raman spectra in sections 7.4.1 and 7.4.2, the GNPs with high surface areas are discovered to maintain the high graphitic ordering. As shown in **Figure 7.4.11 (a)**, GNPs-500 obviously contains an aggregation of much smaller particles at nanometric scale in comparison to GNPs-20. Further increase of the magnification in **Figure 7.4.11 (b)** reveals curved and bent graphitic nanoribbons of several layers stacked, which is due to the softened flakes with a reduced number of packed layers. The potentially wrapped edges in **Figure 7.4.11 (c)** are over 0.55 nm. As the interlayer spacing of single-crystal graphite is only 0.355 nm, the wrapped edge could possibly to be a folded single graphene layer at the grain edge, as indicated by the study of Meyer et al. based on high-resolution TEMs of several-layer graphene [169].

Figure 7.4.11 (d) shows the arrangement of carbon atoms in a single graphene layer, while **Figure 7.4.11 (e)** illustrates the c-axis stacking of graphitic layers. Both the carbon hexagonal layer structure and the stacking ordering are similar for GNPs-500 and GPNs-20, in spite of the dramatic difference in surface areas, as was also verified by the FFT analysis in **Figure 7.4.11 (f)** and **(g)**. The FFT results for the graphene layer in GNPs-500 appear similar to those for GNPs-20, except for the four weak spots in GNPs-20: their absence for GNPs-500 is believed to be caused by less focused images. The FFT of stacking layers indicates an interlayer distance around 0.335 nm, which is consistent with GNPs-20 and pure graphite. The profile plot (**Figure 7.4.11 (h)**) of the red crossing line in **Figure 7.4.11 (e)** covers a total length of 5.05 nm for 15 layers, giving an average of 0.337 nm for the interlayer spacing. Overall, the TEM results for GNPs-500 agree well with those of GNPs-20 in both the interlayer spacing and the distribution of carbon atoms in graphene layers.

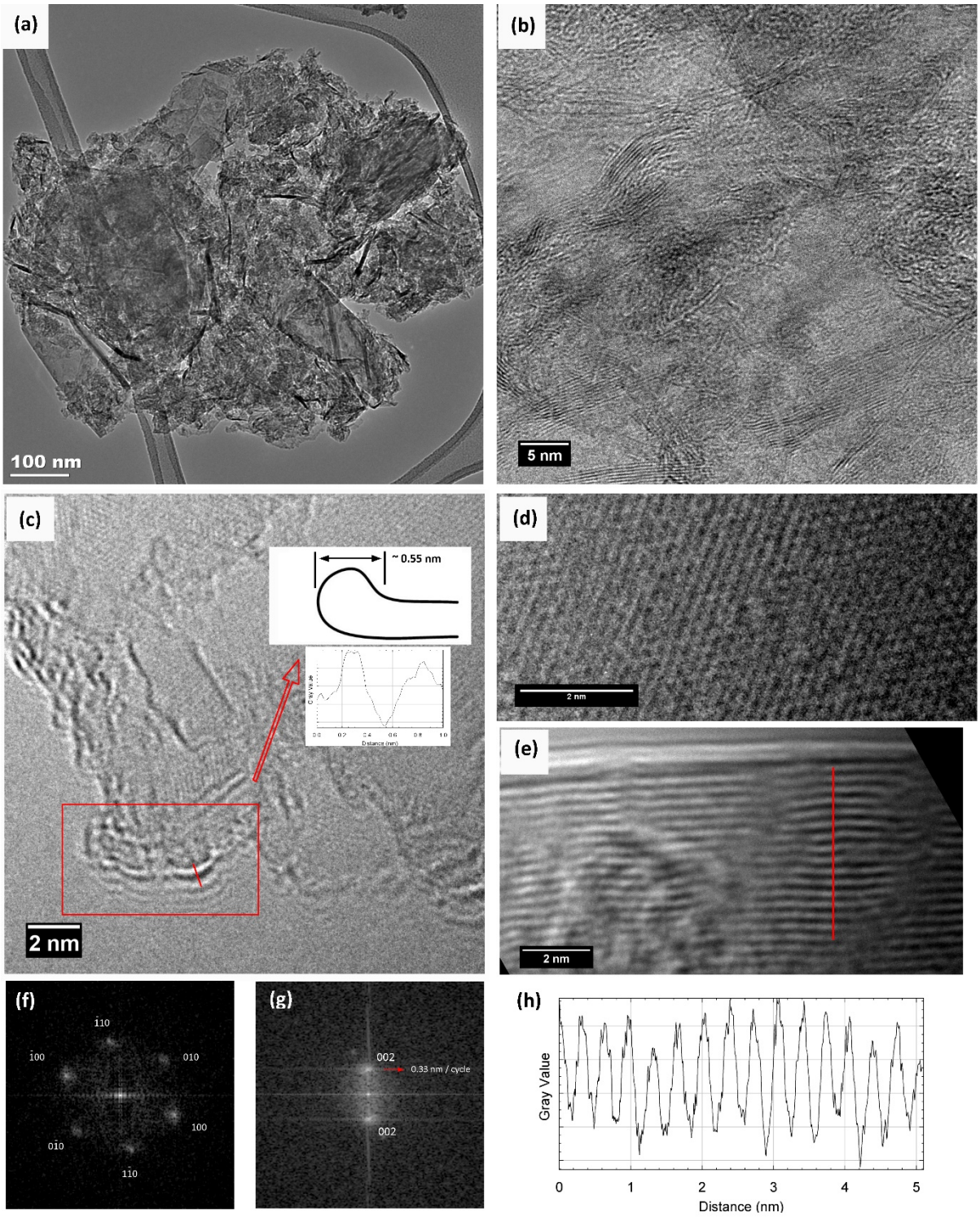

Figure 7.4.11 *TEM images of GNPs-500 at different magnifications (a), (b) and (c). A selection of flat areas at (c) is shown in detail in (d), and (e) shows the stacked graphene layers. (f) and (g) are the FFTs of (d) and (e) respectively, and (h) is the profile plot of the red line in (e).*

As expected for GNPs-700, the sizes of particles are further reduced compared with GNPs-500. As is clear from **Figure 7.4.12 (a)**, the layer sizes are difficult to identify because of the heavy aggregation of small particles, but the sizes seem similar to the values extracted from XRD and Raman spectroscopy analysis. GNPs-700 certainly demonstrates a higher amount of twists and bends in a smaller number of stacked layers by contrast with GNPs-500, as seen in **Figure 7.4.12 (b)**, which had already been suggested by the broadened (002) peaks in XRD patterns. By analogy with GNPs-500, GNPs-700 also exhibits a similar order of c-axis layer stacking as indicated in **Figure 7.4.12 (c)**, and the detected interlayer distance is around 0.33 nm according to the line profile plot of **Figure 7.4.12 (d)**. With the surface area increasing to 700 m^2/g, it becomes problematic to locate a flat layer in order to conduct the FFT analysis. As shown in **Figure 7.4.12 (e)**, the FFT analysis is based on a slightly distorted surface, resulting in the distorted spot positions in reference to GNPs-500. The planar distance of 100 in the FFT analysis is about 0.22 nm/cycle, precisely the same value as in GNPs-20 and GPNs-500, signifying a similar degree of layer stacking ordering.

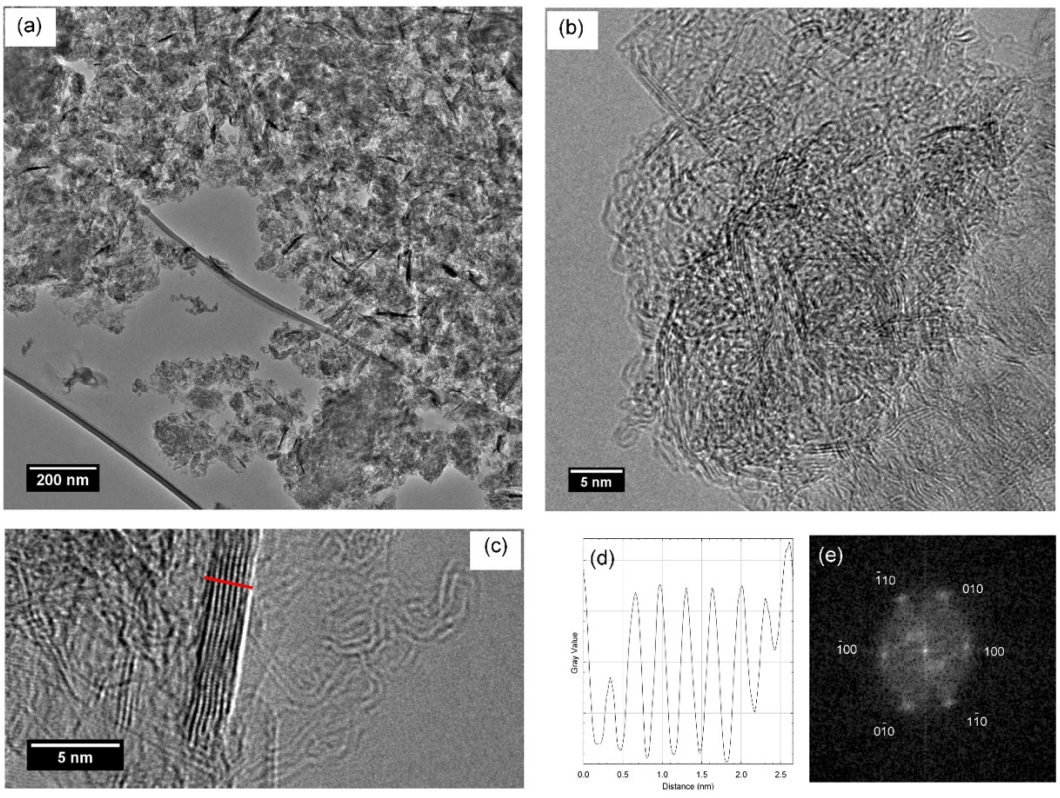

Figure 7.4.12 *TEM images of GNPs-700 in (a), (b) and (c) at various locations and magnifications. (d) is the plot profile along the red line in (c). (e) is the FFT of a flat section.*

7.4.4 Summary

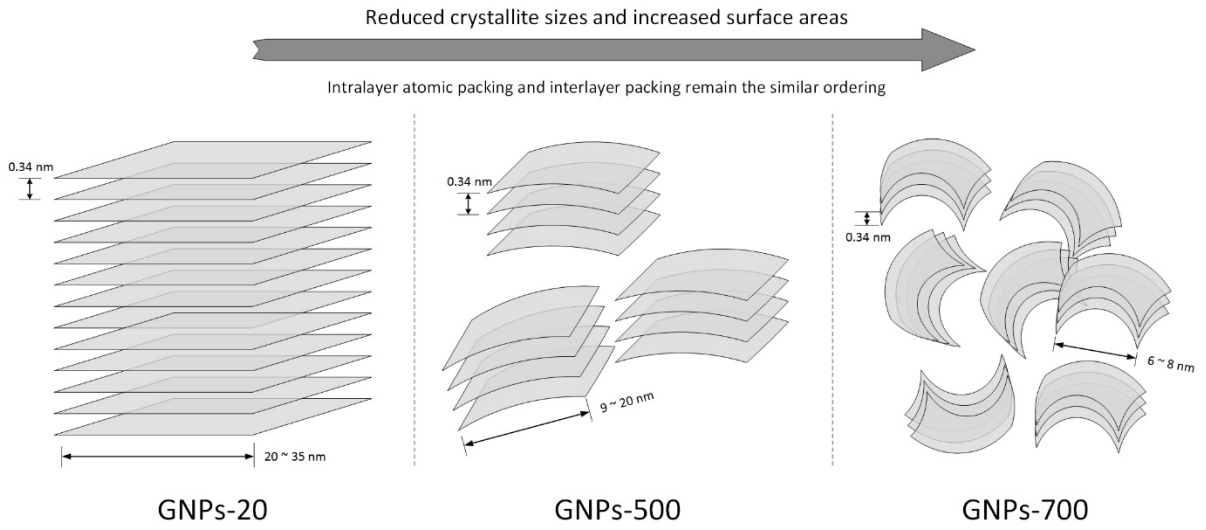

Figure 7.4.13 *The evolution of GNPs with the increase in surface area.*

Graphene nanoplatelets (GNPs) with a broad range of surface areas have been characterised for their structural evolutions using XRD, Raman spectra, SEM and TEM micrographs. By contrast with the activated carbons, in which the high surface areas and porous structures are introduced by highly amorphous graphitic structures in both interlayer stacking and intra-planar ordering, the GNPs with larger surface areas remain highly-ordered graphitic structures with similar interlayer spacing and hexagonal packing of carbon atoms to pure graphite, as shown in **Figure 7.4.13**. It is widely acknowledged that the surface area is closely related to the gas uptake during adsorption. Not only do GNPs have high surface areas that benefit their adsorption uptakes, but they also have well recognisable structures, which is crucial for analysing the adsorption mechanism via control of the structural features of sorbents.

No longer are the crystallites found to be always rigid in high surface area GNPs, but in both GNPs-500 and GNPs-700, they are found to be bent, twisted and aggregated together, which has been spotted in carbons with single-layer graphene or several stacked graphene layers previously. Along with the reduction of crystallite dimension with layer size and c-axis size, the surface-to-volume ratios of both GNPs-500 and GNPs-700 are dramatically increased in contrast with GNPs-20. Since the GNPs-20 and pure graphite have insignificant surface areas, the induced high surface areas of GNPs-500 and GNPs-700 are likely to be caused by the small

crystallites sizes and the high surface-to-volume ratios. In terms of the Raman analysis, the mean graphene layer sizes are projected to be 9 – 20 nm for GNPs-500 and 6 – 8 nm for GNPs-700. The formation of porous structures in the GNPs with high surface areas is caused by the arbitrary assembly of nano-scale crystallites and trapped spaces in the curved graphitic flakes. Thus, the pore sizes of both GNPs-500 and GNPs-700 are expected to be mostly found in the lower-half of mesopore sizes (2 – 50 nm), and micropores (< 2 nm) should also be anticipated to exist, which agrees well with the analysis in section 7.1.

At the edges of GNPs-500 and GNPs-700, the single-layer or double-layer graphene is predicted to exist due to the uneven finishing around the grain boundaries. For some of the crystallites, the stacking number of graphite layers is around 3 – 5. It is possible to have single or double layers with the further growth of surface area in GNPs, closing to the saturated sizes of 2630 m^2/g in pure graphene [50]. The high surface area GNPs have some features similar to single layer graphene, such as the high surface area and the bendable layer structures which are crucial for gas adsorption, high chemical reactivity and potential to be substrates for fabricating functional groups. By contrast with expensive pure graphene materials, the GNPs are much more cost-effective and have already been developed for mass productions, which makes the GNPs suitable candidates for potential industrial applications.

7.5 Pd decoration of porous carbons and its effects on hydrogen cryosorption

Palladium decorated carbon is a type of material produced by the dispersion of palladium particles on the surfaces of porous activated carbons so that a high surface-to-volume ratio of Pd particles can be achieved for improved activity. A lot of work has been done for studying palladium decoration on various types of carbon materials, such as highly ordered graphite, porous activated carbons, carbon nanostructures, carbon blacks, etc. [97], [113], [170]–[177]. Crystalline materials like graphite have well-defined structures but are generally non-porous and have small surface areas, which is not favourable for gas sorption. The activated carbons are normally highly porous materials with high surface areas, but their structures are difficult to characterise preciously because of the amorphous material present. There are many studies focussing on the hydrogen adsorption of palladium carbon materials at room temperature and medium-to-high pressures [97], [172], [173], [178], observing that the formation of palladium hydride in Pd carbons considerably improves the hydrogen uptake at room temperature, compared with the raw carbon substrates. A carbon template (CT) with a fairly ordered structure and high surface area was studied by Campesi to compare the overall uptakes between the pure CT and a 10 wt% Pd decorated CT at 77 K, discovering that the additional palladium content was not able to increase the total uptake [115]. However, the pore size distributions of the CTs and Pd-CTs remain unknown, so it has not been established whether the palladium was mostly coated in the pores or on large surfaces, and the results were not conclusive, as only one set of palladium-doped CT was tested. Since the hydrogen adsorption is slowed down at 77 K, it is also not clear whether the palladium content influences the adsorption kinetics for reaching equilibrium. As discussed in section 7.4, graphene nanoplatelets (GNPs) have well-defined structures for both their crystallite sizes and their porous properties. In this section, a detailed investigation of palladium doped GNPs is reported for evaluating the influence of the Pd content on the hydrogen adsorption uptake at 77 K, as well as the pore size distributions of the materials and the cryosorption kinetics, in comparison with Pd decorated AC Norit GSX.

7.5.1 Growth of Pd in decorated activated carbons and GNPs-700

Two carbon materials, AC Norit GSX with non-uniform sizes of interconnected pores and GNPs-700 with various sizes of slit-like pores, were selected for decoration with palladium particles. As shown in **Figure 7.5.1**, GNPs-700 has a high degree of graphitic c-axis ordering in terms of the (002) position at $2\vartheta = 26°$. A sharp peak is also observed at 26° in the XRD pattern of AC Norit GSX. This is believed to be caused by impurities of pure graphite, because the sharp peak is extremely distinct above a much broader (002) peak at 23° that is a common indication of the amorphous structures in AC Norit GSX. Several sharp peaks with weak intensities are observed at 20° – 23 ° and 35° – 70°, which can be related to the residual oxygen and hydrogen groups from organic raw materials as shown in reference data [179]. In comparison with the (002) peak of GNPs-700, the (002) peak of AC Norit GSX is not only much broader but also shifted to a lower angle, which clearly implies disordered structures of layer stacking in AC Norit GSX. As pure graphite has very low porosity and surface area, the high surface area of AC Norit GSX for acting as the doping substrate is principally attributed to the amorphous phase.

As described in section 4.3, there are several stages in the decoration process. After the raw carbon materials were mixed with Pd^{2+} solution, the materials were kept at 60 °C until they were dry, after which the XRD patterns were measured and shown in **Figure 7.5.1 (b)**. With increasing Pd^{2+} content in carbons, the XRD pattern becomes noisier, and the intensity of background diffraction becomes more significant, which obscures the small sharp peaks found in the raw AC Norit GSX (see **Figure 7.5.1 (a)**). This noisy background is caused by the presence of $PdCl_2$, contributing a large quantity of peaks with various intensities over the whole range of 10 – 70 °, according to the reference pattern [180]. The peaks introduced by $PdCl_2$ are stronger in the carbon with 40 wt% Pd^{2+} than the 20 wt% Pd^{2+}.

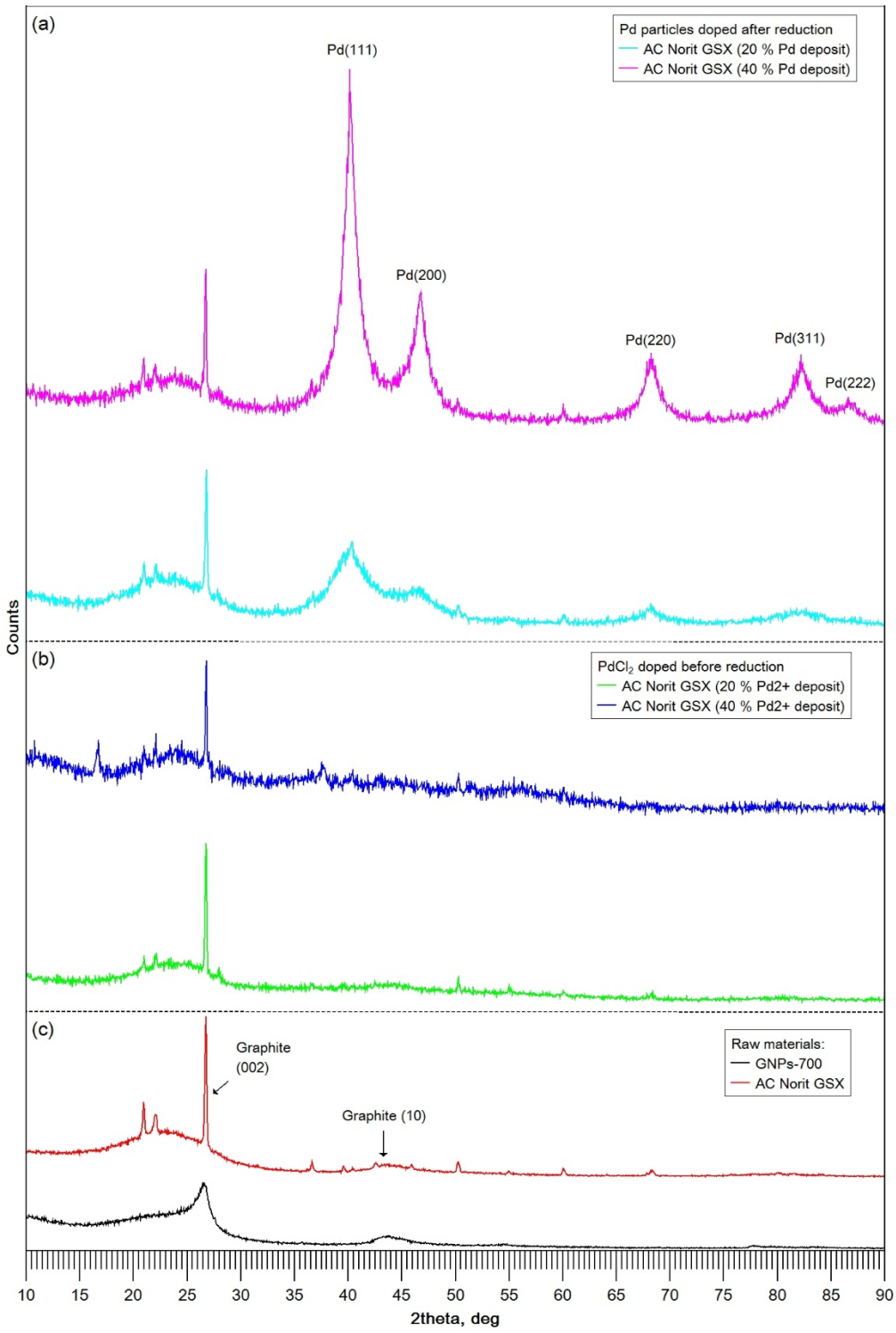

Figure 7.5.1 *XRD patterns of carbons at different stages of decoration: (a) Pd AC Norit GSX after reduction, (b) Pd AC Norit GSX before reduction and (c) raw carbons. The intensities of (002) broad peaks of AC Norit GSX derived carbons are scaled to a similar level with raw carbon. 20/40 % are deposit fraction of Pd conent in the decorated carbon in preparation as described in section 4.3.*

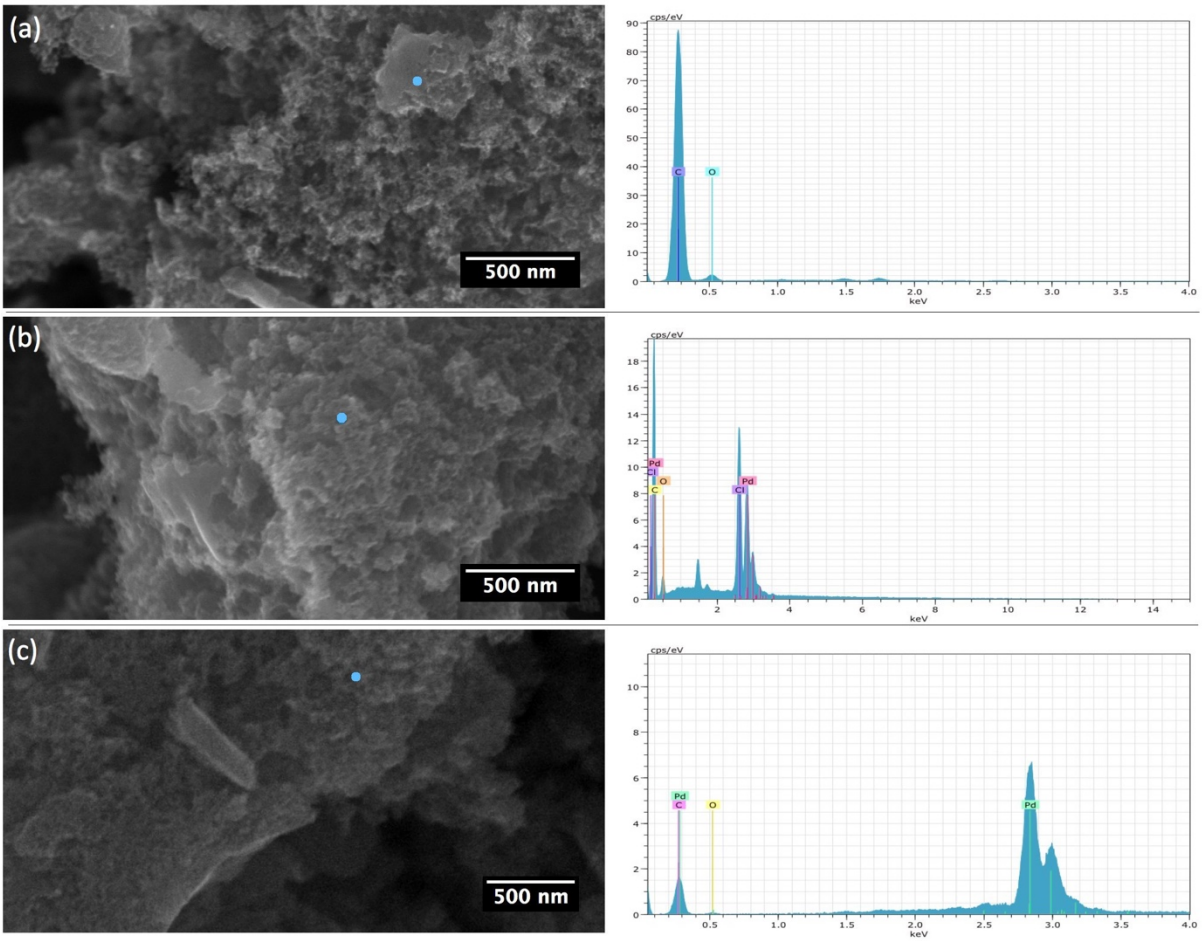

Figure 7.5.2 *SEM micrographs and EDX analysis on a selected spot (blue dot in the images): (a) raw AC Norit GSX, (b) 40 % Pd^{2+} AC Norit GSX mixture before reduction, (c) reduced 40% Pd decorated AC Norit GSX.*

The SEM micrographs and EDX spectra on selected spots of the AC Norit GSX at different stages of decoration are presented in **Figure 7.5.2**. The oxygen content of AC Norit GSX detected in the XRD patterns has been further verified by the EDX analysis. The EDX spectrum of 40% Pd^{2+} AC Norit GSX prior to reduction suggests a large quantity of Pd^{2+} and Cl^{-1} with a constant ratio of 1:2, indicating the presence of $PdCl_2$, which is consistent with the strong background observed in the related XRD patterns. After the reduction treatment under flowing hydrogen at 300 °C, the Pd(II) is completely converted into Pd. Hence, Cl is not detectable in the 40% Pd decorated AC Norit GSX in **Figure 7.5.2 (c)**. It is also understood that the palladium hydride can be produced with the exposure to hydrogen at room temperature. But the absorption of hydrogen, as discussed in section 2.1.1, does not modify the lattice structure of palladium metal. Since the hydrogen absorbed can be reversibly removed by high

temperatures or vacuum, the existences of palladium hydride in SEM characterision, BET measurement and vacuum degassing of cryosorption experiment are avoided thanks to the vacuum condition or procedure in the test. The mass variance caused by hydrogen absorbed (normally 0.6 H/Pd, 0.56 wt% of Pd) is negligible small for all analysis below. Therefore, all palladium content is treated as pure palladium particles in our discussed. With the progress of Pd decoration, there is no significant modification observed on the surface morphology of the carbons, as is apparent from the SEM images. Because the surfaces of the samples in the SEM were not flat, it was difficult to perform EDX analysis in order to investigate the localised variations of Pd content in the decorated carbons.

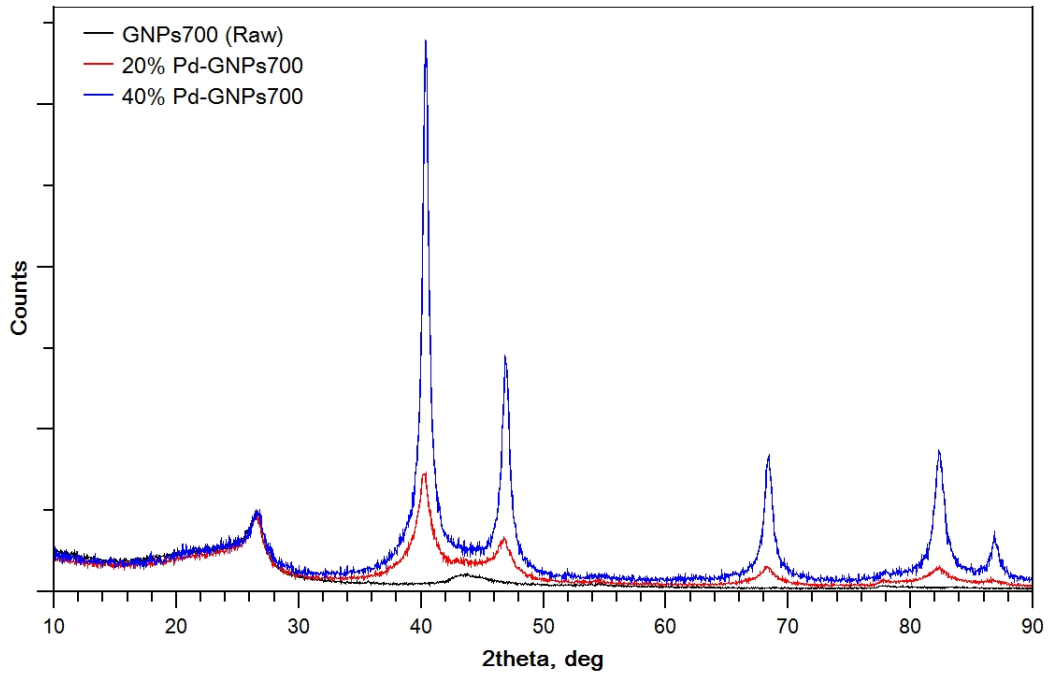

Figure 7.5.3 *The XRD patterns of GNPs-700 and doped GNPs-700 with 20 wt% and 40 wt% Pd.*

Pd nanocrystallites can be identified in the XRD patterns after reduction in hydrogen, as shown in **Figure 7.5.1** for AC Norit GSX and **Figure 7.5.3** for GNPs-700. Five XRD peaks related to different groups of equivalent reflection planes in palladium exhibit higher intensities with the increased Pd content in the carbon composites. The relative intensities among Pd peaks are in good accordance with the published patterns of crystalline palladium [181], confirming the formation of crystalline Pd particles in the AC Norit GSX substrates. A similar trend in peak development is also found in the decoration of GNPs700 as shown in **Figure 7.5.3**. It is obvious

that the peaks become shaper with higher Pd content, indicating the formation of larger crystallite sizes of Pd particles.

Scherrer's equation (see section 5.1) was applied to determine the crystallite sizes of Pd particles, and the shape factor *K* was defined as 0.89 with the assumption of sphere-like shapes of formed particles. The results listed in **Table 7.5.4** were obtained from the profile fitting of XRD patterns using Highscore Plus software. Instrumental broadening is neglected because of its negligible values compared with the broad FWHMs. According to **Table 7.5.4**, except for the 20 % Pd-AC Norit GSX that has various values of crystallite size based on different directions of the structure, the other decorated carbons reveal similar crystallite sizes around all five directions evaluated, indicating the occurrence of mostly isotropic shaped crystallites. The XRD peaks related to Pd content among the decorated carbons show negligible shifts in position, suggesting the consistent interplanar distances of Pd crystalline structures in different carbons.

Although both carbon materials were mixed with identical 20 wt% and 40 wt% Pd deposit of the total composite mass, the determined crystallite sizes exhibit obvious differences between AC Norit GSX and GNPs-700. For example, 1.5 – 3.5 nm Pd particle sizes in 20% Pd-AC Nort GSX, by contrast with 4 – 6 nm Pd particles in 20 % Pd-GNPs700. In order to verify whether the differences of Pd crystallite sizes are caused by the actual composition variation of the Pd content in the carbon composite, and how much Pd contents have been doped in each carbon sample, the thermogravimetric analysis (TGA) was conducted in air flow for both the raw carbons and the Pd decorated carbons, as shown in **Figure 7.5.5**. The raw AC Norit GSX and GNPs-700 gradually lose their weights with the temperature increase, eventually reaching a plateau above 650 °C and 700 °C respectively, while a dramatic weight reduction at around 400 °C is widely observed in all Pd-decorated carbons, indicating the significant catalytic effects of the palladium content. The catalytic effects of Pd during the TGA tests are in good agreement with the work of Kim et al. [182] on palladium decorated carbon nanofibers. Although the carbon content of Pd-decorated composites is mostly lost on heating at around 400 °C, a small fraction of carbon-related residue is not entirely removed until 700 °C for both AC Norit GSX and GNPs-700. Further weight loss occurs at a temperature

of 800 – 850 °C, which is attributed to the decomposition of the palladium (II) oxide that is formed at lower temperatures [124], [183].

Table 7.5.4 *The measured palladium crystallite sizes based on XRD patterns of decorated carbons.*

		AC Norit GSX		GNPs-700	
Reflection planes	**Parameters**	**20 wt% Pd**	**40 wt% Pd**	**20 wt% Pd**	**40 wt% Pd**
(111)	**FWHM [°2θ]**	2.37	1.41	1.41	0.67
	Peak Position [°2θ]	40.15	40.19	40.22	40.38
	Crystallite size [nm]	3.5	5.9	5.9	12.5
(200)	**FWHM [°2θ]**	5.1	1.36	1.67	0.74
	Peak Position [°2θ]	46.11	46.64	46.7	46.91
	Crystallite size [nm]	1.7	6.3	5.1	11.6
(220)	**FWHM [°2θ]**	2.5	1.68	1.79	0.77
	Peak Position [°2θ]	68.15	68.19	68.23	68.36
	Crystallite size [nm]	3.8	5.6	5.3	12.3
(311)	**FWHM [°2θ]**	6.6	2.3	2.4	0.92
	Peak Position [°2θ]	81.7	82.14	82.23	82.32
	Crystallite size [nm]	1.6	4.5	4.3	11.3
(222)	**FWHM [°2θ]**	N/A	1.7	1.7	0.76
	Peak Position [°2θ]		86.72	86.75	86.83
	Crystallite size [nm]		6.4	6.4	14.2

The GNPs-700 has only 0.72 wt% residue remaining at temperatures above 700 °C, which suggests almost pure carbon content. By contrast, AC Norit GSX has a larger weight residual of 11.62 wt%, which is most likely due to the oxygen related impurities that result in temperature-resistant crosslinks in carbons. This type of crosslink is widely detected in the biochars produced by the pyrolysis of *Miscanthus* that have been studied in section 7.3. The residual weight percentages are labelled on each TGA plot in **Figure 7.5.5**. The actual composition of Pd in the decorated carbon can be obtained by deducting the raw materials residual from the Pd-decorated carbon residue in the final plateau region. The real compositions of palladium in 20 % Pd-AC Norit GSX and 40 % Pd-AC Norit GSX are 10.86 wt%

and 18.89 wt% respectively. The 20 % Pd-GNPs700 has a Pd content of 11.23 wt%, and the 40 % Pd-GNPs700 contains 21.58 wt% of Pd particles.

In comparison with the initial Pd deposit during the sample preparation, it became clear that nearly half of the Pd was lost for all four Pd-decorated carbons during mixing and transportation in the decoration process. Since the composition differences between decorated AC Norit GSX and GNPs-700 is not significant, the differences of crystallite sizes between AC Norit GSX and GNPs-700 with a similar Pd composition are unlikely to be caused by the minor composition variance of Pd contents. The reason for the crystallite size variations can be related to intrinsic properties of carbon substrates, for instance, pore volumes, pore size distributions, surface areas, etc.

Overall, as seen in the XRD patterns, the palladium crystallites grow with the increase of Pd content in decorated AC Norit GSX and GNPs-700. The crystallite sizes of Pd particles among the four decorated carbons are situated in the range of 2 – 15 nm on average, which is in the smaller half of the mesopore range. A further analysis of the influence of Pd particles on the porous properties of carbons will be studied in detail in next section.

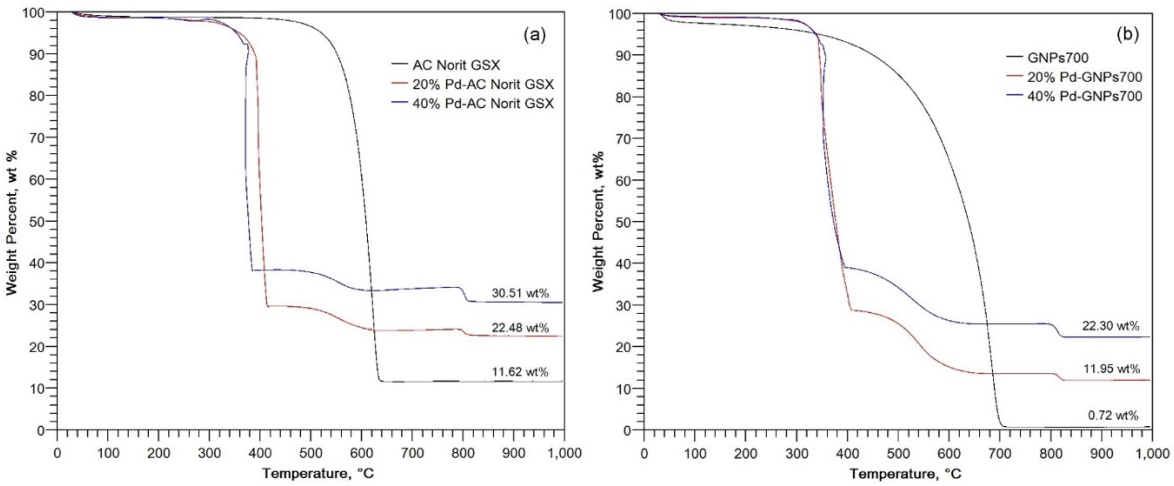

Figure 7.5.5 *TGA analysis of (a) AC Norit GSX and Pd decorated AC Norit GSX; (b) GNPs-700 and Pd decorated GNPs-700.*

7.5.2 The distribution of Pd paricles in the pores of carbons

In order to obtain an overview of the Pd particle distributions inside the carbon materials, both secondary electron (SE) and backscattered electron (BSE) images are compared in **Figure 7.5.6**. The morphology of the carbon surface shows no sign of recognisable modification with additional decorated Pd content. In the BSE pictures in **Figure 7.5.6**, the bright dots, in contrast with the dark background, relate to heavy particles such as palladium particles in this study. It is clearly observed that the Pd particles are small and homogeneously distributed inside the carbon materials, although there are localised agglomerations appearing with higher Pd contents than the average. The large pores that contain large Pd particles are caused by the aggregation of small crystallites. The Pd particles in the decorated AC Norit GSX are observed to be smaller and more homogeneously distributed than in decorated GNPs, which is in accordance with the observation that GNPs-700 exhibits more Pd particles of large sizes (brighter in BSE pictures) than AC Norit GSX. As described in **Figure 7.5.7**, the nitrogen adsorption isotherms of Pd-decorated carbons exhibit the same type IV isotherm and the hysteresis loop as in the raw carbons, which indicates that the porous structures of carbon substrates are not severely affected by the decoration of Pd.

The BET theory is the most commonly used characterisation method for quantitative analysis of surface area and monolayer adsorption capacity. As discussed in section 2.3.5, the relative pressure range that is selected for conducting BET calculations requires additional validation, especially for a BET testing system as used in this report that implements a fixed relative pressure range, because the common p/p_0 range of 0.01 – 0.3 is not appropriate for materials containing micropores. The BET plots of raw carbons and Pd decorated carbons are illustrated in a standard 0.01 – 0.3 relative pressure range in **Figure 7.5.8 (a)**. Curved BET plots, that ought to be linear in terms of BET theory, are observed in AC Norit GSX and related Pd carbon composites, while GNPs-700 (with and without Pd decoration) have slightly better linearity. With reference to the range verification as shown in **Figure 7.5.8 (b)**, the proper range for applying the BET method on AC Norit GSX related carbons is 0.01 – 0.1, and the BET range is slightly higher for GNPs-700, resulting in p/p_0 values less than 0.16.

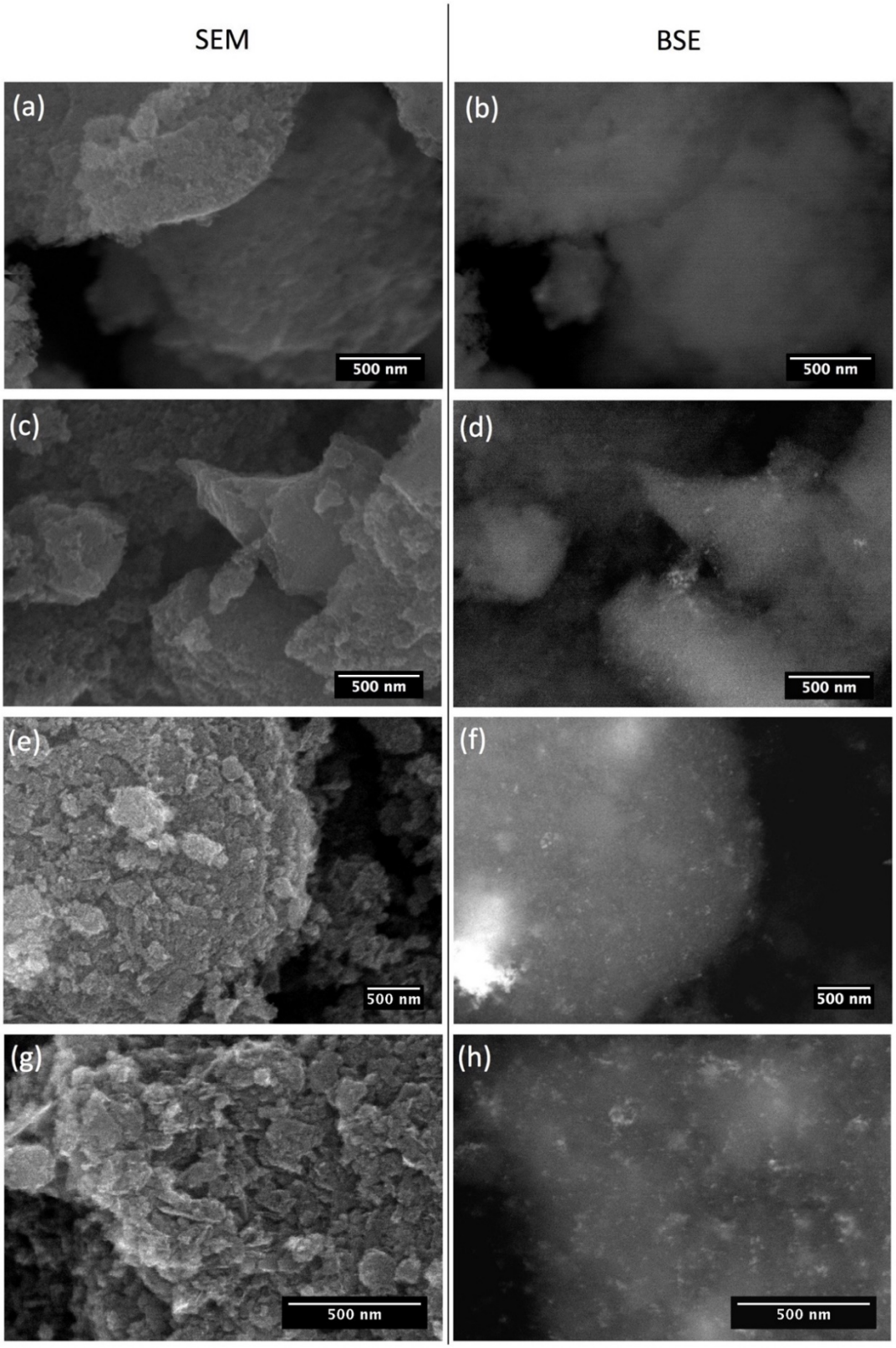

Figure 7.5.6 *SEM micrographs: secondary electron (a), (c), (e), (g) and backscattered electron (b), (d), (f), (h) images of 20 % Pd-AC Norit GSX, 40 % Pd-AC Norit GSX, 20 % Pd-GNPs700 and 40 % Pd-GNPs700 respectively.*

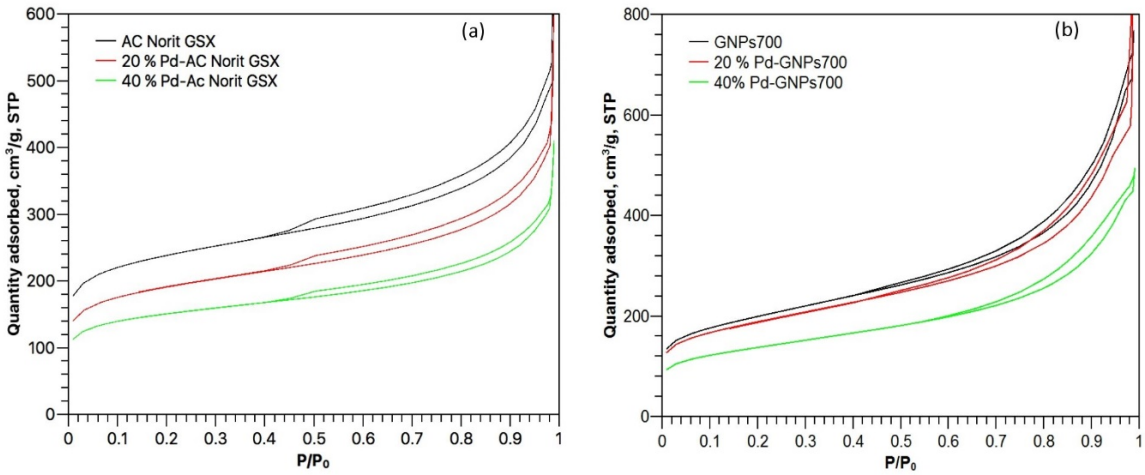

Figure 7.5.7 *The nitrogen adsorption isotherms: (a) AC Norit GSX and Pd decorated AC Norit GSXs, (b) GNPs-700 and Pd decorated GNPs-700s.*

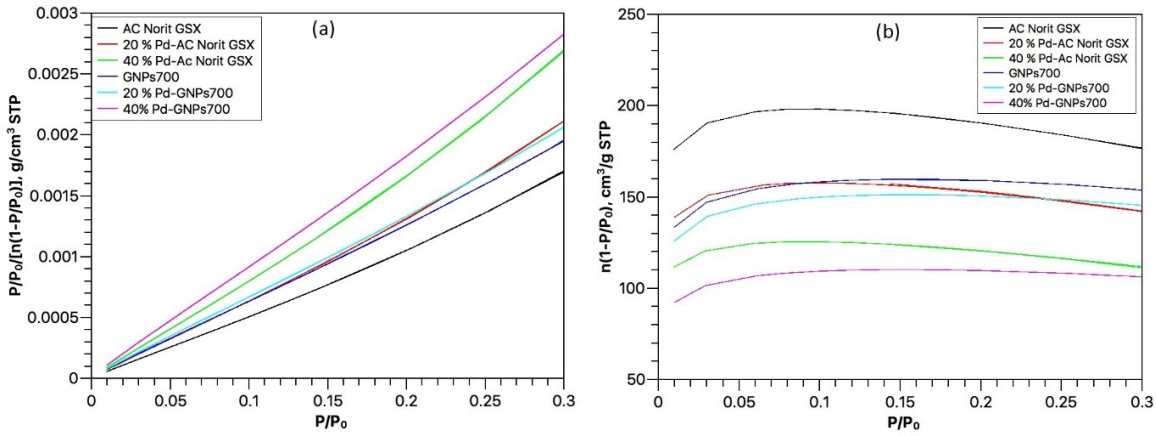

Figure 7.5.8 *(a) BET plots and (b) validation plots for the BET ranges of raw carbons and Pd-decorated carbons.*

The detailed results for the raw carbons and the Pd decorated carbons based on the BET method are listed in **Table 7.5.9**. All four Pd carbons are shown to have certain reductions in surface area compared with the raw materials. Campesi et al. attributed the reduction of surface areas to the extra weight of Pd content in carbons, which can further influence the hydrogen uptakes at 77 K [115]. With the assumption that the decorated Pd particles are non-porous, therefore contributing a negligible amount of surface area to the decorated carbons, the surface areas measured in Pd decorated carbons are assumed to be characteristic of the carbons. As discussed in the previous section, the actual concentration of Pd in the carbon composites are 10.86 wt% for 20 % Pd-AC Norit GSX, 18.89 wt% for 40 % Pd-AC Norit GSX, 11.23 wt% for 20 % Pd-GNPs700 and 21.58 % for 40 % Pd-GNPs700. The equivalent surface

areas were calculated by dividing the surface areas by the weight percent of the carbon contents. The actual surface areas and the equivalent surface areas are compared in **Figure 7.5.10**.

Table 7.5.9 *BET Results of raw carbons and Pd decorated carbons.*

	AC Norit GSX	20% Pd-AC Norit GSX	40% Pd-AC Norit GSX	GNPs700	20% Pd-GNPs700	40% Pd-GNPs700
Slope (10^{-3} g/cm^3 STP)	4.97	6.23	7.85	6.15	6.50	8.92
Intercept (10^{-6} g/cm^3 STP)	7.41	1.06	1.16	1.71	1.81	2.41
n_m (cm^3/g)	200.96	160.20	127.23	162.07	153.48	111.83
C	671	587	680	361	361	371
a_{BET} (m^2/g)	875	697	554	705	668	487

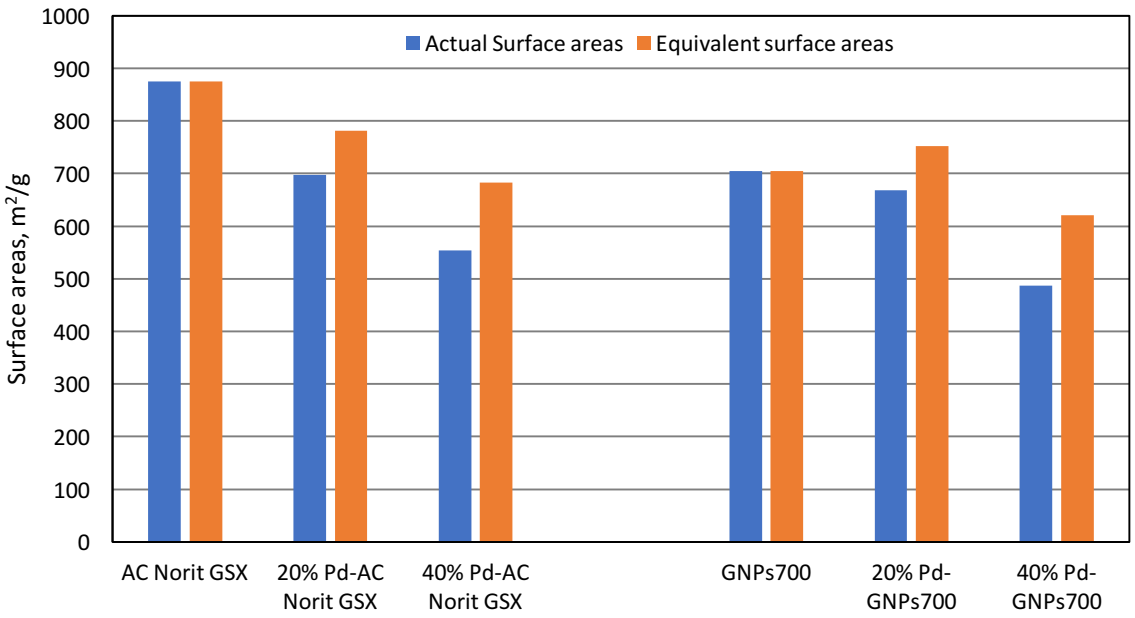

Figure 7.5.10 *The comparison of actual BET surface area and equivalent BET surface area of all carbon samples. The equivalent surface areas assume that the surface areas are totally contributed by the carbon contents.*

As indicated in **Figure 7.5.10**, the calculated equivalent surface areas of the Pd decorated carbon have a significant mismatch with the surface areas of the raw materials. The equivalent surface area of Pd doped AC Norit GSX decreases similarly to the actual surface area with the increase of Pd content in the carbons, while GNPs-700 displays an increase in equivalent surface areas in 20 % Pd decoration compared to the raw material, but with a further drop of equivalent surface areas in the 40 % Pd-GNPs700. The increase of surface areas of 20 % Pd - GNPs700 is likely caused by small Pd particles decorating the surface of the large pores and bringing extra surface areas to decorated carbons. The further decrease of equivalent surface areas at higher Pd % is due to a large fraction of pore volume filled with palladium particles that are inaccessible to probe molecules during the nitrogen adsorption measurements. Hence, the surface areas contributed by the palladium particles are not able to compensate the surface areas of the filled pores. The pore sizes in GNPs-700 are larger than those in AC Norit GSX, so that the fraction of blocked pores by Pd particles in GNPs-700 is less significant. The distinct performance of the equivalent surface areas between AC Norit GSX and GNPs-700 also reveals the different porous properties of the raw carbons, which has already been investigated in section 7.1.

Both the Harkins-Jura t-method and the α_s-method are effective to characterise the external surface area and the micropore volume of sorbents. As shown in **Figure 7.5.11**, both methods assume that the linear section in the middle (0.4 – 0.5 nm in t-plots and 0.8 – 1 in α_s – plots) is related to the ideal multilayer adsorption of nitrogen at 77 K. The results obtained from both models are normally similar to each other, which has been confirmed in section 7.1. With the objective of ensuring consistency within this thesis, the t-method is the primary method used for quantitative analysis. The step-like drop in the hysteresis loops of AC Norit GSX and Pd decorated AC Norit GSX, which is observed at the lower end of the hysteresis loop in nitrogen adsorption isotherms, t-plots (not presented in **Figure 7.5.11 (a)**) and α_s-plots, is an indication of interconnected pore structures, as discussed in section 2.3, while a smaller drop at the lower end of hysteresis loops in GNPs related samples reflects the slit-shaped pores with limited variances in pore sizes. The slope of the linear fit in the t-plot linear region represents the external specific surface area (SSA), by assuming that the mesopore adsorption behaves in the same way as open surfaces and the intercept describes the micropore volumes. The micropore SSA can then be found by deducting the external surface area from the overall

BET surface area. The Harkins-Jura equation used for evaluating the *t* value has been discussed in section 2.3.7. **Table 7.5.12** lists the t-method results of Pd decorated carbons and their raw carbons.

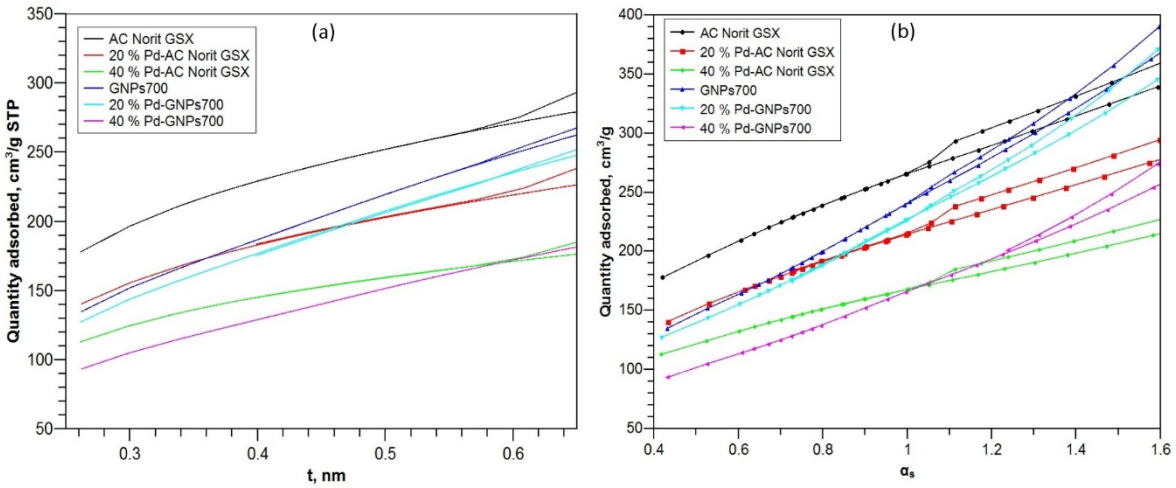

Figure 7.5.11 *(a) t-plots and (b) α_s-plots of Pd decorated carbons and raw carbons.*

Table 7.5.12 *HJ t-method results of raw carbons and Pd decorated carbons (the micropore surface area a_{micro} is obtained by deducting the measured external surface area a_{ext} from the BET surface area).*

	AC Norit GSX	20% Pd-AC Norit GSX	40% Pd-AC Norit GSX	GNPs700	20% Pd-GNPs700	40% Pd-GNPs700
Slope (cm^3/g, STP)	225.08	194.85	140.74	329.81	310.27	226.14
Intercept (cm^3/g, STP)	139.57	105.35	89.06	54.57	52.46	38.27
a_{ext} (m^2/g)	347	300	217	508	478	348
a_{micro} (m^2/g)	528	397	337	197	190	139
V_{micro} (cm^3/g)	0.22	0.16	0.14	0.085	0.081	0.059

The BJH method is well suited to analysing the distribution of pore volumes and pore areas in the mesopore range. In **Figure 7.5.13**, the pore volumes and surface areas of all Pd carbons have been adjusted to equivalent values, with the assumption that the pore volumes and surface areas are entirely contributed by the carbon contents. **Figure 7.5.13 (a)** and **(b)** show

the equivalent pore volume distribution regarding the pores with a diameter of 2 – 50 nm for AC Norit GSX related samples and GNPs-700 related sorbents. The desorption isotherms generally agree with the adsorption isotherms for AC Norit GSX carbons in **Figure 7.5.13 (a)**, except for the sharp peaks of the BJH desorption isotherm at around 4 nm. This distinctive performance of the desorption plots is related to the sudden evaporation of liquid nitrogen trapped in macropores (> 50 nm) after condensed nitrogen in connected small pores with diameters around 4 nm is removed. It is also noticed that BJH adsorption isotherms are more representative of the pore volume distributions in the mesopore range because of the lack of condensation effects, as in the desorption isotherms. 20 % Pd-AC Norit GSX (with actual 10.86 wt% Pd content) does not reveal a significant decrease in pore volume in the range of 2 – 50 nm, while the pore volume reduces more obviously for the 40 % Pd-AC Norit GSX (with actual 18.89 wt% Pd content).

In comparison with the AC Norit GSX samples, the BJH desorption isotherms in GNPs700 carbons generally exhibit higher equivalent pore volumes than BJH adsorption isotherms over the range of 3 – 20 nm, as seen in **Figure 7.5.13 (b)**, which indicates that mesopore pores with various diameters perform as the small “neck” pores for large pores. Similar to the AC Norit GSX carbons, the 20 % Pd-GNPs700 (actually 11.23 wt% Pd content) shows no distinct reduction in pore volumes in contrast with the raw GNPs700, while the reduction of pore volumes in 40 % Pd-GNPs700 (actual 21.58 wt% of Pd contents) is observed through the whole mesopore range. The smaller pore volumes of desorption isotherms are also detected in pore diameters less than 3 nm, which is caused by the overfilling of liquid nitrogen in small pores (micropore filling effect) during adsorption. By comparing the BJH adsorption and desorption isotherms between the AC Norit GSX and GNPs-700 carbons in **Figure 7.5.13**, the GNPs-700 has an overall larger mesopore volume than the AC Norit GSX, while AC Norit GSX exhibits a tendency to have more micropore volume based on the BJH isotherms at the range of 2 – 3 nm, which is further confirmed in **Figure 7.5.15**.

The equivalent BJH pore areas are plotted against the pore size in **Figure 7.5.13 (c)**. The 20 % Pd-GNPs700 has slightly higher equivalent surface area than the raw GNPs-700 over most of the mesopore diameter range, which is in good accordance with the higher equivalent BET surface areas in **Figure 7.5.10**. With the decoration of ~20 wt % of Pd on the carbons, small

Pd particles coated on large mesopore surfaces increase the overall equivalent mesopore surface area because of the high surface-to-volume ratios of small particles. Although the total equivalent BET surface area of 20 % Pd-AC Norit GSX exhibits a reduction in **Figure 7.5.10**, the equivalent surface area over the mesopore sizes is also slightly higher than in the raw material, which has the same performance as in 20% Pd-GNPs700. The decrease of overall equivalent surface area is likely due to the intensively filled micropores which contribute to the significantly decreased micropore surface area. With the further increase of doped amounts of Pd, both samples show noticeably smaller surface areas than the raw materials, indicating the growing Pd coverage on the surface that decreases the surface area by blocking the pores.

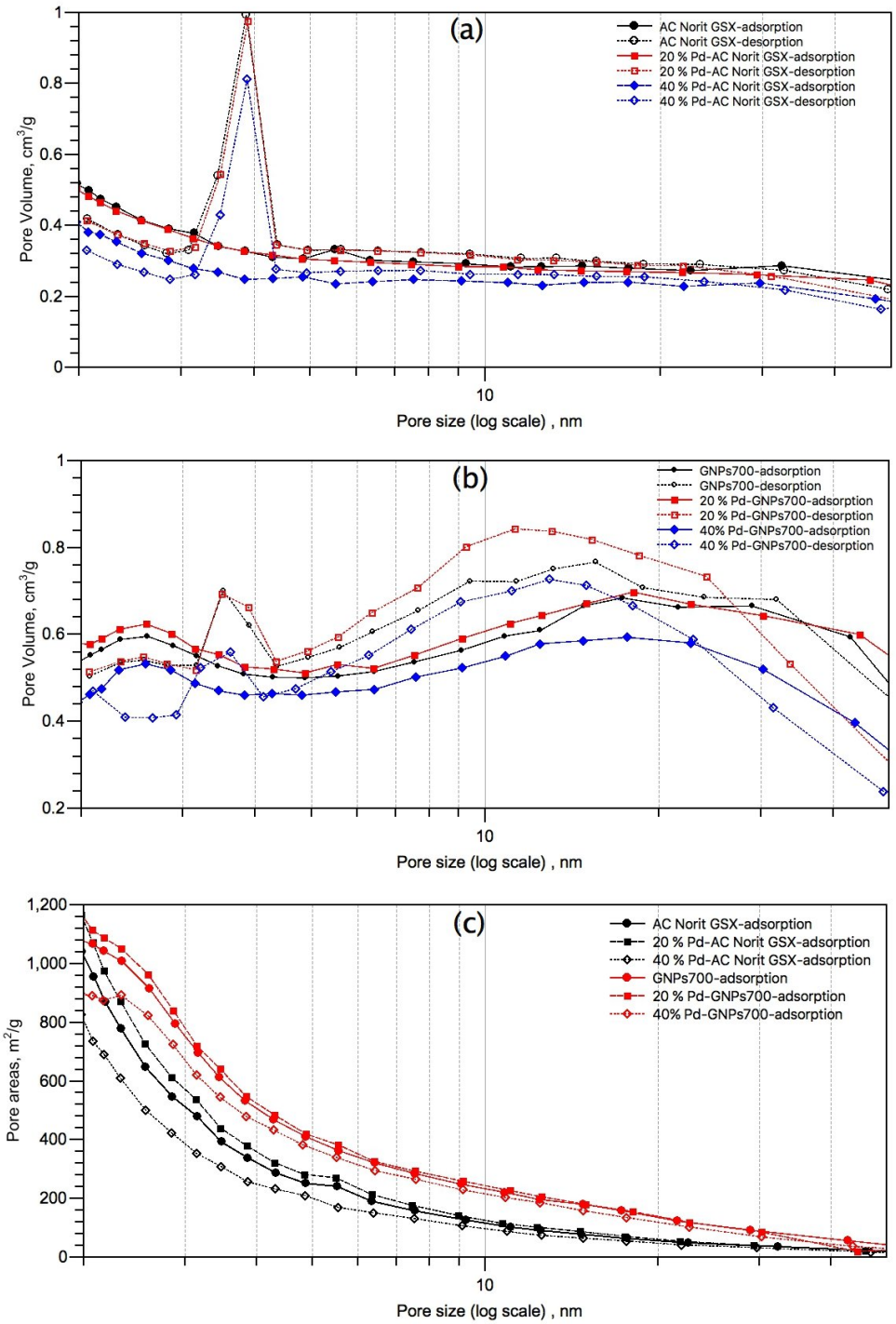

Figure 7.5.13 *The BJH adsorption and desorption plots of pore volumes for (a) AC Norit GSX and Pd decorated AC Norit GSX and (b) GNPs700 and Pd decorated GNPs700. (c) The BJH adsorption distribution plot of surface areas for all samples. The pore volumes and surface areas of all Pd carbons have been adjusted to equivalent values with the assumption that pore volumes and surface areas are entirely contributed by the carbon contents.*

As shown in **Figure 7.5.14**, the external specific surface areas (SSA) obtained from the BJH adsorption accumulation is in good agreement with the external SSA calculated using the Harkins-Jura (HJ) t-method. The slightly smaller external SSA from BJH than HJ can be explained by the surface areas contributed by macropores larger than the BJH maximum range of 200 nm. Since the differences in external SSAs are negligible, the overall meso- and macropore pore volumes are assumed to be represented by pore volumes accumulated from the entire BJH range, so that the large pore volumes can be compared with the micropore values from HJ t-method. Since the Pd particles are non-porous, the equivalent pore volumes of Pd decorated carbons are obtained by regarding the pore volumes to be entirely contributed by the carbon contents.

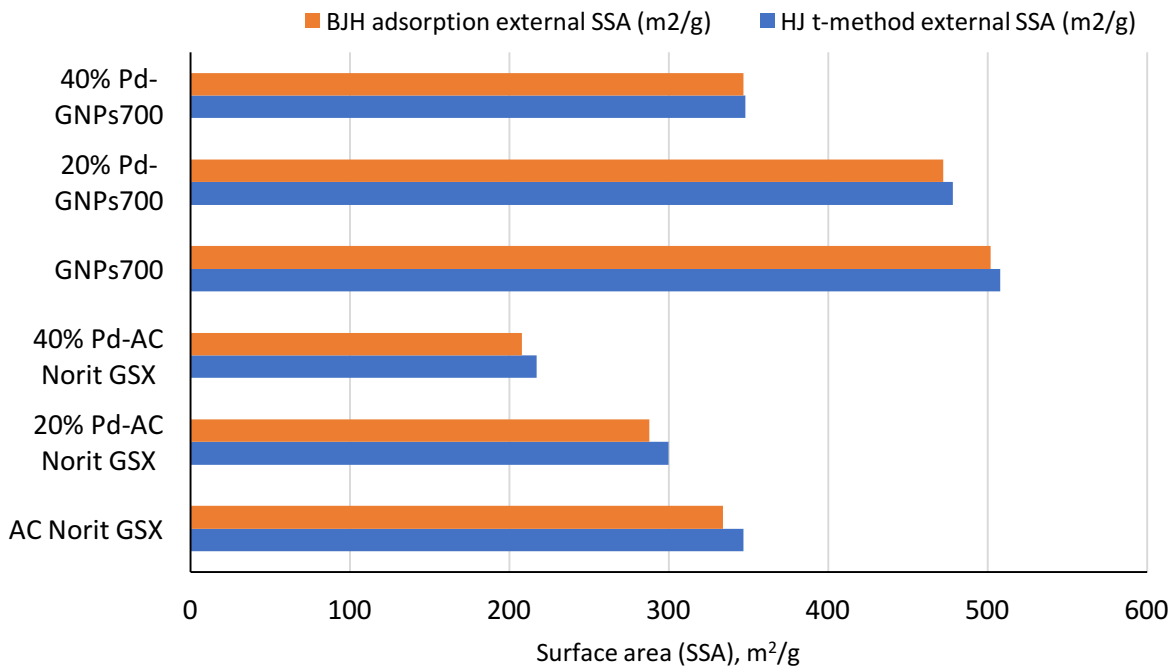

Figure 7.5.14 *The comparison of measured external specific surface areas (SSA) between BJH methods and t-methods.*

As shown in **Figure 7.5.15 (a)**, the equivalent meso-macropore volume decreases with increasing Pd content, with a similar reduction from zero to 10 wt% and from 10 wt% to 20 wt%. Although the trend in micropore volume variations is difficult to identify because of the very small values, there is no doubt that the micropore volumes show an overall reduction with increasing Pd decoration. Furthermore, the decorated Pd appears to spread inside both

micropores and meso-macropores of the carbons without demonstrating a preference for either micropores or larger pores. For every 10 wt% of Pd content in a gram of composite, the Pd volume is estimated to be around 0.01 cm^{-3}. The pore volumes of all Pd carbon composites reduce by an amount far more than the volume of introduced Pd, which implies that some of the Pd particles block a certain number of small pores, making the corresponding pore volumes inaccessible during nitrogen adsorption measurements. The Pd-AC Norit GSX composites are discovered to have a larger reduction of pore volume than the Pd-GNPs700 carbons for a similar Pd composition.

The equivalent micropore specific surface areas (SSA) and equivalent external SSAs are compared in **Figure 7.5.15 (b)**. The decrease of equivalent micropore SSA is more significant than the external SSA from AC Norit GSX to 20 % Pd-AC Norit GSX, while the reduction is observed to be more obvious for equivalent external SSA on increasing Pd deposit from 20 % to 40%. One possible explanation for this phenomenon is due to the large micropore surfaces induced by small micropore volumes, resulting in high surface-to-volume ratios. At the initial stage of decoration, for doping the same volumetric fraction of Pd content in both micropores and large pores, the micropore surface area reduces more significantly, since the surface area per unit volume in micropores is larger. When the supermicropores (0.7 – 2 nm) are filled, the resistance to fill the ultramicropores (< 0.7 nm) by Pd solution during decoration is enhanced with the decrease of the pore diameter in terms of Washburn's law [184]. At this stage, the fraction of filled micropore volumes is comparably less than that in large pores. In the Pd decorated GNPs700s, both the equivalent micropore SSAs and the equivalent external SSAs vary in a similar way with the increase in Pd decoration from GNPs700 to 20% Pd-GNPs700, which may indicate that, in the large pore sizes and slit-like pores, the Pd particles mostly stick on flat surfaces instead of filling the pores, resulting in the growth in equivalent surface area.

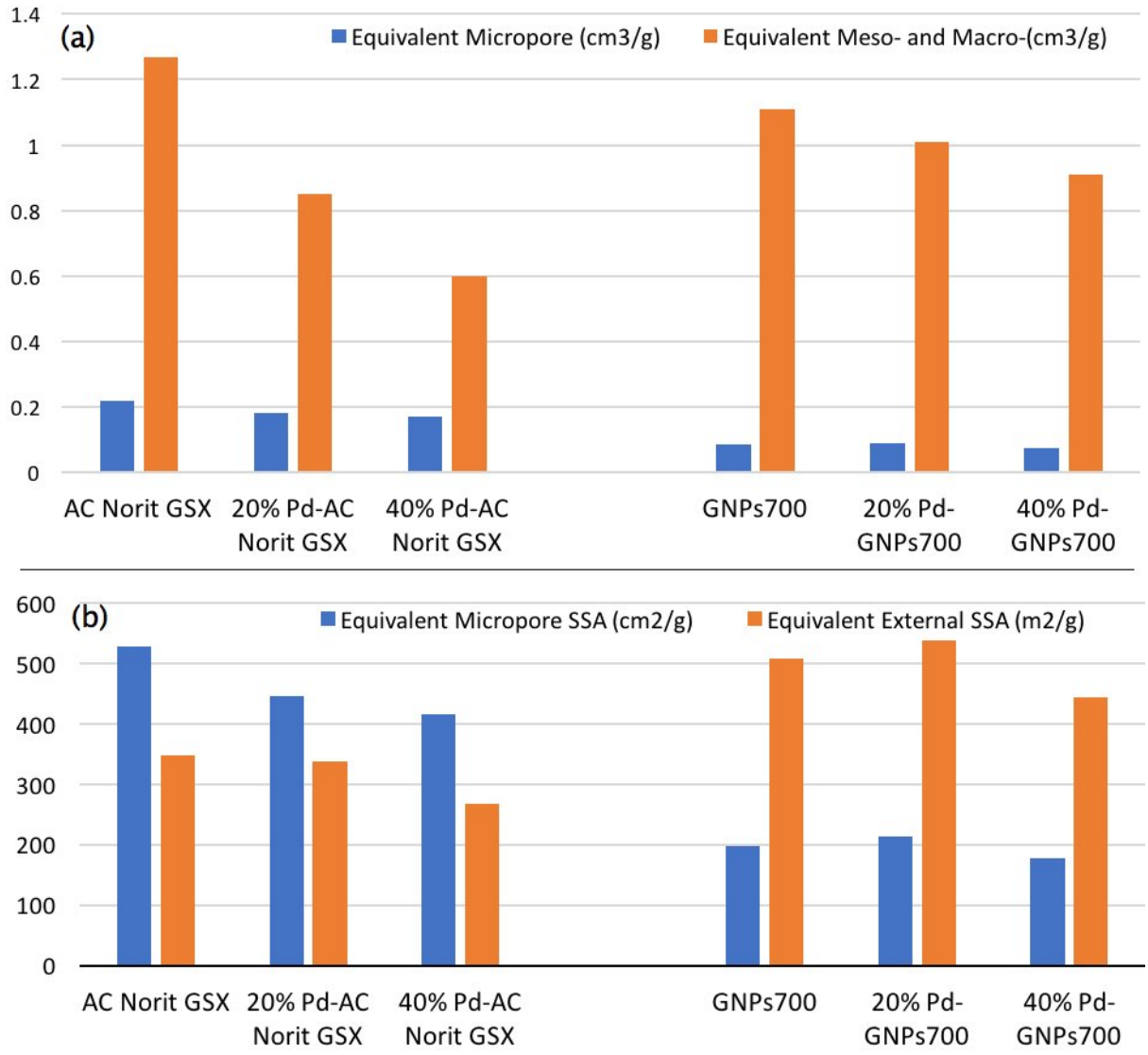

Figure 7.5.15 *(a) Comparison of both the equivalent micropore volume obtained from HJ t-method, and the external pore volume obtained from BJH method, for all samples. (b) Comparison of the equivalent micropore specific surface area (SSA) and the external specific surface area (SSA) of all samples based on t-methods. The pore volumes and surface areas of all Pd carbons have been adjusted to equivalent values with the assumption that the pore volumes and surface areas are entirely contributed by the carbon content.*

Overall, the porous properties of both carbons show no significant modifications with the introduction of additional decorated palladium. Conclusive evidence of Pd filling in micropores could not be found, as the amounts of micropore in both materials are very limited. In terms of the BJH analysis of pore size distributions, the reduction in pore volumes

for Pd decorated samples of both carbons are uniformly spread in the mesopore range, without showing distinct concentrations on specific pore diameters. Both materials exhibit a certain amount of pore volumes blocked by the introduced Pd particles, but the reduction in pore volume for the same amount of Pd decoration is detectably higher in AC Norit GSX than GNPs700, which is believed to correlate with the smaller pore sizes. The pore size of GNPs700 and the Pd-decorated GNPs700 is observed to be more uniformly distributed in the entire mesopore range than for AC Norit GSX related samples.

The characteristic difference of Pd particle sizes with similar Pd compositions in different carbons is probably due to the variation of average pore sizes in different carbon substrates. The AC Norit GSX has greater micropore volume and surface area than GNPs700. Additionally, the mesopores in AC Norit GSX tend to be concentrated in the smaller range (less than 10 nm), while GNPs700 carbons have mesopores concentrated primarily in the size range 10 – 20 nm. The barriers of pore walls ultimately restrict the growth of Pd-particles. Besides, in terms of the previous discussions on GNPs, a certain fraction of pores in GNPs-700 have slit-like shapes, while the pore shapes in amorphous AC Norit GSX are much more irregular. The palladium particles on a smooth slit-like surface are more likely to diffuse toward each other and form large particles than on the irregular and rough surfaces in AC Norit GSX.

The 20% Pd-GNPs700 that contain 11.23 wt% of Pd in the composite exhibit an increase in equivalent surface area on the carbon, which is caused by the small palladium particles attaching on the flat surface of large pores, for instance, slit-like pores. Although the overall surface area per unit mass is reduced by heavy Pd atoms, the overall surface area per unit volume is increased because of the negligible volumetric contribution of decorated Pd. The small size of Pd particles is also beneficial to increasing the surface area of the Pd particles and enhancing their potential catalytic effects. Therefore, slit-like pores and flat pore surfaces have potential for building carbon composites by decoration, and a small amount of Pd or other metal decoration can be used to build porous catalytic carbon composites for gas adsorption.

7.5.3 The effects of Pd on hydrogen cryosorption of two carbon materials

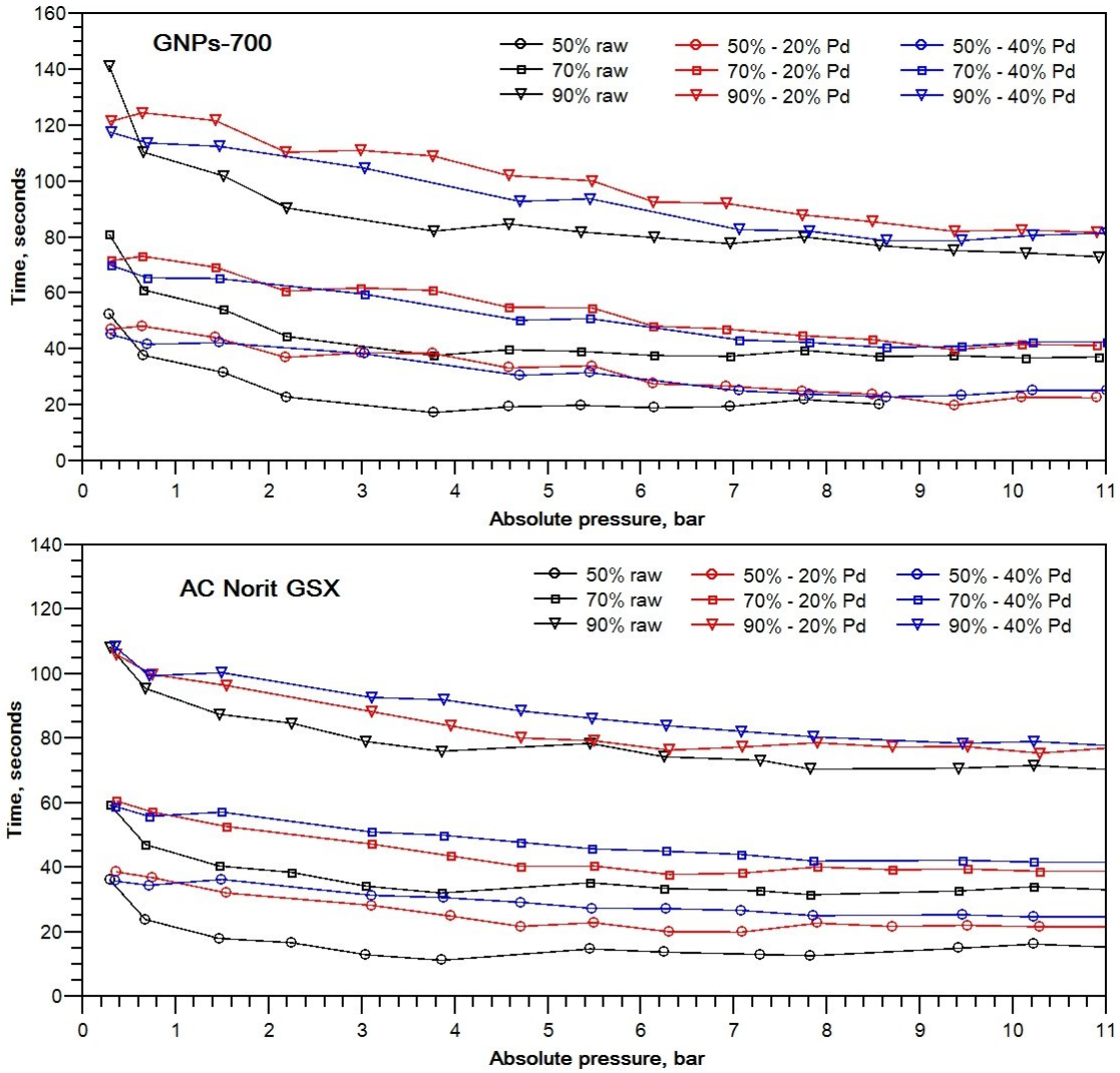

Figure 7.5.16 *The time required to reach the relative 50% (O), 70% (□) and 90% (▽) of saturated H_2 uptakes (usually 400 seconds) at 77 K and various pressures for raw carbon (black), 20% Pd deposition (red) and 40% Pd deposition (blue) of both GNPs-700 and activated carbons.*

As observed in section 7.2.2, the time to reach maximum hydrogen uptake is difficult to define, because the rate of change in uptake becomes very low as the uptake approaches the equilibrium. In order to investigate whether palladium affects the kinetics of hydrogen cryosorption, it is assumed based on experimental experience that the uptakes at 400 seconds can be regarded as the maximum uptake. The time required for reaching 50 %, 70 % and 90 % of the maximum uptake for each measurement are found and plotted for both

GNPs-700 and AC Norit GSX in the raw material, 20 % Pd decoration and 40 % Pd decoration, as shown in **Figure 7.5.16**. There is no significant difference between 20 % Pd (red line) and 40 % Pd (blue line) in the time taken to reach a similar level of uptake, which suggests that the Pd particles do not effectively accelerate or decelerate the adsorption progress. It is also observed that the time difference between the raw carbons and the Pd decorated carbons is less significant at pressures above 5 bar, while adsorption on the raw carbons take noticeably less time than on Pd carbons at low pressures of 1 – 4 bar in all cases. The prolonged time requirement for adsorption on Pd decorated carbons at low pressures might be caused by the reduction of pore sizes by doped Pd particles, in which the flow resistance by pore walls is enhanced according to Washburn's law. By contrast, the resistance effect is less significant at higher pressures, which explains the reduced time difference at high pressures like 10 bar. For hydrogen adsorption at room temperature or higher, the hydrogen adsorption is rapid and the time difference is not detectable.

The hydrogen uptake isotherms of all samples are presented in **Figure 7.5.17**. In order to investigate the potential Pd effects on hydrogen uptake, the isotherms of the Pd decorated samples were also adjusted to represent the expected behaviour if the surface area was equal to that of the raw carbon, and presented in red in **Figure 7.5.17**. Since the most critical parameter for hydrogen adsorption is the surface area, the hydrogen uptakes of Pd-decorated carbons should be comparable to those of the raw materials with similar surface area. However, except for the 20 % Pd-GNPs700 that shows a similar isotherm to that of the raw carbon, the other three Pd carbons exhibit significantly larger amounts of hydrogen uptake for the same BET surface area, which suggests a contribution from Pd decoration. The different performance of these three Pd-carbons is demonstrated in **Figure 7.5.18 (a)**, showing that the hydrogen uptake per unit surface area with Pd decoration is significantly higher than for pure carbon sorbents.

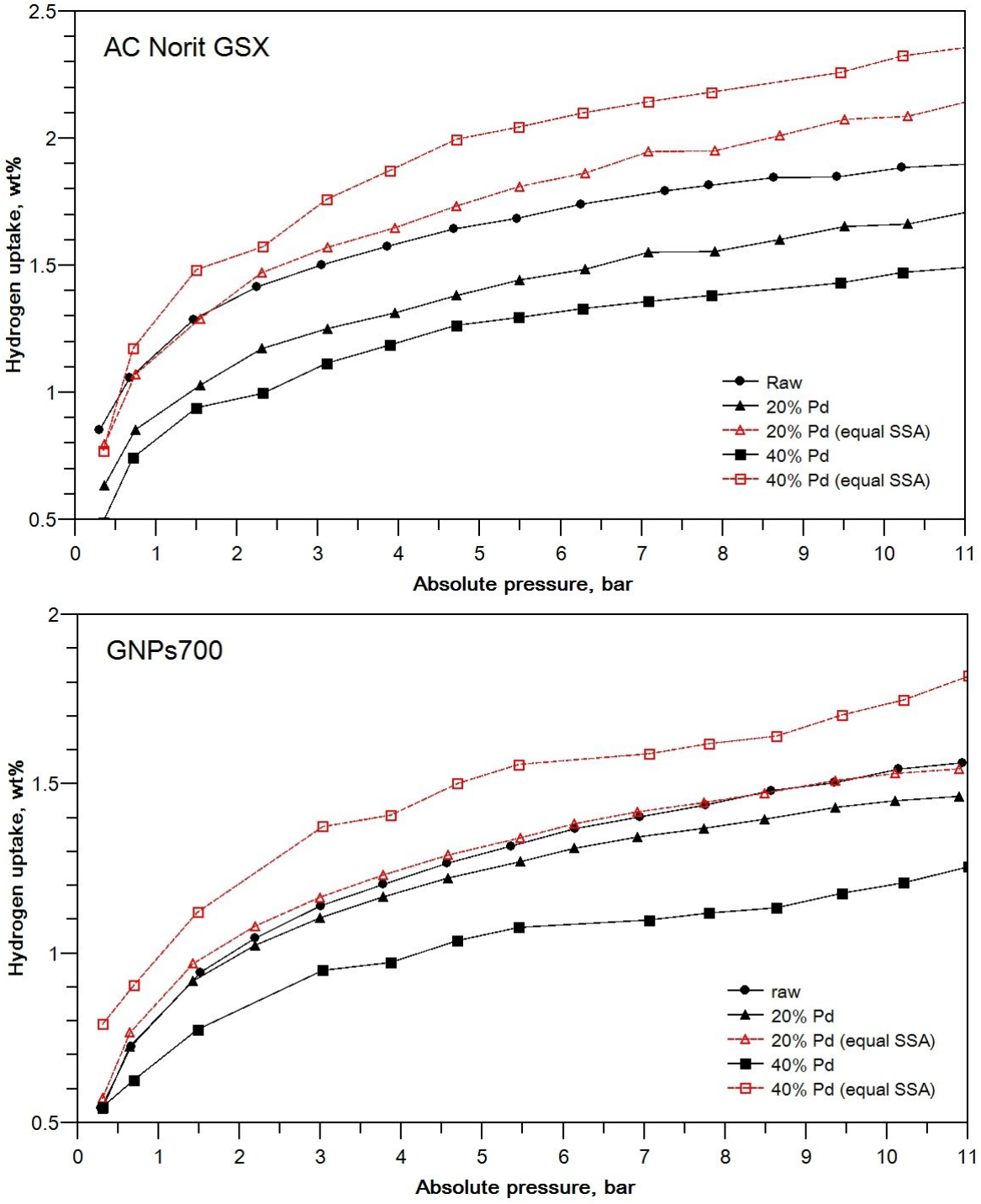

Figure 7.5.17 *The hydrogen isotherms are illustrated as original uptakes (black), and adjusted uptakes for Pd doped carbons to show the expected behaviour with equal BET SSA to raw carbons (red), 20 % Pd deposition (actually around 10 wt%) and 40 % Pd deposition (actually around 20 wt%) for both AC Norit GSX carbons and GNPs-700 carbons.*

There are two possible explanations for this phenomenon. The first explanation is that the sizes of some pores became smaller with the introduction of Pd particles on the surface. If the reduced pore sizes are accessible to hydrogen molecules but small enough to block the nitrogen molecules, the measured BET surface areas are underestimated with the nitrogen adsorption isotherms, which further explains the increase in hydrogen uptakes. The other explanation is the formation of palladium hydride. Unlike with nitrogen adsorption, the formation of palladium hydride is usually expected in the palladium – hydrogen system, in addition to surface physisorption [20]. Hydrogen atoms can fill in the octahedral interstitial sites of palladium crystallites to form palladium hydride PdH_x, where *x* is the coverage ratio of all available vacant sites, for instance, up to 0.6 of *x* representing 60 % coverage at room temperature [20]. The *x* value becomes larger with the decrease of temperature and the increase of pressure. Thus, the *x* is expected to higher than 0.6 at 77K and similar pressure conditions, but the exact value of *x* is still not clear. By conservatively assuming that *x* is equal to 0.6 at 77 K, the uptakes contributed by the formation of palladium hydride can be up to 0.56 wt% in respect of the mass of Pd content, which means that 20 wt% Pd in a carbon composite can bring more than 0.11 wt% hydrogen uptakes in addition to physisorption on the surface. Nevertheless, with the possible extra contribution of PdH alloys, the > 1 wt% of hydrogen uptake from physisorption at 77 K still dominates the overall hydrogen storage performance.

Unlike the other Pd carbons, the adjusted 20 % Pd-GNPs700 has a similar isotherm with raw GNPs-700 in **Figure 7.5.17**. In terms of the pore distribution analysis, the mesopore volume does not reduce noticeably with Pd decoration in 20 % Pd-GNPs700, and its equivalent pore surface area shows a slight increase, which implies that the Pd particles are uniformly distributed on the surfaces. The micropore volume is smaller in 20 % Pd-GNPs700 than 20% Pd-AC Norit GSX, and the pores are larger on average and more slit-like in GNPs-700 than in AC Norit GSX, so that the potential blockage of pore volumes in 20% Pd-GNPs700 by Pd particles, such that those pores become inaccessible to nitrogen, is expected to be less significant than for 20 % Pd-AC Norit GSX. The hydrogen uptake of 20 % Pd-GNPs700 at pressures less than 8 bar was observed to be marginally higher than that of GNPs-700, which might be caused by the formation of palladium hydride. As shown in **Figure 7.5.18 (b)**, the approximate linear expressions presented from the Langmuir plots of carbon samples

indicate the dominance of physisorption in hydrogen cryosorption, as discussed in section 7.2.3. Although the Langmuir model does not encompass any potential formation of PdH, it is still a useful indicative method to investigate the contribution of ideal physisorption in hydrogen adsorption.

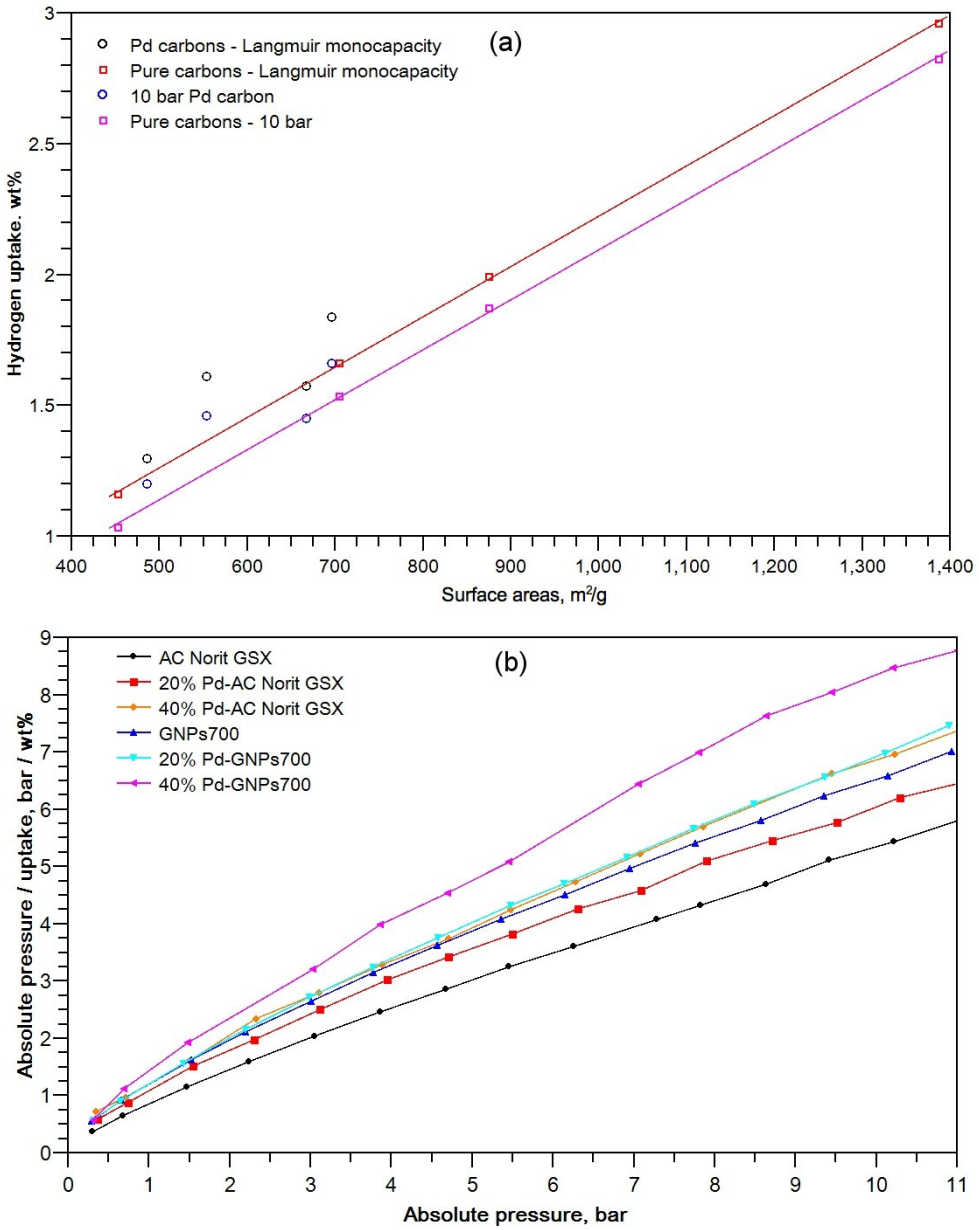

Figure 7.5.18 *(a) Comparison of the measured uptakes at 10 bar pressure and the calculated Langmuir monolayer capacities versus surface area between Pd decorated carbons and pure carbon sorbents studied in section 7.1. (b) Langmuir plots of Pd decorated carbons and their raw carbons.*

Overall, the Pd content in carbon sorbents does not seem to greatly affect the hydrogen adsorption kinetics. The introduction of Pd particles on porous materials can partially shrink the pore sizes, further increasing the resistance to gas flow into the pore and extending the time required for hydrogen adsorption at 77 K. At high pressures, both Pd carbons and raw carbons display similar adsorption kinetics. With the introduction of Pd particles on carbons, the hydrogen uptakes of the resulting composites can no longer be completely explained with the ideal adsorption theory based on BET surface areas. For the same BET surface area, the Pd carbons exhibit extra hydrogen uptake per unit surface area, which might be caused by small pores, obstructed by the introduced Pd particles, becoming inaccessible to probe nitrogen molecules but remaining accessible to hydrogen molecules, resulting in underestimated BET surface areas. The formation of palladium hydride can also be a potential reason to explain the increased hydrogen uptake per unit surface area in Pd decorated carbons. Additional work is required to further investigate the effect.

7.5.4 Summary

In this section, Pd decorated AC Norit GSX and GNPs-700 with two different concentrations were studied with respect to the growth of Pd particles, the properties and size distributions of pores and the effects of Pd on hydrogen adsorption at 77 K.

During the analysis, it was discovered that roughly 50 % of the deposited palladium was lost during the decoration process, resulting in 10.86 wt% and 18.89 wt% for the nominally 20 % and 40 % Pd concentrations on AC Norit GSX. Similarly, for the AC Norit GSX samples, the corresponding concentrations were 11.23 wt% and 21.58 wt%. For the same amount of Pd addition, Pd-GNPs700 carbons have nearly doubled Pd crystallite sizes compared with the decorated AC Norit GSXs, based on XRD analysis. The different sizes of formed Pd particles in different raw carbons are believed to correlate with the average pore sizes of the carbon substrates.

The porous structures of carbon substrates show no significant modifications with the additional Pd decoration. Both micropore volumes and mesopore volumes are reduced with the introduction of Pd particles, and there is no significantly localised Pd decoration observed on either micropores or mesopores. The surface area decreases with the increased concentration of Pd particles, but the reduction in surface area is discovered to be slightly

compensated in 20 % Pd-GNPs700, due to the formation of small Pd particles on larger pores or flat surfaces, which further contribute a certain amount of surface area to the material. Some Pd particles are also found to block the “neck” of large pores, further reducing pore volumes.

The addition of Pd to carbon sorbents was not found to significantly influence the hydrogen adsorption kinetics at high pressures, but at low pressures the adsorption rate was slightly constrained. This is possibly related to the increased flow resistance of the pores, of which the size is reduced by the extra palladium particles. The hydrogen uptake per unit surface area in Pd carbons was observed to be higher than for the raw materials, which may be caused by underestimated pore areas and the formation of palladium hydride. The validation of these explanations requires further experimental work.

8 Conclusions

In the presented thesis, selected carbon sorbents – AC Norit GSX, AC Norit ROW and graphene nanoplatelets GNPs-500 and GNPs-700 – were studied for their pore properties. AC Norit ROW has micropore-dominated structures, exposing large micropore surfaces, while AC Norit GSX, GNPs-500 and GNPs-700 are dominated by mesopores with only small fractions of micropores. The amorphous AC Norit GSX and AC Norit ROW were discovered to have irregular pore shapes and small average pore sizes, while GNPs-500 and GNPs-700 have a certain amount of slit-shaped mesopores and larger average pore sizes. Although GNPs-500 and GNPs-700 exhibit large surface areas of 453 m^2/g and 705 m^2/g respectively, their graphitic structures retain outstanding degrees of ordering in both intralayer atomic arrangement and c-axis layer stacking in comparison with amorphous carbon sorbents, which is beneficial not only for studying adsorption behaviour but also in applications as carbon substrates for building functional porous composites, such as decorated carbons with catalytic metals. The measured hydrogen uptakes and porous properties of involved sorbents are summarised in the following table.

Table 8.1 *The measured hydrogen uptakes and porous properties of six sorbents: 13X, zeolite NaY, AC Norit ROW, AC Norit GSX, GNPs-700 and GNPs-500.*

	H_2 uptake at 10 bar, 77 K (wt%)	Monolayer capacity[a] (wt%)	BET surface area (m^2/g)	Micropore surface area[b] (m^2/g)	Meso- and Macro-surface area[b] (m^2/g)	Micropore volume[b] (cm^3/g)	Meso- and Macro-volume[c] (cm^3/g)
13X	1.62	1.68	720	-	-	-	-
Zeolite NaY	1.84	1.88	900	-	-	-	-
AC Norit ROW	2.82	2.96	1387	1210	177	0.49	0.16
AC Norit GSX	1.87	1.99	875	528	347	0.22	1.27
GNPs-700	1.53	1.66	705	197	508	0.085	1.11
GNPs-500	1.03	1.16	453	101	352	0.044	0.81

[a] referring to Langmuir model;
[b] referring to Harkins-Jura t-method;
[c] referring to Barrett-Joyner-Halenda method.

Two carbons, the plasma carbons and biochars, were obtained via microwave splitting methane and pyrolysis of biomass *Miscanthus* respectively. The structural evolution of these carbons during carbonisation was studied intensively using Raman spectroscopy, XRD, XPS and FTIR. The development of graphitic structures in these carbons agrees with the Ferarri and Robertson "amorphisation trajectory" theory based on Raman spectroscopy. Although both carbons expressed some types of disorder in their graphitic structures, they were discovered to be nonporous with low surface areas, which might be due to the loose packing of lightweight mobile particles in plasma carbons and the lack of an activation process in producing biochars.

AC Norit GSX and GNPs-700 were experimentally decorated with Pd particles. The porous structures of both raw carbons were discovered to have no detectable modifications during the decoration process. The overall pore volumes and surface areas of both carbons were observed to decrease with the increase in Pd content. The reduction of pore volumes was caused not only by the uniform distribution of Pd particles but also by local blockage of pore "necks". The extra Pd contents in these carbons neither promoted nor restricted the hydrogen adsorption kinetics on these carbons at 77 K and 4 – 10 bar pressure. However, the hydrogen uptakes per unit surface area of Pd decorated carbons were significantly higher than those of pure carbon sorbents. This might be caused by underestimated surface areas found during nitrogen adsorption tests as a result of Pd obstructions rendering some pores inaccessible to nitrogen molecules but still accessible to hydrogen molecules. The formation of palladium hydride might also be a potential reason for this phenomenon.

Based on the results presented in this report, the previous hypotheses were reviewed, resulting in the following conclusions:

I. Differential manometry can be implemented affordably for fast hydrogen cryosorption measurements at 77 K and pressures up to 11 bar as presented in this report. The explosive hydrogen gas can be handled safely with special precautions, such as a pneumatic control system, isolated experimental cells and carefully designed experimental procedures. Differential manometry can potentially provide more accurate and sensitive to the small uptake than Sievert's type apparatus

because the hydrogen uptake is measured using a differential pressure transducer with small pressure range.

II. High-vacuum degassing in hydrogen adsorption measurements is discovered to be essential to provide accurate gas uptakes for micropore-dominant sorbents, which is likely to correlate with the micropore filling of condensed nitrogen residual at 77 K. The difference between high-vacuum and medium-vacuum outgassing for measured hydrogen uptakes on the mesoporous sorbent GNPs-700 was not significant, which might be due to the absence of nitrogen condensation on mesopores in comparison with open surfaces, such as the walls of volume chambers.

III. The combination of BET, t-method, α_s-method and BJH-method analyses enabled a systematic study of porous properties on mesoporous sorbents. The results of the t-method are in excellent agreement with both the α_s-method and the BJH-method so that the results obtained from different methods can be compared with each other.

IV. The “amorphisation trajectory” proposed by Ferrari and Robertson is applicable not only to the plasma carbons and biochars, but also to the studied graphene nanoplatelets with a diverse range surface areas. Raman spectroscopy can also be applied to identify the crystallinity of graphitic materials with the assistance of XRD analysis.

V. Graphene nanoplatelets (GNPs) can have large surface areas without reducing the ordering of graphitic structures. The flake-like GNPs with slit-shaped mesopores can be an excellent substrate for decoration with functional additives, such as palladium particles. The decorated carbon with small amounts of palladium does not show a significant reduction of surface areas and pore volumes; in fact, the surface areas per unit volume can be expected to increase with small particles attached on large pore surfaces.

VI. The palladium content of decorated carbons does not significantly affect hydrogen adsorption kinetics except at low pressures. The hydrogen uptake per unit mass of Pd decorated carbons is observed to decrease, due to the decorated heavy Pd content in comparison with carbon substrates. However, the hydrogen uptake per unit surface area of Pd decorated carbons is noticeably higher than that of raw

carbons. The reason for this phenomenon might be that the Pd particles obstruct access to some pores such that they are inaccessible to nitrogen molecules but accessible to hydrogen molecules, and as a result the BET surface areas of decorated carbons are underestimated. The formation of palladium hydride might also be a reason for the increased hydrogen uptake per unit area, which requires further investigation.

Due to the limitation of current equipment design, the hydrogen sorption experiment can be only performed at a single temperature of 77K. With the consideration of future modification on the differential manometry system, a temperature controlling unit should be introduced to adjust the temperature in small increments between 77 K and 673 K, which would provide the possibility of measuring not only the hydrogen uptakes at a wide range of temperature conditions, but also the isosteric heat of hydrogen adsorption. The introduction of heating unit into ATEX zone 2 environment needs considerations of using specifically rated devices that are normally shielded with protective cases and conducting careful risk assessments to comply with the university safety regulations.

Based on the results discussed in this study, Pd decorated carbons have introduced noticeable influences on the hydrogen storage performance of raw carbon sorbents at 77 K. However, there are limited literatures concerning with the formation of palladium hydride and hydrogen spillover effects by palladium at 77 K, which could be a potential direction to investigate the mechanism of hydrogen sorption in Pd decorated carbon sorbents and further improve the overall hydrogen uptakes at cryogenic temperatures.

9 References

[1] J. Watt, “Watt’s Method of Lessening the Consumption of Steam & Fuel in Fire Engines,” U.K. Patent A.D.1769 No.913, 1769.

[2] J. Rifkin, *The Hydrogen Economy: The Creation of the Worldwide Energy Web and the Redistribution of Power on Earth*, First Edit. Oxford: Polity Press, 2002.

[3] J. S. Rigden, *Hydrogen: The Essential Element*. Cambridge, Massachusetts: Harvard Universiy Press, 2003.

[4] L. Schlapbach and A. Züttel, “Hydrogen-storage materials for mobile applications,” *Nature*, vol. 414, no. 6861, pp. 353–358, 2001.

[5] B. Yildiz and M. S. Kazimi, “Efficiency of hydrogen production systems using alternative nuclear energy technologies,” *Int. J. Hydrogen Energy*, vol. 31, no. 1, pp. 77–92, 2006.

[6] U. S. Department of Energy. (2015). *Fuel Cell Technologies Office Multi-Year Research, Development, and Demonstration Plan* [Online]. Available: https://energy.gov/eere/fuelcells/downloads/fuel-cell-technologies-office-multi-year-research-development-and-22.

[7] Toyota. (2017). *Toyota Mirai* [Online]. Available: https://ssl.toyota.com/mirai/fcv.html#module-CarPageHowItWorks.

[8] Hyundai. (2017). *Hyundai ix35 hydrogen fuel cell vehicle* [Online]. Available: http://www.hyundai.co.uk/about-us/environment/hydrogen-fuel-cell.

[9] Honda. (2017). *Clarity Fuel Cell* [Online]. Available: https://automobiles.honda.com/clarity#technology.

[10] D. Mori and K. Hirose, “Recent challenges of hydrogen storage technologies for fuel cell vehicles,” *Int. J. Hydrogen Energy*, vol. 34, no. 10, pp. 4569–4574, 2009.

[11] *Plastics -- Determination of apparent density of material that can be poured from a specified funnel*, ISO 60, 1997.

[12] S. S. Kaye, A. Dailly, O. M. Yaghi, and J. R. Long, “Impact of preparation and handling on the hydrogen storage properties of Zn4O(1,4-benzenedicarboxylate)3 (MOF-5),” *J. Am.*

Chem. Soc., vol. 129, no. 46, pp. 14176–14177, 2007.

[13] K. M. Thomas, "Adsorption and desorption of hydrogen on metal–organic framework materials for storage applications: comparison with other nanoporous materials," *Dalt. Trans.*, no. 9, p. 1487, 2009.

[14] B. Panella, M. Hirscher, and S. Roth, "Hydrogen adsorption in different carbon nanostructures," *Carbon N. Y.*, vol. 43, no. 10, pp. 2209–2214, 2005.

[15] H. W. Langmi, A. Walton, M. M. Al-Mamouri, S. R. johnson, D. Book, J. D. Speight, P. P. Edwards, I. Gameson, P. A. Anderson, and I. R. Harris, "Hydrogen storage in zeolites A, X, Y and RHO," *J. Alloys Compd.*, vol. 356–357, pp. 710–715, 2003.

[16] BMW archieves. (2017). [Online]. Available: http://www.bmwarchive.org/e-code/.

[17] Wired. (2006). Road Testing BMW's Hydrogen 7 [Online]. Available: https://www.wired.com/2006/11/road-testing-bmws-hydrogen-7

[18] J. R. H. Wiswall, J. J. Reilly, and W. E. Wallace, "Hydrogen Storage in Metal Hydrides," *Science*, vol. 186, no. 4170, pp. 1158–1158, Dec. 1974.

[19] G. Sandrock and G. Thomas, "The IEA/DOE/SNL on-line hydride databases," *Appl. Phys. A*, vol. 72, no. 2, pp. 153–155, Feb. 2001.

[20] L. L. Jewell and B. H. Davis, "Review of absorption and adsorption in the hydrogen-palladium system," *Appl. Catal. A Gen.*, vol. 310, no. 1–2, pp. 1–15, 2006.

[21] M. Yamauchi, H. Kobayashi, and H. Kitagawa, "Hydrogen storage mediated by Pd and Pt nanoparticles," *ChemPhysChem*, vol. 10, no. 15, pp. 2566–2576, 2009.

[22] F. A. Lewis, "The Hydrides of Palladium and Palladium Alloys: A Review of Recent Researches," *Platin. Met. Rev.*, vol. 4, no. 4, pp. 132–137, 1960.

[23] M. Johansson, E. Skúlason, G. Nielsen, S. Murphy, R. M. Nielsen, and I. Chorkendorff, "Hydrogen adsorption on palladium and palladium hydride at 1 bar," *Surf. Sci.*, vol. 604, no. 7–8, pp. 718–729, 2010.

[24] A. J. Lachawiec, G. Qi, and R. T. Yang, "Hydrogen storage in nanostructured carbons by spillover: Bridge-building enhancement," *Langmuir*, vol. 21, no. 24, pp. 11418–11424, 2005.

[25] S. Khoobiar, “Particle to Particle Migration of Hydrogen Atoms on Platinum—Alumina Catalysts from Particle to Neighboring Particles,” *J. Phys. Chem.*, vol. 68, no. 2, pp. 411–412, 1964.

[26] J. H. Sinfelt and P. J. Lucchesi, “Kinetic Evidence for the Migration of Reactive Intermediates in Surface Catalysis,” *J. Am. Chem. Soc.*, vol. 85, no. 21, pp. 3365–3367, 1963.

[27] W. C. Conner and J. L. Falconer, “Spillover in Heterogeneous Catalysis,” *Chem. Rev.*, vol. 95, no. 3, pp. 759–788, 1995.

[28] M. Boudart, A. W. Aldag, and M. A. Vannice, “On the slow uptake of hydrogen by platinized carbon,” *J. Catal.*, vol. 18, no. 1, pp. 46–51, 1970.

[29] J. L. C. Rowsell and O. M. Yaghi, “Strategies for Hydrogen Storage in Metal-Organic Frameworks,” *Angew. Chemie Int. Ed.*, vol. 44, no. 30, pp. 4670–4679, Jul. 2005.

[30] D. P. Broom, *Hydrogen Storage Materials: the Characterisation of Their Storage Properties*. London: Springer, 2011.

[31] L. J. Murray, M. Dincă, and J. R. Long, “Hydrogen storage in metal–organic frameworks,” *Chem. Soc. Rev.*, vol. 38, no. 5, p. 1294, 2009.

[32] H. Furukawa, N. Ko, Y. B. Go, N. Aratani, S. B. Choi, E. Choi, A. Ö. Yazaydin, R. Q. Snurr, M. O'Keeffe, J. Kim, and O. M. Yaghi, “Ultrahigh Porosity in Metal-Organic Frameworks,” *Science*, vol. 329, no. 5990, pp. 424–428, 2010.

[33] R. D. Kennedy, V. Krungleviciute, D. J. Clingerman, J. E. Mondloch, Y. Peng, C. E. Wilmer, A. A. Sarjeant, R. Q. Snurr, J. T. Hupp, T. Yildirim, O. K. Farha, and C. A. Mirkin, “Carborane-based metal-organic framework with high methane and hydrogen storage capacities,” *Chem. Mater.*, vol. 25, no. 17, pp. 3539–3543, 2013.

[34] M. P. Suh, H. J. Park, T. K. Prasad, and D. W. Lim, “Hydrogen storage in metal-organic frameworks,” *Chem. Rev.*, vol. 112, no. 2, pp. 782–835, 2012.

[35] Q. Zhao, W. Yuan, J. Liang, and J. Li, “Synthesis and hydrogen storage studies of metal-organic framework UiO-66,” *Int. J. Hydrogen Energy*, vol. 38, no. 29, pp. 13104–13109, 2013.

[36] B. Zheng, R. Yun, J. Bai, Z. Lu, L. Du, and Y. Li, “Expanded porous MOF-505 analogue exhibiting large hydrogen storage capacity and selective carbon dioxide adsorption,” *Inorg. Chem.*, vol. 52, no. 6, pp. 2823–2829, 2013.

[37] O. K. Farha, A. Ö. Yazaydin, I. Eryazici, C. D. Malliakas, B. G. Hauser, M. G. Kanatzidis, S. T. Nguyen, R. Q. Surr, and J. T. Hupp, “De novo synthesis of a metal–organic framework material featuring ultrahigh surface area and gas storage capacities,” *Nat. Chem.*, vol. 2, no. 11, pp. 944–948, 2010.

[38] K. Koh, A. G. Wong-Foy, and A. J. Matzger, “A porous coordination copolymer with over 5000 m^2/g BET surface area.,” *J. Am. Chem. Soc.*, vol. 131, no. 12, pp. 4184–5, 2009.

[39] H. Furukawa, M. A. Miller, and O. M. Yaghi, “Independent verification of the saturation hydrogen uptake in MOF-177 and establishment of a benchmark for hydrogen adsorption in metal–organic frameworks,” *J. Mater. Chem.*, vol. 17, no. 30, p. 3197, 2007.

[40] T. Q. Hua, R. K. Ahluwalia, J. K. Peng, M. Kromer, S. Lasher, and K. McKenney, “Technical assessment of compressed hydrogen storage tank systems for automotive applications,” *Int. J. Hydrogen Energy*, vol. 36, no. 4, pp. 3037–3049, Feb. 2011.

[41] J. Tomioka, K. Kiguchi, Y. Tamura, and H. Mitsuishi, “Influence of temperature on the fatigue strength of compressed-hydrogen tanks for vehicles,” *Int. J. Hydrogen Energy*, vol. 36, no. 3, pp. 2513–2519, Feb. 2011.

[42] J. Dong, X. Wang, H. Xu, Q. Zhao, and J. Li, “Hydrogen storage in several microporous zeolites,” *Int. J. Hydrogen Energy*, vol. 32, no. 18, pp. 4998–5004, Dec. 2007.

[43] Y. Li and R. T. Yang, “Hydrogen Storage in Low Silica Type X Zeolites,” *J. Phys. Chem. B*, vol. 110, no. 34, pp. 17175–17181, Aug. 2006.

[44] R. Chahine and T. K. Bose, “Low-pressure adsorption storage of hydrogen,” *Int. J. Hydrogen Energy*, vol. 19, no. 2, pp. 161–164, 1994.

[45] H. W. Langmi, D. Book, A. Walton, S. R. Johnson, M. M. Al-Mamouri, J. D. Speight, P. P. Edwards, I. R. Harrison, and P. A. Anderson, “Hydrogen storage in ion-exchanged zeolites,” *J. Alloys Compd.*, vol. 404–406, pp. 637–642, 2005.

[46] H. Wang, Q. Gao, and J. Hu, “High hydrogen storage capacity of porous carbons prepared by using activated carbon,” *J. Am. Chem. Soc.*, vol. 131, no. 20, pp. 7016–7022, 2009.

[47] N. Texier-Mandoki, J. Dentzer, T. Piquero, S. Saadallah, P. David, and C. Vix-Guterl, “Hydrogen storage in activated carbon materials: Role of the nanoporous texture,” *Carbon N. Y.*, vol. 42, no. 12–13, pp. 2744–2747, 2004.

[48] M. G. Nijkamp, J. E. M. J. Raaymakers, A. J. van Dillen, and K. P. de Jong, “Hydrogen storage using physisorption – materials demands,” *Appl. Phys. A Mater. Sci. Process.*, vol. 72, no. 5, pp. 619–623, May 2001.

[49] K. S. Novoselov, A. K. Geim, S. V. Morozov, D. Jiang, Y. Zhang, S. V. Dubonos, I. V. Grigorieva, and A. A. Firsov, “Electric Field Effect in Atomically Thin Carbon Films,” *Science*, vol. 306, no. 5696, pp. 666–669, Oct. 2004.

[50] F. Bonaccorso, L. Colombo, G. Yu, M. Stoller, V. Tozzini, A. C. Ferrari, R. S. Ruoff, and V. Pellegrini, “Graphene, related two-dimensional crystals, and hybrid systems for energy conversion and storage,” *Science*, vol. 347, no. 6217, p. 1246501, 2015.

[51] A. Zuttel, P. Sudan, P. Mauron, and P. Wenger, “Model for the hydrogen adsorption on carbon nanostructures,” *Appl. Phys. A-Materials Sci. Process.*, vol. 78, no. 7, pp. 941–946, 2004.

[52] J. O. Sofo, A. S. Chaudhari, and G. D. Barber, “Graphane: A two-dimensional hydrocarbon,” *Phys. Rev. B*, vol. 75, no. 15, p. 153401, Apr. 2007.

[53] D. C. Elias, R. R. Nair, T. M. G. Mohiuddin, S. V. Morozov, P. Blake, M. P. Halsall, A. C. Ferrari, D. W. Boukhvalov, M. I. Katsnelson, A. K. Geim, and K. S. Novoselov, “Control of Graphene’s Properties by Reversible Hydrogenation: Evidence for Graphane,” *Science*, vol. 323, no. 5914, pp. 610–613, Jan. 2009.

[54] H.-M. Cheng, Q.-H. Yang, and C. Liu, “Hydrogen storage in carbon nanotubes,” *Carbon N. Y.*, vol. 39, no. 10, pp. 1447–1454, Aug. 2001.

[55] C. Liu, Y. Y. Fan, M. Liu, H. T. Cong, H. M. Cheng, and M. S. Dresselhaus, “Hydrogen Storage in Single-Walled Carbon Nanotubes at Room Temperature,” *Science*, vol. 286,

no. 5442, pp. 1127–1129, Nov. 1999.

[56] D. P. Broom and M. Hirscher, “Irreproducibility in hydrogen storage material research,” *Energy Environ. Sci.*, vol. 9, no. 11, pp. 3368–3380, 2016.

[57] B. B. Pradhan, A. R. Harutyunyan, D. Stojkovic, J. C. Grossman, P. Zhang, M. W. Cole, V. Crespi, H. Goto, J. Fujiwara, and P. C. Eklund, “Large cryogenic storage of hydrogen in carbon nanotubes at low pressures,” *J. Mater. Res.*, vol. 17, no. 9, pp. 2209–2216, Sep. 2002.

[58] F. D. Masla and T. M. Littman, “Compressibility Chart for Hydrogen and Inert Gases,” *Ind. Eng. Chem.*, vol. 45, no. 7, pp. 1566–1568, 1953.

[59] R. H. Newton, “Activity Coefficients of Gases,” *Ind. Eng. Chem.*, vol. 27, pp. 302–306, 1935.

[60] K. S. W. Sing, “Reporting physisorption data for gas/solid systems with special reference to the determination of surface area and porosity (Recommendations 1984),” *Pure Appl. Chem.*, vol. 57, no. 4, pp. 2201–2218, Jan. 1985.

[61] F. Rouquerol, J. Rouquerol, K. S. W. Sing, P. Llewellyn, and G. Maurin, *Adsorption by powders and porous solids: princicles, methodology and applications*, 2nd ed. Kidlington, Oxford: Academic Press, 2014.

[62] P. Malbrunot, D. Vidal, J. Vermesse, R. Chahine, and T. K. Bose, “Adsorbent Helium Density Measurement and Its Effect on Adsorption Isotherms at High Pressure,” *Langmuir*, vol. 13, no. 3, pp. 539–544, 1997.

[63] *Determination of the specific surface area of solids by gas adsorption - BET method*, ISO 9277, 2010.

[64] D. Dollimore, P. Spooner, and A. Turner, “The BET method of analysis of gas adsoprtion and its relevance to the calculation of surface area,” *Surf. Technol.*, vol. 4, pp. 121–160, 1976.

[65] A. Züttel, P. Sudan, P. Mauron, T. Kiyobayashi, C. Emmenegger, and L. Schlapbach, “Hydrogen storage in carbon nanostructures,” *Int. J. Hydrogen Energy*, vol. 27, no. 2, pp. 203–212, 2002.

[66] P. H. Emmett and S. Brunauer, “The Adsorption of Nitrogen by Iron Synthetic Ammonia Catalysts,” *J. Am. Chem. Soc.*, vol. 56, no. 1, pp. 35–41, 1934.

[67] P. H. Emmett and S. Brunauer, “The Use of Low Temperature van der Waals Adsorption Isotherms in Determining the Surface Areas of Iron Synthetic Ammonia Catalysts,” *J. Am. Chem. Soc.*, vol. 59, no. 8, pp. 1553–1564, 1937.

[68] S. Brunauer and P. H. Emmett, “The Use of Low Temperature van der Waals Adsorption Isotherms in Determining the Surface Areas of Various Adsorbents,” *J. Am. Chem. Soc.*, vol. 59, no. 12, pp. 2682–2689, 1937.

[69] P. H. Emmett and S. Brunauer, “Accumulation of Alkali Promoters on Surfaces of Iron Synthetic Ammonia Catalysts,” *J. Am. Chem. Soc.*, vol. 59, no. 2, pp. 310–315, 1937.

[70] S. Brunauer, P. H. Emmett, and E. Teller, “Adsorption of Gases in Multimolecular Layers,” *J. Am. Chem. Soc.*, vol. 60, no. 1, pp. 309–319, 1938.

[71] J. Rouquerol, P. Llewellyn, and F. Rouquerol, “Is the BET equation applicable to microporous adsorbents?,” *Stud. Surf. Sci. Catal.*, vol. 160, pp. 49–56, 2007.

[72] S. Storck, H. Bretinger, and W. F. Maier, “Characterization of micro- and mesoporous solids by physisorption methods and pore-size analysis,” *Appl. Catal. A Gen.*, vol. 174, no. 1–2, pp. 137–146, 1998.

[73] M. R. Bhambhani, P. A. Cutting, K. S. W. Sing, and D. H. Turk, “Analysis of Nitrogen Adsorption Isotherms on Porous and Nonporous Silicas by the BET and αs Methods,” *J. Colloid Interface Sci.*, vol. 38, no. 1, pp. 109–117, 1972.

[74] L. F. Gleysteen and V. R. Deitz, “Hysteresis in the physical adsortion of nitrogen on bone char and other adsorbents,” *J. Res. Natl. Bur. Stand.*, vol. 35, pp. 285–307, 1945.

[75] M. D. Donohue and G. L. Aranovich, “Adsorption Hysteresis in Porous Solids,” *J. Colloid Interface Sci.*, vol. 205, no. 1, pp. 121-130, 1998.

[76] K. S. W. Sing, “Adsorption methods for the characterization of porous materials,” *Adv. Colloid Interface Sci.*, vol. 76–77, pp. 3–11, 1998.

[77] C. A. Jessop, S. M. Riddiford, N. A. Seaton, J. P. R. B. Walton, and N. Quirke, “The Determination of The Pore Size Distribution of Porous Solids Using A Molecular Model

to Interpret Nitrogen Adsorption Measurements," in *Studies in Surface Science and Catalysis, Volume 62*, Elsevier Science, 1991, pp. 123–132.

[78] C. Lastoskie, K. E. Gubbins, and N. Quirke, "Pore size distribution analysis of microporous carbons: a density functional theory approach," *J. Phys. Chem.*, vol. 97, no. 18, pp. 4786–4796, May 1993.

[79] C. M. Lastoskie and K. E. Gubbins, "Characterization of Porous Materials Using Density Functional Theory and Molecular Simulation," in *Studies in Surface Science and Catalysis: Volume 128, Characterisation of Porous Solids V*, Amsterdam: Elsevier Science, 2000, pp. 41–50.

[80] P. I. Ravikovitch, A. Vishnyakov, R. Russo, and A. V. Neimark, "Unified Approach to Pore Size Characterization of Microporous Carbonaceous Materials from N2, Ar,and CO2 Adsorption Isotherms," *Langmuir*, vol. 16, no. 5, pp. 2311–2320, 2000.

[81] E. P. Barrett, L. G. Joyner, and P. P. Halenda, "The Determination of Pore Volume and Area Distributions in Porous Substances. I. Computations from Nitrogen Isotherms," *J. Am. Chem. Soc.*, vol. 73, no. 1, pp. 373–380, Jan. 1951.

[82] B. C. Lippens and J. H. de Boer, "Studies on pore systems in catalysts V. The t method," *J. Catal.*, vol. 4, no. 3, pp. 319–323, Jun. 1965.

[83] W. D. Harkins and G. Jura, "Surfaces of Solids. XIII. A Vapor Adsorption Method for the Determination of the Area of a Solid without the Assumption of a Molecular Area, and the Areas Occupied by Nitrogen and Other Molecules on the Surface of a Solid," *J. Am. Chem. Soc.*, vol. 66, no. 8, pp. 1366–1373, 1944.

[84] A. W. Marczewski. (2002). *A Practical Guide to Isotherms of ADSORPTION on Heterogeneous Surfaces* [Online]. Available: http://adsorption.org/awm/ads/Ads.htm

[85] D. Y. Murzin, *Engineering Catalysis*. Berlin/Boston: Walter de Gruyter GmbH, 2013.

[86] M. Jaroniec, M. Kruk, and J. P. Olivier, "Standard nitrogen adsorption data for characterization of nanoporous silicas," *Langmuir*, vol. 15, no. 16, pp. 5410–5413, 1999.

[87] P. J. M. Carrott, K. S. W. Sing, and J. H. Raistrick, "The adsorption of nitrogen and water vapour by carbon-coated precipitated silica," *Colloids and Surfaces*, vol. 21, no. C, pp.

9–15, 1986.

[88] P. J. M. Carrott, R. A. Roberts, and K. S. W. Sing, “Adsorption of Nitrogen By Porous and Non-Porous Carbons,” *Carbon N. Y.*, vol. 25, no. 1, pp. 59–68, 1987.

[89] A. F. Kloutse, R. Zacharia, D. Cossement, R. Chahine, R. Balderas-Xicohténcatl, H. Oh, B. Streppel, M. Schlichtenmayer, and M. Hirscher, “Isosteric heat of hydrogen adsorption on MOFs: comparison between adsorption calorimetry, sorption isosteric method, and analytical models,” *Appl. Phys. A Mater. Sci. Process.*, pp. 1417–1424, 2015.

[90] Q. Zheng, X. Ji, S. Gao, and X. Wang, “Analysis of adsorption equilibrium of hydrogen on graphene sheets,” *Int. J. Hydrogen Energy*, vol. 38, no. 25, pp. 10896–10902, 2013.

[91] Z. W. Zhu, Q. R. Zheng, Z. H. Wang, Z. Tang, and W. Chen, “Hydrogen adsorption on graphene sheets and nonporous graphitized thermal carbon black at low surface coverage,” *Int. J. Hydrogen Energy*, vol. 42, no. 29, pp. 18465–18472, 2017.

[92] H. Y. Tian, C. E. Buckley, M. Paskevicius, D. A. Sheppard, S. B. Wang, C. J. Webb, and E. M. Gray, “Nanoscale cobalt doped carbon aerogel: Microstructure and isosteric heat of hydrogen adsorption,” *Int. J. Hydrogen Energy*, vol. 36, no. 17, pp. 10855–10860, 2011.

[93] G. Yushin, R. Dash, J. Jagiello, J. E. Fischer, and Y. Gogotsi, “Carbide-derived carbons: Effect of pore size on hydrogen uptake and heat of adsorption,” *Adv. Funct. Mater.*, vol. 16, no. 17, pp. 2288–2293, 2006.

[94] B. Schmitz, U. Müller, N. Trukhan, M. Schubert, G. Férey, and M. Hirscher, “Heat of adsorption for hydrogen in microporous high-surface-area materials,” *ChemPhysChem*, vol. 9, no. 15, pp. 2181–2184, 2008.

[95] S. H. Jhung, J. Sun Lee, J. Woong Yoon, D. Pyo Kim, and J. S. Chang, “Low-temperature adsorption of hydrogen on ion-exchanged Y zeolites,” *Int. J. Hydrogen Energy*, vol. 32, no. 17, pp. 4233–4237, 2007.

[96] R. Checchetto, G. Trettel, and A. Miotello, “Sievert-type apparatus for the study of hydrogen storage in solids,” *Meas. Sci. Technol.*, vol. 15, no. 1, pp. 127–130, 2004.

[97] R. Zacharia, K. Y. Kim, A. K. M. Fazle Kibria, and K. S. Nahm, “Enhancement of hydrogen

storage capacity of carbon nanotubes via spill-over from vanadium and palladium nanoparticles," *Chem. Phys. Lett.*, vol. 412, no. 4–6, pp. 369–375, 2005.

[98] R. Haul and G. Dümbgen, "Vereinfachte Methode zur Messung von Oberfliichengrofien durch Gasadsorption," *Chemie Ing. Tech.*, vol. 5, p. 349, 1960.

[99] F. Rouquerol, J. Rouquerol, and K. S. W. Sing, *Adsorption by powders and porous solids : principles, methodology, and applications*. San Diego: Academic Press, 1999.

[100] J. M. Blackman, J. W. Patrick, and C. E. Snape, "An accurate volumetric differential pressure method for the determination of hydrogen storage capacity at high pressures in carbon materials," *Carbon N. Y.*, vol. 44, no. 5, pp. 918–927, 2006.

[101] D. J. Browning, M. L. Gerrard, J. B. Lakeman, I. M. Mellor, R. J. Mortimer, and M. C. Turpin, "Studies into the Storage of Hydrogen in Carbon Nanofibers: Proposal of a Possible Reaction Mechanism," *Nano Lett.*, vol. 2, no. 3, pp. 201–205, 2002.

[102] A. Qajar, M. Peer, R. Rajagopalan, and H. C. Foley, "High pressure hydrogen adsorption apparatus: Design and error analysis," *Int. J. Hydrogen Energy*, vol. 37, no. 11, pp. 9123–9136, 2012.

[103] S. Sircar, C. Y. Wang, and A. D. Lueking, "Design of high pressure differential volumetric adsorption measurements with increased accuracy," *Adsorption*, vol. 19, no. 6, pp. 1211–1234, 2013.

[104] J. M. Zielinski, C. G. Coe, R. J. Nickel, A. M. Romeo, A. C. Cooper, and G. P. Pez, "High pressure sorption isotherms via differential pressure measurements," *Adsorption*, vol. 13, no. 1, pp. 1–7, 2007.

[105] J. W. McBain and A. M. Bakr, "A NEW SORPTION BALANCE," *J. Am. Chem. Soc.*, vol. 48, no. 3, pp. 690–695, Mar. 1926.

[106] C. Eyraud, "Forty years in instrumental thermogravimetry and microcalorimetry. Consequences in the study of solid transformations and for characterization of the texture of porous materials," *Thermochim. Acta*, vol. 100, no. 1, pp. 223–253, May 1986.

[107] P. Le Parlouër, "Combination of DSC 111 and thekmobalance : new setaram simultaneous TG-DSC 111," *Thermochim. Acta*, vol. 92, pp. 371–374, Sep. 1985.

[108] J. Rouquerol and L. Davy, “Automatic gravimetric apparatus for recording the adsorption isotherms of gases or vapours onto solids,” *Thermochim. Acta*, vol. 24, no. 2, pp. 391–397, Jun. 1978.

[109] F. Dreisbach, R. Staudt, M. Tomalla, and J. U. Keller, “Measurement of Adsorption Equilibria of Pure and Mixed Corrosive Gases: The Magnetic Suspension Balance,” in *Fundamentals of Adsorption: Proceedings of the Fifth International Confereence on Fundamentals of Adsorption*, Boston / Dordrecht / London: Kluwer Academic Publishers, 1996, pp. 259–268.

[110] V. N. Tsaneva, W. Kwapinski, X. Teng, and B. A. Glowacki, “Assessment of the structural evolution of carbons from microwave plasma natural gas reforming and biomass pyrolysis using Raman spectroscopy,” *Carbon N. Y.*, vol. 80, no. 1, pp. 617–628, 2014.

[111] M. Jasiński, M. Dors, and J. Mizeraczyk, “Production of hydrogen via methane reforming using atmospheric pressure microwave plasma,” *J. Power Sources*, vol. 181, no. 1, pp. 41–45, 2008.

[112] K. L. Juda, “Synthesis of carbon nanoforms by atmospheric pressure microwave plasma reforming of natural gas,” M.Phil. dissertation, Cambridge Univ., Cambridge, UK, 2013.

[113] P. Albers, R. Burmeister, K. Seibold, G. Prescher, S. F. Parker, and D. K. Ross, “Investigations of Palladium Catalysts on Different Carbon Supports,” *J. Catal.*, vol. 181, no. 1, pp. 145–154, 1999.

[114] M. L. Toebes, J. A. Van Dillen, and K. P. De Jong, “Synthesis of supported palladium catalysts,” *J. Mol. Catal. A Chem.*, vol. 173, no. 1–2, pp. 75–98, 2001.

[115] R. Campesi, F. Cuevas, R. Gadiou, E. Leroy, M. Hirscher, C. Vix-Guterl, and M. Latroche, “Hydrogen storage properties of Pd nanoparticle/carbon template composites,” *Carbon N. Y.*, vol. 46, no. 2, pp. 206–214, 2008.

[116] B. E. Warren and P. Bodenstein, “The shape of two-dimensional carbon black reflections,” *Acta Crystallogr.*, vol. 20, no. 5, pp. 602–605, 1966.

[117] B. E. Warren and P. Bodenstein, “The diffraction pattern of fine particle carbon blacks,” *Acta Crystallogr.*, vol. 18, no. 2, pp. 282–286, 1965.

[118] Y. Yürüm, A. Taralp, and T. N. Veziroglu, “Storage of hydrogen in nanostructured carbon materials,” *Int. J. Hydrogen Energy*, vol. 34, no. 9, pp. 3784–3798, 2009.

[119] V. C. Menon and S. Komarneni, “Porous adsorbents for vehicular natural gas storage: a review,” *J. Porous Mater.*, vol. 5, no. 1, pp. 43–58, 1998.

[120] B. Balasubramanian, F. Barbir, and J. Neutzler, “Optimal operating temperature and pressure of PEM fuel cell systems in automotive applications,” pp. 977–981, 1999.

[121] B. S. Ghoman, “Hydrogen Storage in Tubular Carbon Nano-Structures,” Ph.D. dissertation, Cambridge Univ, Cambridge, UK, 2008.

[122] K. M. Thomas, “Hydrogen adsorption and storage on porous materials,” *Catal. Today*, vol. 120, no. 3–4 SPEC. ISS., pp. 389–398, 2007.

[123] P. Bénard and R. Chahine, “Storage of hydrogen by physisorption on carbon and nanostructured materials,” *Scr. Mater.*, vol. 56, no. 10, pp. 803–808, 2007.

[124] S. Kishore, J. A. Nelson, J. H. Adair, and P. C. Eklund, “Hydrogen storage in spherical and platelet palladium nanoparticles,” *J. Alloys Compd.*, vol. 389, no. 1–2, pp. 234–242, 2005.

[125] W. C. Xu, K. Takahashi, Y. Matsuo, Y. Hattori, M. Kumagai, S. Ishiyama, K. Kaneko, and S. Iijima, “Investigation of hydrogen storage capacity of various carbon materials,” *Int. J. Hydrogen Energy*, vol. 32, no. 13, pp. 2504–2512, 2007.

[126] H. Jin, Y. S. Lee, and I. Hong, “Hydrogen adsorption characteristics of activated carbon,” *Catal. Today*, vol. 120, pp. 399–406, 2007.

[127] H. Wang, Q. Gao, J. Hu, and Z. Chen, “High performance of nanoporous carbon in cryogenic hydrogen storage and electrochemical capacitance,” *Carbon N. Y.*, vol. 47, no. 9, pp. 2259–2268, 2009.

[128] B. Streppel and M. Hirscher, “BET specific surface area and pore structure of MOFs determined by hydrogen adsorption at 20 K,” *Phys. Chem. Chem. Phys.*, vol. 13, no. 8, pp. 3220–3222, 2011.

[129] A. C. Ferrari and J. Robertson, “Interpretation of Raman spectra of disordered and amorphous carbon,” *Phys. Rev. B*, vol. 61, no. 20, pp. 14095–14107, 2000.

[130] F. Tuinstra and L. Koenig, “Raman Spectrum of Graphite,” *J. Chem. Phys.*, vol. 53, no. 3, pp. 1126–1130, 1970.

[131] A. C. Ferrari and J. Robertson, “Raman spectroscopy of amorphous, nanostructured, diamond-like carbon, and nanodiamond,” *Philos. Trans. R. Soc. A Math. Phys. Eng. Sci.*, vol. 362, no. 1824, pp. 2477–2512, 2004.

[132] V. Y. Osipov, A. V. Baranov, V. A. Ermakov, T. L. Makarova, L. F. Chungong, A. I. Shames, K. Takai, T. Enoki, Y. Kaburagi, M. Endo, and A. Ya. Vul, “Raman characterization and UV optical absorption studies of surface plasmon resonance in multishell nanographite,” *Diam. Relat. Mater.*, vol. 20, no. 2, pp. 205–209, 2011.

[133] J. McDonald-Wharry, M. Manley-Harris, and K. Pickering, “Carbonisation of biomass-derived chars and the thermal reduction of a graphene oxide sample studied using Raman spectroscopy,” *Carbon N. Y.*, vol. 59, pp. 383–405, 2013.

[134] S. K. Sze, N. Siddique, J. J. Sloan, and R. Escribano, “Raman spectroscopic characterization of carbonaceous aerosols,” *Atmos. Environ.*, vol. 35, no. 3, pp. 561–568, 2001.

[135] A. Cuesta, P. Dhamelincourt, J. Laureyns, A. Martínez-Alonso, and J. M. D. Tascón, “Raman microprobe studies on carbon materials,” *Carbon N. Y.*, vol. 32, no. 8, pp. 1523–1532, 1994.

[136] A. C. Ferrari and J. Robertson, “Origin of the 1150-cm^{-1} Raman mode in nanocrystalline diamond,” *Phys. Rev. B*, vol. 63, no. 12, p. 121405, 2001.

[137] A. C. Ferrari, J. C. Meyer, V. Scardaci, C. Casiraghi, M. Lazzeri, F. Mauri, S. Piscanec, D. Jiang, K. S. Novoselov, S. Roth, and A. K. Geim, “Raman spectrum of graphene and graphene layers,” *Phys. Rev. Lett.*, vol. 97, no. 187401, pp. 1–4, 2006.

[138] International Centre for Diffraction Data, "PDF: 01-089-7213."

[139] N. Gierlinger, T. Keplinger, and M. Harrington, “Imaging of plant cell walls by confocal Raman microscopy,” *Nat. Protoc.*, vol. 7, no. 9, pp. 1694–1708, 2012.

[140] E. Quirico, J. N. Rouzaud, L. Bonal, and G. Montagnac, “Maturation grade of coals as revealed by Raman spectroscopy: Progress and problems,” *Spectrochim. Acta Part A*,

vol. 61, pp. 2368–2377, 2005.

[141] N. Gierlinger, T. Keplinger, and M. Harrington, “Imaging of plant cell walls by confocal Raman microscopy,” *Nat. Protoc.*, vol. 7, no. 9, pp. 1694–1708, 2012.

[142] K. Ishimaru, T. Hata, P. Bronsveld, D. Meier, and Y. Imamura, “Spectroscopic analysis of carbonization behavior of wood, cellulose and lignin,” *J. Mater. Sci.*, vol. 42, no. 1, pp. 122–129, 2007.

[143] M. Monthioux, M. Oberlin, A. Oberlin, and X. Bourrat, “Heavy Petroleum Products : Microtexture and Ability To Graphite,” *Carbon N. Y.*, vol. 20, no. 3, pp. 167–176, 1982.

[144] P. J. F. Harris and S. C. Tsang, “High-resolution electron microscopy studies of non-graphitizing carbons,” *Philos. Mag. A Phys. Condens. matter, Struct. defects Mech. Prop.*, vol. 76, no. 3, pp. 667–677, 1997.

[145] N. S. Murthy, S. O. Dantas, Z. Iqbal, and R. H. Baughman, “X-ray diffraction evidence for the formation of a discotic phase during graphitization,” *Carbon N. Y.*, vol. 39, no. 6, pp. 809–813, 2001.

[146] B. Manoj and A. G. Kunjomana, “Study of stacking structure of amorphous carbon by X-ray diffraction technique,” *Int. J. Electrochem. Sci.*, vol. 7, no. 4, pp. 3127–3134, 2012.

[147] R. E. Franklin, “Crystallite Growth in Graphitizing and Non-Graphitizing Carbons,” *Proc. R. Soc. London A Math. Phys. Eng. Sci.*, vol. 209, no. 1097, pp. 196–218, 1951.

[148] C. R. Houska and B. E. Warren, “X-ray study of the graphitization of carbon black,” *J. Appl. Phys.*, vol. 25, no. 12, pp. 1503–1509, 1954.

[149] S. V. Vassilev, D. Baxter, L. K. Andersen, C. G. Vassileva, and T. J. Morgan, “An overview of the organic and inorganic phase composition of biomass,” *Fuel*, vol. 94, pp. 1–33, 2012.

[150] H. Fujimoto, “Theoretical X-ray scattering intensity of carbons with turbostratic stacking and AB stacking structures,” *Carbon N. Y.*, vol. 41, no. 8, pp. 1585–1592, 2003.

[151] A. Oya and S. Otani, “CATALYTIC GRAPHITIZATION OF CARBONS BY VARIOUS METALS,” *Carbon N. Y.*, vol. 17, pp. 131–37, 1979.

[152] C. L. Burket, R. Rajagopalan, and H. C. Foley, “Overcoming the barrier to graphitization

in a polymer-derived nanoporous carbon," *Carbon N. Y.*, vol. 46, no. 3, pp. 501–510, 2008.

[153] C.-F. Chang, C.-Y. Chang, and W.-T. Tsai, "Effects of Burn-off and Activation Temperature on Preparation of Activated Carbon from Corn Cob Agrowaste by CO2 and Steam," *J. Colloid Interface Sci.*, vol. 232, no. 1, pp. 45–49, Dec. 2000.

[154] E. N. El Qada, S. J. Allen, and G. M. Walker, "Adsorption of Methylene Blue onto activated carbon produced from steam activated bituminous coal: A study of equilibrium adsorption isotherm," *Chem. Eng. J.*, vol. 124, no. 1–3, pp. 103–110, Nov. 2006.

[155] O. Ioannidou and A. Zabaniotou, "Agricultural residues as precursors for activated carbon production-A review," *Renew. Sustain. Energy Rev.*, vol. 11, no. 9, pp. 1966–2005, 2007.

[156] Suhas, P. J. M. Carrott, and M. M. L. Ribeiro Carrott, "Lignin - from natural adsorbent to activated carbon: A review," *Bioresour. Technol.*, vol. 98, no. 12, pp. 2301–2312, 2007.

[157] J. Hayashi, A. Kazehaya, K. Muroyama, and A. P. Watkinson, "Preparation of activated carbon from lignin by chemical activation," *Carbon N. Y.*, vol. 38, no. 13, pp. 1873–1878, 2000.

[158] L. Khezami, A. Chetouani, B. Taouk, and R. Capart, "Production and characterisation of activated carbon from wood components in powder: Cellulose, lignin, xylan," *Powder Technol.*, vol. 157, no. 1–3, pp. 48–56, 2005.

[159] J. B. Aladekomo and R. H. Bragg, "Structural Transformations Induced in Graphite by Grinding - Analysis of 002 X-Ray Diffraction Line-Profiles," *Carbon N. Y.*, vol. 28, no. 6, pp. 897–906, 1990.

[160] T. D. Shen, W. Q. Ge, K. Y. Wang, M. X. Quan, J. T. Wang, W. D. Wei, and C. C. Koch, "Structural Disorder and Phase-Transformation in Graphite Produced by Ball Milling," *Nanostruct. Mater.*, vol. 7, no. 4, pp. 393–399, 1996.

[161] R. E. Franklin, "The interpretation of diffuse X-ray diagrams of carbon," *Acta*

Crystallogr., vol. 3, no. 2, pp. 107–121, 1950.

[162] P. B. Hirsch, "X-ray scattering from coals," *Proc. R. Soc. London. Ser. A Math. Phys. Sci.*, vol. 226, no. 1165, pp. 143–169, 1954.

[163] J. Y. Howe, C. J. Rawn, L. E. Jones, and H. Ow, "Improved crystallographic data for graphite," *Powder Diffr.*, vol. 18, no. 2, pp. 150–154, 2003.

[164] B. E. Warren, "X-Ray Diffraction in Random Layer Lattices," *Phys. Rev.*, vol. 59, no. 9, p. 693, 1941.

[165] A. C. Ferrari, "Raman spectroscopy of graphene and graphite: Disorder, electron-phonon coupling, doping and nonadiabatic effects," *Solid State Commun.*, vol. 143, no. 1–2, pp. 47–57, 2007.

[166] M. H. Gass, U. Bangert, A. L. Bleloch, P. Wang, R. R. Nair, and A. K. Geim, "Free-standing graphene at atomic resolution," *Nat. Nanotechnol.*, vol. 3, pp. 676–681, 2008.

[167] C. Cong, K. Li, X. X. Zhang, and T. Yu, "Visualization of arrangements of carbon atoms in graphene layers by Raman mapping and atomic-resolution TEM," *Sci. Rep.*, vol. 3, p. 1195, 2013.

[168] J. Campos-Delgado, J. M. Romo-Herrera, X. Jia, D. A. Cullen, H. Muramatsu, Y. A. Kim, T. Hayashi, Z. Ren, D. J. Smith, Y. Okuno, T. Ohba, H. Kanoh, K. Kaneko, M. Endo, H. Terrones, M. S. Dresselhaus, and M. Terrones, "Bulk production of a new form of sp2 carbon: Crystalline graphene nanoribbons," *Nano Lett.*, vol. 8, no. 9, pp. 2773–2778, 2008.

[169] J. C. Meyer, A. K. Geim, M. I. Katsnelson, K. S. Novoselov, T. J. Booth, and S. Roth, "The structure of suspended graphene sheets," *Nature*, vol. 446, pp. 60–63, 2007.

[170] W. Xu, X. Wang, Q. Zhou, B. Meng, J. Zhao, J. Qiu, and Y. Gogotsi, "Low-temperature plasma-assisted preparation of graphene supported palladium nanoparticles with high hydrodesulfurization activity," *J. Mater. Chem.*, vol. 22, no. 29, pp. 14363–14368, 2012.

[171] S. Rather, R. Zacharia, S. W. Hwang, M. Naik, and K. S. Nahm, "Hydrogen uptake of palladium-embedded MWCNTs produced by impregnation and condensed phase reduction method," *Chem. Phys. Lett.*, vol. 441, no. 4–6, pp. 261–267, 2007.

[172] C.-C. Huang, N.-W. Pu, C.-A. Wang, J.-C. Huang, Y. Sung, and M.-D. Ger, "Hydrogen storage in graphene decorated with Pd and Pt nano-particles using an electroless deposition technique," *Sep. Purif. Technol.*, vol. 82, pp. 210–215, 2011.

[173] C. H. Chen, T. Y. Chung, C. C. Shen, M. S. Yu, C. S. Tsao, G. N. Shi, C. C. Huang, M. D. Ger, and W. L. Lee, "Hydrogen storage performance in palladium-doped graphene/carbon composites," *Int. J. Hydrogen Energy*, vol. 38, no. 9, pp. 3681–3688, 2013.

[174] A. E. Aksoylu, M. Madalena, A. Freitas, M. F. R. Pereira, and J. L. Figueiredo, "Effects of different activated carbon supports and support modifications on the properties of Pt/AC catalysts," *Carbon N. Y.*, vol. 39, no. 2, pp. 175–185, 2001.

[175] M. A. Fraga, E. Jordão, M. J. Mendes, M. M. a. Freitas, J. L. Faria, and J. L. Figueiredo, "Properties of Carbon-Supported Platinum Catalysts: Role of Carbon Surface Sites," *J. Catal.*, vol. 209, no. 2, pp. 355–364, 2002.

[176] P. A. Simonov, A. V. Romanenko, I. P. Prosvirin, E. M. Moroz, A. I. Boronin, A. L. Chuvilin, and V. A. Likholobov, "On the nature of the interaction of H_2PdCl_4 with the surface of graphite-like carbon materials," *Carbon N. Y.*, vol. 35, no. 1, pp. 73–82, 1997.

[177] L. B. Okhlopkova, A. S. Lisitsyn, V. A. Likholobov, M. Gurrath, and H. P. Boehm, "Properties of Pt/C and Pd/C catalysts prepared by reduction with hydrogen of adsorbed metal chlorides. Influence of pore structure of the support," *Appl. Catal. A Gen.*, vol. 204, no. 2, pp. 229–240, 2000.

[178] S. C. Mu, H. L. Tang, S. H. Qian, M. Pan, and R. Z. Yuan, "Hydrogen storage in carbon nanotubes modified by microwave plasma etching and Pd decoration," *Carbon N. Y.*, vol. 44, no. 4, pp. 762–767, 2006.

[179] International Centre for Diffraction Data, "PDF: 01-075-0871."

[180] International Centre for Diffraction Data, "PDF: 01-086-1888."

[181] International Centre for Diffraction Data, "PDF: 00-005-0681."

[182] C. Kim, Y. A. Kim, J. H. Kim, M. Kataoka, and M. Endo, "Self-assembled palladium nanoparticles on carbon nanofibers.," *Nanotechnology*, vol. 19, no. 14, p. 145602, 2008.

[183] R. J. Farrauto, J. K. Lampert, M. C. Hobson, and E. Waterman M., "Thermal

decomposition and reformation of PdO catalysis; support effects," *Appl. Catal. B Environ.*, vol. 6, no. 95, pp. 263–270, 1995.

[184] E. W. Washburn, "The dynamics of capillary flow," *Phys. Rev.*, vol. 17, no. 3, pp. 273–283, 1921.